The SCUBA Local Universe Galaxy Survey
– Dust along the Hubble sequence –

Catherine Vlahakis

A thesis submitted to
Cardiff University
for the degree of

Doctor of Philosophy

September 2005

UMI Number: U584736

UMI

Dissertation Publishing

ProQuest
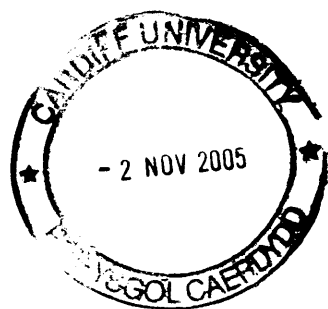
Abstract

This thesis presents new results from the SCUBA Local Universe Galaxy Survey (SLUGS) — the optically-selected sample. SLUGS is the first large systematic submillimetre survey of the local Universe, and was carried out with the SCUBA camera on the James Clerk Maxwell Telescope. Since SCUBA is sensitive to the 90% of dust too cold to radiate significantly in the *IRAS* bands this new sample, taken from the Center for Astrophysics (CfA) optical redshift survey (Huchra et al. 1983) and hence selected on the basis of optical emission alone, represents the first unbiased survey of dust in galaxies along the whole length of the Hubble sequence. There is little change found in the properties of dust in galaxies along the Hubble sequence, except a marginally significant trend for early-type galaxies to be less luminous submillimetre sources than late-types. Nevertheless, 6 out of 11 elliptical galaxies were detected, although some of the emission may possibly be synchrotron rather than dust emission. The *IRAS* and submillimetre fluxes are found to be well-fitted by a two-component dust model with dust emissivity index β=2. The ratio of the mass of cold dust to the mass of warm dust is found to be much higher for the optically-selected galaxies than found for the previous *IRAS*-selected SLUGS sample (Dunne et al. 2000; Dunne & Eales 2001), and can reach values of $\sim$1000. Comparison of the results for the *IRAS*- and optically-selected samples shows that there is a population of galaxies containing a large proportion of cold dust that is unrepresented in the *IRAS* sample. Local submillimetre luminosity and dust mass functions are derived, both directly from the optically-selected SLUGS sample, and by extrapolation from the *IRAS* PSCz survey using the method of Serjeant & Harrison (2005) (by extrapolating the spectral energy distributions of the *IRAS* PSCz survey galaxies out to 850 μm we probe a wider range of luminosities than probed directly by the SLUGS samples), and excellent agreement is found between the two. They are found to be well-fitted by Schechter functions except at the highest luminosities. As a consequence of the omission of cold galaxies from the *IRAS* sample the previous *IRAS*-selected luminosity function is found to be too low by a factor of 2, reducing the amount of cosmic evolution required between the low-z and high-z universe. Finally, the results of the OS SLUGS are used to assess the reliability of the Carilli & Yun (1999, 2000a) radio–submillimetre redshift estimator technique, for the first time using a sample of 'normal' local galaxies.

Acknowledgements

Publications

Vlahakis C., Dunne L., Eales S., 2005, MNRAS in press, *The SCUBA Local Universe Galaxy Survey - III. Dust along the Hubble sequence*; (includes the results presented in Chapters 3, 4 and 5 of this Thesis)

Vlahakis C., Dunne L., Eales S., 2005, *The SCUBA Local Universe Galaxy Survey*, in proceedings of *The Dusty and Molecular Universe 2004 - A Prelude to HERSCHEL and ALMA, Paris, October 2004*, ESA Publications

Mortier A.M.J. et al., 2005, accepted in MNRAS, *The SCUBA Half Degree Extragalactic Survey (SHADES)*

Vlahakis C., Dunne L., Eales S., 2004, astro-ph/0408466, *The SCUBA Local Universe Galaxy Survey Optically-Selected Sample*, in proceedings of *Penetrating Bars Through Masks of Cosmic Dust — The Hubble Tuning Fork strikes a New Note, South Africa, June 2004*, Springer

Vlahakis C., Eales S., in preparation, *The SCUBA Local Universe Galaxy Survey - IV. Constraining the radio-submillimetre redshift indicator*; (includes the results presented in Chapter 6 of this Thesis)

Vlahakis C., Eales S., Dye S., in preparation, *The SCUBA Local Universe Galaxy Survey - V. Optical data*

Vlahakis C., Eales S., Davies J.I., in preparation, *The SCUBA Local Universe Galaxy Survey - VI. Cold dust in Elliptical Galaxies*

List of Acronyms

AGN Active Galactic Nucleus

CCD Charge Coupled Device

DSS Digitised Sky Surveys

FIR Far-Infrared

FSC *IRAS* Faint Source Catalogue

FWHM Full Width Half Maximum

IPAC Infrared Processing and Analysis Center

IRAS Infrared Astronomical Satellite

IRS *IRAS*-Selected (with respect to the SLUGS samples, see below)

IRSA Infrared Science Archive

ISM Interstellar Medium

ISRF Interstellar Radiation Field

JCMT James Clerk Maxwell Telescope

LEDA Lyon-Meudon Extragalactic Database

NASA National Aeronautics and Space Administration

NED NASA Extragalactic Database

OS Optically-Selected (with respect to the SLUGS samples, see below)

PSC *IRAS* Point Source Catalogue

PSCz *IRAS* PSCz redshift survey (a redshift survey of the PSC, see above)

SCANPI *IRAS* Scan Processing and Integration

SCUBA Submillimetre Common-User Bolometer Array

SDSS Sloan Digital Sky Survey

SED Spectral Energy Distribution

SLUGS SCUBA Local Universe Galaxy Survey

UV Ultraviolet

2MASS Two Micron All Sky Survey

Contents

List of Figures

List of Tables

Chapter 1

Introduction

The first investigations of dust in relatively large samples of galaxies began in the 1980s with the advent of *IRAS*, the *InfraRed Astronomical Satellite*, (e.g. the Devereux & Young (1990) sample of 58 nearby spiral galaxies). *IRAS* surveyed more than 96% of the sky at wavelengths of 12, 25, 60 and 100 μm. However, the limitations of investigating dust at far-IR wavelengths are marked; the strong temperature dependence of thermal emission means that even a small amount of warm dust can dominate the emission from a substantially larger proportion of cold dust, and *IRAS* is insensitive to dust with $T \lesssim 30$ K. Devereux & Young (1990) found the value of the gas-to-dust ratio ($\sim$1000) to be an order of magnitude higher than was typically found for the Milky Way, and hence suggested that *IRAS* may have 'missed' up to 90% of the dust in late-type galaxies (this 90% of dust being too cold to be detected by *IRAS*, since *IRAS* does not have spectral coverage at λ >100 μm but the peak in the FIR emission should occur between 100 and 200 μm). Furthermore, *IRAS* revealed relatively little about the dust in early-type galaxies, since only $\sim$15% of ellipticals were detected by *IRAS* (Bregman et al. 1998).

The next major step in the study of dust in galaxies is to make observations in the submillimetre waveband (100 μm $\leq \lambda \leq$ 1 mm) since the 90% of dust that is too cold to

radiate in the far-IR will be producing most of its emission in this waveband. The advent of the SCUBA camera on the James Clark Maxwell Telescope (JCMT)[1] (Holland et al. 1999) opened up the submillimetre waveband for astronomy and made it possible, for the first time, to investigate the submillimetre emission of large samples of galaxies. SCUBA has 2 bolometer arrays (850 μm and 450 μm) which operate simultaneously with a field of view of $\sim$2 arcminutes. At 850 μm SCUBA is sensitive to thermal emission from dust with fairly cool temperatures ($T \geq 10$ K) so crucially, whereas *IRAS* was insensitive to cooler dust ($T \lesssim 30$ K), SCUBA should trace most of the dust mass. Prior to SCUBA only a handful of submillimetre measurements had been made of nearby galaxies, using single-element bolometers (e.g. Eales, Wynn-Williams & Duncan 1989; Stark et al. 1989; Clements, Andreani & Chase 1993). In particular, in contrast to the extensive survey work going on at other wavelengths, prior to SCUBA it was not possible to carry out a large survey in the submillimetre waveband.

1.1   Investigating dust using the submillimetre

"Surely, there is a hole in the heavens!"

— Sir William Herschel (1785)

For 75 years interstellar dust has been known to have a profound effect on our optical view of the Universe, although its effects have been observed since the 18th Century when Herschel first pointed out dark patches in the Milky Way. In an astrophysics text in 1903 it was written of these structures that:

---

[1]The JCMT is operated by the Joint Astronomy Center on behalf of the UK Particle Physics and Astronomy Research Council, the Netherlands Organisation for Scientific Research and the Canadian National Research Council.

"The fact is a general one, that in all the forest of the universe there are glades and clearings. How they come to be thus diversified we cannot pretend to say; but we can see that the peculiarity is structural — that it is an outcome of the fundamental laws governing the distribution of cosmic matter. Hence the futility of trying to explain its origin, as a consequence, for instance, of the stoppage of light by the interposition of obscure bodies, or aggregations of bodies, invisibly thronging space."

— Agnes Clerke (1903)

In fact, far from futile, it was not to be many years before an explanation of these 'obscuring bodies' was shown. It was in 1930 that Trumpler first showed that the existence of solid dust particles in interstellar space (whose size is comparable to the wavelength of light) could explain the observed dimming and reddening of starlight. These solid dust particles are believed to have a wide range of grain sizes, ranging from a few tens of atoms to a few microns, and are mainly composed of carbon and silicates (Li 2004). Over the past century astronomers' perception of dust has moved from its role as an annoying cause of extinction and obscuration to its important roles as a component of the interstellar medium and in many aspects of astronomy, from galaxy evolution to the formation of stars and planets. We now know we live in a dusty universe, with dust seen in a multitude of astrophysical environments — in interstellar clouds, star-forming regions, supernova ejecta, comets, planetary systems, and distant galaxies, to mention just a few. A consequence of this is that our optical/UV view of the high-redshift universe may be significantly biased by dust obscuration. This is highlighted by the discovery of the cosmic IR background (Puget et al 1996; Fixsen et al. 1998; Hauser et al. 1998), which has shown that about half of the stellar energy emitted in the universe has been absorbed by dust.

"Light may be absorbed by...solid particles of extremely small size."

— Robert J. Trumpler (1930)

The presence and nature of dust is mainly inferred from its interaction with starlight. A dust grain lying in the line of sight between a star and the observer will cause the starlight reaching the observer to be dimmed and reddened by a combination of scattering and absorption, the absorbed stellar energy then being re-radiated at far-infrared (FIR) wavelengths. The existence of radiation from dust was predicted in 1946 by van der Hulst (van der Hulst 1946); when a dust grain absorbs optical or UV photons it is heated and, because of Kirchhoff's law, emits an equal power to that absorbed. With the advent of *IRAS* in the 1980s such dust emission has been found to constitute more than one third of a nearby normal spiral galaxy's total (bolometric) luminosity; in other words $\sim 30\%$ of the total stellar radiation in normal spiral galaxies is thus converted into dust emission (Soifer & Neugebauer 1991; Calzetti 2001).

The emission from a grain at a given wavelength depends on the quantity $Q_{em}(\lambda)$ — its *emissivity*. This quantity can be calculated at a particular wavelength using Mie theory, and its behaviour at different wavelengths is very different — for example at UV wavelengths the emissivity $Q_{em}(\lambda) \sim 1$ since the grain size $a \approx \lambda$; in the FIR $a \ll \lambda$ and so $Q_{em}(\lambda) \ll 1$. At FIR and submillimetre wavelengths dust radiates as as a modified Planck function (a 'grey-body'; two example grey-bodies are shown in Figure 1.1), modified by an emissivity term (β) such that the emission can be parameterised by

$$Q_{em}(\nu) \propto \nu^{\beta} \qquad \text{or} \qquad Q_{em}(\lambda) \propto \lambda^{-\beta} \tag{1.1}$$

where the quantity β is known as the *dust emissivity index*. Until recently the value of β was quite uncertain, with suggested values for FIR–submillimetre wavelengths lying between 1 and 2 (Hildebrand 1983). Recent multi-wavelength studies of galaxies including submillimetre observations, however, have consistently found $1.5 \leq \beta \leq 2$ with $\beta=2$ tending to be favoured (Chini et al. 1989; Chini & Krügel 1993; Braine et al. 1997; Alton et al. 1998b; Bianchi et al. 1998; Frayer et al. 1999; DE01). This agrees with the values found in *COBE*/FIRAS studies of the diffuse ISM in the Galaxy (Masi et al. 1995; Reach et al. 1995; Sodroski et al. 1997).

The flux density S_λ of the dust emission can be described by

$$S_\lambda \propto Q_{em}(\lambda)\, B(\lambda, T_d) \tag{1.2}$$

where B(λ, T_d) is the Planck function

$$B(\lambda, T_d) = \frac{2hc^2}{\lambda^5 e^{hc/\lambda k T_d} - 1} \tag{1.3}$$

or in terms of frequency, ν,

$$B(\nu, T_d) = \frac{2h}{c^2} \frac{\nu^3}{e^{h\nu/kT_d} - 1}. \tag{1.4}$$

Thus, in the Rayleigh-Jeans part of the Planck function, which is sampled when looking at submillimetre wavelengths, the slope is very steep, since the submillimetre spectral index is then the sum of the Rayleigh-Jeans spectral index and the dust emissivity index β such that

$$S_\nu \propto \nu^{2+\beta} \qquad \text{or} \qquad S_\lambda \propto \lambda^{-(4+\beta)} \tag{1.5}$$

(since the Rayleigh-Jeans approximation is $(B(\lambda, T) \approx 2ckT/\lambda^4)$).

The way dust grains absorb and emit radiation is related to their optical properties and sizes and this, together with the strength of the interstellar radiation field (ISRF) in which they are immersed, determines the temperature to which dust in galaxies is heated by the visible/UV radiation from stars. The equilibrium or 'steady-state' temperature of a dust grain immersed in a typical ISRF can be predicted by

$$T_{eq} \sim T_{eff}\, W^{1/(4+\beta)} \tag{1.6}$$

(van der Hulst 1946; Purcell 1976; Disney et al. 1989), where T_{eq} is the equilibrium temperature of a dust grain, T_{eff} is the effective mean temperature of the ISRF (usually assumed to be a blackbody of temperature $\approx 10\,000$ K, i.e. the equivalent stellar temperature) and W a dilution factor ($\approx 10^{-14}$). For $\beta \sim 1$ (an appropriate value for the
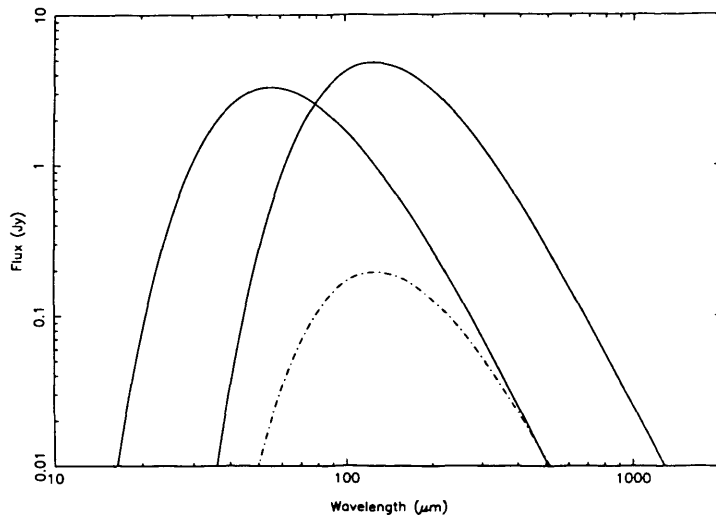
Figure 1.1:   Two example grey-body curves (solid curves), corresponding to T_d=55 K (left) and T_d=20 K (right), and assuming β=2. The *IRAS* bands (whose longest wavelength was ~100 μm) encompass the peak of the hotter grey-body curve, but clearly measurements at longer wavelengths (>100 μm, i.e in the submillimetre) are required in order to describe any dust component at ~20 K. In this example the ratio of the mass of cold dust to the mass of warm dust is ~100. It is interesting to note that, in this example, up to four times as much cold dust compared to warm dust could be systematically "hidden" by the hotter grey-body curve; this is shown as the dashed line.

visible/UV wavelengths where most of the absorption occurs; Bianchi 1999) this gives $T_{eq} \sim 16$ K. Although this is a simplistic model (many more detailed models have been produced; Mathis, Mezger & Panagia 1983; Draine & Lee 1984; Li & Draine 2001) this nonetheless gives us a prediction of the temperature we should expect for an interstellar dust grain (without assuming a grain size) in a typical low-density environment, gaining energy mainly by absorbing UV photons from the ISRF. In fact Mathis, Mezger & Panagia (1983), Draine & Lee (1984) and Li & Draine (2001) show that, with the exception of very small grains, equilibrium temperatures would be in the range 15–25 K. Dust grains immersed in stronger radiation fields, such as star-forming regions or near to an AGN, will be heated to higher temperatures.

1.1.1 The paradigm for dust in galaxies

The current paradigm for dust in galaxies is that there are two main components: (i) a warm component (T > 30 K) arising from dust grains near to star-forming regions and heated by Lyman α photons from young (OB) stars, and (ii) a cool 'cirrus' component (T = 15–25 K) arising from diffuse dust associated with the HI and heated by the general interstellar radiation field (ISRF) (Cox, Krügel & Mezger 1986; Lonsdale Persson & Helou 1987; Rowan-Robinson & Crawford 1989). *IRAS* would only have detected the warm component (see Figure 1.1), hence using *IRAS* fluxes alone to estimate dust temperature would result in an overestimate of the dust temperature and an underestimate of the dust mass. Conversely, using the submillimetre to estimate dust masses has clear advantages. The flux is more sensitive to the mass of the emitting material and less sensitive to temperature in the Rayleigh-Jeans part of the Planck function, which is sampled when looking at longer submillimetre wavelengths.

1.1.2 The advantage of the submillimetre

By analogy with the Wien displacement law the wavelength at which the spectral energy distribution (SED) peaks can be related to the dust temperature by

$$\lambda_p \sim \frac{3000}{T_d} \left(\frac{5}{5 + \beta} \right) \tag{1.7}$$

which reduces to the standard form of Wien's law if we set $\beta = 0$, but as described above for dust grains we expect $1 < \beta < 2$ so the peak of the spectrum lies at FIR–submillimetre wavelengths for $T_d < 100$ K. This is significant, because it means that *IRAS* was insensitive to cooler dust ($T \lesssim 30$ K). Also, the fact that the bolometric luminosity emitted by dust depends on $T^{4+\beta}$ means that even a small amount of warm dust can dominate the emission from a substantially larger proportion of cold dust. The mass of dust M_D is given by

$$M_d = \frac{S_\nu D^2}{\kappa_d(\nu) B(\nu, T_d)} \tag{1.8}$$

(Hildebrand 1983), where S_ν is the measured flux at a frequency ν, $B(\nu, T_d)$ is the Planck function for the temperature T_d, and D is the distance to the source; κ_d is the dust mass opacity coefficient ($\kappa_d(\nu) = 4a\rho/3Q_{em}(\nu)$, where a is the grain radius and ρ is its density). Thus using *IRAS* measurements alone will not give accurate temperature estimates, and consequently is likely to underestimate the dust mass, since the FIR emission from a galaxy will be dominated by warm dust even if this component has relatively little mass. This bias towards higher temperatures in the fits of grey-body curves to FIR fluxes is one of the reasons why it was for so long difficult to show the presence of cold dust in galaxies. However, using the submillimetre flux to estimate dust masses will provide much more accurate estimates than using *IRAS* fluxes alone because the submillimetre is less sensitive to temperature and more sensitive to mass (the Rayleigh-Jeans approximation means that $M_d \propto T^{-1}$), and also is sensitive to thermal emission from dust with fairly cool temperatures ($T \geq 10\,\mathrm{K}$); so crucially, whereas *IRAS* was insensitive to cooler dust ($T \lesssim 30\,\mathrm{K}$), SCUBA should trace most of the dust mass.

1.2   Previous investigations of cold dust in galaxies

As discussed in the previous section, the strong advantage of investigating dust at sub-millimetre wavelengths is the sensitivity to the 90% of dust (Devereux & Young 1990) too cold to radiate significantly in the *IRAS* bands. Studies at the longer wavelengths (170–850 μm; e.g. ISO, SCUBA) have confirmed the existence of cold dust components ($15 < T_d < 25\,\mathrm{K}$), in line with the theoretical prediction of grain heating by the general ISRF (Cox et al. 1986), both in nearby spiral galaxies and in more IR-luminous/interacting systems (e.g. Guélin et al. 1993, 1995; Sievers et al. 1994; Sodroski et al. 1994; Neininger et al. 1996; Braine et al. 1997; Dumke et al. 1997; Alton et al. 1998a,b, 2001; Haas et al. 1998; Davies et al. 1999; Frayer et al. 1999; Papadopoulos & Seaquist 1999; Xilouris et al. 1999; Haas et al. 2000; DE01; Popescu et al. 2002; Spinoglio et al. 2002; Hippelein et al.

2003; Stevens, Amure & Gear 2005). Many of these authors find an order of magnitude more dust than *IRAS* observations alone would indicate. Alton et al. (1998a), for example, find, by comparing their 200 μm images of nearby galaxies to B-band images, that the cold dust is increasingly dominant at larger radii and has a greater radial extent than the stars; they conclude that *IRAS* 'missed' the majority of dust grains lying in the spiral disks. For the cold component they find a dust temperature (18–21 K) which is close to the theoretical prediction for grain heating by the ISRF.

Other studies find evidence of cold dust components in a large proportion of galaxies. Stickel et al. (2000) find a large fraction of their 170 μm Serendipity Survey of compact sources to have high S_{170}/S_{100} flux ratios and suggest this indicates a cold dust component ($T \leq 20$ K) exists in many galaxies. By studying mid- and far-IR properties, Contursi et al. (2001) find evidence of a cold dust component ($T \sim 22$ K) for most of their sample of late-type galaxies; they suggest that it arises from big dust grains in thermal equilibrium with the ISRF. Popescu et al. (2002) find, for their sample of late-type (later than S0) galaxies in the Virgo Cluster, that 30 out of 38 galaxies detected in all three observed wavebands (60, 100 and 170 μm) exhibit a cold dust component; they find this to be true across all types of late-type systems, from early giant spirals to blue compact dwarfs.

1.3 The need for a local submillimetre galaxy survey

A survey of the dust in nearby galaxies is important not only because of the advantages of investigating dust using the submillimetre discussed in Section 1.1.2 but also because of the need to interpret the results from submillimetre surveys of the distant Universe. Many deep SCUBA surveys have now been carried out (e.g. Smail, Ivison & Blain 1997; Hughes et al. 1998; Barger et al. 1998, 1999; Blain et al. 1999a; Eales et al. 1999; Lilly et al. 1999; Mortier et al. 2005), however studies of the high redshift Universe, and in particular studies of cosmological evolution (e.g. Eales et al. 1999; Blain et al. 1999b), have until now

depended critically on assumptions about, rather than measurements of, the submillimetre properties of the *local* Universe. Prior to the existence of a direct local measurement of the submillimetre luminosity function (LF; the space density of galaxies as a function of their submillimetre luminosity) most deep submillimetre investigations have started from a local *IRAS* 60 μm LF, extrapolating out to submillimetre wavelengths by making assumptions about the average FIR-submm SED. However, Dunne et al. (2000) showed that this underestimates the local submillimetre LF, and thus a direct measurement of the local submillimetre LF is vital for overcoming this significant limitation in the interpretation of the results of high-redshift surveys.

The ideal way in which to carry out a submillimetre survey of the local Universe, with the aim of producing a local submillimetre LF, would be to survey a large area of the sky and then measure the redshifts of all the submillimetre sources found by the survey. However, with current submillimetre instruments such a survey is effectively impossible since, for example, SCUBA's field of view is only $\sim$2 arcminutes. The alternative method, and the only one that is currently practical, is to carry out targeted submillimetre observations of galaxies selected from statistically complete samples selected in other wavebands. With an important proviso, explained below, it is then possible to produce an unbiased estimate of the submillimetre LF using 'accessible volume' techniques (Avni & Bahcall 1980; see Chapter 5).

To this end several years ago we began the SCUBA Local Universe Galaxy Survey (SLUGS). Dunne et al. (2000, hereafter D00), Dunne & Eales (2001, hereafter DE01), and Dunne (2000, PhD Thesis, hereafter LD00) presented the results of SCUBA observations of a sample selected at 60 μm (the *IRAS*-Selected sample, hereafter the IRS sample). This thesis presents the results of SCUBA observations of an optically-selected sample (hereafter the OS sample).

1.4 The need for an optically-selected sample

1.4.1 Investigating cold dust

The IRS SLUGS sample was selected from the *IRAS* Bright Galaxy Sample (BGS; Soifer et al. 1989), and so by definition will contain bright submillimetre sources. Such a sample will also, by definition, be biased towards warmer dust temperatures. It is then entirely possible that 'normal' (i.e. more quiescent, rather than starburst) galaxies have quite different submillimetre properties to these bright *IRAS* galaxies, especially if 'normal' galaxies contain larger proportions of cold dust (see Section 1.2 for details of previous investigations of cold dust in nearby galaxies).

The accessible volume method will produce unbiased estimates of the LF provided that no class of galaxy is unrepresented in the sample used to construct the LF. D00 produced the first direct measurements of the submillimetre LF and dust mass function (DMF; the space-density of galaxies as a function of their dust mass) using the IRS sample, but this LF would be biased if there exists a 'missed' population of submillimetre-emitting galaxies, i.e. a population *that is not represented at all in the IRS sample*. In this earlier work D00/LD00 found that the slope of the submillimetre LF at lower luminosities was steeper than -2, which suggested that the submillimetre sky should be infinitely bright (a submillimetre 'Olbers' Paradox'). Since in reality this is obviously not the case this indicated that the IRS sample may not be fully representative of all submillimetre-emitting sources in the local Universe. This 'missed' population could consist of cold-dust-dominated galaxies, i.e. galaxies containing large amounts of 'cold' dust (at $T < 25\,\mathrm{K}$), which would be strong emitters at $850\,\mu\mathrm{m}$ but weak $60\,\mu\mathrm{m}$-emitters. The OS sample is selected on the basis of the optical emission alone and so, unlike the IRS sample which was biased towards warmer dust, the OS sample should be free from dust temperature selection effects and should include any 'cold' population missed by *IRAS*. The results from the OS sample will therefore test the idea that the earlier LF derived from the IRS

Table 1.1: Parameters describing the bulge-to-disk ratio for different Hubble types: B/T is from Kent (1985), and B/D is calculated from these values as described in the text.

Type	B/T	B/D
S0–S0/a	0.63	1.70
Sa–Sab	0.45	0.82
Sb–Sbc	0.24	0.32
Sc+	0.11	0.12

SLUGS sample was an underestimate.

1.4.2   Investigating dust along the Hubble sequence

Since the OS sample is selected on the basis of optical emission and therefore (unlike the IRS sample) will not biased towards warmer dust, the OS sample also allows us to determine, for the first time, the amount of cold dust contained in galaxies across all Hubble types. A study of how the submillimetre properties of galaxies changes along the Hubble sequence allows us to investigate, for example, how the mass of dust in late-type galaxies differs from that in early-type galaxies. Since only ~15% of ellipticals were detected by *IRAS* (Bregman et al. 1998), *IRAS* revealed relatively little about the dust in early-type galaxies.

We can investigate how much dust one might expect to find in a galaxy of given Hubble type with the following simple analysis. Suppose we first make the broad assumption that the dust and gas are associated with the population of young stars and are contained within the galaxy's disk, while the galaxy's bulge contains only the population of old stars (and contains no dust and gas). In this scenario an elliptical galaxy would be expected to be devoid of dust and gas. We can then investigate the proportions of dust we would expect in other types of galaxy using the bulge-to-disk ratios for different Hubble types

found by Kent (1985). Kent (1985) described the bulge-to-disk ratio by the term B/T which in fact expresses the bulge as a fraction of the total galaxy T (T=B+D). This is simply related to the bulge-to-disk ratio in the true sense (B/D), which we will adopt for this analysis, such that

$$\left(\frac{D}{B}\right) = \left(\frac{B}{T}\right)^{-1} - 1 \ . \tag{1.9}$$

Both these parameters are shown in Table 1.1. Then, for example, for S0–S0/a galaxies B=1.7 D. Since we are interested in mass, if we assume the parameter T represents the total galaxy mass M_{gal} and the bulge and disk parameters represent the relative masses of the bulge and the disk components, we can then also relate the total galaxy mass M_{gal} to the bulge and disk parameters such that:

$$M_{gal} = B + D \qquad \text{or} \qquad M_{gal} = 1.7D + D \tag{1.10}$$

and thus,

$$D = M_{gal}/2.7 \ . \tag{1.11}$$

If we then return to our original assumption that all the dust is located in the galaxy's disk then we can simply say that the mass of dust M_{dust} is

$$M_{dust} = k\,D \tag{1.12}$$

where k is a constant, and hence

$$M_{dust} \propto \frac{M_{gal}}{2.7} \ . \tag{1.13}$$

In other words, from this analysis we would expect the mass of dust for an S0–S0/a galaxy to be proportional to 37% of the total galaxy mass. Similarly, the expected fraction of dust for each of the Hubble types listed in Table 1.1 is shown in Table 1.2. The calculated dust fraction quite clearly increases towards later Hubble types; thus, if the above assumption is even broadly true then we would expect to see fractionally (and proportionately) more dust in galaxies as we move along the Hubble sequence.

Table 1.2: The mass of dust M_{dust} as a fraction proportional to the total galaxy mass M_{gal}, for galaxies of different Hubble types.

Type	dust fraction
S0–S0/a	0.37
Sa–Sab	0.55
Sb–Sbc	0.76
Sc+	0.89

However, though it was once thought that ellipticals were entirely devoid of dust and gas (as would be expected from the above rough analysis) optical absorption studies now show that dust is usually present (Goudfrooij et al. 1994; van Dokkum & Franx 1995), and furthermore dust masses for ellipticals detected by *IRAS* have been found to be as much as a factor of 10–100 higher when estimated from their FIR emission compared to estimates from optical absorption (Goudfrooij & de Jong 1995). Thus, although it seems that early-types do usually contain dust it is still quite unclear how much dust one is typically likely to find in an early type galaxy compared to a later type. The OS sample will thus provide a useful probe of if, and how, the properties of dust change along the Hubble sequence.

1.4.3   Investigating dust in 'normal' galaxies

As I have already discussed in the previous sections, while the IRS sample contained bright *IRAS* galaxies the OS sample will contain more 'normal' (i.e. more quiescent, rather than starburst) galaxies. Thus the OS sample will allow us to investigate the submillimetre properties of normal galaxies in the local universe, such as the mass of dust they contain, the temperature of the dust, and how the dust is distributed. We can investigate these properties not only as a function of Hubble type (as discussed in the previous section) but also in comparison to the *IRAS*-bright objects. For example, the submillimetre emission

in the IRS sample galaxies tends to follow a compact nuclear morphology, but if the OS sample contains larger proportions of colder dust it might be expected to be distributed throughout the disk and even follow the spiral arm structure (see discussion of previous investigations of cold dust in galaxies in Section 1.2). The OS sample is therefore also a useful probe of the submillimetre morphology of 'normal' galaxies.

1.5 Outline of Thesis

This thesis presents the results from the SCUBA Local Universe Galaxy Survey (SLUGS) optically-selected sample. This OS sample is taken from the Center for Astrophysics (CfA) optical redshift survey (Huchra et al. 1983), and includes galaxies drawn from right along the Hubble sequence. Since it is selected on the basis of optical emission alone the OS sample is not biased towards galaxies with large FIR fluxes or warm dust. In this thesis I will compare my results for the OS SLUGS to the previous SLUGS results for the IRS sample (D00; DE01; LD00) and will address the possibility that the IRS sample 'missed' a population of cold-dust-dominated galaxies (since the IRS sample was a complete sample of 104 60μm-selected galaxies, selected from the IRAS Bright Galaxy Sample (BGS) it was, by definition, biased towards galaxies with large FIR fluxes). If there exists a population of cold, strong submillimetre-emitting galaxies *that is not represented at all in the IRS sample* then the submillimetre luminosity function and dust mass function presented in D00/LD00 will be biased. As such one of the key aims of this work on the OS sample was to produce a sample which is more fully representative of the submillimetre-emitting population.

Chapter 2. In this chapter I discuss the observation and data reduction techniques applied to the OS SLUGS sample.

Chapter 3 presents the OS sample results. The 850 μm and 450 μm fluxes are presented, together with dust models fitted to the SEDs of the detected galaxies, their corresponding fitted dust temperatures, emissivity indices (β) and calculated dust masses. 850 μm S/N maps of the detected galaxies are presented, along with discussion of individual objects and the submillimetre features of the overall sample.

Chapter 4 presents an analysis of the submillimetre properties of the OS sample. I discuss the relationships of global properties, including luminosities, dust mass and gas mass and, by comparison with the previous IRS sample (D00/LD00), how these vary depending on optical or IR selection. I investigate the implications of any population of cold-dust-dominated galaxies that was 'missed' by *IRAS* but detected by the OS sample, and finally use the OS sample results to investigate whether the submillimetre properties of galaxies vary as one moves along the Hubble sequence.

Chapter 5. I use the OS sample results to produce new estimates of the local submillimetre luminosity and dust mass functions by two different methods: 1) directly from the OS sample and 2) using a method from Serjeant & Harrison (2005) to extrapolate the *IRAS* PSCz galaxies' (Saunders et al. 2000) SEDs out to 850 μm in order to probe a wider range of luminosities. By comparison with the previous IRS sample results I then investigate whether the IRS sample LF and DMF were biased.

Chapter 6. I use the results of the OS and IRS samples to investigate the FIR–radio and submillimetre–radio luminosity correlations in 'normal' local galaxies compared to bright *IRAS* galaxies, as well as any correlations with radio–submillimetre spectral index. Using the radio–submillimetre redshift indicator technique of Carilli & Yun (1999, 2000a) I predict the variation of the the radio-submillimetre ratio with redshift for the OS SLUGS galaxies, which I then compare to real observations of deep

SCUBA sources from Chapman et al. (2005). Using the above results I attempt to assess the usefulness and reliability of the Carilli & Yun technique.

Chapter 7. Finally, in this chapter I summarise the results of the OS SLUGS sample along with suggestions for future work.

A Hubble constant $H_0 = 75$ km s^{-1} Mpc^{-1} and a 'concordance' universe with $\Omega_M = 0.3$ and $\Omega_\Lambda = 0.7$ are assumed throughout.

Chapter 2

Observations and Data Reduction

2.1 Overview

In this Chapter I will describe how the OS sample was selected and how it was observed. I will also outline the data reduction and flux measurement methods used, as well as the production of signal-to-noise maps. These methods are very similar to those carried out, and described in detail, by LD00, D00 and DE01 for the IRS sample.

2.2 The Sample

This OS sample is taken from the Center for Astrophysics (CfA) optical redshift survey (Huchra et al. 1983), which is a magnitude-limited sample of optically-selected galaxies, complete to $m_B \leq 14.5$ mag. It has complete information on magnitude, redshift and morphological-type, and also avoids the Galactic plane. The OS sample consists of all galaxies in the CfA sample lying within three arbitrary strips of sky: (i) all declinations from (B1950.0) $16.1 < \text{RA} < 21.5$, (ii) all RAs from $15 < \text{Dec} < 16$ and (iii) RAs from $9.6 < \text{RA} < 12.8$ with declinations from $25 < \text{Dec} < 26$. This is shown graphically in Fig-
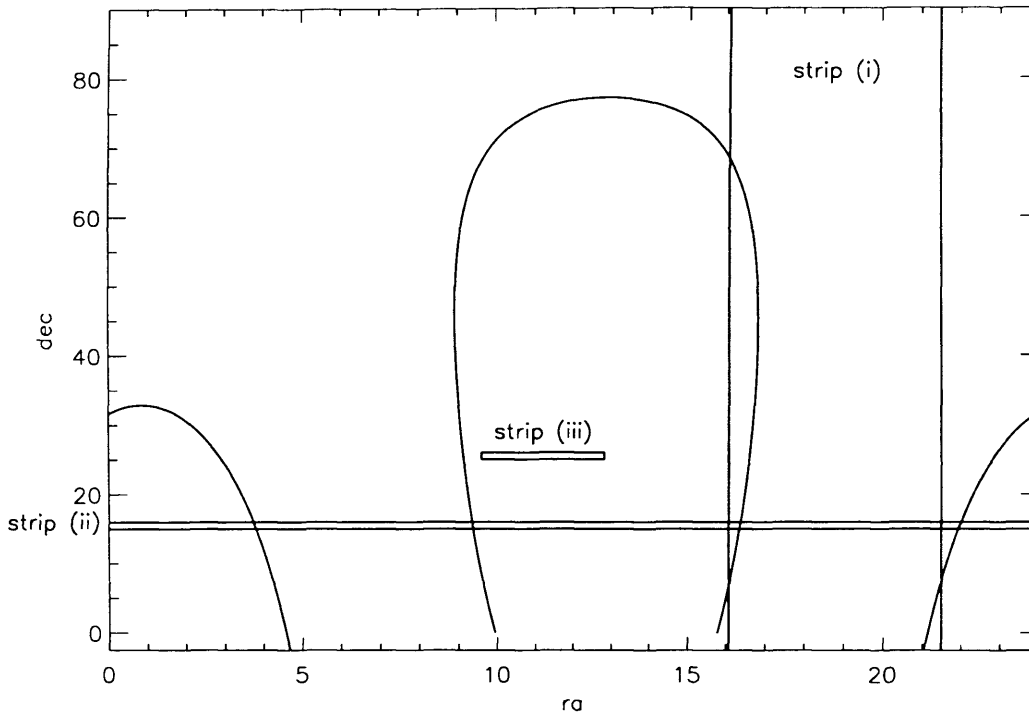
Figure 2.1: The sky area covered by the OS sample. The curved lines enclose the regions covered by the CfA optical redshift survey, from which the OS sample was selected. The sample consists of all galaxies in the CfA sample lying within three arbitrary strips of sky as indicated.

ure 2.1. A lower velocity limit of $1900\,\mathrm{km\,s^{-1}}$ was also imposed to try to ensure that the galaxies did not have an angular diameter larger than SCUBA's field of view. There are 97 galaxies in the CfA survey meeting these selection criteria and 81 of these were observed (which were at convenient positions given the observing schedule). The OS sample covers an area of ~ 570 square degrees and is listed in Table 3.1. Unlike the IRS sample which contained many interacting pairs (most of which were resolved by SCUBA but not by IRAS), the OS sample contains just 2 such pairs.

2.3 Observations

The OS sample galaxies were observed using the SCUBA bolometer array at the 15-m James Clark Maxwell Telescope (JCMT) on Mauna Kea, Hawaii, between December 1997 and January 2001, with a handful of additional observations in February 2003 (due to bad data obtained when observed the first time round; see Section 2.4). Observational methods and techniques were similar to those for the IRS sample described in D00 and LD00. A brief description of these is given below.

The SCUBA camera has 2 bolometer arrays (850 μm and 450 μm, with 37 and 91 bolometers respectively) which operate simultaneously with a field of view of ~ 2.3 arcminutes at 850 μm (slightly smaller at 450 μm). Beamsizes are measured to be typically $\sim$15 arcsec at 850 μm and $\sim$8 arcsec at 450 μm, depending on chop throw and conditions, usng the maps of the calibrator objects (see below). Observations were made in 'jiggle-map' mode which, for sources smaller than the field of view, is the most efficient mapping mode. Since the arrangement of the bolometers is such that the sky is instantaneously undersampled, and since we observed using both arrays, the secondary mirror was stepped in a 64-point jiggle pattern in order to fully sample the sky. The cancellation of rapid sky variations is provided by the telescope's chopping secondary mirror, operating at 7.8 Hz. Linear sky gradients and the gradual increase or decrease in sky brightness are compensated for by nodding the telescope to the 'off' position every 16 seconds. A chop throw of 120 arcsec in azimuth was used, except where the galaxy had a nearby companion, in which case a chop direction which avoided the companion was chosen.

The zenith opacity τ was measured by performing regular skydips. The observations were carried out under a wide range of weather conditions, with opacities at 225GHz τ_{225} ranging from 0.03 to 0.13 (weather grade 1 to 4 in JCMT terminology). This means that some galaxies were observed in excellent conditions ($\tau_{225} < 0.05$) while others were observed in far less than ideal conditions. As a result useful 450 μm data was obtained

for only a fraction of the sample. This is discussed in more detail in Section 2.6. The observations were centred on the coordinates taken from the NASA/IPAC Extragalactic Database[1] (NED). Regular checks were made on the pointing and it was found to be generally good to ~2 arcsec. The integration times depended on source strength and weather conditions. Since most of the OS sample are relatively faint submillimetre sources typically ~12 integrations (~30 mins) were used, although many sources were observed in poorer weather and so required longer integration times.

The data was calibrated by making jiggle maps of Uranus and Mars, or, when these planets were unavailable, of the secondary calibrators CRL 618 and HL Tau. The planet fluxes were taken from the JCMT FLUXES program, and CRL 618 and HL Tau were assumed to have fluxes of 4.56 and 2.32 Jy beam^{-1} respectively at 850 μm. (In practice the primary (planet) calibrators were available for all but one or two observations, and all the useable 450 μm data (see Section 2.6) had primary calibrators).

2.4 Data reduction

The 850 μm and 450 μm data were reduced using standard SCUBA specific tasks in the SURF package (Jenness & Lightfoot 1998, 2000; Jenness et al. 2002), where possible via the XORACDR automated data reduction pipeline (Economou et al. 2004). The data-reduction process is shown schematically in Figure 2.2.

The off-nod position was subtracted from the on-nod in the raw beam-switched data (REDUCE_SWITCH) and the data was then flat-fielded. FLATFIELD removes variations in the bolometer response by taking the data output from REDUCE_SWITCH and dividing the data arrays present (both or either 850 μm and 450 μm) by a standard flatfield which is stored in the raw data-file. The data was then corrected for atmospheric extinction

---

[1] The NASA/IPAC Extragalactic Database (NED) is operated by the Jet Propulsion Laboratory, California Institute of Technology, under contract with the National Aeronautics and Space Administration.

(EXTINCTION).

In order to correct SCUBA data for atmospheric extinction we must accurately know the value of the zenith sky opacity, τ. Although less crucial at 850 μm if the observation is made in good weather ($\tau_{225} < 0.08$) and at low airmass, in worse weather or at 450 μm the measured source flux can be severely affected by an error in τ. τ is most commonly estimated either by performing a skydip or by extrapolating to the required wavelength (using relations given in the JCMT literature/webpages and in Archibald et al. (2002)) from polynomial fits to the continuous measurements of τ at 225GHz made at the nearby Caltech Submillimetre Observatory. Since skydips are measured relatively infrequently, the polynomial fits to the CSO τ_{225} data are recommended in the JCMT literature to be the more reliable way of estimating τ for both SCUBA arrays. As such, for both 850 μm and 450 μm data wherever possible (the large majority of observations) the derived (using the ORAC-DR *csofit* calibration routine) CSO opacity at 225 GHz (τ_{cso}) was used. Where τ_{cso} values were not available the opacities were derived from 850 μm skydip measurements (at 450 μm using the τ_{850}-to-τ_{450} relation described in the JCMT literature and Archibald et al. (2002)).

The raw data was inspected, using standard KAPPA tasks, an example of which is shown in Figure 2.3. Noisy bolometers and 'bad' integrations were noted but not removed at this stage (it was frequently found to be the case that flagging a noisy bolometer as 'bad' creates even worse noise spikes in the final map around the position of the removed bolometer data). Large spikes were removed from the data using standard SURF routines (SIGCLIP). SIGCLIP clips the data to a user-specified number of σ (in this case 4σ) from the mean of the whole array, and therefore is useful for making noisy bolometers less noisy since it is on these bolometers that the task has greatest effect. It should be noted that this clipping method was only valid because the sample consists of relatively faint objects. This method would *not*, however, be appropriate for bright point sources (see section on Calibrators), since the source signal would be interpreted as noise and significant source
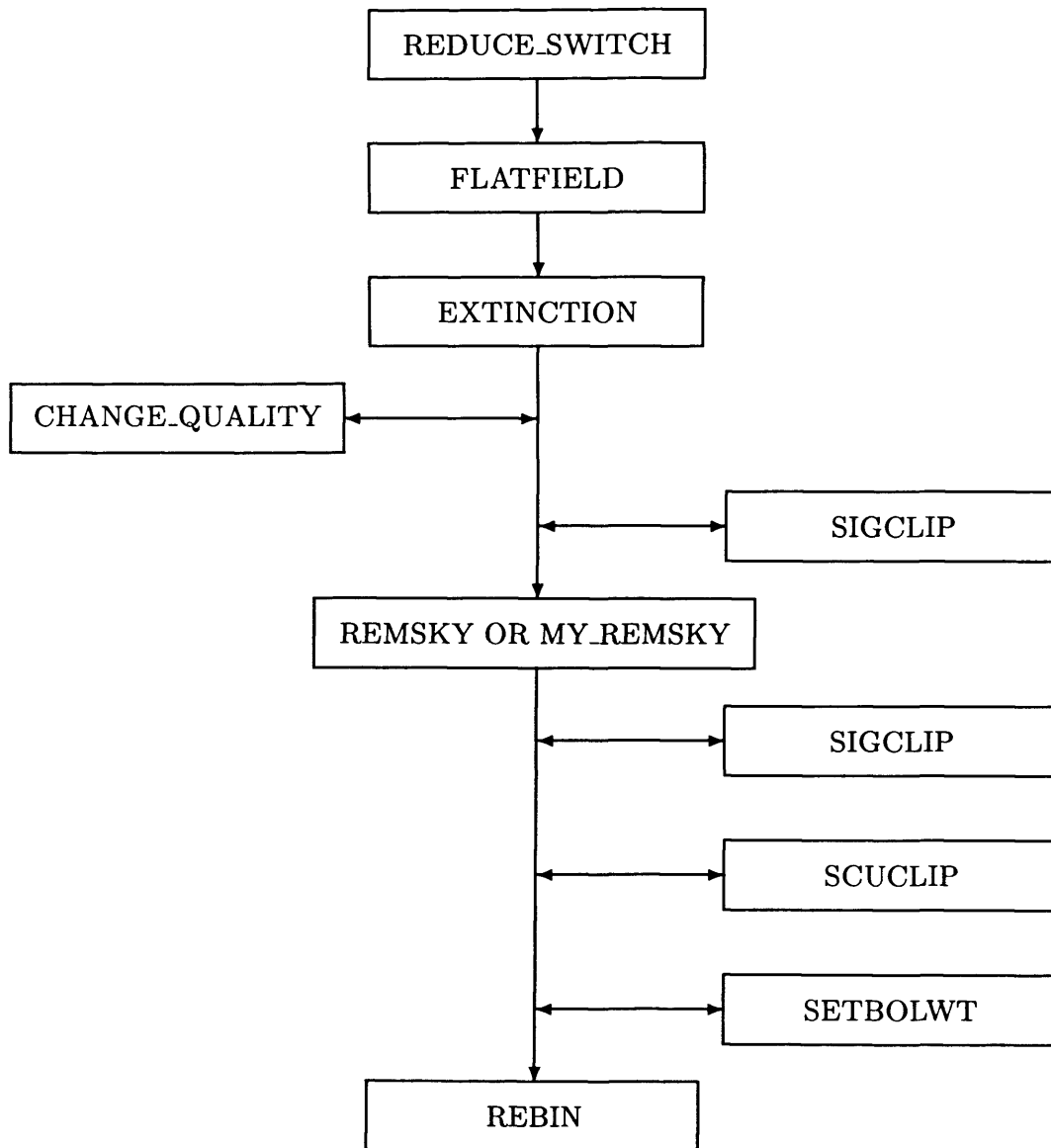
Figure 2.2:   A flow diagram for SURF Jiggle Map data reduction.

pgc3563
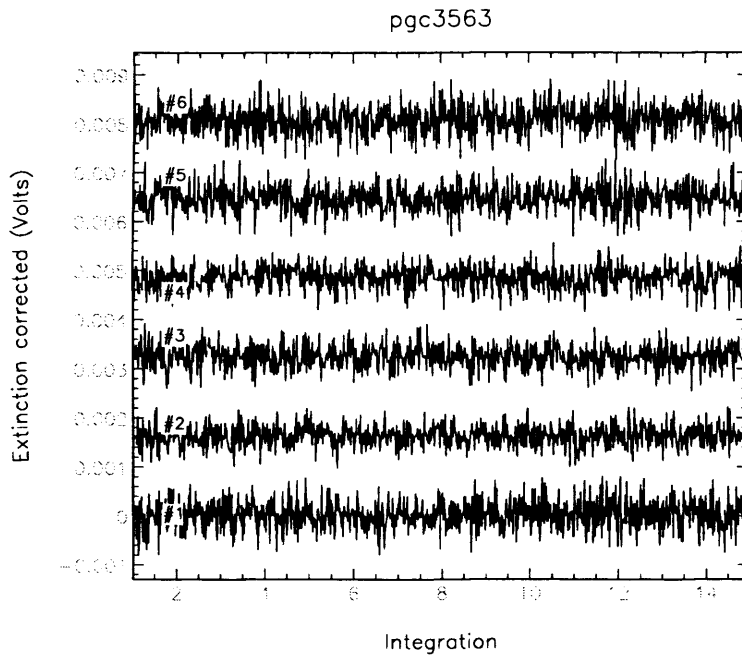
Figure 2.3: An example of looking at individual bolometer data using KAPPA tasks.

signal would be clipped away; large variations in source signal are created due to the 'jiggle' pattern, which moves the source in and out of the bolometers, and so on-source bolometers will appear noisy and would be clipped by a task such as SIGCLIP.

The nodding and chopping should remove any noise which is correlated between the different bolometers. In reality, since the data was not observed in the driest and most stable conditions the signal on different bolometers was often highly correlated due to incomplete sky subtraction. In the majority of cases the SURF task REMSKY was used, which takes a set of user-specified bolometers to estimate the sky variation as a function of time. More explicitly, in each time step REMSKY takes the median signal from the specified sky bolometers and subtracts it from the whole array. To ensure that the sky bolometers specified were looking at sky alone and did not contain any source emission I used a rough SCUBA map together with optical (*Digitised Sky Survey*[2] (DSS)) images

[2]The Digitised Sky Surveys were produced at the Space Telescope Science Institute under U.S. Gov-
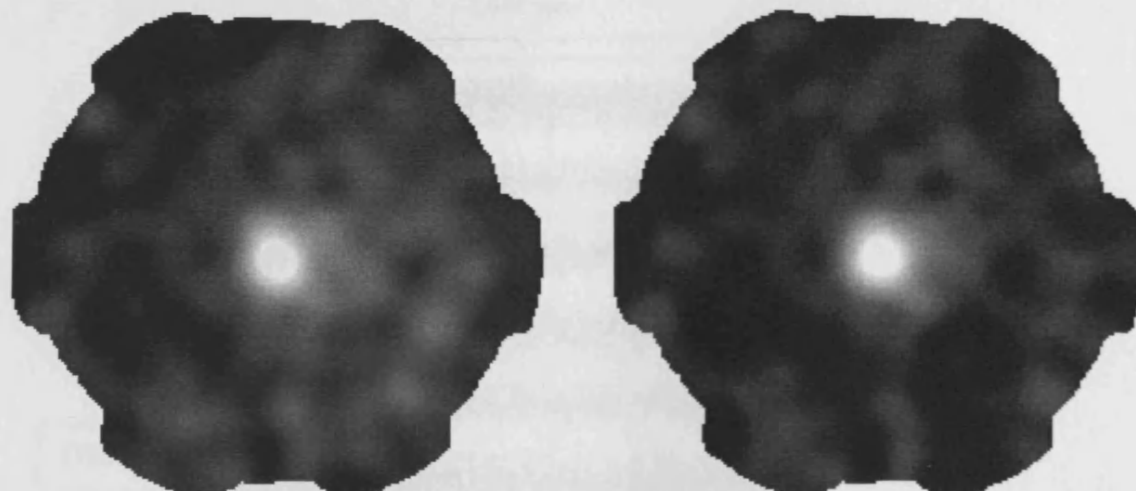
       (a) sky removal using REMSKY   (b) sky removal using MY_REMSKY

Figure 2.4: An example of the removal of 'tilted sky' planes (IC 5090 shown here). In (a) the sky was removed using REMSKY, leaving a 'tilted sky' – the RHS has a positive background while the LHS is negative. In (b) the sky was removed using MY_REMSKY – the 'tilted sky' is removed.

as a guide when choosing the bolometers, though in this sample there are so few bright sources that in the majority of cases all bolometers could be safely used.

Even after this step, however, due to the relatively poor conditions in which much of the data was observed the residual sky level was sometimes found to vary linearly across the array, giving a 'tilted plane' on the array. An example of a 'tilted sky' is shown in Figure 2.4(a). Moreover, in a number of cases a noisy 'striped' sky (due possibly to some short-term instrumentation problem) was found. An example of this is shown in Figure 2.5(a). Though the SURF task REMSKY was designed to remove the sky noise,

(a) sky removal using REMSKY   (b) sky removal using MY_REMSKY
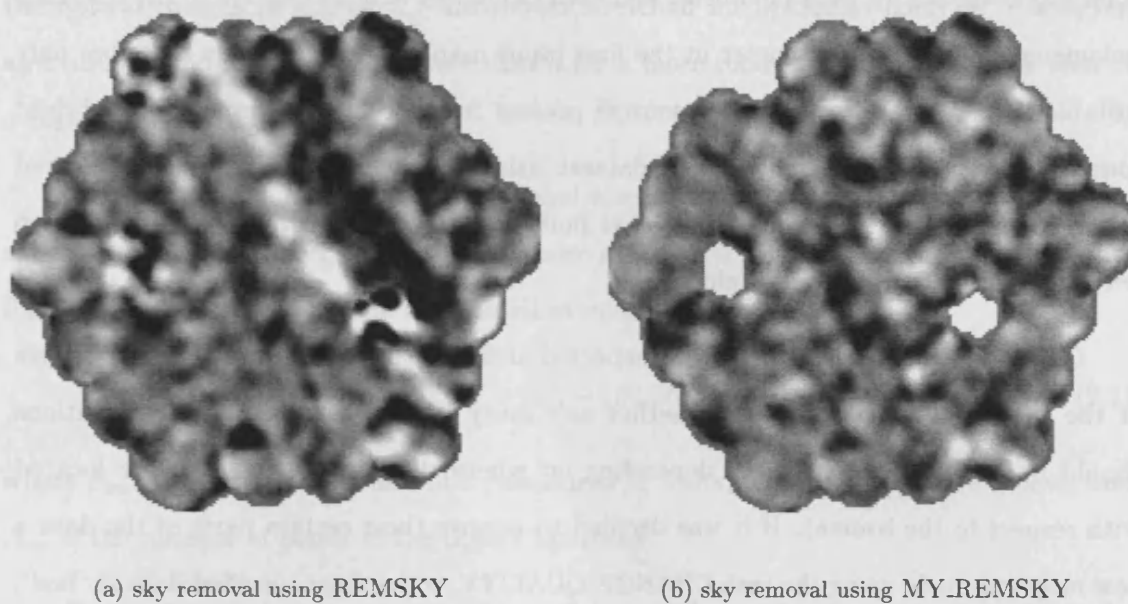
Figure 2.5: An example of the removal of a 'stripey sky', in this case for UGC7157. In (a) the sky was removed using REMSKY, leaving a 'stripey sky'. In (b) the sky was removed using MY_REMSKY – the 'stripey sky' is removed.

it is relatively simplistic and cannot remove such spatially varying 'tilted' or 'striped' sky backgrounds. In these cases, as for the IRS sample (D00), one of our own programs (MY_REMSKY; written by Steve Eales) was used in place of REMSKY. As can be seen in Figures 2.4 and 2.5, using this custom program the sky is then successfully removed. However, in a handful of cases the 'striped' sky was so severe that it could not be removed, so these objects were re-observed in February 2003.

Once the effects of the sky were removed the data was despiked again (using SIGCLIP and SCUCLIP and the final map produced by re-gridding the data into a pixel grid to form an image on 1 arcsecond pixels (REBIN). Where there were multiple data-sets for a given source they were binned together into a co-added final map. In these cases each data set was weighted prior to co-adding using the SURF task SETBOLWT, which calculates the

standard deviation for each bolometer and then calculates weights relative to the reference bolometer (the central bolometer in the first input map). This method is therefore only suitable if there are no very bright sources present in the central bolometer (if a bright source was present we weighted each dataset using the inverse square of its measured average noise). This step also ensures that noisy bolometers contribute to the final map with their correct statistical weight.

Once a first map was made it was inspected and compared with optical (DSS) images of the galaxy in order to decide whether any noisy bolometers and 'bad' integrations should be removed (for example depending on where the bad bolometers were located with respect to the source). If it was decided to remove these certain parts of the data a new map was made using the task CHANGE_QUALITY, which flags specified data as 'bad', after the EXTINCTION stage; the rest of the data reduction process was then carried out as before (see Figure 2.2).

As a final step, for presentation purposes, a version of the map was made calibrated in units of Jy/beam. This was done by multiplying the map by its *Flux Conversion Factor* (FCF) (see Section 2.7 for a description of how the FCF value is calculated). This map calibrated in Jy/beam was only used for flux measurement if the source was smaller than the beam, in which case it was treated as a point source and the total source flux (S_{tot}) was taken to be equal to the peak source flux (S_{peak}): $S_{tot} = S_{peak}$.

2.5   850 μm flux measurement

The fluxes were measured from the SCUBA maps by choosing a source aperture over which to integrate the flux, such that the signal-to-noise was maximised. The galaxy's extent in the optical (DSS) images and the extent of the submillimetre source on the S/N map (see Section 2.9) were used to select an aperture that included as much of the galaxy's submillimetre flux as possible while minimising the amount of sky included. Note

the optical images in Figure 3.1 are shown stretched for optimum contrast – however, apertures for flux measurement were drawn for a more modest optical extent, as seen at a standard level of contrast.

Estimates of the noise and the sky level were made by placing a number of smaller apertures on off-source regions of the map (also see Section 2.8 below). The object aperture flux was then corrected for the sky contribution by using:

$$S_{corr} = S_{ap} - (S_{ms}N_{ap}) \qquad (2.1)$$

where S_{ap} is the object aperture flux (measured in Volts), S_{ms} is the mean sky level and N_{ap} is the number of pixels in the object aperture.

Conversion of the measured aperture flux in volts to Janskys was carried out by measuring the calibrator flux for that night using the same aperture as for the object. The orientation of the aperture (relative to the chop throw) was also kept the same as for the object, as this has a significant effect (due to the error lobe contribution to the flux), particularly for more elliptical apertures.

The calibrated object flux (i.e. in Jy) is then given by:

$$S_{obj}(Jy) = S_{obj_{corr}}(V) \times \frac{S_{cal_{tot}}(Jy)}{S_{cal_{ap}}(V)} \qquad (2.2)$$

where $S_{cal_{tot}}$ is the total calibrator flux (whose value was obtained as described in Section 2.3), $S_{obj_{corr}}$ is the measured object flux in the aperture corrected for the sky contribution (see above), and $S_{cal_{ap}}$ is the measured calibrator flux in that same aperture.

Objects are said to be detected at $> 3\sigma$ if either: (a) the peak S/N in the S/N map was $> 3\sigma$ or (b) the flux in the aperture was greater than 3 times the noise in that aperture (where the noise is defined as described in Section 2.8).

2.6 450 μm data

Due to the increased sensitivity to weather conditions at 450 μm, sources emitting at 450 μm will only be detected if they are relatively bright at 850 μm. This, together with the wide range of observing conditions for this sample, meant that useful 450 μm data was found for only 19 objects.

Where possible the 450 μm emission was measured in an aperture the same size as used for the 850 μm data. In some cases a smaller aperture had to be used for the 450 μm data, and these individual cases are discussed in Section 3.3.

2.7 FCF calculation

The major and minor HPBWs, with major and minor axes here θ_{m1} and θ_{m2}, and the peak flux value (V_{peak}), were measured on the calibrator map using Gaia. The Flux Conversion Factor (FCF) was then found as follows:

Firstly the true HPBW θ_A of the telescope is determined. For a planet calibrator the measured beamsize θ_m needs to be deconvolved, since a planet is usually not a point source. So:

$$\theta_{A1} = \sqrt{\theta_{m1}^2 - \left(\frac{\ln 2}{2}W\right)^2} \qquad (2.3)$$

where W is the diameter of the planet (in arcseconds) and θ_m is the measured beam size (in arcseconds). Likewise for θ_{A2}. Then:

$$\theta_A = \sqrt{\theta_{A1} \times \theta_{A2}} \qquad (2.4)$$

Next, the coupling factor, K, is derived — this is a measure of how much of the total flux

is picked up by the beam. This is given by:

$$K = \frac{x^2}{1 - e^{-x^2}}$$ (2.5)

where

$$x = \frac{SD}{0.6 \times \theta_A}$$ (2.6)

and SD is the semi-diameter of the planet (in arcseconds). The flux in the beam is then

$$S_{beam} = \frac{S_{tot}}{K}$$ (2.7)

where S_{tot} is the planet's total flux.

Finally, the FCF, C_λ, is given by

$$C_\lambda = \frac{S_{beam}}{V_{peak}} .$$ (2.8)

2.8   Error analysis

The error on the flux measurement is made up of three components:

- A background sky subtraction error σ_{sky} due to the uncertainty in the sky level.

- A shot (Poisson) noise term σ_{shot} due to pixel-to-pixel variations within the sky aperture. Unlike CCD images, in SCUBA maps the signal in adjoining pixels is correlated; this correlated noise depends on a number of factors, including the method by which the data is binned at the data reduction stage. This has been discussed in some detail by D00, who find that a correction factor is required for each array

to account for the fact that pixels are correlated; they find the factor to be 8 at 850 μm and 4.4 at 450 μm.

- A calibration error term σ_{cal} which for SCUBA observations at 850 μm is typically less than 10%. A conservative calibration factor of 10% at 850 μm has therefore been assumed. The calibration error at 450 μm was taken to be 15%, following DE01.

The relationships used to calculate the noise terms are as follows:

$$\sigma_{sky} = \sigma_{ms} N_{ap} \tag{2.9}$$

and

$$\sigma_{shot} = 8\sigma_{pix}\sqrt{N_{ap}} \quad \text{or} \quad \sigma_{shot} = 4.4\sigma_{pix}\sqrt{N_{ap}} \tag{2.10}$$

for 850 μm and 450 μm flux measurements respectively. The error in the mean sky $\sigma_{ms} = S.D./\sqrt{n}$, where S.D is the standard deviation of the mean sky values in 'n' apertures placed on off-source regions of the map. N_{ap} is the number of pixels in the object aperture; σ_{pix} is the mean standard deviation of the pixels within the sky apertures. The total error for each flux measurement is then given by

$$\sigma_{tot} = (\sigma_{sky}^2 + \sigma_{shot}^2 + \sigma_{cal}^2)^{1/2} \tag{2.11}$$

as for the IRS sample. This error analysis is discussed in detail in D00 and DE01.

850 μm fluxes were found to have total errors σ_{tot} typically in the range 15–30 %. 450 μm fluxes were found to have total errors σ_{tot} typically in the range 25–35 %. Note, the σ_{tot} used to determine whether a source was detected at the 3σ level is defined as in Equation 2.11 but without the calibration error term.
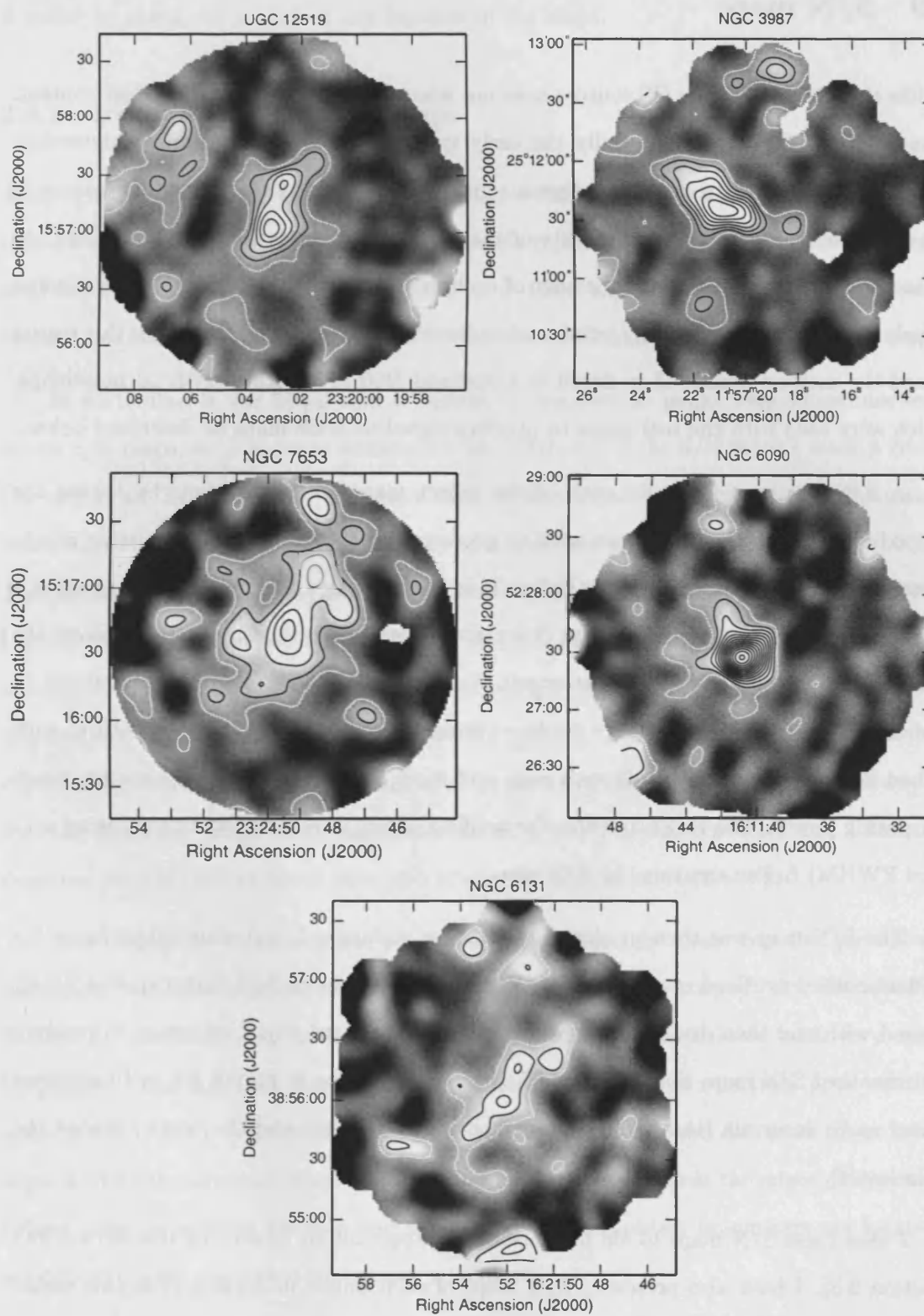
Figure 2.6:   Some example S/N maps. Contours show 1σ intervals (the white contour shows the 1σ level and the black contour the $\geq 2\sigma$ levels).

2.9 S/N maps

Unlike the IRS sources the OS sources were not selected on the basis of their dust content. Many of the OS sources, especially the early types, are close to the limit of detection. Also, it is often hard to assess whether a source is detected, or whether some feature of the source is real, due to the variability of the noise across the array. This is due both to an increase in the noise towards the edge of each map, caused by a decrease in the number of bolometers sampling each sky point, and to individual noisy bolometers. For this reason I used the method described in detail in LD00 and D00 to generate artificial noisemaps, which were used with the real maps to produce signal-to-noise maps as described below.

A S/N map was made for each of the object maps. This was done by taking the clipped object data that had been used to produce the object map and inputting it into a custom program written by Steve Eales. This program uses the 'real' data to produce a user-defined number of artificial maps (for a given observation this simulation replaces the real data for each bolometer by the output of a Gaussian random number generator). In this case 1000 artificial maps were made — fewer than this and very noisy features such as bad bolometers are not dealt with well, and more than this simply requires too much computing power. The real maps and the artificial maps were then smoothed (using a 12 pixel FWHM) before creating the S/N map.

The S/N map was then produced by making a standard deviation image using the 1000 smoothed artificial maps (using KAPPA tasks). The smoothed real map was finally aligned with and then divided by its corresponding standard deviation 'map' to produce the smoothed S/N map. Some example S/N maps are shown in Figure 2.6, with contours shown at 1σ intervals (the white contour shows the 1σ level and the black contour the $\geq 2\sigma$ levels).

I used these S/N maps to aid in choosing the aperture for measuring the 850 μm flux (Section 2.5). I have also presented S/N maps of each source in Section 3, as this makes

it easier to assess the reality of any features in the maps.

2.9.1 Reliability of the S/N maps

Although the S/N maps were produced using artificial noisemaps (as described in Section 2.9 above) which should normally adequately represent the noise across the given real map there are certain circumstances, such as a 'tilted-sky' (see Section 2.4) or the very noisiest bolometers, where residual 'noisy' features are found to remain in the S/N maps.

In particular, it was noted that a number of negative 3σ peaks were sometimes seen in the S/N maps, so in order to investigate the reliability of the S/N maps I made a count (by eye) of all the negative 3σ sources in each of the smoothed S/N maps. From Gaussian statistics the standard normal probability of a (positive or negative) 3σ result is 0.0026. This means that about 0.3 3σ sources per map would be expected by chance. In practice I found that 63% of all the S/N maps had either 0 or 1 negative source, with the mean number of negative 3σ peaks for those maps being 0.4 (the maps in which galaxies were detected and not detected gave the same overall results). This result is close to the number expected by chance, and so gives confidence in the reliability of the S/N maps. However, 8 of the 'detected' maps had 2 negative sources, 6 had 3 negative sources and 4 had > 4 negative sources (the numbers were also similar for the 'non-detections').

The reason for these negative sources is not completely clear, but the various atmospheric and instrumental effects such as the 'tilted' and 'stripey' sky described in Section 2.4 probably play an important role, and many are associated with very noisy bolometers. The fact that these observations were often made in relatively poor weather and the fact that the number of bolometers sampling each sky point decreases towards the edges of the submillimetre maps hence increasing the noise towards the edges of the maps (where more 3σ sources are seen and where some of the noisiest bolometers are located) are probably also important contributory factors.

For these few maps it is then often difficult to assess whether or not a source, or some feature of a source, is real. This means that any submillimetre emission seen beyond the main optical extent (and away from the centre of the map) should be regarded with some caution. For this reason, and in order to aid distinction between probable residual 'noisy' features in the S/N map and potential extended submillimetre emission, in Section 3.3 along with the presentation of all the S/N maps for the detected galaxies I also give a detailed discussion of the features of each individual individual S/N map.

2.10 *IRAS* fluxes

IRAS 100 μm and 60 μm fluxes, where available, were taken from the *IRAS Faint Source Catalogue* (Moshir et al. 1990; herein FSC) via the NED database. Where literature fluxes were unavailable the NASA/IPAC Infrared Science Archive[3] (IRSA) SCANPI (previously ADDSCAN) scan coadd tool was used to measure a flux from the *IRAS* survey data.

The small number of SCANPI fluxes are indicated by 's' in Table 3.1, and any special cases are discussed individually in Section 3.3. We take SCANPI fluxes to be detections if the measurements are formal detections at $> 4.5\sigma$ at 100 μm or $> 4\sigma$ at 60 μm, which Cox et al. (1995) conclude are actually detections at the 98% confidence level. Otherwise a 98% confidence upper limit (4.5σ at 100 μm or 4σ at 60 μm) is given using the 1σ error found from SCANPI (again following Cox et al. (1995)). If both fluxes are SCANPI measurements I mark the subsequent fitted values by '*' if there is any doubt as to their viability (for example possible source confusion, confusion with galactic cirrus, or no literature *IRAS* fluxes in NED for either band).

---

[3]The NASA/IPAC Infrared Science Archive is operated by the Jet Propulsion Laboratory, California Institute of Technology, under contract with the National Aeronautics and Space Administration.

Chapter 3

The OS Sample Results

3.1 Overview

This Chapter presents the results of the OS SLUGS sample. The 850 μm and 450 μm fluxes are presented, along with *IRAS* fluxes from the literature. Two-component dust models are fitted for the 19 galaxies with SCUBA fluxes at both wavelengths and isothermal dust models are fitted for all the galaxies detected. These fitted spectral energy distributions (SEDs) are presented, together with the fitted dust temperatures and emissivity index (β), and the corresponding calculated dust masses. 850 μm S/N maps of all the detected galaxies are presented, and individual objects discussed. The overall submillimetre features of the OS sample are also discussed. Analysis of these results will be presented in Chapter 4.

3.2 The overall sample

Of the 81 galaxies observed in the OS sample, 52 were detected. Table 3.1 lists the 850 μm fluxes and other parameters, including *IRAS* fluxes from the FSC (see Chapter 2) and Hubble types taken from the Lyon-Meudon Extragalactic Database (LEDA; Paturel

37

et al. 1989, 2003). For interacting systems resolved by SCUBA but not resolved by *IRAS* the 850 μm fluxes given are for the individual galaxies; the 850 μm fluxes measured for the combined system are listed in Table 3.2 along with the *IRAS* fluxes for the system. Table 3.3 lists the 450 μm fluxes for the 19 galaxies which are also detected at the shorter wavelength. The galaxies detected in the OS sample are shown in Figure 3.1, with our 850 μm SCUBA S/N maps overlaid onto optical (DSS) images. Comments on the individual maps are given in Section 3.3, together with any additional images.

3.2.1   Submillimetre morphology

The 850 μm images have several common features. Firstly, many spiral galaxies exhibit two peaks of 850 μm emission, seemingly coincident with the spiral arms. This is most obvious for the more face-on galaxies (for example NGC 99 and NGC 7442), but it is also seen for more edge-on spirals (e.g. NGC 7047 and UGC 12519). This 'two-peak' morphology is not seen for all the spirals, however. Some, for example NGC 3689 or IC 5090, are core-dominated and exhibit a single central peak of submillimetre emission (similar to the submillimetre morphology of the IRS galaxies), while others (NGC 6131 and NGC 6189 are clear examples) exhibit a combination of these features, with both a bright nucleus and peaks coincident with the spiral arms. In a number of cases the 850 μm peaks clearly follow a prominent dust lane (e.g. NGC 3987 and NGC 7722). These results are consistent with the results of numerous mm/submm studies. For example, Sievers et al. (1994) observe 3 distinct peaks in NGC 3627 and note that the two outer peaks are coincident with the transition region between the central bulge and the spiral arms – they also observe dust emission tracing the dust lanes of the spiral arms; Guélin et al. (1995), Bianchi et al. (2000), Hippelein et al. (2003) and Meijerink et al. (2005) observe a bright nucleus together with extended dust emission tracing the spiral arms. Many of the features seen in our OS sample 850 μm maps are also found by Stevens et al. (2005) in their SCUBA observations of nearby spirals.

Table 3.1: 850 μm flux densities and isothermal SED parameters. (Notes on individual objects are listed in Section 3.3).

(1) Name	(2) R.A. (J2000)	(3) Decl. (J2000)	(4) cz (km s^{-1})	(5) S_{60} (Jy)	(6) S_{100} (Jy)	(7) S_{850} (Jy)	(8) σ_{850} (Jy)	(9) T_{dust} (K)	(10) β	(11) Type
UGC 148	00 15 51.2	+16 05 23	4213	2.21	5.04	0.055	0.012	31.6	1.4	4
NGC 99	00 23 59.4	+15 46 14	5322	0.81	1.49	0.063	0.015	41.8	0.4	6
PGC 3563	00 59 40.1	+15 19 51	5517	0.35	^{s}1.05	0.027	0.008	31.0	1.0	2
NGC 786	02 01 24.7	+15 38 48	4520	1.09	2.46	0.066	0.019	35.2	0.8	4M
NGC 803	02 03 44.7	+16 01 52	2101	0.69	2.84	0.093	0.019	27.4	1.1	5
UGC 5129	09 37 57.9	+25 29 41	4059	0.27	0.92	<0.034	...	...	...	1
NGC 2954	09 40 24.0	+14 55 22	3821	<0.18	<0.59	<0.027	...	...	...	-5
UGC 5342	09 56 42.6	+15 38 15	4560	0.85	1.66	0.032	0.008	36.4	0.9	4
PGC 29536	10 09 12.4	+15 00 19	9226	<0.18	<0.52	<0.041	...	...	...	-5
NGC 3209	10 20 38.4	+25 30 18	6161	<0.16	<0.65	<0.022	...	...	...	-5
NGC 3270	10 31 29.9	+24 52 10	6264	0.59	2.39	0.059	0.014	26.8	1.3	3
NGC 3323	10 39 39.0	+25 19 22	5164	1.48	3.30	0.070	0.014	34.0	1.0	5
NGC 3689	11 28 11.0	+25 39 40	2739	^{s}2.86	^{s}9.70	0.101	0.017	26.8	1.7	5
UGC 6496	11 29 51.4	+24 56 16	6277	...	...	<0.018	...	...	...	-2
PGC 35952	11 37 01.8	+15 34 14	3963	0.47	1.32	0.051	0.013	32.2	0.8	4
NGC 3799^p	11 40 09.4	+15 19 38	3312	U	U	<0.268	...	...	...	3
NGC 3800^p	11 40 13.5	+15 20 33	3312	U	U	0.117	0.025	...	...	3
NGC 3812	11 41 07.7	+24 49 18	3632	<0.23	<0.56	<0.038	...	...	...	-5
NGC 3815	11 41 39.3	+24 48 02	3711	0.70	1.88	0.041	0.011	31.0	1.1	2
NGC 3920	11 50 05.9	+24 55 12	3635	0.75	1.68	0.034	0.009	34.0	1.0	-2
NGC 3987	11 57 20.9	+25 11 43	4502	4.78	15.06	0.186	0.030	27.4	1.6	3

Continued on Next Page...

Table 3.1: – *continued*

(1) Name	(2) R.A. (J2000)	(3) Decl. (J2000)	(4) cz (km s^{-1})	(5) S_{60} (Jy)	(6) S_{100} (Jy)	(7) S_{850} (Jy)	(8) σ_{850} (Jy)	(9) T_{dust} (K)	(10) β	(11) Type
NGC 3997	11 57 48.2	+25 16 14	4771	1.16	^{s}1.95	<0.023	...	...	...	3M
NGC 4005	11 58 10.1	+25 07 20	4469	U	U	<0.015	...	...	...	3
NGC 4015	11 58 42.9	+25 02 25	4341	0.25	^{s}0.80	<0.050	...	...	...	10M
UGC 7115	12 08 05.5	+25 14 14	6789	<0.20	<0.68	0.051	0.011	...	...	-5
UGC 7157	12 10 14.6	+25 18 32	6019	<0.24	<0.63	<0.032	...	...	...	-2
IC 797	12 31 54.7	+15 07 26	2097	0.74	2.18	0.085	0.021	31.6	0.8	6
IC 800	12 33 56.7	+15 21 16	2330	0.38	1.10	0.076	0.019	34.6	0.4	5
NGC 4712	12 49 34.2	+25 28 12	4384	0.48	2.02	0.102	0.023	28.0	0.9	4
PGC 47122	13 27 09.9	+15 05 42	7060	<0.11	0.55	<0.035	...	...	...	-2
MRK 1365	13 54 31.1	+15 02 39	5534	4.20	6.11	0.032	0.009	35.2	1.6	-2
UGC 8872	13 57 18.9	+15 27 30	5529	<0.22	<0.45	<0.021	...	...	...	-2
UGC 8883	13 58 04.6	+15 18 53	5587	0.45	1.19	<0.040	...	...	...	4
UGC 8902	13 59 02.7	+15 33 56	7667	1.23	3.32	0.067	0.018	30.4	1.2	3
IC 979	14 09 32.3	+14 49 54	7719	^{s}*0.19	^{s}*0.60	0.057	0.017	34.0*	0.3*	2
UGC 9110	14 14 13.4	+15 37 21	4644	U	U	<0.046	...	...	...	3
NGC 5522	14 14 50.3	+15 08 48	4573	2.06	4.05	0.072	0.014	35.8	1.0	3
NGC 5953$^{\dagger p}$	15 34 32.4	+15 11 38	1965	U	U	0.184	0.024	...	...	1
NGC 5954$^{\dagger p}$	15 34 35.2	+15 11 54	1959	U	U	0.112	0.019	...	...	6
NGC 5980	15 41 30.4	+15 47 16	4092	3.45	8.37	0.253	0.043	34.0	0.8	5
IC 1174	16 05 26.8	+15 01 31	4706	<0.18	<0.32	0.025	0.009	...	...	0
UGC 10200	16 05 45.8	+41 20 41	1972	1.41	1.67	<0.020	...	...	...	2M
UGC 10205	16 06 40.2	+30 05 55	6556	0.39	1.54	0.058	0.015	28.0	1.0	1

Table 3.1: – *continued*

(1) Name	(2) R.A. (J2000)	(3) Decl. (J2000)	(4) cz (km s^{-1})	(5) S_{60} (Jy)	(6) S_{100} (Jy)	(7) S_{850} (Jy)	(8) σ_{850} (Jy)	(9) T_{dust} (K)	(10) β	(11) Type
NGC 6090	16 11 40.7	+52 27 24	8785	6.66	8.94	0.091	0.015	40.6	1.1	10M
NGC 6103	16 15 44.6	+31 57 51	9420	0.64	1.67	0.052	0.012	33.4	0.8	5
NGC 6104	16 16 30.6	+35 42 29	8428	0.50	1.76	<0.033	...	...	...	1
IC 1211	16 16 51.9	+53 00 22	5618	<0.12	<0.53	0.028	0.009	...	...	-5
UGC 10325§	16 17 30.6	+46 05 30	5691	1.57	3.72	0.041	0.009	31.0	1.4	10M
NGC 6127	16 19 11.5	+57 59 03	4831	<0.10	<0.30	0.086	0.020	...	...	-5
NGC 6120	16 19 48.1	+37 46 28	9170	3.99	8.03	0.065	0.011	32.2	1.5	8
NGC 6126	16 21 27.9	+36 22 36	9759	<0.15	<0.43	0.023	0.008	...	...	-2
NGC 6131	16 21 52.2	+38 55 57	5117	0.72	2.42	0.054	0.013	28.6	1.2	6
NGC 6137	16 23 03.1	+37 55 21	9303	<0.18	<0.53	0.029	0.010	...	...	-5
NGC 6146	16 25 10.3	+40 53 34	8820	<0.12	<0.48	0.028	0.007	...	...	-5
NGC 6154	16 25 30.4	+49 50 25	6015	<0.15	<0.36	<0.040	...	...	...	1
NGC 6155	16 26 08.3	+48 22 01	2418	1.90	5.45	0.116	0.022	29.8	1.2	6
UGC 10407	16 28 28.1	+41 13 05	8446	1.62	3.12	0.026	0.009	32.8	1.5	10M
NGC 6166	16 28 38.4	+39 33 06	9100	^{s}0.10	^{s}0.63	0.073	0.017	26.2	0.6	-5
NGC 6173	16 29 44.8	+40 48 42	8784	<0.17	<0.23	<0.024	...	...	...	-5
NGC 6189	16 31 40.9	+59 37 34	5638	0.75	2.57	0.072	0.019	28.6	1.1	6
NGC 6190	16 32 06.7	+58 26 20	3351	0.58	2.37	0.099	0.024	28.0	1.0	6
NGC 6185	16 33 17.8	+35 20 32	10301	0.17	0.56	<0.030	...	...	...	1
UGC 10486	16 37 34.3	+50 20 44	6085	<0.19	<0.60	<0.029	...	...	...	-3
NGC 6196	16 37 53.9	+36 04 23	9424	<0.12	<0.44	<0.023	...	...	...	-3
UGC 10500	16 38 59.3	+57 43 27	5218	^{s*}0.16	^{s*}0.71	<0.028	...	...	...	0

Continued on Next Page...

(1) Name	(2) R.A. (J2000)	(3) Decl. (J2000)	(4) cz (km s^{-1})	(5) S_{60} (Jy)	(6) S_{100} (Jy)	(7) S_{850} (Jy)	(8) σ_{850} (Jy)	(9) T_{dust} (K)	(10) β	(11) Type
IC 5090	21 11 30.4	−02 01 57	9340	3.04	7.39	0.118	0.017	31.6	1.2	1
IC 1368	21 14 12.5	+02 10 41	3912	4.03	5.80	0.047	0.011	37.6	1.3	1
NGC 7047	21 16 27.6	−00 49 35	5626	0.43	1.65	0.055	0.013	28.0	1.1	3
NGC 7081	21 31 24.1	+02 29 29	3273	1.79	3.87	0.044	0.010	32.8	1.3	3
NGC 7280	22 26 27.5	+16 08 54	1844	<0.12	<0.48	<0.040	...	...	...	-1
NGC 7442	22 59 26.5	+15 32 54	7268	0.78	2.22	0.046	0.009	31.0	1.1	5
NGC 7448†	23 00 03.6	+15 58 49	2194	7.23	17.43	0.193	0.032	31.0	1.4	5
NGC 7461	23 01 48.3	+15 34 57	4272	<0.176	<0.64	<0.022	...	...	...	-2
NGC 7463	23 01 51.9	+15 58 55	2341	U	U	0.045	0.010	...	...	3M
III ZW 093	23 07 21.0	+15 51 11	14962	0.48	<3.16	<0.026	...	...	...	10Z
III ZW 095	23 12 43.3	+15 54 12	7506	<0.09	<0.80	<0.019	...	...	...	10Z
UGC 12519	23 20 02.7	+15 57 10	4378	0.76	2.59	0.074	0.016	29.2	1.1	5
NGC 7653	23 24 49.3	+15 16 32	4265	1.31	4.46	0.112	0.020	28.6	1.2	3
NGC 7691	23 32 24.4	+15 50 52	4041	0.53	1.67	<0.025	...	...	...	4
NGC 7711	23 35 39.3	+15 18 07	4057	<0.15	<0.50	<0.027	...	...	...	-2
NGC 7722	23 38 41.2	+15 57 17	4026	0.78	3.03	0.061	0.015	26.8	1.4	0

(1) Most commonly used name.

(2) Right ascension, J2000 epoch.

(3) Declination, J2000 epoch.

(4) Recessional velocity taken from NED. [The NASA/IPAC Extragalactic Database (NED) is operated by the Jet Propulsion Laboratory, California Institute of Technology, under contract with the National Aeronautics and Space Administration.]

(5) $60\,\mu$m flux from the *IRAS* Faint Source Catalogue (Moshir et al. 1990); upper limits listed are measured using SCANPI as described in Section 2.10.

(6) $100\,\mu$m flux from the *IRAS* Faint Source Catalogue (Moshir et al. 1990); upper limits listed are measured using SCANPI as described in Section 2.10.

(7) $850\,\mu$m flux (this work).

(8) Error on $850\,\mu$m flux, calculated as described in Section 2.8.

(9) Dust temperature derived from a single-component fit to the 60, 100 and $850\,\mu$m data points, as described in Section 3.5.

(10) Emissivity index derived from the single-component fit, as described in Section 3.5.

(11) Hubble type (t-type) taken from the LEDA database (which uses the standard numerical codes for the de Vaucoulers morphological type, as defined in RC2); I have assigned t=10 to any multiple systems unresolved by *IRAS* or SCUBA (indicated by '10M') and any systems with no type listed in LEDA (indicated by '10Z'; these 2 objects are listed as 'compact' sources in NED); all other types marked 'M' are listed as multiple systems in LEDA.

^{p} Part of a close or interacting pair which was resolved by SCUBA. Fluxes here are the individual galaxy fluxes; fluxes measured for the combined pair are given in Table 3.2.

U Unresolved by *IRAS*.

^{s} The *IRAS* flux is our own SCANPI measurement (see Section 2.10); any individual comments are listed in Section 3.3.

* SCANPI measurements and fitted values should be used with caution (see Section 2.10).

§ The coordinates of this object refer to one galaxy (NED01) of a the *pair* UGC 10325.

† Objects are also in the *IRAS*-selected sample (DE00).

Table 3.2: Combined SCUBA fluxes for pairs unresolved by *IRAS*. (Notes on individual objects are listed in Section 3.3).

(1) Name	(2) R.A. (J2000)	(3) Decl. (J2000)	(4) cz (km s^{-1})	(5) S_{60} (Jy)	(6) S_{100} (Jy)	(7) S_{850} (Jy)	(8) σ_{850} (Jy)	(9) T_{dust} (K)	(10) β	(11) Type
NGC 3799/3800	11 40 11.4	+15 20 05	3312	4.81	11.85	0.135	0.035	29.8	1.5	10M
NGC 5953/4	15 34 33.7	+15 11 49	1966	10.04	18.97	0.273	0.034	35.2	1.1	10M

Note. Columns have the same meanings as in Table 3.1.

Secondly, a number of galaxies appear to be extended at 850 μm compared to the optical emission seen in the DSS images. In many cases this extended 850 μm emission appears to correspond to very faint optical features, as can be seen for NGC 7081 and NGC 7442 in Figure 3.1. In order to investigate this further I have already carried out deeper follow-up optical imaging for around half the sample detected at 850 μm.

3.3 Notes on individual objects

In the following discussion of individual objects I note that since the number of bolometers sampling each sky point decreases towards the edges of the submillimetre maps the noise increases towards the edge of the maps. Although the S/N maps in Figure 3.1 were produced using artificial noisemaps (Section 2.9) which should normally account for this effect there are certain circumstances, such as a 'tilted-sky' (see Section 2.4) or the very noisiest bolometers, where residual 'noisy' features may remain in the S/N maps. This means that any submillimetre emission in Figure 3.1 seen beyond the main optical extent (and away from the centre of the map) should be regarded with some caution. However, in order to aid distinction between probable residual noisy features in the S/N map and potential extended submillimetre emission I have made a thorough investigation of each individual map. In the following discussion, unless otherwise stated I have found all $\geq 2\sigma$ submillimetre peaks away from the main optical galaxy to be associated with noisy bolometers or a tilted sky.

UGC 148. Data points for this object are not well-fitted by the two-component dust model (Section 3.5), probably due to the 850 μm flux having been underestimated – the 850 μm S/N contours shown in Figure 3.1 for this object show evidence of a residual tilted sky plane (the sky is more positive on one side of the map than the other), suggesting that sky removal techniques may have been inadequate in this case and that therefore the source flux may have been under- (or over-) estimated. Also, since the E-NE part of the galaxy
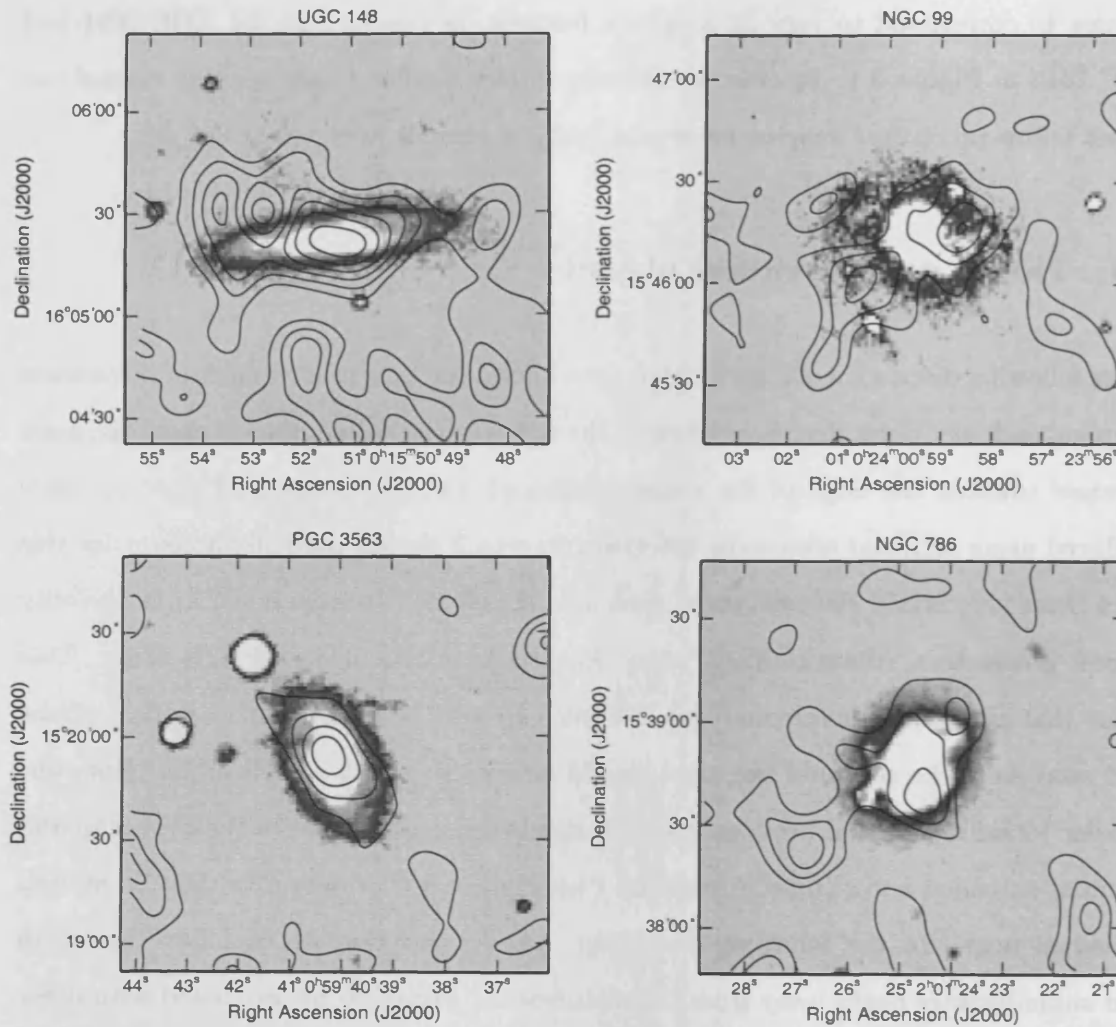
Figure 3.1:   The optically-selected SLUGS: 850 μm SCUBA S/N maps (produced as described in Chapter 2 Section 2.9; 1σ contours) overlaid onto DSS optical images (2′×2′, except for NGC 803 and NGC 6155 which are 3′ × 3′); the point spread function in the SCUBA S/N maps is ~19 arcsec (see Chapter 2 Section 2.9). (Optical images are shown here with a contrast that optimises the optical features, however when used as a guide for drawing SCUBA flux measurement apertures a more conservative stretch was applied).
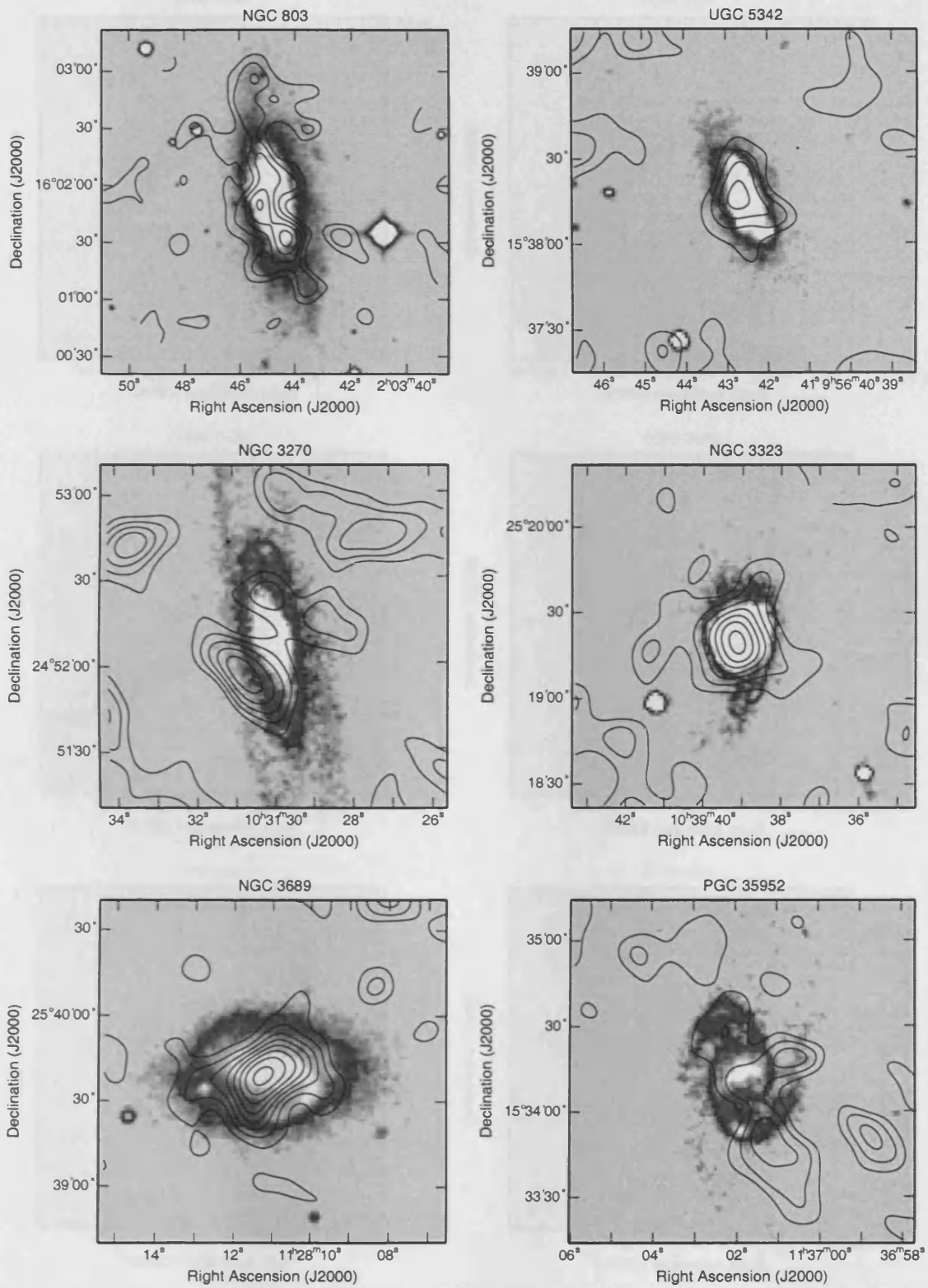
Figure 3.1: – *continued*
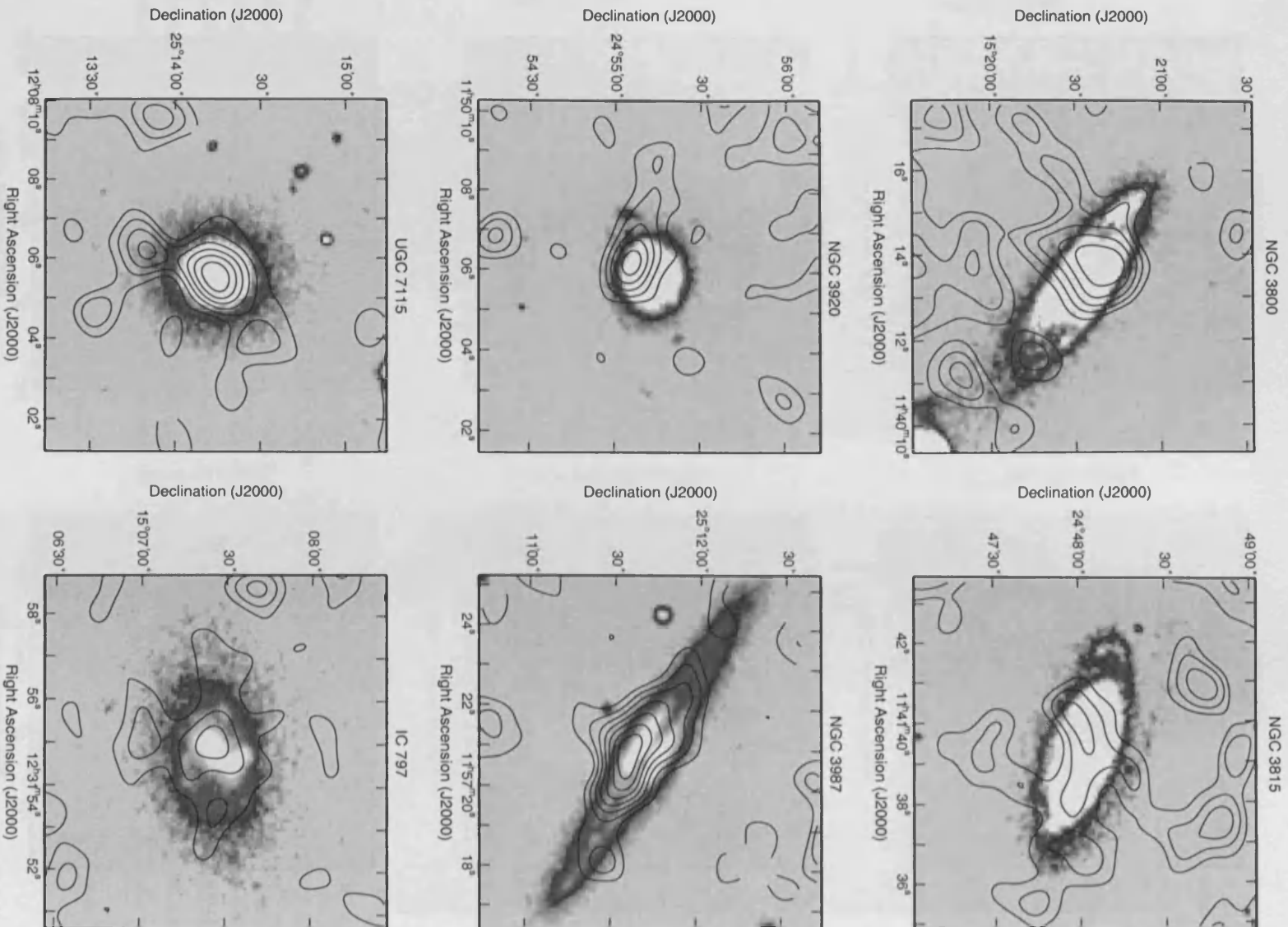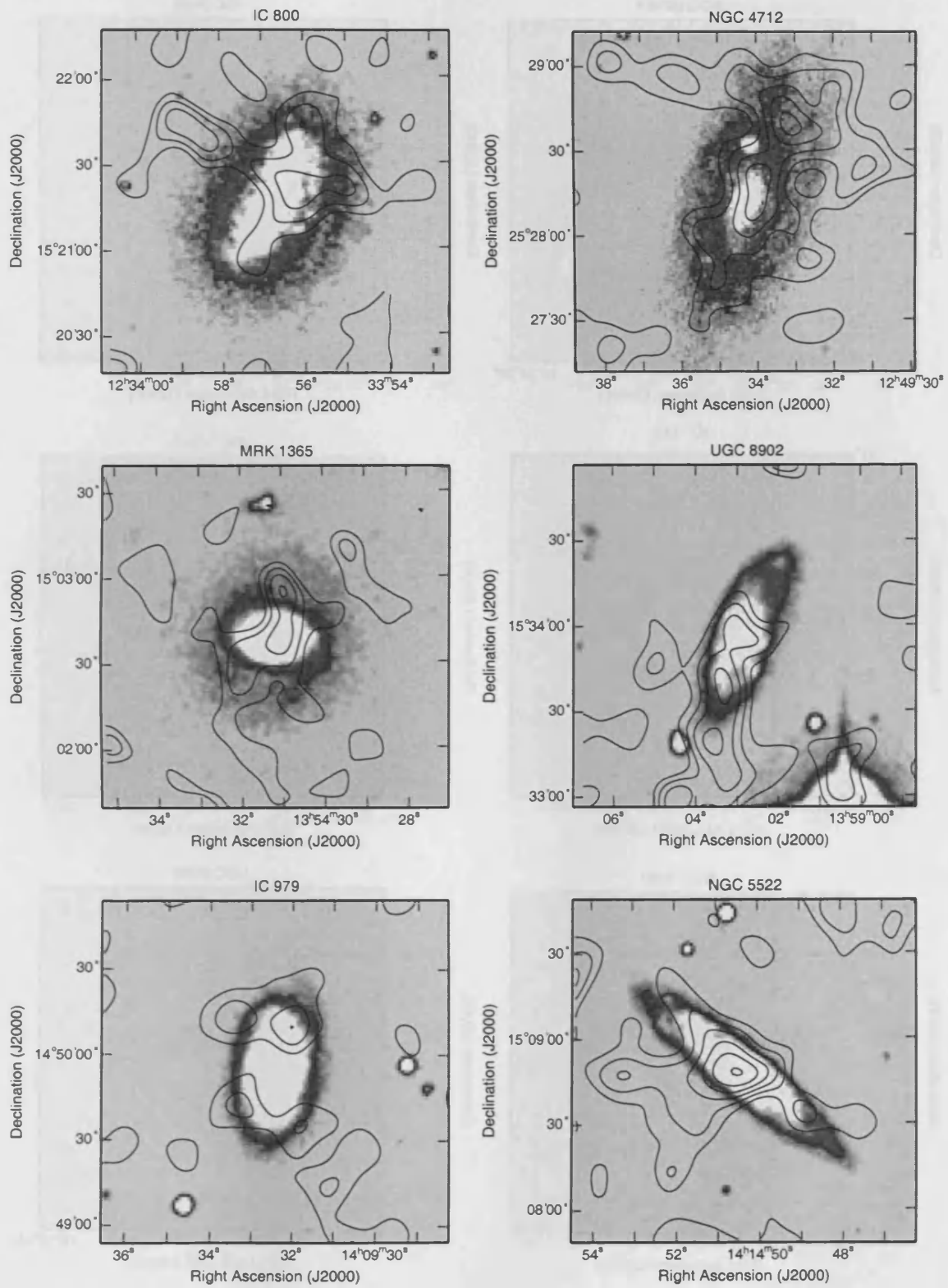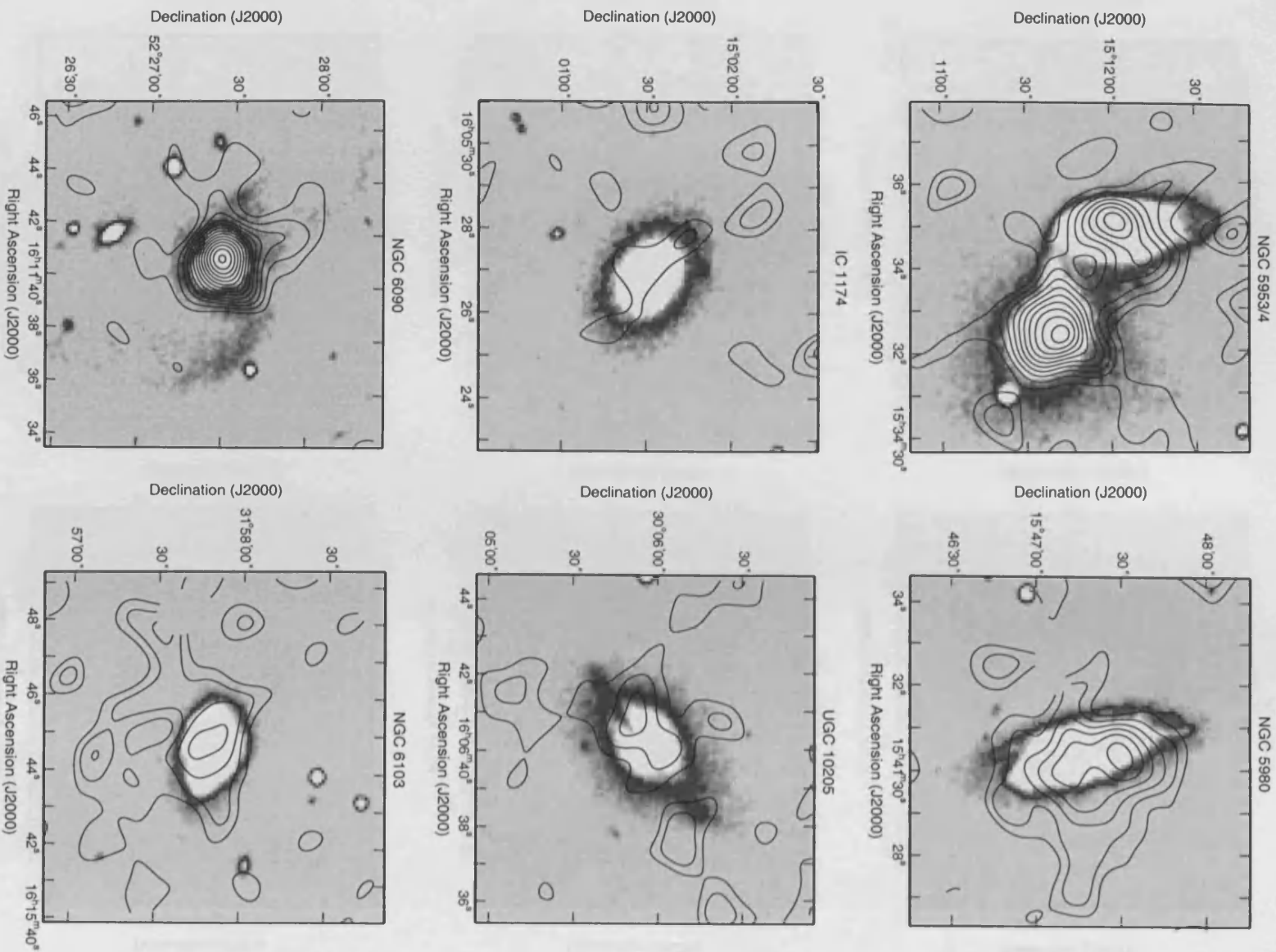
Figure 3.1: – *continued*

Figure 3.1: – *continued*

Figure 3.1: — continued
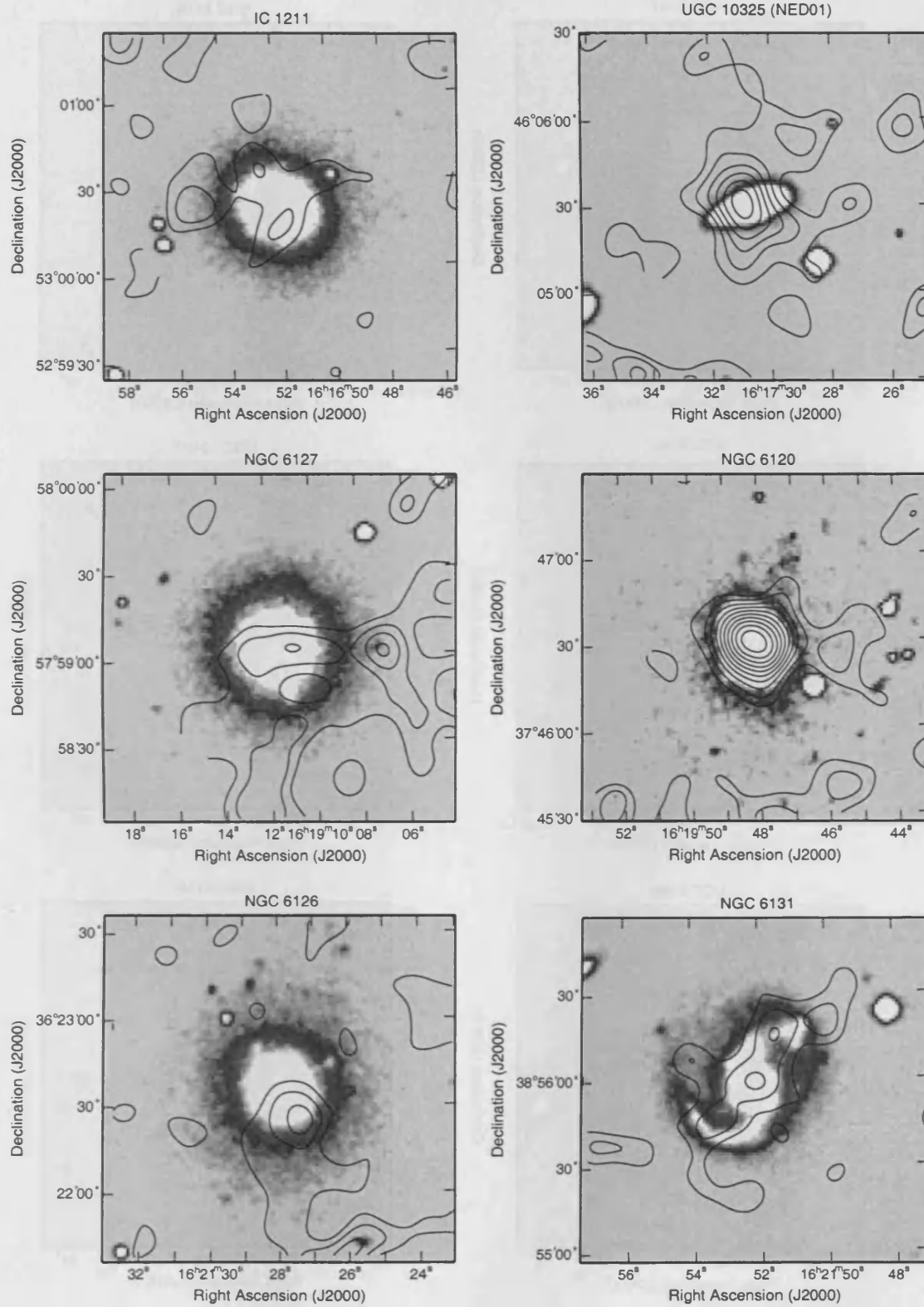
Figure 3.1: – *continued*
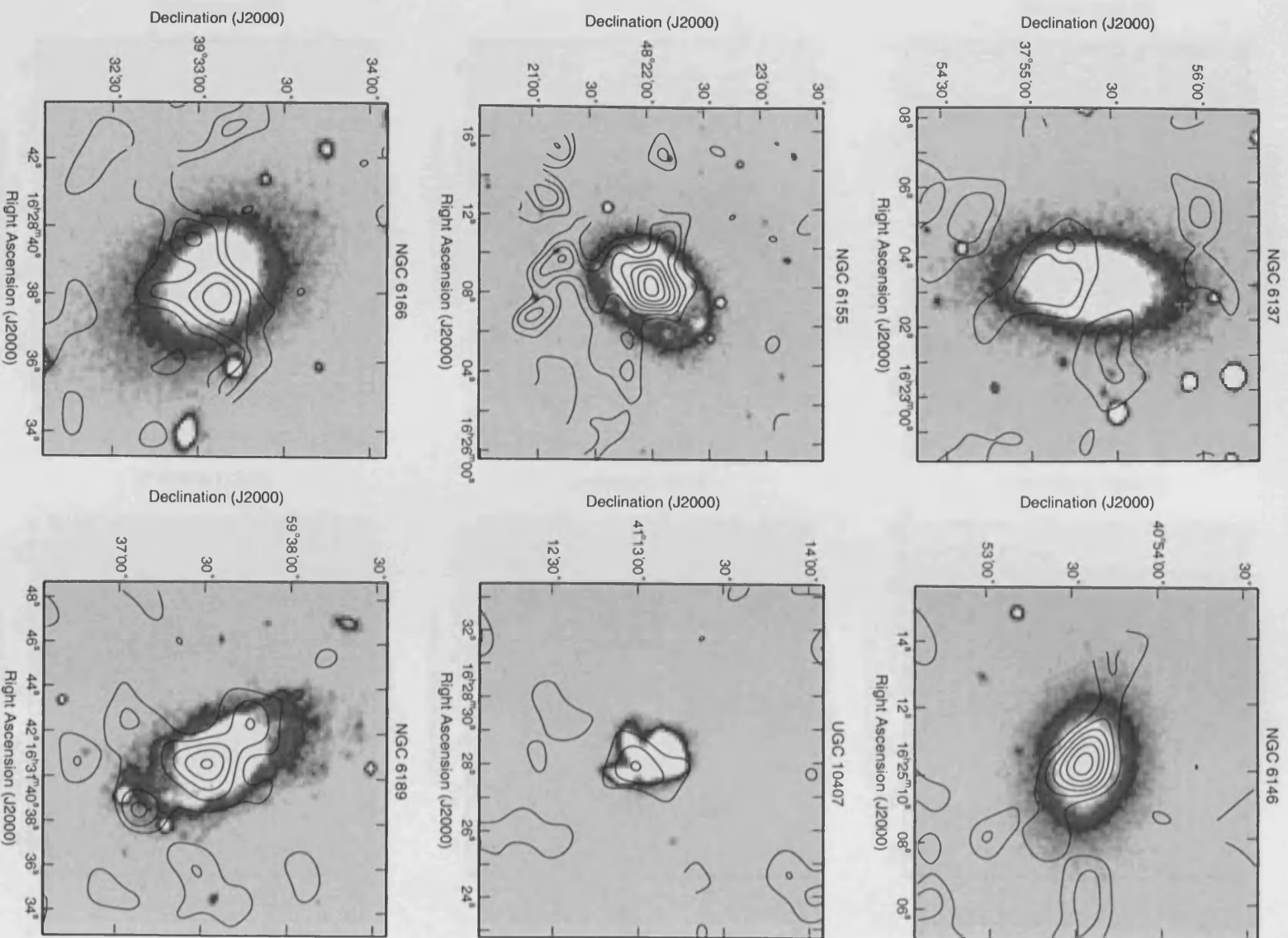
Figure 3.1: — continued
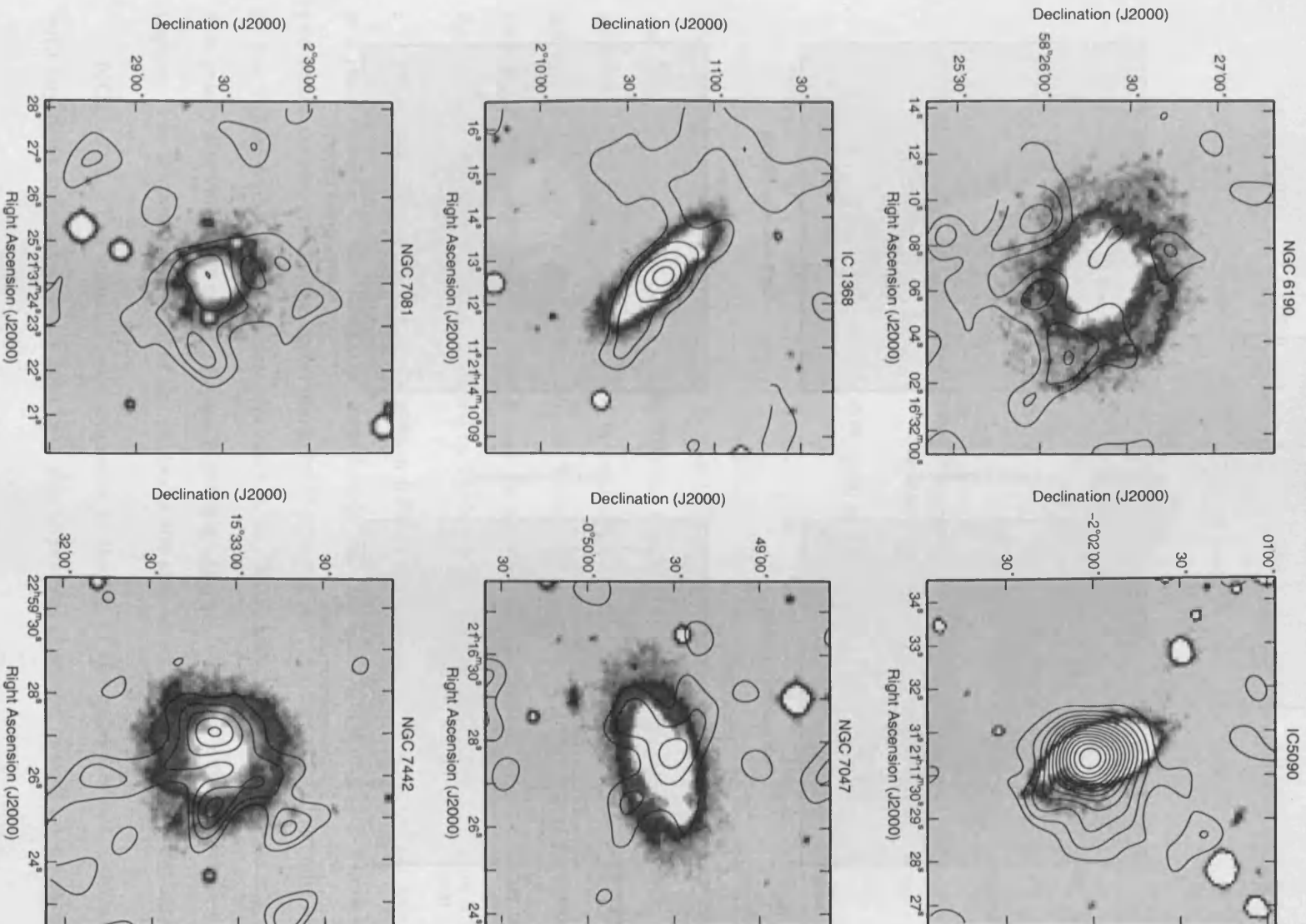
Figure 3.1: – *continued*
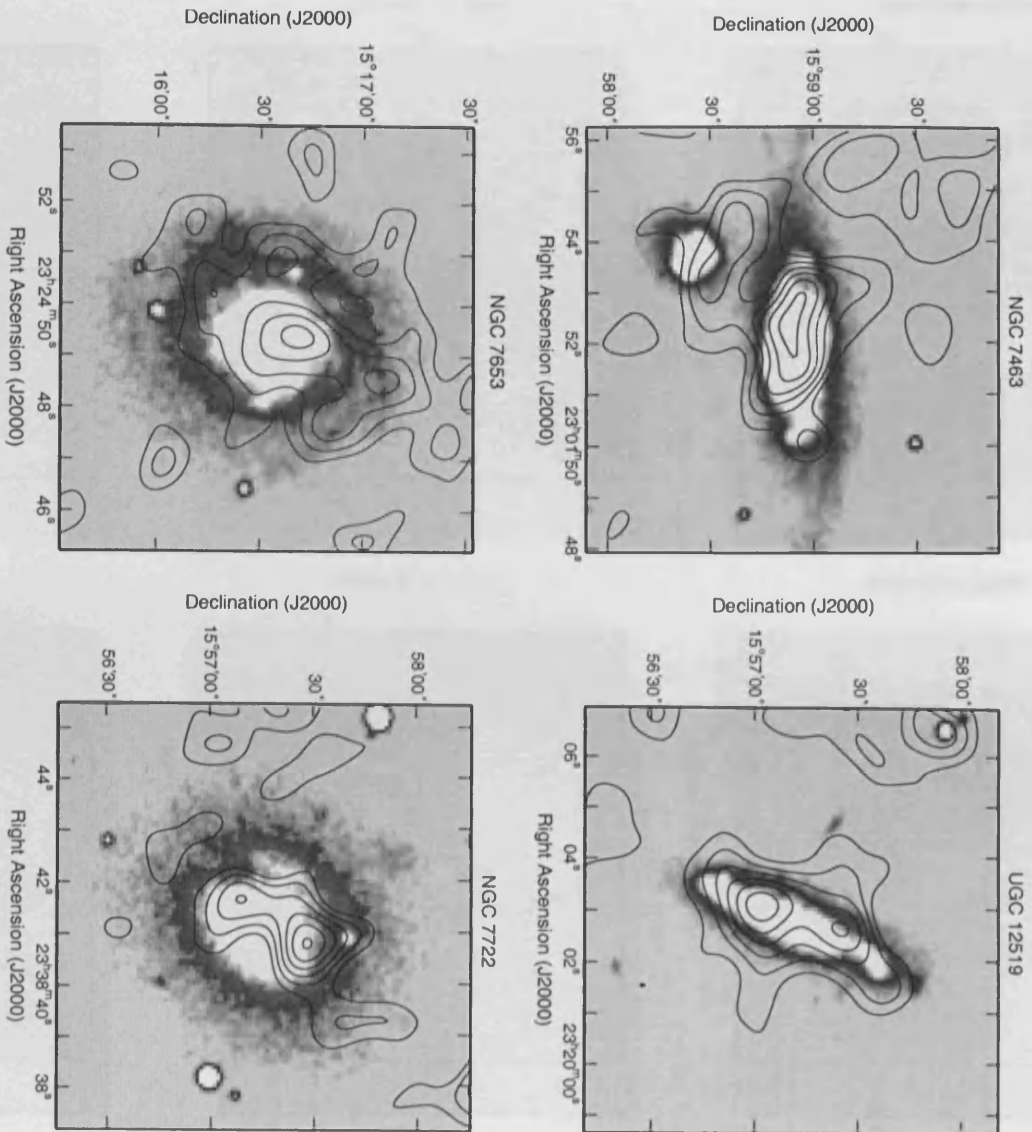
Figure 3.1: — continued
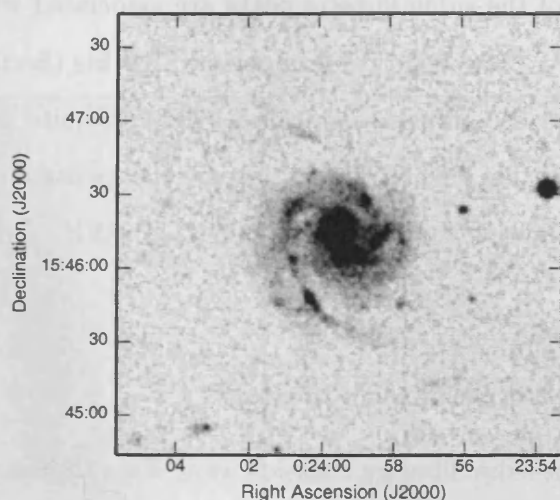
Figure 3.2: SuperCOSMOS B-band image of NGC 99.

is coincident with noisy bolometers in the 850 μm map the flux-measurement aperture was drawn to avoid this region, so the 850 μm flux may be underestimated. However, an additional data point at 170 μm (ISO) is available from the literature (Stickel et al. 2000, 2004). Using the 60, 100, 170 and 450 μm fluxes I find that the data points are well-fitted by the two-component dust model (I take an average of all 170 μm fluxes available, see Section 3.5), and these results are listed in Table 3.3 and the SED is shown in Figure 3.20.

NGC 99. The submillimetre emission follows the spiral arm structure. This galaxy is a good example of the 'two-peak' morphology seen for some spiral galaxies, where the two peaks correspond to the spiral arms/inter-arm regions. As can more clearly be seen in the SuperCOSMOS Sky Survey (Hambly et al., 2001) image shown in Figure 3.2, for this galaxy the two peaks of submillimetre emission appear to correspond to the inter-arm regions. The 2σ peak to the NE of the galaxy is not associated with any noisy bolometers.

NGC 786. The submillimetre emission to the SE of the galaxy is not associated with any noisy bolometers but I note that this object was observed in *very* poor weather.

NGC 803. None of the submillimetre peaks are associated with noisy bolometers. Due to the high ratio of S_{25}/S_{60} good two-component SED fits (Section 3.5) to the 4 data points (60, 100, 450 and 850 μm) can be achieved for two quite different values of the warm component temperature. In addition to the parameters listed in Table 3.3 a good fit is also found with the following parameters: T_w=60 K, T_c=19 K, $\frac{N_c}{N_w}$=2597, log M_{d2}=6.99 and log L_{fir}=9.48.

UGC 5342. This observation had a tilted sky.

NGC 3270. All the submillimetre emission away from the main optical extent, and the emission to the N of the galaxy, is associated with noisy bolometers. This observation also suffered from a tilted sky, which may explain much of the submillimetre emission in the N part of the map. However, the emission towards the centre of the map, coinciding with the main optical galaxy, is not associated with any noisy bolometers. The three peaks lying on the main optical extent are coincident with the inner spiral arms. As the SuperCOSMOS B- and R-band images (Figure 3.3) show more clearly, this emission seems to occur where the galaxy bulge ends and the inter-arm region begins, as was found for NGC 3627 by Sievers et al. (1994).

NGC 3689. Very few scans were available via SCANPI, so *IRAS* fluxes (and corresponding fitted parameters) for this object should be used with caution.

PGC 35952. The submillimetre emission to the S and SW is not associated with any noisy bolometers. The submillimetre peaks coincident with the main optical extent of the galaxy appear to follow the spiral arm structure, as for NGC 6131 and NGC 99, and it is possible the extended submillimetre emission to the S relates to the very extended faint spiral arms seen in the optical, which are clearly seen in the SuperCOSMOS image shown in Figure 3.4.
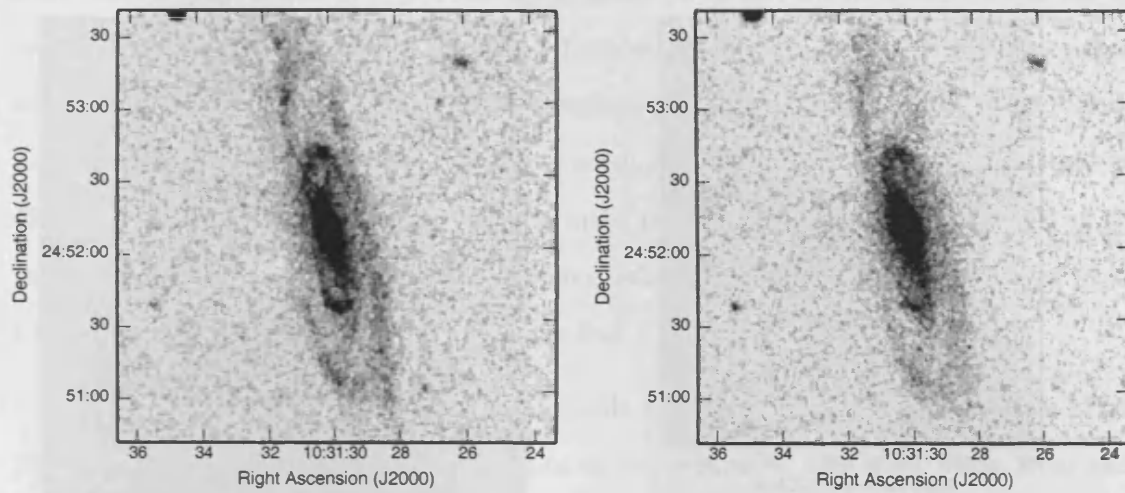
Figure 3.3: NGC 3270. SuperCOSMOS B-band (left) and R-band (right) images.
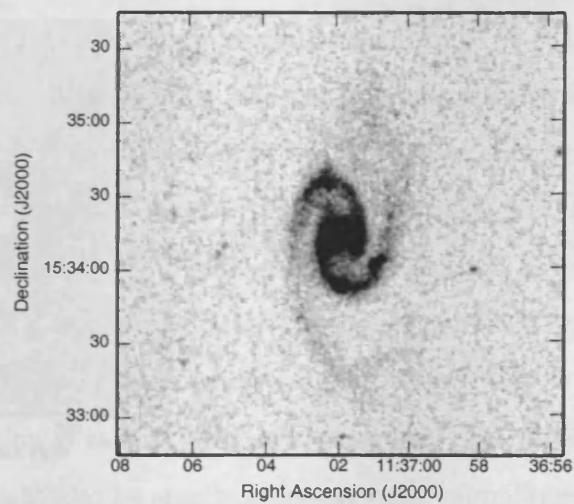
Figure 3.4: SuperCOSMOS B-band image of PGC 35952.
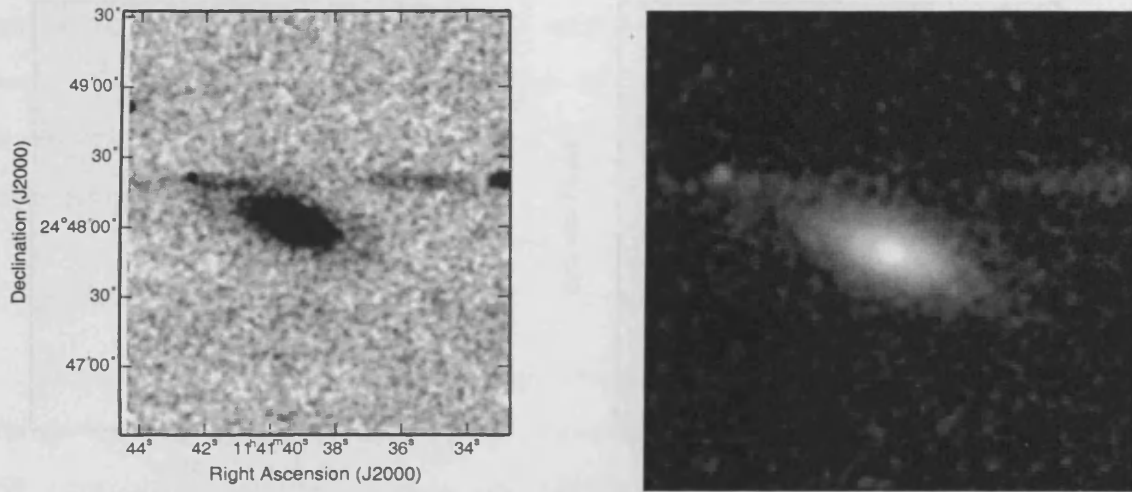
Figure 3.5:   NGC 3815. 2MASS J-band (left) and JHK composite (right).
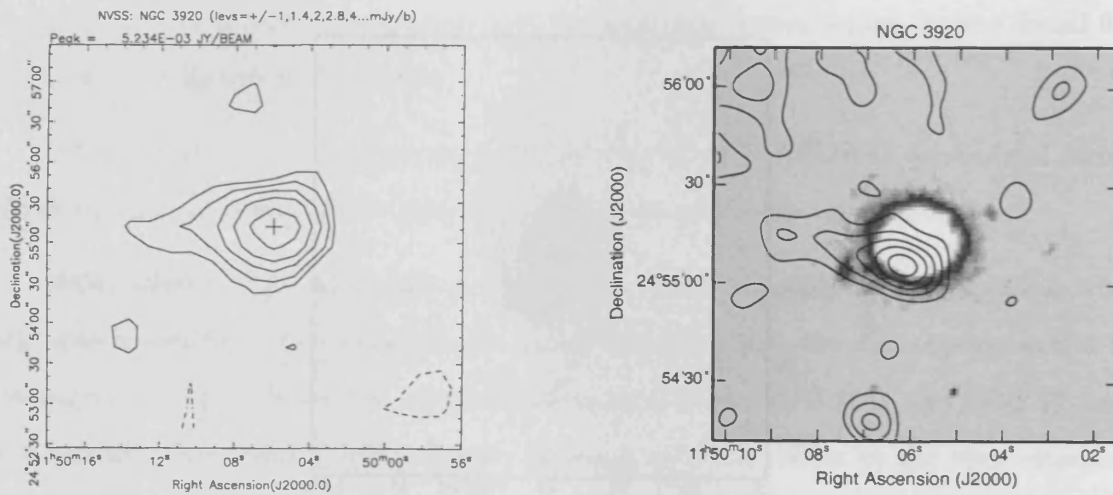
Figure 3.6:   NGC 3920. NVSS 1.4 GHz image (left; taken from the online NVSS postage stamp server) compared to the OS SLUGS 850 μm contours overlaid on DSS optical image (right).

NGC 3799/3800. NGC 3799 and NGC 3800 were observed in separate maps. NGC 3799 individually is not detected at the 3σ level (although we measure flux at the 2σ level). For NGC 3800 (shown in Figure 3.1) most of the integrations for the bolometers to the S of the map were unusable, and consequently this part of the map is very much noisier. Generally this observation is very noisy, and especially bad at $450\,\mu$m; thus no $450\,\mu$m flux is available. In fact only the main region of submillimetre emission at the centre of the map is in an area free from noisy bolometers, and it is this region over which I have measured the galaxy's submillimetre flux.

The S_{850} listed for NGC 3799/3800 in Table 3.2 is a conservative measurement of the $850\,\mu$m emission from the system, the sum of the separately measured fluxes from each of the two component galaxies. In coadding the two maps there appears to be a 'bridge' of $850\,\mu$m emission between the two galaxies, consistent with emission seen in the optical (NGC 3799 is to the SW of NGC 3800 in Figure 3.1). However, since this region of the map has several noisy bolometers I only measure fluxes for the main optical extent of the galaxies.

NGC 3815. The submillimetre emission to the NE and W of the galaxy is associated with noisy bolometers. However, the arm-like submillimetre structures seen extending from the galaxy to the N and S are *not*. Both of these 'arms' extend in the direction of faint optical features seen in the DSS and 2MASS images. The optical images also show evidence of extended optical emission around the main optical extent (just visible to the NE in Figure 3.1), but 2MASS (JHK) images (Figure 3.5) show a band of emission stretching E-W between two nearby galaxies either side of NGC 3815. It seems clear that some kind of interaction is taking place in this system, and therefore it is perhaps not unlikely that there might also be significantly extended submillimetre emission.

NGC 3920. The submillimetre emission to the E and S is not associated with any noisy bolometers. It is noted that a similar 'extended' region to the E is seen for the

NRAO VLA Sky Survey (NVSS; Condon et al. 1998) 1.4GHz radio emission (Figure 3.6).

NGC 3987. This edge-on galaxy has a prominent dust lane in the optical. Though the submillimetre emission follows the dust lane it is seen slightly offset. A similar result was found for another edge-on spiral by Stevens et al. (2005), who conclude this effect is simply an effect of the inclination of the galaxy on the sky.

NGC 3997. The FSC gives an upper limit <3.101 Jy for S_{100}, likely due to possible source confusion with NGC 3993. The S_{100} I have measured with SCANPI should therefore be used with some caution.

NGC 4005. This object is detected at 850 μm at only the 2.5σ level. It is unresolved by *IRAS* and may be confused with *IRAS* source IRASF11554+2524 (NGC 4000).

UGC 7115. With the exception of the submillimetre emission to the SE, none of the submillimetre emission in this map is associated with noisy bolometers. However, I found this SCUBA observation to have a tilted sky. I estimate that as much as 80% of the 850 μm flux from this elliptical may be due to synchrotron contamination from a radio source associated with the galaxy (see Section 3.4).

IC 800. The submillimetre emission to the E of this galaxy corresponds to a region of the map which is only slightly noisy, making it unlikely any residual features of this noise remains in the S/N map (Section 2.9). This arm-like feature stretching to the E/N-E appears to extend from a point on the main galaxy extent where DSS IR and SuperCOSMOS B-band images appear to show an area of dust obscuration (Figure 3.7). However, I also note that this object was observed in poor weather.

NGC 4712. None of the submillimetre emission is associated with noisy bolometers, with the exception of the 2σ peak closest to the galaxy in the arm-like structure extending to the E. However, I note that this arm-like feature, though faint, is also evident in the optical (though not reproduced in the optical image in Figure 3.1); it appears to originate from the main galaxy extent, where there appears to be a significant amount of dust
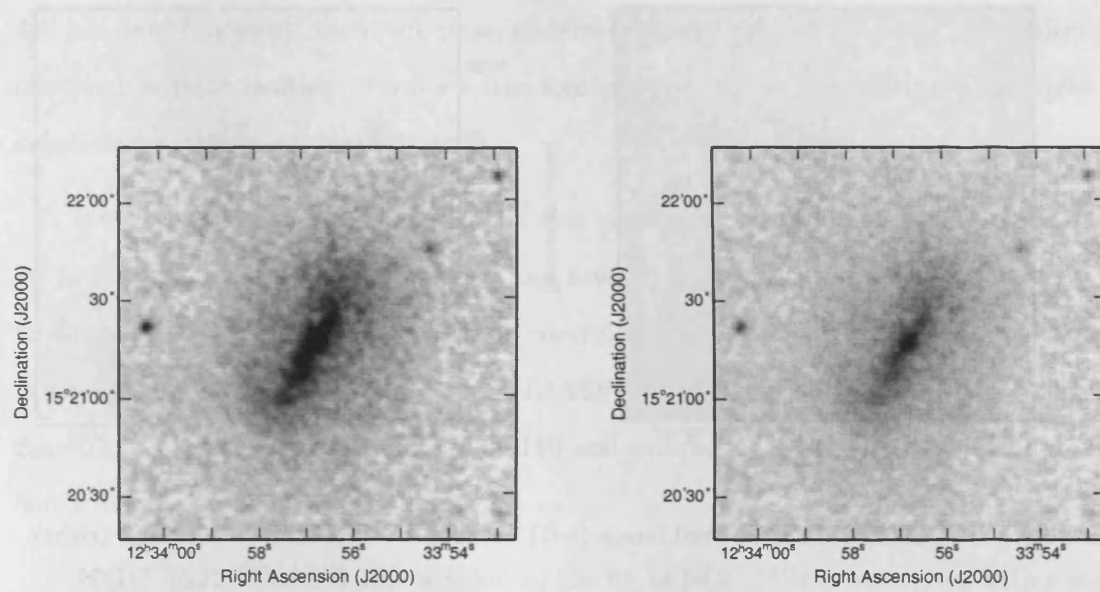
Figure 3.7: IC 800. Clockwise from top left: DSS IR (high contrast), DSS IR (low contrast).
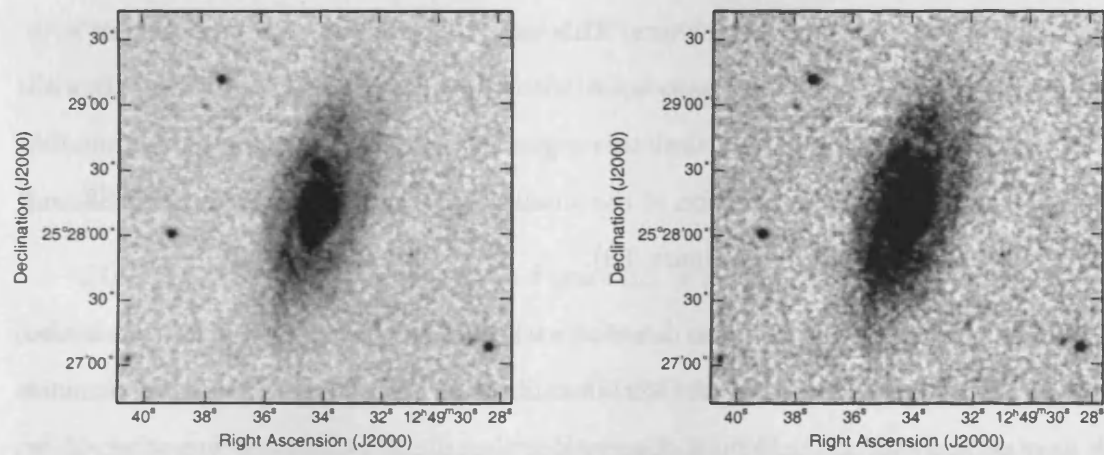
Figure 3.8: NGC 4712. DSS IR ($3' \times 3'$) image at low (left) and high (right) contrast.
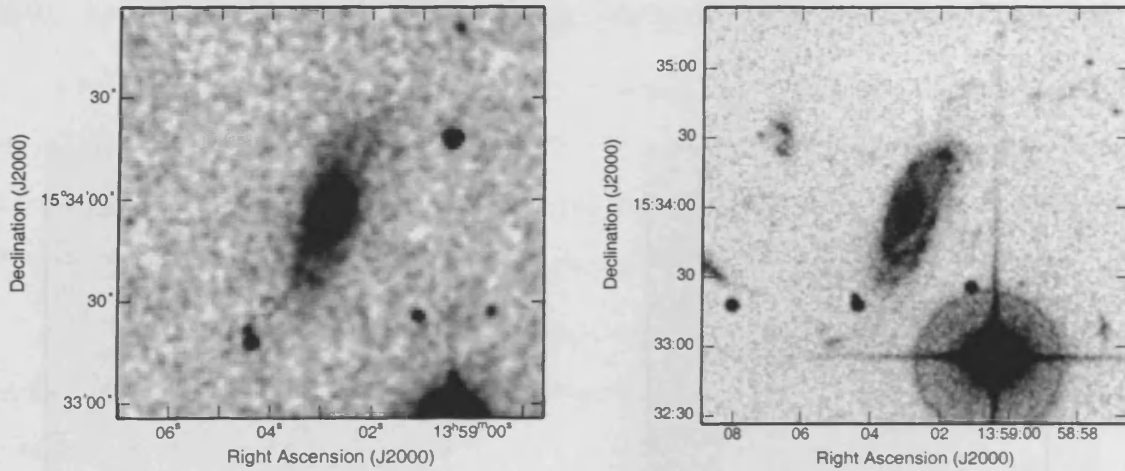
Figure 3.9:   UGC 8902. 2MASS H-band image (left) and SuperCOSMOS B-band image (right).

obscuration (see the DSS IR image shown in Figure 3.8).

UGC 8902. The region of submillimetre emission to the E, far SW and far S are all associated with noisy bolometers. However, the 4σ submillimetre peak lying to the S/SE beyond the main optical extent, at a similar declination to the small galaxy to the SE, is not associated with any noisy bolometers. This submillimetre emission is consistent with the fact that the overall emission associated with the galaxy is offset to the S/SE with respect to the optical. I also note that this region in the optical/IR contains a number of faint condensations in the direction of the small galaxy to the SE (see the 2MASS and SuperCOSMOS images shown in Figure 3.9).

IC 979. Although this galaxy is detected with relatively low S/N at $850\,\mu$m it is also detected at $450\,\mu$m. I allocate a higher $450\,\mu$m calibration error (25%) for this source, since there were no good $450\,\mu$m calibrator observations that night (calibration was achieved by taking the mean results from a number of calibrators observed that and the previous night). Note also that no two-component fit could be made to the data since the $450\,\mu$m data point is higher than the $100\,\mu$m value, possibly due to the problems with calibrating the

450 μm data but more likely due to an underestimate of the 100 μm flux. This object was observed in poor weather. However, the four peaks lying on the main optical extent are coincident with the outer spiral arms.

UGC 9110. There appears to be flux present at both 850 μm and 450 μm at the 2σ level, but the maps are very noisy and several integrations unusable, most likely due to unstable and deteriorating weather conditions during the observation. This object is unresolved by *IRAS*: *IRAS* source IRASF14119+1551 (FSC fluxes S_{100}=2.341 and S_{60}=0.802 Jy) is likely a blend of UGC9110 and companion CGCG103-124 (Condon, Cotton & Broderick 2002).

NGC 5522. The 850 μm emission to the SE of NGC 5522 is associated with a region of the map which is slightly noisy and where there are a number of spikes in the data. This observation was carried out in poor weather.

NGC 5953/4 is also in the IRS SLUGS sample. While D00 used colour-corrected *IRAS* fluxes as listed in the *IRAS* BGS (from Soifer et al. (1989)) I present here, as for all the OS sample, fluxes from the *IRAS* FSC.

NGC 5980. This observation suffered from a tilted sky, which potentially explains the extended 850 μm emission to the W of the galaxy. The aperture used to measure the 450 μm flux was smaller than at 850 μm in order to avoid a noisy bolometer, thus source flux at 450 μm may be underestimated.

UGC 10205. The 850 μm map in Figure 3.1 is a coadd of two observations. Since emission at the optical galaxy position is very clear in one observation (both at 850 μm *and* 450 μm) and not in the other observation, and since I find no explanation for this, I simply coadd the two observations (see Chapter 2 Section 2.3). This galaxy has a prominent dust lane in the optical which, as can be seen in the SuperCOSMOS and *Sloan Digital Sky Survey* (SDSS; Abazajian K. et al. 2005) images shown Figure 3.10, is most prominent to the SE of the galaxy (coincident with the 3σ peak in the submillimetre map. The
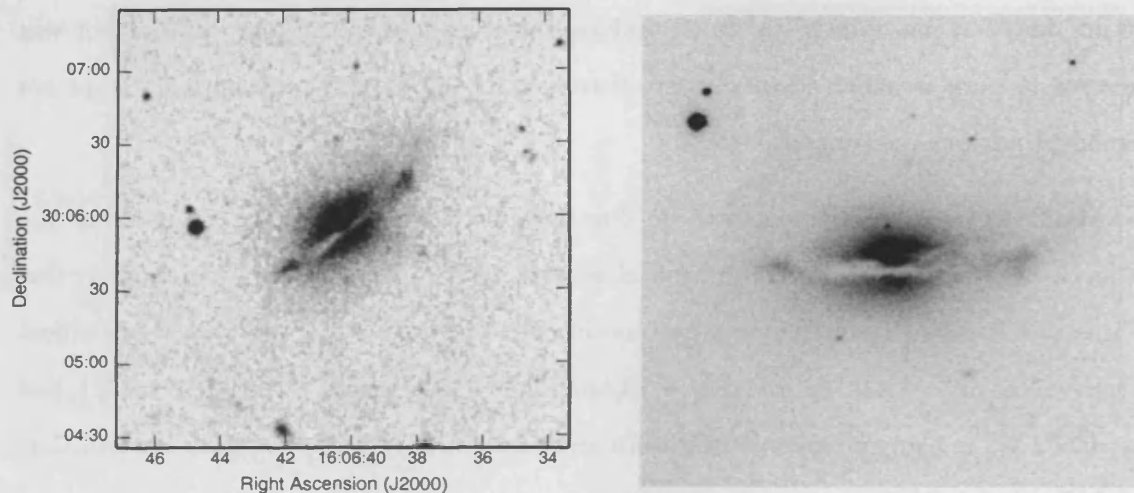
Figure 3.10:   UGC 10205. SuperCOSMOS B-band and SDSS g-band images.

submillimetre emission coincident with the main optical galaxy extent, and also the peak to the S, are not associated with any noisy bolometers. Peaks to the N and W of the galaxy lie in a region of the map which is slightly noisy. I note that this observation was carried out in less than ideal weather.

NGC 6090 is a closely interacting/merging pair, and is also in the IRS SLUGS sample.

NGC 6103. The submillimetre emission to the S of the galaxy is not associated with any noisy bolometers. This region contains a number of faint features seen in optical (DSS) and 2MASS images. This object was observed in less than ideal weather.

IC 1211. I find in the literature no known radio sources associated with this elliptical galaxy (NVSS 1.4GHz 3σ upper limit is <1.2 mJy), and therefore cannot attribute the $850\,\mu$m flux detected here to contamination from synchrotron radiation.

UGC 10325 (NED01) is one galaxy of the pair UGC 10325. The SCUBA map is

centred on this galaxy (NED01), but NED02 can be seen at the SE edge of the DSS image in Figure 3.1. Thus all fluxes given are for the individual galaxy UGC 10325 NED01.

NGC 6127. I find in the literature no known radio sources associated with this elliptical galaxy (NVSS 1.4GHz 3σ upper limit is <1.2 mJy), and therefore cannot attribute the 850 μm flux detected here to contamination from synchrotron radiation. The 4σ submillimetre peak to the W of the galaxy, coincident with a knot seen in the optical and 2MASS images (see Figure 3.11), is not associated with any noisy bolometers.

NGC 6120. The submillimetre emission to the W of the galaxy, and at the S of the map, is associated with noisy bolometers.

NGC 6126. The submillimetre source (which we measured as a point source) is offset to the S of the optical extent of the galaxy. I note that, at minimum contrast, a small satellite/companion object can be seen in this region in the DSS and 2MASS images shown in Figure 3.12. The 3σ peak to the S of the map is not associated with any noisy bolometers and is coincident with a small object visible in the optical. This observation, however, was carried out in poor weather.

NGC 6131. The submillimetre emission to the very NW of the galaxy (beyond the main optical extent) may be associated with a noisy bolometer.

NGC 6137. I estimate that $\sim 20\%$ of the 850 μm flux from this elliptical galaxy could be due to synchrotron contamination from a radio source associated with the galaxy (see Section 3.4). Although only the submillimetre emission to the W of the galaxy coincides with a noisy bolometer I note that this observation had a tilted sky.

NGC 6146. I estimate that as much as 80% of the 850 μm flux from this elliptical may be due to synchrotron contamination from a radio source associated with the galaxy (see Section 3.4).
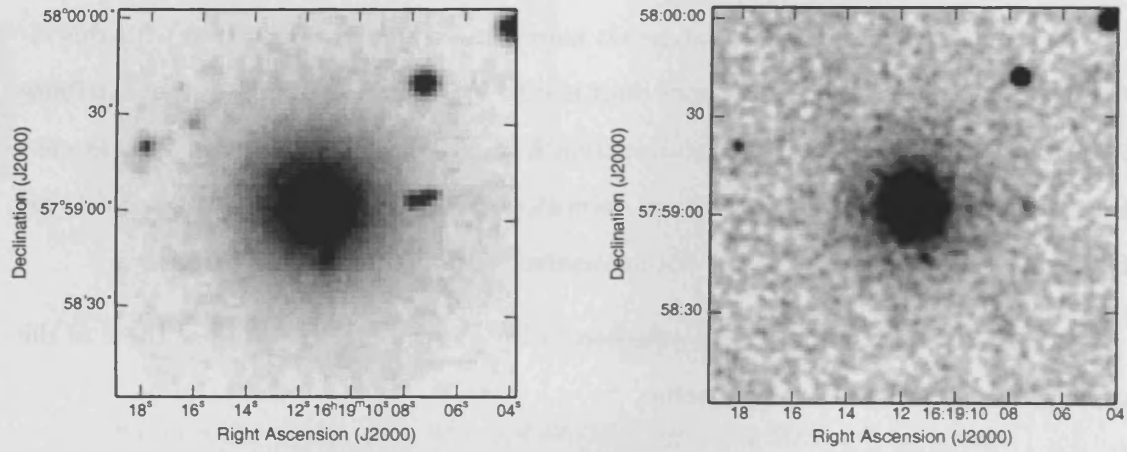
Figure 3.11:   NGC 6127. DSS 1st Gen (left) and 2MASS K-band (right) images.
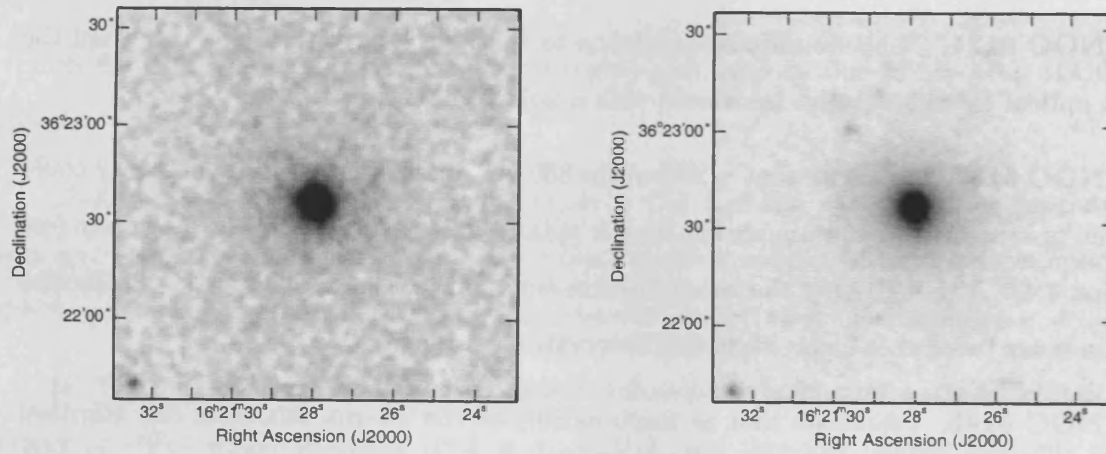
Figure 3.12:   NGC 6126. 2MASS J-band (left) and DSS IR (right) images.

NGC 6155 The submillimetre map shows extended emission to the S and SE of the galaxy at 850 μm, coincident with a number of small galaxies/condensations in the optical. Márquez et al. (1999) find one of the spiral arms in this galaxy is directed towards the SE. None of the submillimetre peaks in this map are associated with noisy bolometers.

A large aperture was used to measure all the flux associated with this object, and these results are listed in Table 3.1. However at 450 μm any flux appears confined to the main optical extent (though the map at 450 μm is very noisy), and thus the flux measurement at 450 μm was made using a smaller aperture. Using these values of the 850 μm and 450 μm flux I found a two-component SED could not be fitted (Section 3.5); the S_{450}/S_{850} ratio is simply too low, most likely because I have measured extended emission at 850 μm. Thus I also measured the S_{850} using a smaller aperture the same size as used at 450 μm, and find $S_{850} = 0.069 \pm 0.013$ Jy. For this smaller aperture I find that a two-component model can just be fitted to the data, and those parameters are listed in Table 3.3.

NGC 6166 is an elliptical and is located in a very busy field – it is the dominant galaxy in the cluster Abell 2199. The presence of dust lanes is well documented in the literature. I note that my SCANPI measurements (see Chapter 2) are in good agreement with those of Knapp et al. (1989). Using all available radio fluxes from the literature I estimate that as little as 4% or as much as 100% of the 850 μm flux from this elliptical may be due to synchrotron contamination from a radio source associated with the galaxy (depending whether a spectral index is assumed constant over the whole galaxy or whether it is assumed to have a flatter core) – see Section 3.4. However, the S_{60}/S_{100}:S_{60}/S_{850} submm:far-IR colours for this galaxy (the submm:far-IR colours being strongly correlated as shown in Chapter 4) indicate that, if the SCANPI fluxes measured are true, the 850 μm flux is unlikely to be significantly contaminated by synchrotron emission (the position of this galaxy on the colour-colour plane agrees extremely well with the fitted linear relation).

Figure 3.13:   NGC 6189. SuperCOSMOS B-band (left) and R-band (right) images.
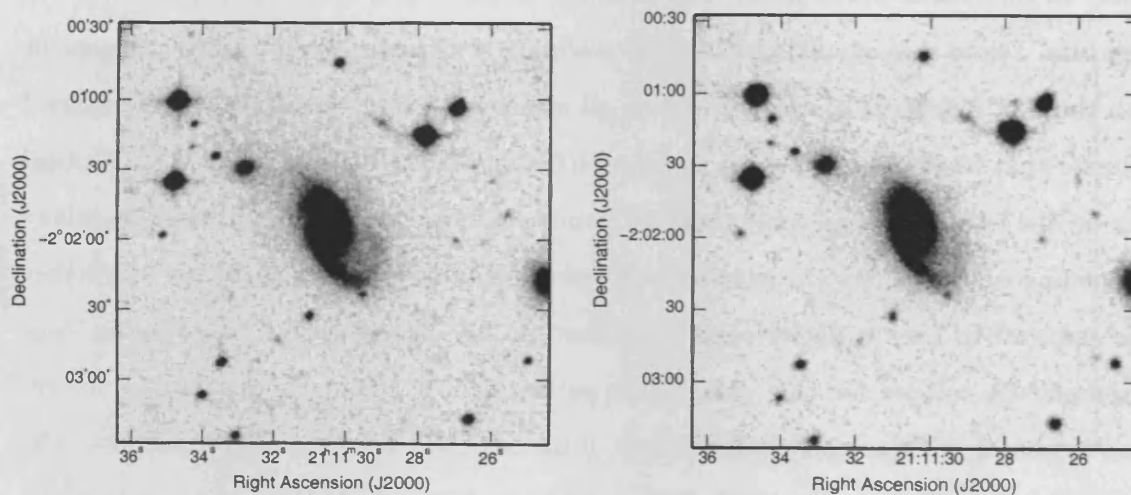
Figure 3.14:   IC 5090. SuperCOSMOS B-band (left) and R-band (right) images.

NGC 6173. I measure S_{100}=0.20 Jy with SCANPI but the detection is unconvincing since the coadds do not agree. Therefore I give an upper limit at 100 μm in Table 3.1.

NGC 6189. This source has three submillimetre peaks associated with the optical galaxy — both a bright nucleus and peaks coincident with the spiral arms. More specifically the outer two peaks appear to correspond to the inter-arm regions, as can be seen more clearly in the SuperCOSMOS B- and R-band images (Figure 3.13).

NGC 6190. Some of the data for this object was very noisy and unusable. Consequently the remaining data may not be reliable. The submillimetre emission to the W of the galaxy lies in a region where there is a noisy bolometer in the 850 μm flux map. Thus the apertures used also unavoidably encompass some noisy bolometers, particularly at 450 μm, and results for this object should be used with caution. However, the rest of the 850 μm emission in the map is not associated with any noisy bolometers, so while the flux measurements may be unreliable this does not apply to the emission extent, which appears to follow the outer spiral arm structure (or more explicitly the inter-arm region).

IC 5090. The submillimetre emission of this very strong source is extended to the W. Although this map had a tilted sky, the extended submillimetre emission is consistent with one of the (possibly disturbed) spiral arms clearly evident in the SuperCOSMOS B- and R-band images (Figure 3.14) but which is too faint to be seen in the DSS image shown in Figure 3.1.

NGC 7081. The submillimetre emission to the E and W of this galaxy are not associated with any noisy bolometers. The emission to the N and SE is coincident with regions of the map which are only slightly noisy, and since this observation was carried out in very good weather it is unlikely that any residual features of this noise remain in the S/N map (Section 2.9). Though from the optical DSS image only the central region of the galaxy (coincident with the main submillimetre peak) is clearly visible, there is evidence that this spiral has a very faint extended spiral arm structure. This is confirmed
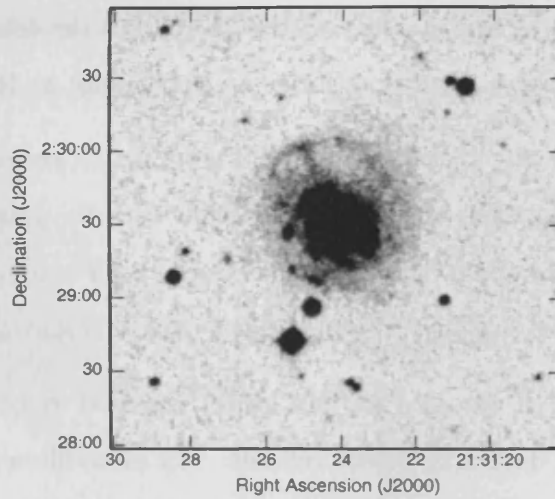
Figure 3.15:   NGC 7081. SuperCOSMOS B-band image.

by optical images from SuperCOSMOS (see Figure 3.15) which clearly show very knotty and irregular faint spiral arms coincident with the peaks of submillimetre emission to the N and W of the galaxy.

NGC 7442. The 3σ submillimetre peak to NW of main optical extent is coincident with faint optical knots and (unlike the 2σ peaks elsewhere in the submillimetre map) is not associated with any noisy bolometers. The two main submillimetre peaks appear to correspond to the spiral arms/inter-arm regions, as can be seen more clearly in the SuperCOSMOS B- and R-band images shown in Figure 3.16.

NGC 7463. This galaxy is part of a triple system with NGC 7464 (to the S of NGC 7463) and NGC 7465 (not shown in Figure 3.1). At $850\,\mu$m emission is clearly detected from both NGC 7463 and NGC 7464, which seem to be joined by a bridge of submillimetre emission. The flux listed in Table 3.1 is for NGC 7463 alone, measured in an aperture corresponding to its main optical extent. Unfortunately a very noisy bolometer to the SE prevents us measuring the flux from the eastern half of NGC 7464, but excluding this
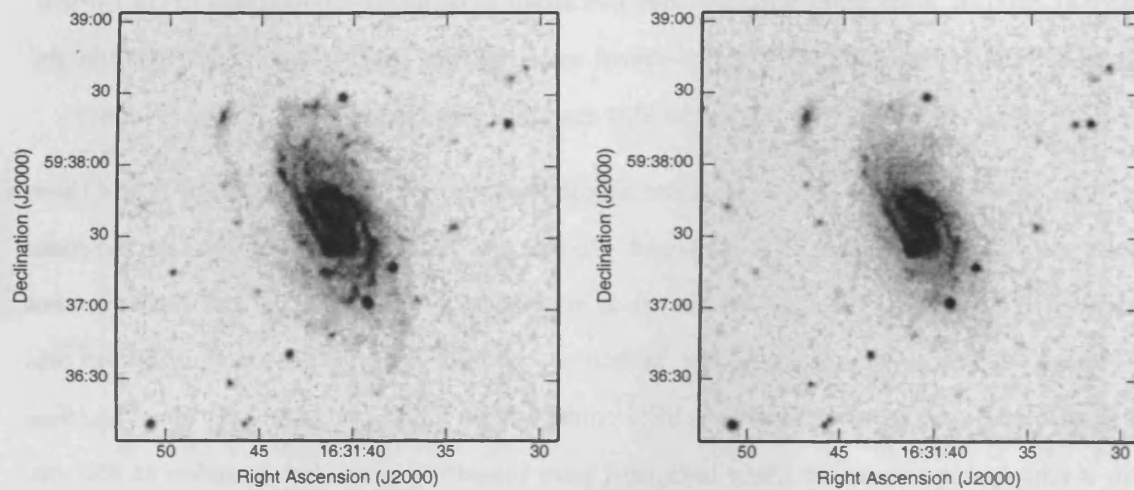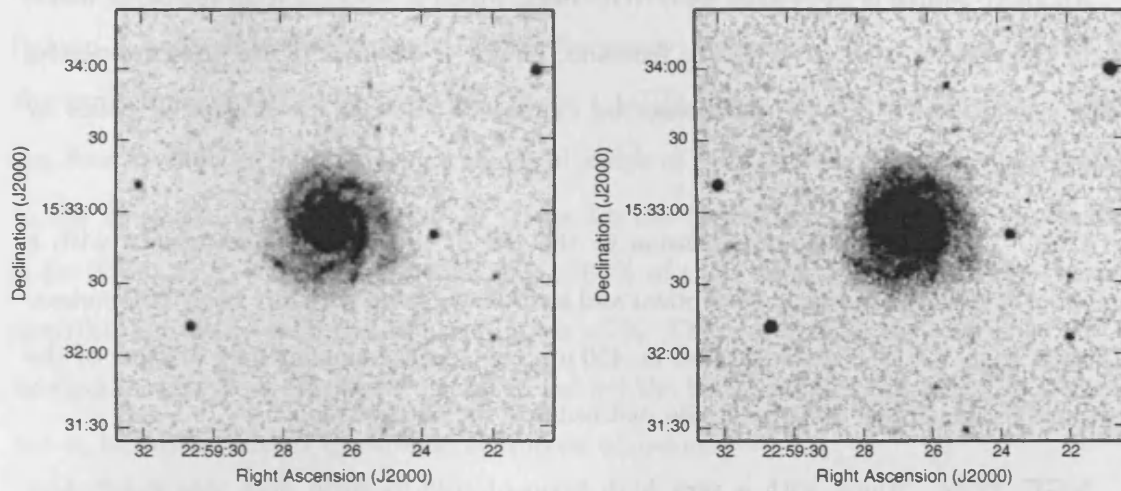
Figure 3.16:   NGC 7442. SuperCOSMOS B-band (left) and R-band (right) images.
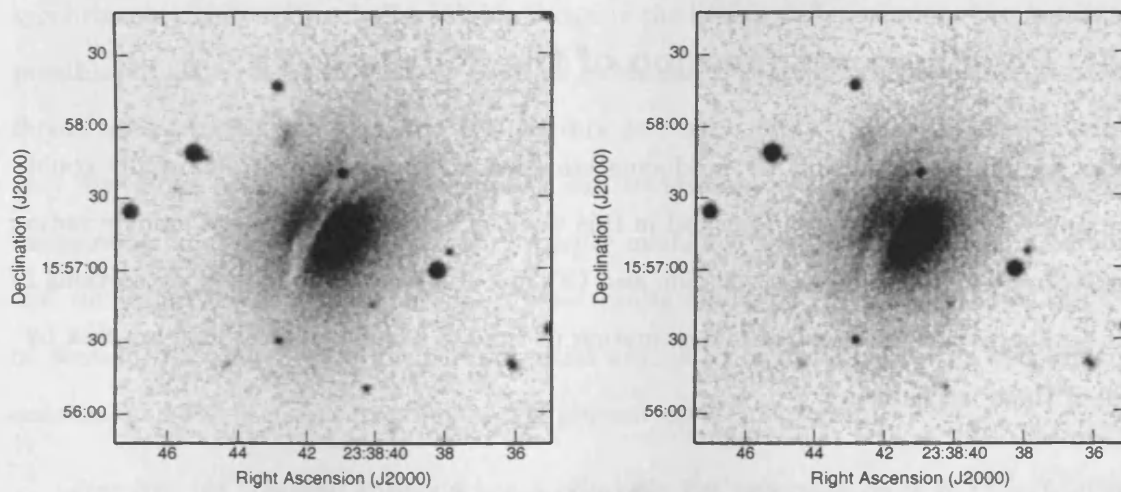
Figure 3.17:   NGC 7722. SuperCOSMOS B-band (left) and R-band (right) images.

region I measure a flux for the pair of 0.051 ± 0.012 Jy, though obviously a lower limit.

An *IRAS* source is associated with NGC 7465, which is resolved from the other members of the system at 60 μm (HIRES; Aumann, Fowler & Melnyk 1990). Dust properties of this system (using SCUBA data observed as part of SLUGS) are studied in detail by Thomas et al. (2002).

UGC 12519. The 850 μm emission to the NE of this galaxy is coincident with a number of small objects seen in the optical and is not associated with any noisy bolometers. Although UGC 12519 is also detected at 450 μm the slightly smaller field of view of the short array means these NE objects lie just outside the 450 μm map.

NGC 7722. Along with a very high ratio of cold-to-warm dust this object also has a very prominent dust lane, extending over most of the NE 'half' of the galaxy (this can be seen more clearly in the SuperCOSMOS images shown in Figure 3.17). The 850 μm emission clearly follows the dust lane evident in the optical. The 2σ submillimetre peak to the NW of the galaxy is not associated with any noisy bolometers.

3.4 Possible contamination of the 850 μm flux

There are other mechanisms for producing emission at 850 μm, which potentially could contaminate the 850 μm flux measured in this work. These mechanisms are namely radio synchrotron emission, free-free emission and CO line emission. In the following sections I will briefly discuss the possible contamination of the OS sample galaxies' 850 μm flux by each of these mechanisms.

3.4.1 Radio synchrotron and free-free emission

The contribution of radio synchrotron (or non-thermal) emission to the 850 μm flux can be estimated by assuming a spectral index and extrapolating the 1.4 GHz flux out to 850 μm.

Synchrotron radio emission in most 'normal' galaxies (I will treat the ellipticals separately in this discussion, see below) has a steep spectral slope, typically $S_{\text{synch}} \propto \nu^{-(0.7-0.8)}$ (where S is the flux density and ν is the frequency) (Condon 1992). 1.4 GHz fluxes for the sample are given in Chapter 6. These 1.4 GHz fluxes are on average only 25% of the flux at 850 μm, so assuming a spectral index of -0.7 the non-thermal contribution to the measured 850 μm flux is <1%. Even for the highest relative 1.4 GHz flux (which is for NGC 7653, where the 1.4 GHz flux is 82% of the flux at 850 μm) the non-thermal contribution to the measured 850 μm flux is <2%. Therefore for all the sample (with the exception of the four ellipticals discussed below) the 850 μm fluxes can safely be assumed not to be contaminated by radio synchrotron emission.

There are a few exceptions in the sample, and these are the elliptical galaxies (NGC 6137, NGC 6146, NGC 6166 and UGC 7115, the other two ellipticals having no radio source associated with the galaxy as discussed in Section 3.3). These four ellipticals all have 1.4 GHz fluxes larger than their measured 850 μm fluxes. In order to estimate what proportion of these ellipticals' measured 850 μm emission is due to contamination by synchrotron emission I used all available fluxes in the literature (at as many frequencies as possible) to make an estimate of the spectral index and the extrapolation to 850 μm (these fluxes are plotted along with the 850 μm flux in Figure 3.18). Since there were often very few fluxes available in the literature, and sometimes disagreement between various measurements at the same frequency, I simply made a rough estimate of the maximum and minimum possible contribution. These results are listed for the individual objects in Section 3.3 above. Overall, the potential amount of contamination by synchrotron emission at 850 μm ranges from just a few percent up to 100 percent.

Free-free (or thermal) emission has a relatively flat spectrum $S_{\text{ff}} \propto \nu^{-(0.1)}$. Condon & Yin (1990) suggest that the ratio of non-thermal to thermal radio fluxes $S_{\text{synch}}/S_{\text{ff}}$ is
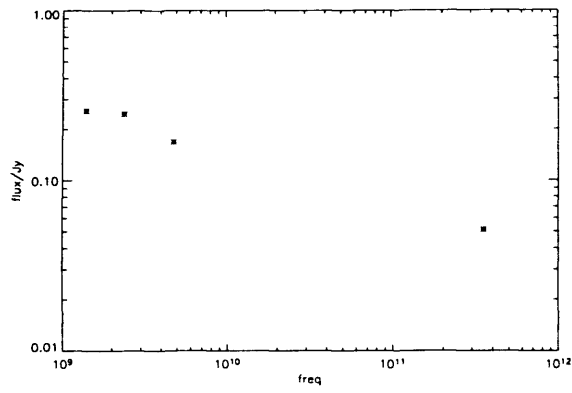
(a) UGC 7115
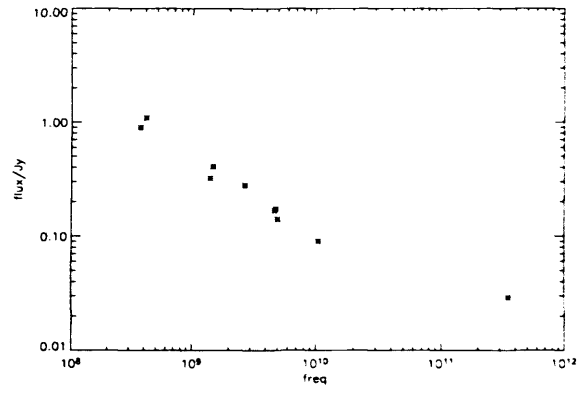
(b) NGC 6137
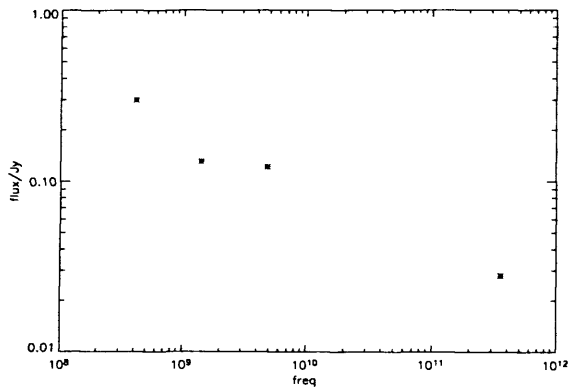
(c) NGC 6146
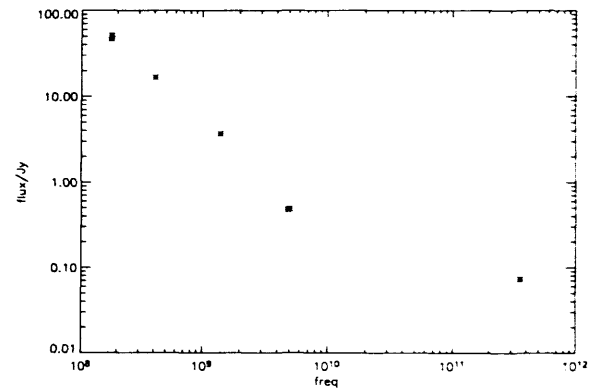
(d) NGC 6166

Figure 3.18:   Radio fluxes for the four ellipticals with fluxes available in the literature. Also plotted is the 850 μm flux measured in this work. These radio fluxes are extrapolated to 850 μm to estimate the potential contamination of the 850 μm flux by radio synchrotron emission.

similar for most spiral galaxies and on average can be estimated by the approximation

$$\frac{S_{\text{synch}}}{S_{\text{ff}}} \sim 10(\nu/1GHz)^{0.1-\alpha} \tag{3.1}$$

where ν is the radio frequency and α is the non-thermal spectral index ($\sim$0.7–0.8). This means that at 1.4 GHz the thermal flux is only about 0.1 times the non-thermal flux, and this is in good agreement with the results of Kennicutt (1983). Consequently, given that (as above) the 1.4 GHz fluxes are on average only 25% of the flux at 850 μm, the potential free-free contribution at 850 μm is $\sim$1%. This is in good agreement with Gordon (1995) who estimated a contribution at 1300 μm of <5%, this contibution decreasing for shorter wavelengths. The 850 μm fluxes can therefore also quite safely be assumed not to be contaminated by free-free emission.

3.4.2   CO line emission

There are virtually no CO measurements in the literature for the OS sample galaxies, so another potential problem with the measured 850 μm fluxes is any contribution to the SCUBA 850 μm measurements by CO(3-2) line emission. Seaquist et al. (2004) find, for a representative subsample of the IRS SLUGS galaxies from D00, that contamination of 850 μm SCUBA fluxes by CO(3-2) reduces the average dust mass by 25–38%, though this does not affect the shape of the dust mass function derived using the IRS SLUGS sample in D00. However, the OS galaxies are relatively faint submillimetre sources compared with the IRS sample. From the fractional contribution of CO(3-2) line emission derived by Seaquist et al. (a linear fit to the plot of SCUBA-equivalent flux produced by the CO line versus measured SCUBA flux, shown in Figure 3.19) I estimate that for the OS sample the CO line contribution to the 850 μm flux is small and is well within the uncertainties on the 850 μm fluxes given in Table 3.1.
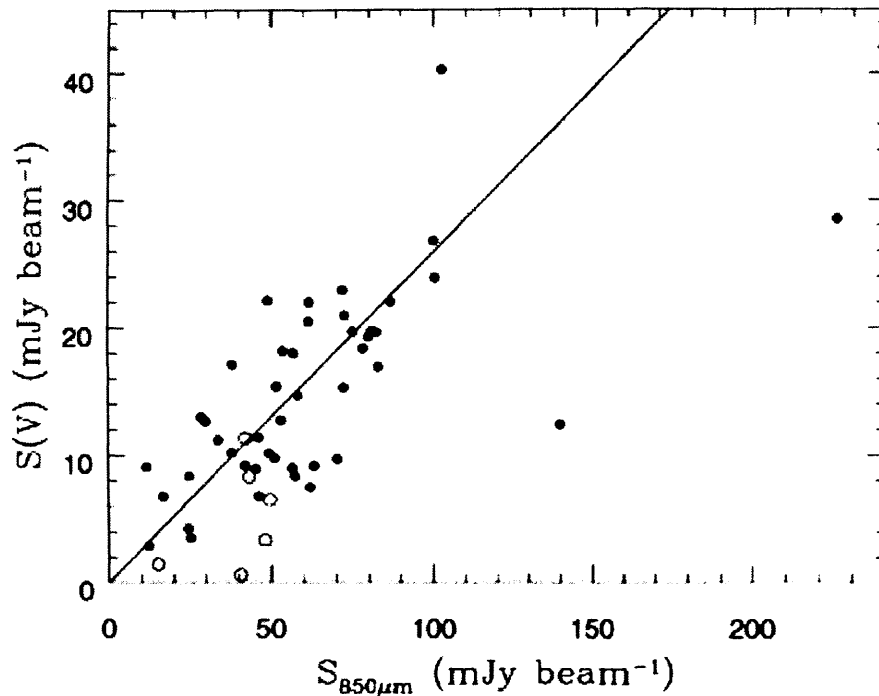
Figure 3.19:   SCUBA-equivalent flux produced by the CO line versus measured SCUBA flux for a subsample of the IRS SLUGS sample galaxies observed in a CO survey, taken from Seaquist et al. (2004). Filled and open points indicate velocities less than and greater than $10\,000\,\mathrm{km\,s^{-1}}$ respectively.

3.5   Spectral fits

In this section I will describe the dust models I have fitted to the spectral energy distributions (SEDs) of the OS sample galaxies and present the results of these fits. Comparison of the results of the OS and IRS samples is discussed in Section 4.

D00 found that for the IRS sample the $60\,\mu$m, $100\,\mu$m and $850\,\mu$m fluxes could be fitted by a single-temperature dust model. However, with the addition of the $450\,\mu$m data (DE01) they found that a single dust emission temperature no longer gives an adequate fit to the data, and that in fact two temperature components are needed, in line with the paradigm that there are two main dust components in galaxies (Section 1.2). For the OS
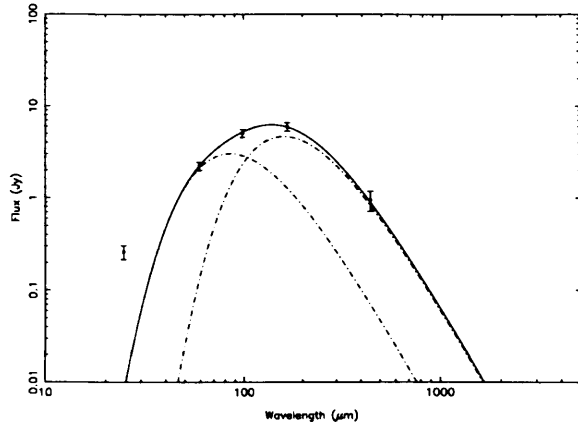
(a) UGC 148: T=(34,18), n=37
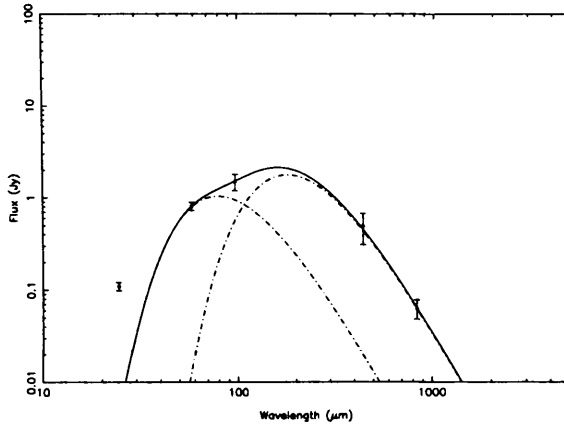
(b) NGC 99: T=(47,17), n=542
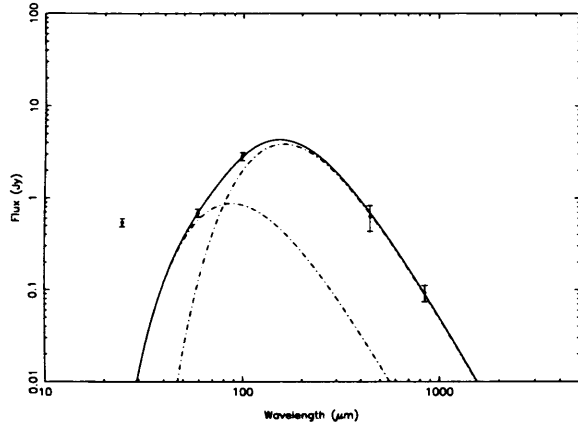
(c) NGC 803: T=(33,18), n=92 (shown) or T=(60,19), n=2597
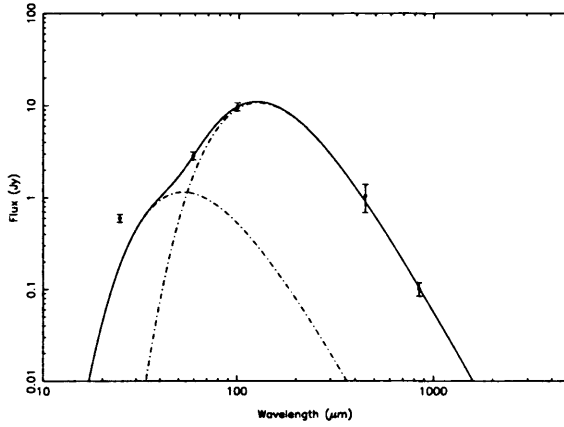
(d) NGC 3689: T=(59,23), n=910
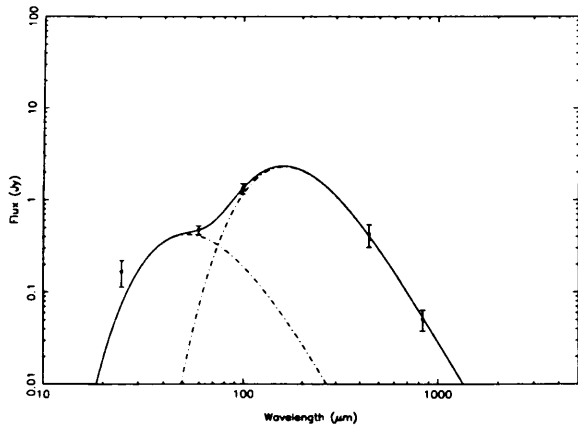
(e) PGC 35952: T=(58,18), n=1859
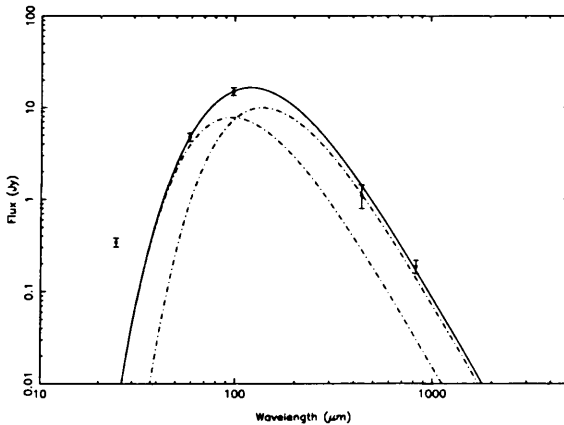
(f) NGC 3987: T=(44,22), n=279

Figure 3.20:   Best-fitting two-component SEDs assuming $\beta = 2$, fitted to the 60, 100, 450 and 850 μm fluxes (with the exception of (a): see Section 3.3). Solid lines represent the composite two-component SED and dot-dash lines indicate the warm and cold components. Any additional 170 μm (ISO) fluxes from the literature (Stickel et al. 2000, 2004) are also plotted, though (with the exception of (a)) not fitted. Note, captions show the fitted parameters (T_w, T_c and N_c/N_w) as listed in Table 3.3, so may be the averaged values (see Section 3.5).
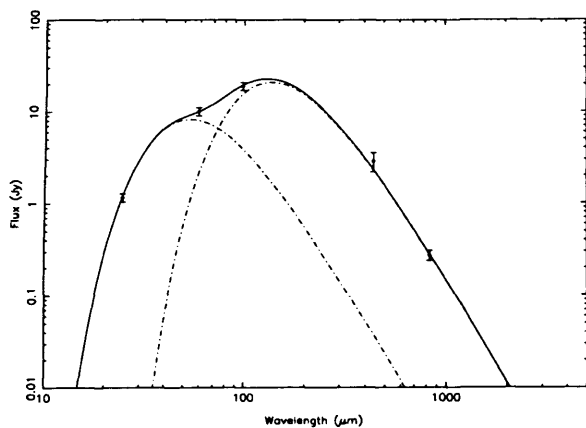
(g) NGC 5953/4: T=(54,21), n=277
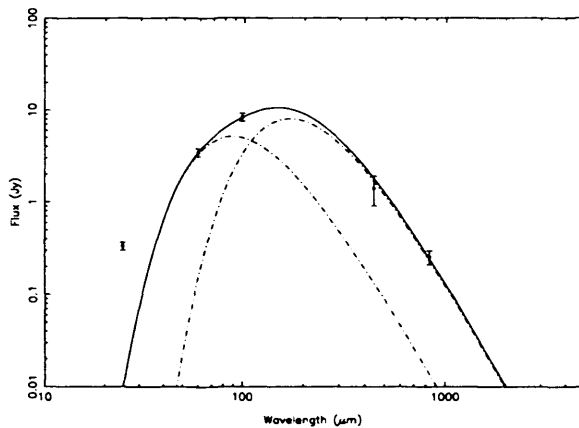
(h) NGC 5980: T=(43,18), n=321
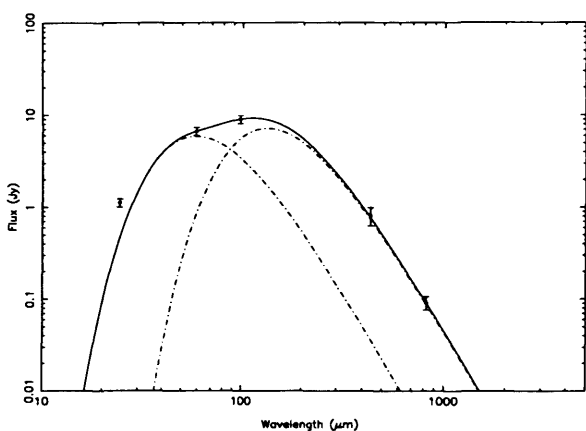
(i) NGC 6090: T=(55,22), n=122
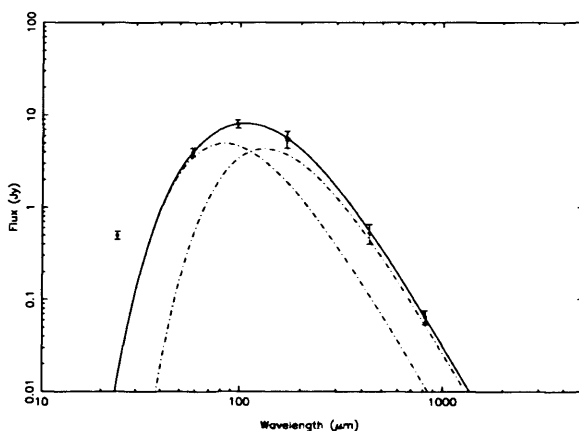
(j) NGC 6120: T=(45,24), n=76
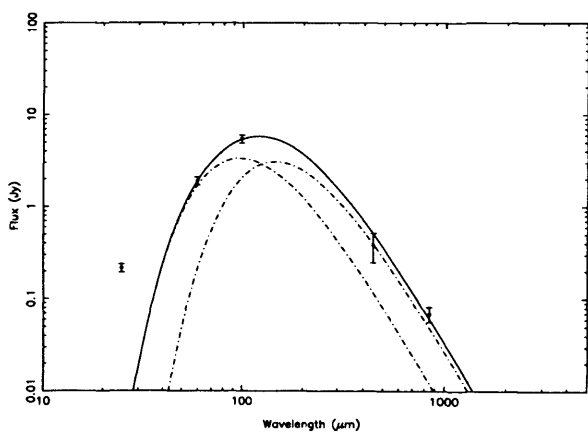
(k) NGC 6155: T=(30,20), n=7
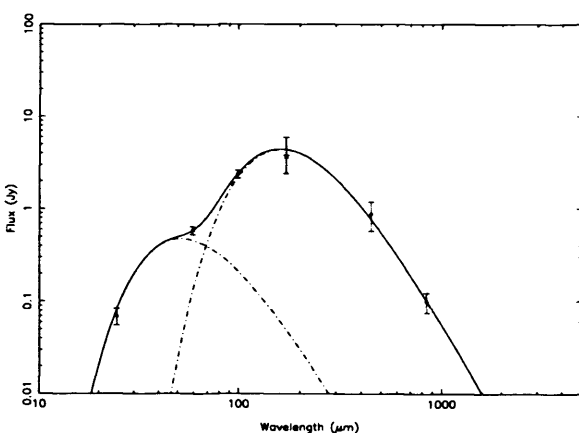
(l) NGC 6190: T=(56,18), n=2684

Figure 3.20: – *continued*
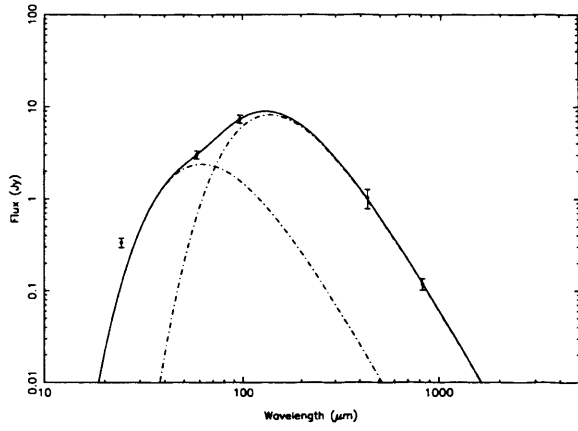
(m) IC 5090: T=(52,21), n=346
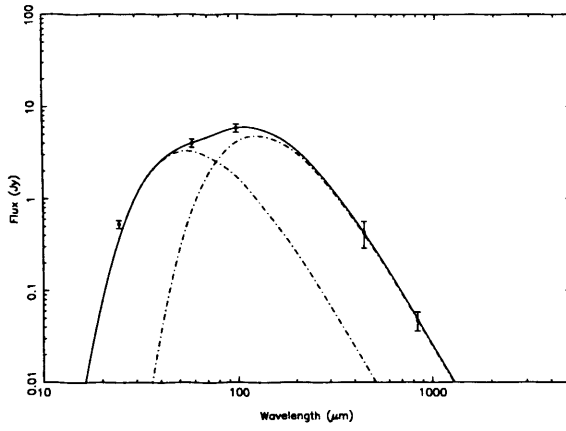
(n) IC 1368: T=(55,23), n=110
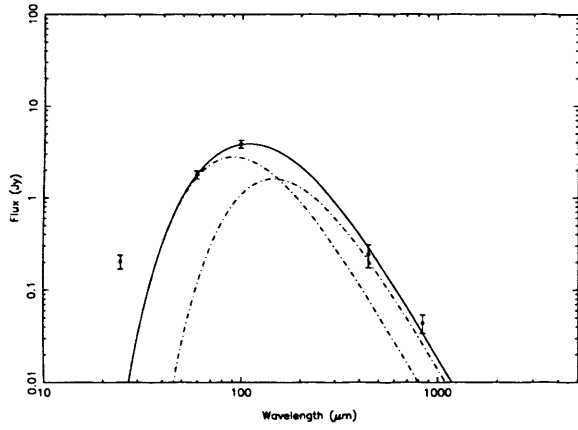
(o) NGC 7081: T=(32,20), n=6
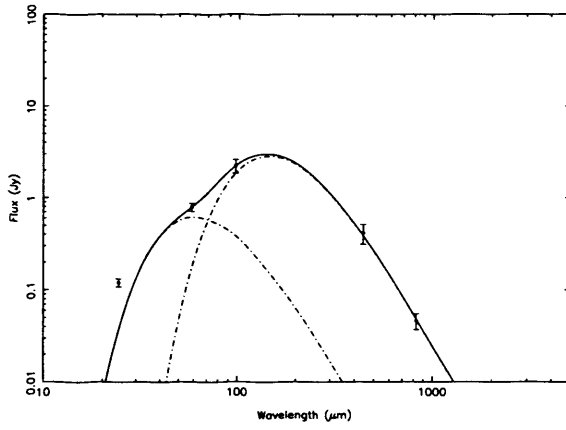
(p) NGC 7442: T=(54,20), n=665
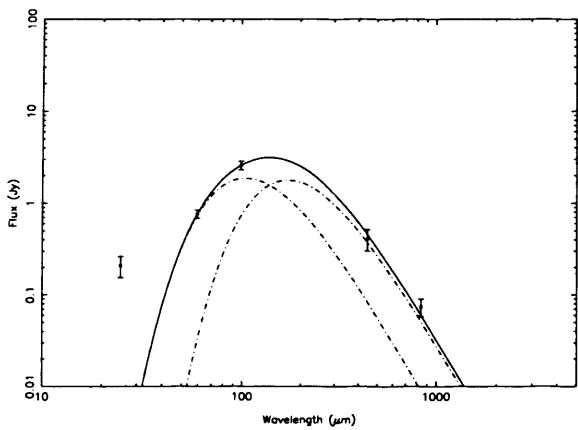
(q) UGC 12519: T=(28,17), n=12
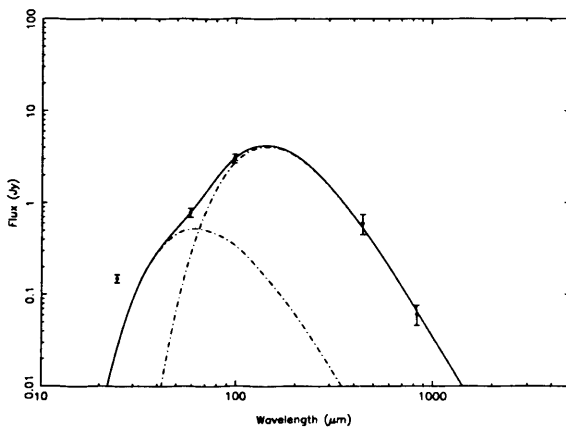
(r) NGC 7722: T=(54,20), n=1224

Figure 3.20: – *continued*

galaxies I have fitted a two-component dust model where there is a 450 μm flux available. Since only 19 of the galaxies have 450 μm flux densities I have also fitted an isothermal model to the data for all the galaxies in the OS sample which were detected at 850 μm.

3.5.1 Two-component SED fits

I fitted two-component dust SEDs to the 60 μm, 100 μm (*IRAS*), 450 μm and 850 μm (SCUBA) fluxes, by minimising the sum of the χ^2 residuals. This two-component model expresses the emission at a particular frequency, S_ν, as the sum of two modified Planck functions or 'grey-bodies' (see Chapter 1), each having a different characteristic temperature, such that

$$S_\nu = N_w \times \nu^\beta B(\nu, T_w) + N_c \times \nu^\beta B(\nu, T_c) \tag{3.2}$$

for the optically thin regime. Here N_w and N_c represent the relative masses in the warm and cold components, T_w and T_c the temperatures in those components, β is the dust emissivity index, and $B(\nu, T)$ is the Planck function which (see Chapter 1), is given by

$$B(\nu, T_d) = \frac{2h}{c^2} \frac{\nu^3}{e^{h\nu/kT_d} - 1} \, . \tag{3.3}$$

Normalisation for N_w is at 60 μm, such that it can represent any fraction of the 60 μm flux, the cold dust then being taken to constitute the remainder of the 60 μm emission. N_c and N_w are therefore not independent as such.

DE01 used the high value for the ratio of S_{450}/S_{850} and the tight correlation between S_{60}/S_{450} and S_{60}/S_{850} for the IRS galaxies to argue that $\beta \approx 2$. The OS galaxies follow a similar tight correlation (Section 4.2). For the OS sample the mean S_{450}/S_{850}=8.6 with σ=3.3, which is slightly higher than found for the IRS sample (where S_{450}/S_{850}=7.9

with $\sigma=1.6$) and with a slightly less tight distribution (though still consistent with being produced by the uncertainties in the fluxes). Both the OS and IRS values are somewhat higher than that found for the Stevens et al. (2005) sample of 14 local spiral galaxies, where the mean $S_{450}/S_{850}=5.9$ and $\sigma=1.0$. Since the OS galaxies have a similar high value for this ratio to the IRS galaxies I follow DE01 in assuming $\beta=2$.

T_w was constrained by the *IRAS* $25\,\mu$m flux (the fit was not allowed to exceed this value), though I did not actually fit this data point, and T_c was allowed to take any value lower than T_w. This method is the same as that used in DE01 for the IRS sample, but while many of the IRS galaxies with $450\,\mu$m data also had fluxes at several other wavelengths in the literature for the OS sample galaxies there are only four data points to fit. Since this is not enough data points to provide a well-constrained fit the values of χ^2_{min} may be unrealistically low. In Table 3.3 I list the parameters producing the best fits or, where more than one set of parameters produces an acceptable fit, I list an average of all those parameters. In practice I find that it is only T_w (and hence N_c/N_w) for which there is sometimes a fairly large range of acceptable values, and this is likely due to not fitting any data points below $60\,\mu$m. All the fitted two-component SEDs are shown in Figure 3.20 (for the best-fitting, not averaged, parameters). Any additional $170\,\mu$m (ISO) fluxes available from the literature (Stickel et al. 2000, 2004) are also plotted in Figure 3.20, though (with the exception of UGC 148 (see Section 3.3)) *not* fitted; where there are several $170\,\mu$m measurements available the mean value is plotted.

The mean warm component temperature is $T_w = 47.4 \pm 2.4\,\mathrm{K}$ and the mean cold component temperature $T_c = 20.2 \pm 0.5\,\mathrm{K}$. The fitted warm component temperatures are in the range $28 < T_w < 59\,\mathrm{K}$ and cold component temperatures are in the range $17 < T_c < 24\,\mathrm{K}$. Thus, the cold component temperature is close to that expected for dust heated by the general ISRF (Cox et al. 1986), one of the two components in the current paradigm (see Chapter 1).

The mean ratio of the mass of cold dust to the mass of warm dust is $N_c/N_w = 532 \pm 172$ (or higher if we include the higher value found for NGC 803 (see notes to Table 3.3 and Section 3.3)). For the IRS sample DE01 found a large variation in the relative contribution of the cold component to the SEDs (described by the parameter N_c/N_w) — for the OS sample we find an even larger variation. Objects NGC 6190 and PGC 35952 in Figure 3.20, for example, clearly exhibit very 'cold' SEDs with a strikingly prominent cold component (with ≈ 2000 times as much cold dust as warm dust). Comparison of the two samples will be discussed in detail in Chapter 4.

3.5.2 Isothermal SED fits

Since 450 μm fluxes are only available for only $\sim$ one third of the sample I have in addition fitted single-component SEDs for all sources in the OS sample. While in the previous section I described how the two-component model is a sum of two 'grey-bodies', in the isothermal model the emission at a particular frequency, S_ν, is then simply described by

$$S_\nu = N \times \nu^\beta B(\nu, T_d) \tag{3.4}$$

where N is the normalisation term (normalisation was at 60 μm), $B(\nu,T_d)$ is the Planck function as described in in Equation 3.3, β is the dust emissivity index and T_d is the dust temperature. Equation 3.4 therefore assumes that all of the emission between 60 μm and 100 μm comes from dust emitting at a single temperature.

In these fits β has been allowed to vary as well as T_d, since it is rarely possible to get an acceptable fit with β=2. The best fitting T_d and β are listed in Table 3.1. Once again, there are not enough data points to provide a well-constrained fit (3 data points and 3 free parameters), and so β and T_d should be considered good empirical descriptors of the data rather than the *actual* values. I include fitted parameters only for those objects with
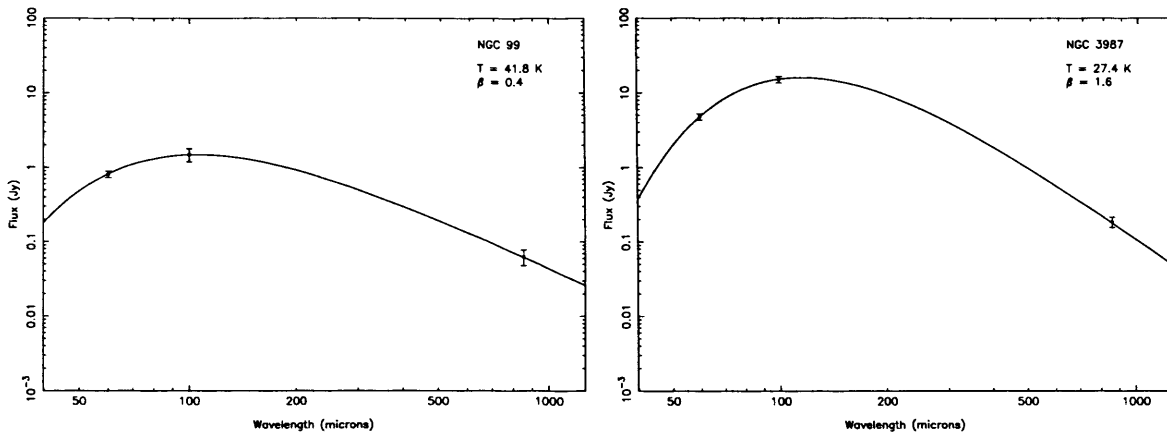
Figure 3.21: Two representative isothermal SEDs. The isothermal SEDs for the full OS sample are shown in Appendix A.

detections in all 3 wavebands (60 μm, 100 μm and 850 μm).

The sample mean and error in the mean for the best-fitting temperature is $\bar{T_d} = 31.6 \pm 0.6$ K and for the dust emissivity index $\bar{\beta} = 1.11 \pm 0.05$. Figure 3.21 shows two representative isothermal SEDs (the isothermal SEDs for the full OS sample are shown in Appendix A). As an example of the potential dangers of fitting single-temperature SEDs, I note one of these objects (NGC 99) is also fitted with the two-component model (shown in Figure 3.20). NGC 99 can clearly be well-fitted by both an isothermal dust model with very flat β (β=0.4 in this case) *and* a two-component model with much steeper β (β=2); this is also the case for NGC 6190 and PGC 35952 described above. I also note that the low values of β found from the isothermal fits are not the *true* values of β but rather is evidence that galaxies across all Hubble types contain a significant proportion of dust that is colder than these fitted temperatures, and it is likely that these objects (as for NGC 99) require a two-component model to adequately describe their SED.

Table 3.3: 450 μm flux densities and two-component SED parameters. (Notes on individual objects are listed in Section 3.3).

(1) Name	(2) S_{450} (Jy)	(3) σ_{450} (Jy)	(4) $\frac{S_{450}}{S_{850}}$	(5) T_w (K)	(6) T_c (K)	(7) $\frac{N_c}{N_w}$	(8) M_{d2} (log $M_\odot$)	(9) L_{fir} (log $L_\odot$)
UGC 148†	0.944	0.236	17.18	34	18	37	...	10.33
NGC 99	0.490	0.182	7.73	47	17	542	7.72	10.08
NGC 803‡	0.631	0.196	6.79	33	18	92	7.02	9.46
NGC 3689*	1.045	0.357	10.30	59	23	910	7.13	10.16
PGC 35952	0.421	0.116	8.26	58	18	1859	7.31	9.77
NGC 3987	1.110	0.319	5.98	44	22	279	7.85	10.78
IC 979§	0.874	0.341	15.39	...	...	...	...	...
NGC 5953/4	2.879	0.683	10.54	54	21	277	7.33	10.28
NGC 5980	1.398	0.495	5.53	43	18	321	8.06	10.53
NGC 6090	0.803	0.180	8.82	55	22	122	8.09	11.29
NGC 6120	0.528	0.127	8.08	45	24	76	7.96	11.17
NGC 6155*	0.381	0.135	3.30	30	20	7	6.92	9.80
NGC 6190*	0.880	0.308	8.89	56	18	2684	7.16	9.85
IC 5090	1.018	0.240	8.66	52	21	346	8.28	11.19
IC 1368	0.425	0.137	9.10	55	23	110	7.10	10.37
NGC 7081	0.241	0.067	5.43	32	20	6	6.98	9.93
NGC 7442	0.410	0.099	9.02	54	20	665	7.70	10.45
UGC 12519	0.408	0.108	5.54	28	17	12	7.57	10.02
NGC 7722	0.595	0.148	9.78	54	20	1224	7.33	10.04

(1) Most commonly used name.

(2) 450 μm flux (this work).

(3) Error on 450 μm flux, calculated as described in Section 2.8.

(4) Ratio of 450- to 850-μm fluxes.

(5) Warm temperature using $\beta = 2$.

(6) Cold temperature using $\beta = 2$.

(7) Ratio of cold-to-warm dust.

(8) Dust mass calculated using parameters in columns (5)-(7).

(9) FIR luminosity (40–1000μm) integrated under the two-component SED.

* Some caution is advised (see Section 3.3).

§ The data could not be fitted with a 2-component model (see Section 3.3).

† Not well-fitted by two-component model using 850 μm data point; fitted parameters here are from 2-component fit to the 60, 100, 450 and 170 μm (ISO) data points; (see Section 3.3).

‡ The data for NGC 803 are also well-fitted by the parameters: T_w=60 K, T_c=19 K, $\frac{N_c}{N_w}$=2597, log M_{d2}=6.99 and log L_{fir}=9.48, (see Section 3.3).

3.6 Dust masses

Dust masses for the OS galaxies are calculated using the measured 850 μm fluxes and dust temperatures (T_d) from the isothermal fits (listed in Table 3.1) using

$$M_d = \frac{S_{850}D^2}{\kappa_d(\nu)B(\nu, T_d)} \tag{3.5}$$

where κ_d is the dust mass opacity coefficient at 850 μm, $B(\nu, T_d)$ is the Planck function at 850 μm for the temperature T_d and D is the distance. As for the IRS sample (D00, LD00) I assume a value for $\kappa_d(\nu)$ of 0.077m^{2}kg^{-1}, which is consistent with the value derived by James et al. (2002) from the global properties of galaxies. Though the true value of $\kappa_d(\nu)$ is uncertain, with suggested values ranging from 0.04m^{2}kg^{-1} for the diffuse ISM to 1.1m^{2}kg^{-1} in laboratory studies (the different values of $\kappa_d(\nu)$ in the literature are discussed in detail in Dunne et al. 2003), as long as dust has similar properties in all galaxies then the relative dust masses will be correct. The uncertainties in the relative dust masses then depend only on errors in S_{850} and T_d.

Values for dust masses (calculated using T_d from our isothermal fits) are given in Table 3.4. I find a mean dust mass $\bar{M}_d = (2.34 \pm 0.36) \times 10^7$ M$_\odot$ (where the $\pm$ error is the error on the mean), which is comparable to that found for the IRS sample (D00). This, together with the fact that for the OS sample I find significantly lower values of β, poses a number of issues. As shown by DE01, if more than one temperature component is present the use of a single-temperature model will have given values of β which are lower than actually true, biased the T_d estimates to higher temperatures, and lead to underestimates of the dust masses.

For those galaxies for which I have made two-component fits (Table 3.3) I also calculate the two-component dust mass (M_{d2}), using

$$M_{d2} = \frac{S_{850}D^2}{\kappa_d} \times \left[\frac{N_c}{B(\nu, T_c)} + \frac{N_w}{B(\nu, T_w)} \right]$$ (3.6)

where parameters are the same as in Equation 3.5 and T_c, T_w, N_c and N_w are the fitted two-component parameters as in Equation 3.2 (and listed in Table 3.3). The mean two-component dust mass is found to be $\bar{M}_{d2} = (4.89 \pm 1.20) \times 10^7$ M$_\odot$, and the two-component dust masses are typically a factor of 2 higher than found from fitting single-temperature SEDs, though in some cases (such as NGC 99) as much as a factor of 4 higher.

3.7   Gas masses

The neutral hydrogen masses (M_{HI}) listed in Table 3.4 were calculated from HI fluxes taken from the literature[1] using the standard equation

$$M_{HI} = 2.356 \times 10^5 D^2 S_{HI}$$ (3.7)

where D is the distance in Mpc and S_{HI} is in Jy km s^{-1}.

Only a small handful of objects in the OS sample had CO fluxes in the literature, and so in this work I will not present any molecular gas masses.

3.8   Far-infrared luminosities

The FIR luminosity (L_{fir}) is usually calculated using

$$FIR = 1.26 \times 10^{-14}(2.58S_{60} + S_{100})$$ (3.8)

---

[1]See notes to Table 3.4.

Table 3.4: Luminosities and masses.

(1) Name	(2) log L_{60} (W Hz^{-1}sr^{-1})	(3) log L_{850} (W Hz^{-1}sr^{-1})	(4) log L_{fir} ($L_\odot$)	(5) log M_d ($M_\odot$)	(6) log M_{HI} ($M_\odot$)	(7) log L_B ($L_\odot$)
UGC 148	22.80	21.20	10.22	7.05	9.82	10.39
NGC 99	22.57	21.46	9.94	7.17	10.29	10.37
PGC 3563	22.24	21.13	9.76	6.99	...	10.03
NGC 786	22.56	21.34	9.99	7.14	...	9.94
NGC 803	21.69	20.82	9.37	6.76	9.78	10.13
UGC 5129	21.86	<20.96	<9.46	<7.09	9.34	10.01
NGC 2954	<21.60	<20.81	<9.23	...	8.09	10.25
UGC 5342	22.46	21.03	9.84	6.81	...	10.40
PGC 29536	<22.40	<21.76	<9.94	...	...	10.74
NGC 3209	<21.99	<21.13	<9.66	...	...	10.45
NGC 3270	22.58	21.58	10.23	7.53	10.49	10.78
NGC 3323	22.81	21.48	10.23	7.30	9.68	10.12
NGC 3689	^{s}22.54	21.09	10.09	7.04	9.14	10.29
UGC 6496	...	...	...	...	...	10.10
PGC 35952	22.08	21.11	9.61	6.96	9.73	10.07
NGC 3799/3800^P	22.93	21.38	10.39	7.27	9.34	...
NGC 3812	<21.68	<20.91	<9.17	...	...	9.95
NGC 3815	22.19	20.96	9.70	6.83	9.62	10.15
NGC 3920	22.21	20.86	9.63	6.68	...	9.87
NGC 3987	23.20	21.79	10.74	7.72	9.75	10.63
NGC 3997	22.63	<20.93	<9.96	<7.06	9.83	10.30
NGC 4005	...	<20.69	...	<6.82	9.22	10.35
NGC 4015	21.88	<21.18	<9.49	<7.31	...	...
UGC 7115	<22.17	21.59	<9.80	†7.71	...	10.45
UGC 7157	<22.15	<21.27	<9.65	...	...	10.32
IC 797	21.72	20.78	9.27	6.63	8.50	9.77
IC 800	21.52	20.82	9.07	6.63	8.51	9.67
NGC 4712	22.18	21.50	9.87	7.43	10.18	10.50
PGC 47122	<21.95	<21.46	<9.71	<7.58	...	10.32
MRK 1365	23.32	21.20	10.61	7.00	9.23	10.00
UGC 8872	<22.04	<21.02	<9.44	...	...	10.29
UGC 8883	22.36	<21.31	<9.86	<7.44	...	10.00
UGC 8902	23.07	21.81	10.57	7.69	...	10.80
IC 979	^{s*}22.27	21.75	*9.85	*7.56	...	10.64
UGC 9110	U	<21.21	...	...	9.72	10.27
NGC 5522	22.84	21.39	10.22	7.17	9.77	10.51
NGC 5953/4^P	22.80	21.22	10.17	7.03	9.32	...
NGC 5980	22.97	21.84	10.44	7.65	...	10.53
IC 1174	<21.80	20.95	<9.19	†7.08	...	10.18
UGC 10200	21.95	<20.10	<9.21	<6.22	9.54	9.05
UGC 10205	22.44	21.61	10.10	7.53	9.57	10.55
NGC 6090	23.93	22.06	11.20	7.78	8.82	10.73

Table 3.4: – continued

(1) Name	(2) $\log L_{60}$ (W Hz^{-1}sr^{-1})	(3) $\log L_{850}$ (W Hz^{-1}sr^{-1})	(4) $\log L_{fir}$ ($L_\odot$)	(5) $\log M_d$ ($M_\odot$)	(6) $\log M_{HI}$ ($M_\odot$)	(7) $\log L_B$ ($L_\odot$)
NGC 6103	22.97	21.88	10.45	7.71	...	10.83
NGC 6104	22.77	<21.59	<10.35	<7.71	...	10.62
IC 1211	<21.78	21.16	<9.52	†7.29	...	10.37
UGC 10325	22.92	21.34	10.35	7.20	9.92	...
NGC 6127	<21.57	21.51	<9.17	†7.64	...	10.66
NGC 6120	23.74	21.95	11.11	7.80	...	10.73
NGC 6126	<22.37	21.56	<9.89	†7.69	...	10.61
NGC 6131	22.49	21.36	10.07	7.27	9.83	10.37
NGC 6137	<22.41	21.62	<9.94	†7.75	...	11.04
NGC 6146	<22.18	21.55	<9.83	†7.68	...	11.01
NGC 6154	<21.95	<21.37	<9.44	...	9.86	10.38
NGC 6155	22.25	21.04	9.78	6.93	8.95	9.82
UGC 10407	23.28	21.48	10.63	7.32	...	10.62
NGC 6166	^{S}22.14	22.00	10.03	7.96	...	11.30
NGC 6173	<22.33	<21.48	<9.63	...	...	11.14
NGC 6189	22.59	21.57	10.19	7.48	10.07	10.68
NGC 6190	22.02	21.24	9.69	7.18	9.48	9.97
NGC 6185	22.47	<21.72	<10.06	<7.85	...	10.96
UGC 10486	<22.06	<21.24	<9.63	...	...	10.31
NGC 6196	<22.24	<21.53	<9.86	...	...	10.85
UGC 10500	^{S*}21.85	<21.09	<9.56	<7.22	...	10.20
IC 5090	23.64	22.23	11.09	8.08	...	10.46
IC 1368	23.00	21.07	10.30	6.83	...	10.14
NGC 7047	22.35	21.45	9.98	7.38	9.08	10.50
NGC 7081	22.49	20.88	9.89	6.72	9.51	9.75
NGC 7280	<20.80	<20.34	<8.51	...	8.16	9.85
NGC 7442	22.83	21.60	10.32	7.47	9.75	10.48
NGC 7448	22.84	21.19	10.19	7.04	9.75	10.39
NGC 7461	<21.70	<20.81	<9.33	...	...	9.90
NGC 7463	U	20.60	...	^{r}6.73	9.33	10.12
III ZW 093	23.26	<21.99	<11.06	<8.12	9.95	11.60
III ZW 095	<21.92	<21.24	<9.93	...	...	9.90
UGC 12519	22.37	21.36	9.95	7.26	9.53	10.27
NGC 7653	22.59	21.52	10.17	7.43	...	10.49
NGC 7691	22.15	<20.82	<9.68	<6.95	9.59	10.24
NGC 7711	<21.60	<20.86	<9.20	...	...	10.57
NGC 7722	22.31	21.20	9.94	7.15	9.51	10.48

(1) Most commonly used name.

(2) 60 μm luminosity.

(3) 850 μm luminosity.

(4) FIR luminosity, calculated by integrating measured SED from 40–1000 μm.

Table 3.4: – *continued*

(5) Dust mass, calculated using a single temperature, T_d, as listed in Table 3.1 (T_d derived from fitted SED to the 60, 100 and 850 μm data points). Upper limits are calculated using T_d=20 K.

(6) HI mass taken from the literature; refs.: Chamaraux, Balkowski & Fontanelli (1987), Haynes & Giovanelli (1988, 1991), Huchtmeier & Richter (1989), Giovanelli & Haynes (1993), Lu et al. (1993), Freudling (1995), DuPrie & Schneider (1996), Huchtmeier (1997), Theureau et al. (1998), Haynes et al. (1999).

(7) Blue luminosity, calculated from corrected blue magnitudes taken from the LEDA database.

^{p} A close or interacting pair which was resolved by SCUBA; parameters given refer to the combined system, as in Table 3.2.

* Values should be used with caution (see * notes to Table 3.1).

† Object was only detected at 850 μm (and not in either *IRAS* band), so these dust masses should be used with caution; these are all early types; dust masses calculated using T_d=20 K.

^{r} Dust mass calculated using T_d=20 K, since no fitted value of T_d.

U Unresolved by *IRAS*.

Notes on HI fluxes:-

NGC 7463 Giovanelli & Haynes (1993) note confused HI profile, many neighbours.

UGC 12519 HI flux from Giovanelli & Haynes (1993) gives HI mass of log $M_\odot$=9.65.

NGC 7691 Haynes et al. (1999) gives log $M_\odot$=9.88.

NGC 5953/4 HI flux from Freudling (1995); Huchtmeier & Richter (1989) give log $M_\odot$ in the range 8.82 – 9.20.

NGC 3799/3800 flux for NGC 3800 but sources may be confused (Lu et al. 1993).

NGC 803 Giovanelli & Haynes (1993) give log $M_\odot$=9.68, and note optical disk larger than beam.

NGC 6090 Huchtmeier & Richter (1989) give values up to log $M_\odot$=10.24.

NGC 6131 confused with neighbour.

NGC 6189 Haynes et al. (1999) gives log $M_\odot$=10.26.

NGC 7081 Huchtmeier & Richter (1989) give values up to log $M_\odot$=9.69.

NGC 4712 Huchtmeier & Richter (1989) give log $M_\odot$=9.91.

and

$$L_{fir} = 4\pi D^2 \times FIR \times C \qquad (3.9)$$

as described in the Appendix of *Catalogued Galaxies and Quasars Observed in the IRAS Survey* (Version 2, 1989), where S_{60} and S_{100} are the $60\,\mu$m and $100\,\mu$m *IRAS* fluxes (in Janskys), D is the distance, and C is a colour-correction factor dependent on the ratio S_{60}/S_{100} and the assumed emissivity index. The purpose of this correction factor is to account for emission outside the *IRAS* bands, and is explained by Helou et al. (1988).

However, since I have submillimetre fluxes I can use our derived T_d and β to integrate the total flux under the SED out to $1000\,\mu$m. This method gives more accurate values of L_{fir} since it makes no general assumptions. I list in Table 3.4 L_{fir} calculated using this method and the fitted isothermal SEDs. The mean FIR luminosity is $\bar{L}_{fir} = (2.38 \pm 0.54) \times 10^{10}$ M$_\odot$ (where the $\pm$ error is the error on the mean). This is an order of magnitude lower than found for the IRS sample ($\bar{L}_{fir} = (1.16 \pm 0.15) \times 10^{11}$ M$_\odot$). I will discuss this difference further in Chapter 4. L_{fir} values calculated using the two-component SEDs are listed in Table 3.3. The mean two-component FIR luminosity is $\bar{L}_{fir} = (4.24 \pm 0.92) \times 10^{10}$ M$_\odot$.

3.9 Optical luminosities

The blue luminosities given in Table 3.4 are converted (using M$_{B\odot}$=5.48) from blue apparent magnitudes (m_B) taken from the Lyon-Meudon Extragalactic Database (LEDA; Paturel et al. 1989, 2003) which have already been corrected for galactic extinction, internal extinction and k-correction, using

$$\log(L_B) = \frac{M_{B\odot} + 5\log\left(\frac{d}{10}\right) - m_B}{2.5} \qquad (3.10)$$

where d is the distance in parsecs and L_B is in solar luminosities.

3.10 Summary

Out of 81 galaxies observed in the OS sample, 52 were detected at 850 μm and 19 were detected at 450 μm. Many of these galaxies have 850 μm emission which appears extended with respect to the DSS optical emission, and which appears to correspond to very faint optical features.

I have produced 850 μm S/N maps of the OS galaxies and by comparing them to optical DSS images I have found that there is a variety of submillimetre morphologies in the sample. Some galaxies exhibit core-dominated emission, similar to that found for the previous IRS SLUGS sample of bright *IRAS* galaxies, while others exhibit two distinct peaks of emission associated with the spiral arm structure. These results are consistent with numerous other mm/submm studies of nearby galaxies in the literature.

I have fitted two-component dust spectral energy distributions to the 60, 100, 450 and 850 μm flux densities for 18 of the galaxies which were detected at 850 μm *and* at 450 μm. I have shown that the *IRAS* and submillimetre fluxes are well-fitted by a two-component dust model with dust emissivity index β=2. The tight and fairly constant ratio of S_{450}/S_{850} for both the OS galaxies and the IRS galaxies is evidence that $\beta \approx 2$. The temperatures of the warm component range from 28 to 59 K; the cold component temperatures range from 17 to 24 K.

I have found the ratio of the mass of cold dust to the mass of warm dust is much higher for our optically-selected galaxies than for the previous SLUGS sample of *IRAS*-selected galaxies (DE01), and can reach values of $\sim$1000.

I also fitted single-temperature dust spectral energy distributions (to the 60, 100 and 850 μm flux densities) for the 41 galaxies in the OS sample with detections in all 3 wavebands. The mean best-fitting temperature for the sample is $\bar{T}_d = 31.6 \pm 0.6$K and the mean dust emissivity index is $\bar{\beta} = 1.12 \pm 0.05$. These values are significantly lower than

for the IRS sample. The very low value of β is additional evidence that galaxies, across all Hubble types, contain a significant amount of cold dust.

I have found a mean dust mass $\bar{M_d} = (2.34 \pm 0.36) \times 10^7 \, M_\odot$ using the isothermal fits. However, using the two-component fits I have found a mean dust mass a factor of two higher.

Out of 11 elliptical galaxies in the sample 6 were detected, and are found to have dust masses in excess of $10^7 \, M_\odot$. It is possible, however, that for some of these galaxies the submillimetre emission may be synchrotron emission rather than dust emission.

Chapter 4

The Submillimetre Properties of Galaxies

4.1 Overview

In this Chapter I will present an analysis of the OS sample results. I will discuss the global properties of the OS sample, including luminosities, dust mass and gas mass, and in particular any relationships, distributions and correlations of these parameters. Unless otherwise stated the analysis in this Chapter will include only those OS objects which were detected at the relevant wavelength. I will compare my results for the OS sample to those previously found for the IRS sample (D00/LD00) and discuss any differences and similarities, and in particular what this tells us about the submillimetre properties of galaxies in the local Universe. In the previous Chapter I described the detection in the OS sample of a population of cold-dust-dominated galaxies that was missed by the previous *IRAS*-selected sample — in this Chapter I will investigate the implications of this for the submillimetre properties of galaxies. Using the results of the OS sample, which includes galaxies drawn from right along the Hubble sequence, I will also investigate whether the
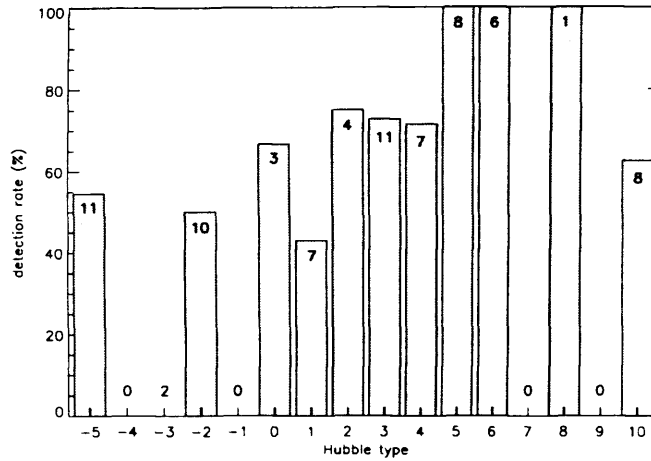
Figure 4.1: Detection rate as function of Hubble type for the OS sample. The total number of each Hubble type in the sample is also indicated.

submillimetre properties of galaxies vary as one moves along the Hubble sequence.

4.2 Optical Selection versus IR Selection

4.2.1 Global properties

In this section I describe the relationships, distributions and correlations of various global properties of the OS sample, and compare them to the results from the IRS sample (D00/LD00). The correlations and their corresponding parameters for the OS sample alone and the *combined* OS + IRS samples are listed in Table 4.1. In the following sections, as well as investigating any differences between the properties of optically- and *IRAS*-selected galaxies I will also use the OS sample to investigate how galaxy properties might vary as function of Hubble type. For clarity I simply divide the OS sample into 4 broad groups based on the galaxies' t-type parameter given in the LEDA database: E-S0 (t=-5 to 0), Early-type spirals (t=1 to 4), S? (t=5) and Late-type spirals (t=6 to 10)

(as described in Chapter 3, Hubble types (t-types) used are those given in LEDA, which uses the standard numerical codes for the de Vaucoulers morphological type, as defined in RC2). The investigation of submillimetre properties along the Hubble sequence will be the subject of Section 4.3.

If a galaxy's dust and gas are associated with its disk, then one might expect that early-type galaxies should be less likely to be submillimetre-emitting sources (see Chapter 1). The detection rate at $850\,\mu$m for the OS sample as function of Hubble type is shown in Figure 4.1, and it appears that the detection rate does tend to be higher for later types. However, it is worth noting here that, while the IRS sample contained no elliptical galaxies and just one or two S0s (early types therefore constituting $< 3\%$ of the IRS sample), for the OS sample 6 ellipticals and 5 S0s were detected — $\sim 20\%$ of the OS sample.

Luminosities

The distributions of $850\,\mu$m, $60\,\mu$m, FIR, and optical (blue) luminosity, for the OS and IRS samples are shown in Figure 4.2 (line-filled and shaded histograms respectively). While there is little difference between the distributions of optical luminosity for the two samples, the OS galaxies tend to have consistently lower $850\,\mu$m luminosities. As expected from the basis of their optical selection, the OS galaxies have very much lower $60\,\mu$m luminosities, more than half of them lower than any in the IRS sample. The OS galaxies also have very much lower FIR luminosities, with the mean FIR luminosity (as discussed in Chapter 3) being an order of magnitude lower. This is probably due to a combination of the fact that the IRS sample, by definition of their selection at $60\,\mu$m, will include much more FIR-luminous objects and the fact that the OS sample contains much larger proportions of cold (~ 20 K) dust (with the ratio of the mass of cold dust to the mass of warm dust reaching values of ~ 1000; see Chapter 3).
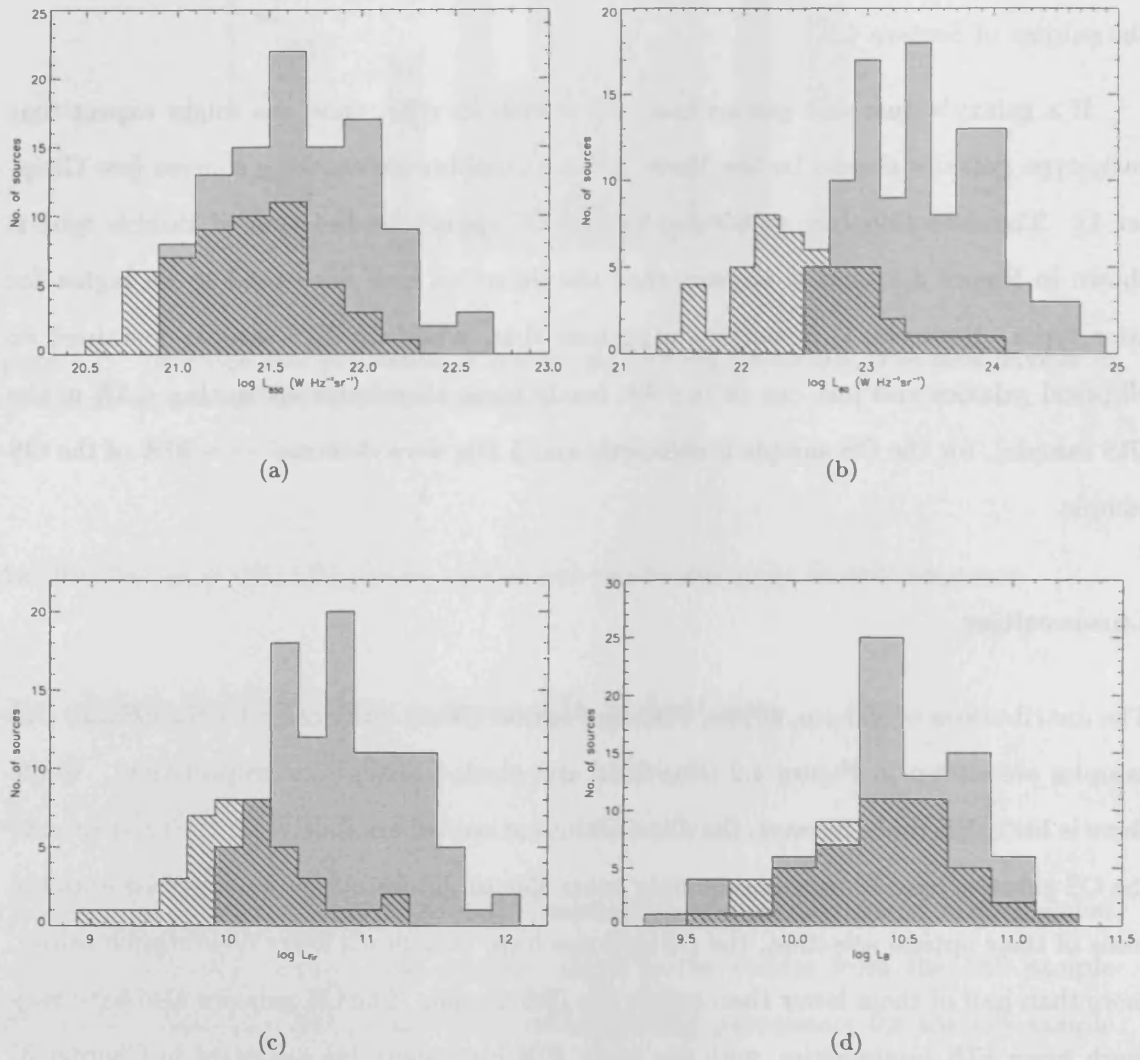
Figure 4.2:   Distributions of (a) $850\,\mu$m luminosity, (b) $60\,\mu$m luminosity, (c) FIR luminosity, and (d) optical blue luminosity, for the OS and IRS SLUGS (line-filled and shaded histograms respectively).

(a)

(b)

Figure 4.3: 60 μm luminosity versus 850 μm luminosity. (a) for the OS sample and IRS sample (star and cross symbols respectively). (b) for the OS sample, with different Hubble types indicated by different symbols: E-S0(t=-5 to 0), Early-type spirals(t=1 to 4), S?(t=5), Late-type spirals(t=6 to 10): circles, triangles, stars, and squares respectively.
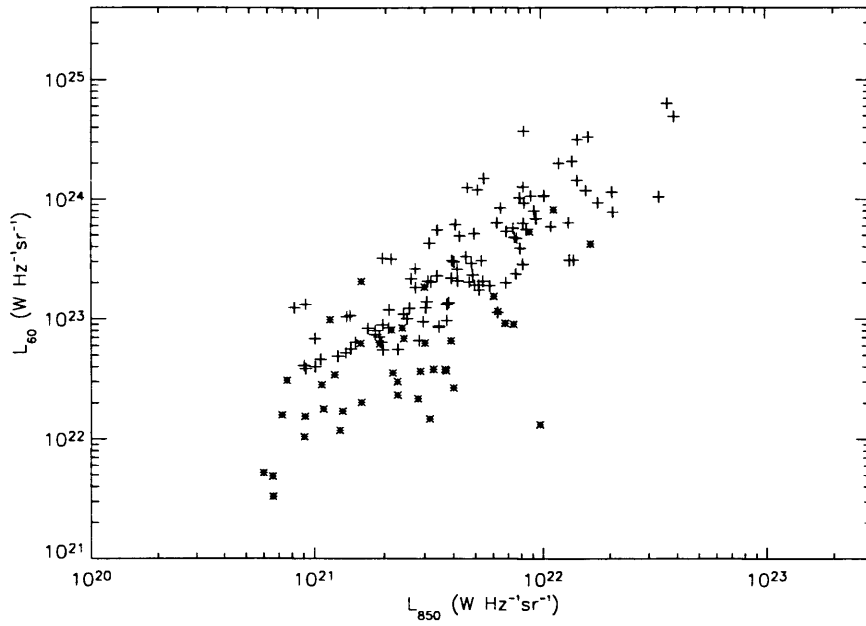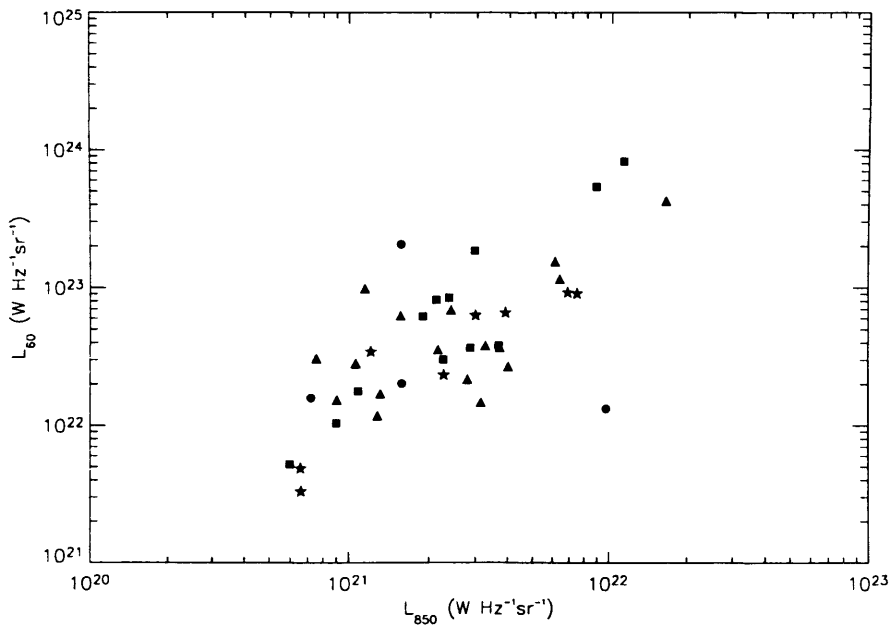
Figure 4.3 shows a plot of $60\,\mu$m luminosity versus $850\,\mu$m luminosity, for the OS and IRS samples (Figure 4.3(a)) and for the OS sample with different Hubble types indicated by different symbols (Figure 4.3(b)). As expected there is a correlation between these two luminosities ($r_s = 0.62$, probability $= 1.48$e-5 for the OS sample; 'probability' refers to the probability that x and y are unrelated). The OS sample extends to lower $850\,\mu$m and $60\,\mu$m luminosities and for a given $60\,\mu$m luminosity has consistently higher $850\,\mu$m luminosities compared to the IRS galaxies. This would be expected if the OS sample is probing a population of galaxies that contain larger proportions of cold dust, as opposed to the larger proportions of warm dust that is probed by the IRS sample. I will return to this subject and its implications throughout this Chapter. Finally, for the OS sample galaxies there is also no obvious tendency for the ratio L_{60}/L_{850} to vary with Hubble type (Figure 4.3(b)).

The FIR luminosity is shown plotted against optical blue luminosity in Figure 4.4. There are clearly differences between the OS and IRS samples. Although L_{fir} is correlated with L_B for both samples, the slope of the linear relationship (in log–log parameter space) appears to be about twice as steep for the OS sample as the IRS sample (Figure 4.4(a); slope $= 0.77$ for OS compared to 0.43 for IRS), with a fairly large scatter for both relationships (rms scatter is 0.37 and 0.43 respectively). The L_{fir} is also consistently lower for the OS sample (as described above), although the range of optical luminosites covered is very similar; in fact, at the lower optical luminosities the OS galaxies have FIR luminosities lower than any in the IRS sample, and with only one or two exceptions the IRS galaxies have L_{fir} at least an order of magnitude higher. This would perhaps be expected, since the IRS sample would miss galaxies with lower L_{fir}, and hence lower L_{fir}/L_B, due to the $60\,\mu$m selection limit, and because for a given range of L_{fir}/L_B the selection limit also means the IRS sample will miss more objects towards lower L_B. The different slopes, however, potentially suggest a more fundamental difference between the properties of optically- and *IRAS*-selected galaxies. If L_{fir} is sensitive to emission from
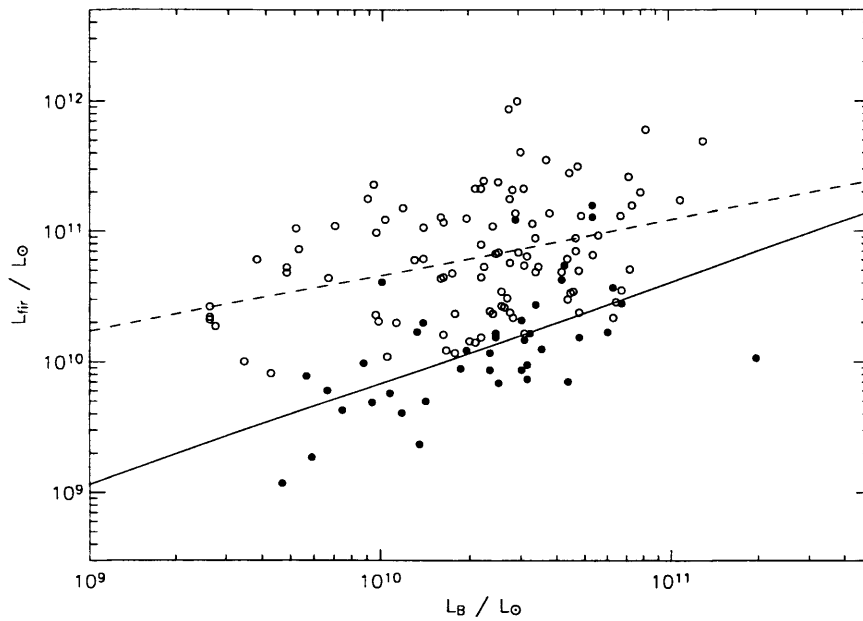
(a)
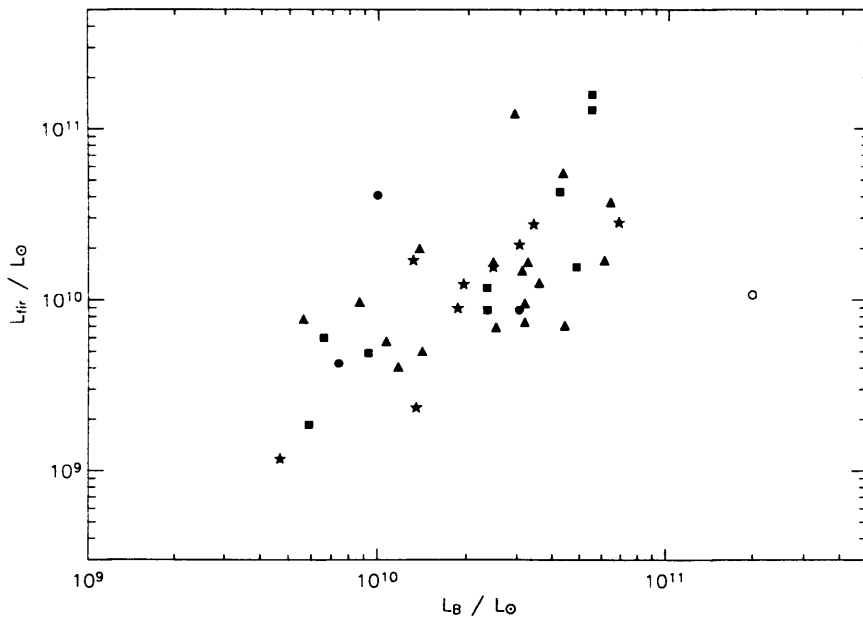
(b)

Figure 4.4: Far-IR luminosity versus optical blue luminosity. (a) for the OS and IRS samples (filled and open points respectively). The solid line is a fit to the OS data and has slope = 0.77±0.17, while the dashed line is a fit to the IRS data and has slope = 0.43±0.11. (b) for the OS sample, with different Hubble types indicated by different symbols: E-S0(t=-5 to 0), Early-type spirals(t=1 to 4), S?(t=5), Late-type spirals(t=6 to 10): circles, triangles, stars, and squares respectively, with ellipticals indicated by open circles.

dust heated in star-forming regions, and as such is tracer of the star formation rate, then we would expect to see a slope of unity when plotted against L_B (in log–log parameter space). However, we might expect a slope less than unity if there is also a contribution to the FIR luminosity from a component of cold dust heated by the ISRF (see Chapter 1), as was found by Devereux & Eales (1989). For the OS galaxies, which as shown in the previous chapter do contain significant proportions of cold dust, a slope less than unity is indeed seen as expected. Conversely, for the IRS galaxies, whose L_{fir} should be dominated by warm dust heated by massive star formation, the expected slope close to unity is *not* seen; certainly if the IRS galaxies contain smaller proportions of cold dust than the OS galaxies then the IRS slope should be steeper than the OS slope, not vice versa. One possible explanation, however, could be that the optical luminosities for the IRS galaxies are significantly affected by extinction. The IRS galaxies lying in the upper left region of the plot, i.e. those with high L_{fir} and low L_B, are perhaps the most obvious candidates for any such extinction effects. If the optical luminosities have been underestimated it would explain the deviation from unity of the IRS sample slope. I will return to this subject later in this section. The OS sample, in probing low ratios of L_{fir}/L_B, can also probe any population of elliptical galaxies (which would have very large L_B and would occupy the lower right region of the plot) — the object indicated as an open circle in Figure 4.4(b) is the elliptical NGC 6166.

The ratio of 850 μm-to-optical blue luminosity is plotted against FIR luminosity in Figure 4.5 (in log–log parameter space). For galaxies containing large proportions of cold dust we might expect to see a constant ratio of L_{850}/L_B, since in this case the majority of the dust emission at 850 μm would be associated with the population of older stars and thus the dust mass and blue lumonosity will both be proportional to the mass of the galaxy; the L_{fir} on the other hand will be dominated by any component of warm dust emission associated with the young OB stars, and thus may well be independent of dust mass and blue luminosity. In fact for the OS sample, which, as shown in Chapter 3 does contain
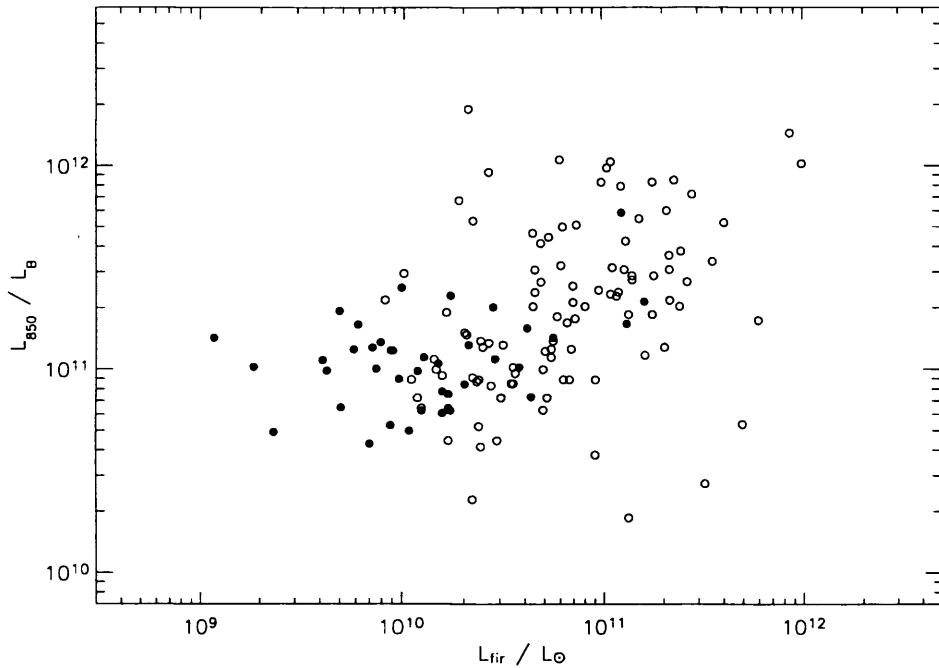
Figure 4.5: The ratio of 850 μm luminosity to optical blue luminosity versus far-IR luminosity, for the OS and IRS samples (filled and open points respectively).

large proportions of cold dust, there is little correlation (r_s=0.23, probability=0.149) and it does appear that the ratio L_{850}/L_B remains constant with L_{fir} (with the exception of the highest FIR luminosites). However, there is a correlation for the IRS sample (albeit with quite a large amount of scatter, 0.42), with L_{850}/L_B increasing with increasing L_{fir}, as would be expected for galaxies containing large proportions of warm dust (and the IRS galaxies by definition of their selection at 60 μm are dominated by warm dust), since in this case the 850 μm emission and the FIR emission are both tracing the warm dust. In fact, the majority of the IRS data points are consistent with a relation of slope unity, with the exception of a few outliers (i.e. the 6 objects lying to the lower right of the relation) which on closer inspection are 'unusual' objects: among them are IR 0857+39 which D00 finds to be a very warm object, an interacting pair, and a candidate post-starburst. Thus
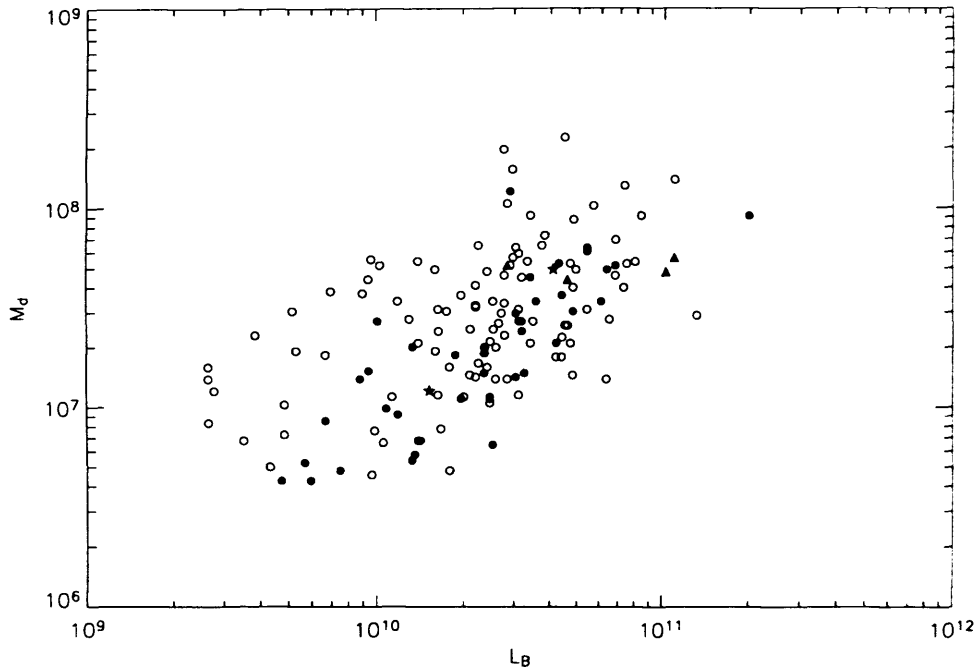
Figure 4.6: Dust mass versus optical blue luminosity for the OS and IRS samples (filled and open points respectively). The ellipticals and other early types which were only detected at 850 μm (but not in either *IRAS* band) are plotted for comparison (as triangles and stars respectively) but (as described in Table 3.4 in Chapter 3) are not included for fitting.

this diagram is indicative of the marked difference in the proportions of cold dust in the OS and IRS samples.

Dust mass

Dust mass (calculated using T_d from the isothermal fits, listed in Chapter 3 Table 3.4) is plotted versus optical luminosity in Figure 4.6 (in log–log parameter space). The relationships for the OS and IRS samples seem to agree well at lower M_d/L_B, however there are also IRS galaxies with higher values of M_d/L_B than almost any seen in the OS sample. The fact that this effect appears more pronounced at the lower optical luminosities would

Table 4.1: Parameters of fits and correlations for the OS sample and the *combined* (OS + IRS) samples.

Parameters for the OS sample.

y	x	No.	rs	significance	linear fit (y=mx+c) m	c
T_d	$\log L_{60}$	41	0.37	0.017		
T_d	$\log M_d$	41	-0.19	0.25		
T_d	$\log L_B$	38	-0.22	0.16		
$\log M_d$	$\log M_{HI}$	25	0.40	0.050		
$\log M_d$	$\log L_B$	40	0.82	8.88e-11	0.86 ± 0.10	-1.68 ± 1.08
$\log L_{850}$	$\log L_B$	49	0.84	6.73e-14	12.80 ± 0.99	0.82 ± 0.10
$\log L_{60}$	$\log L_{850}$	41	0.62	1.48e-5	1.00 ± 0.16	1.33 ± 3.51
$\log L_{fir}$	$\log L_B$	40	0.62	1.74e-5	0.77 ± 0.17	2.11 ± 1.79
$\log L_{850}/L_B$	$\log L_{fir}$	40	0.23	0.149		

Parameters for the *combined* (OS + IRS) SLUGS samples.

y	x	No.	rs	significance	m	c
T_d	$\log L_{60}$	145	0.55	8.8e-13	4.51 ± 0.57	-70.1 ± 13.3
$\log M_d$	$\log L_B$	140	0.58	9.06e-14	0.57 ± 0.07	1.46 ± 0.73
$\log L_{60}$	$\log L_{850}$	145	0.80	1.23e-33	1.31 ± 0.08	-4.98 ± 1.74
$\log L_{fir}$	$\log L_B$	140	0.32	1.09e-4	0.50 ± 0.12	5.43 ± 1.25
$\log L_{850}/L_B$	$\log L_{fir}$	140	0.49	6.13e-10	0.31 ± 0.05	7.91 ± 0.57

Parameters for the IRS sample.

y	x	No.	rs	significance	m	c
$\log L_{fir}$	$\log L_B$	100	0.33	6.77e-4	0.43 ± 0.11	6.40 ± 1.18
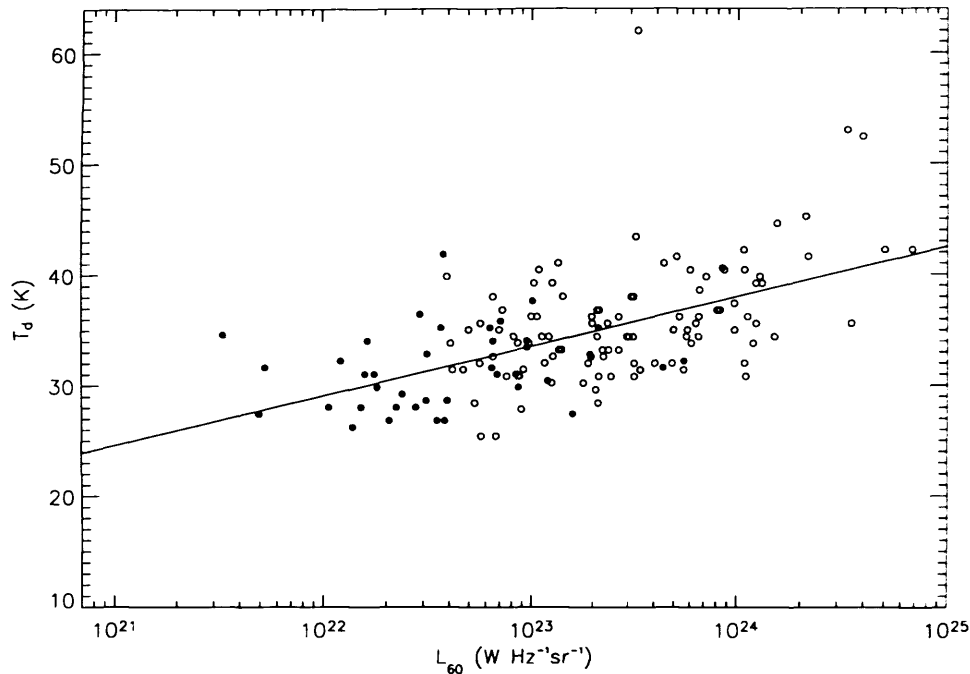
Figure 4.7:   Dust temperature T_d versus 60μm luminosity for the OS and IRS SLUGS samples (filled and open circles respectively). The solid line shows the linear fit for this *combined* SLUGS sample (parameters listed in Table 4.1).

suggest, once again, that extinction effects are probably an important factor for the optical luminosities of the IRS galaxies. However, it should be noted that these dust masses for both the samples are calulated from *isothermal* fitted SEDs and, as shown in Chapter 3 for the OS galaxies with two-component fits, if large proportions of cold dust are present these dust masses are likely to be underestimated by at least a factor of two. Thus much of the difference between the OS and IRS samples in this plot may be due to the much larger fractions of cold dust in the OS galaxies and hence the larger underestimates of the dust mass compared to the IRS sample.

It is interesting that no galaxies occupy the lower right region of the plot where ellipticals (if they contained very little or no dust; see Chapter 1) would reside. The fact
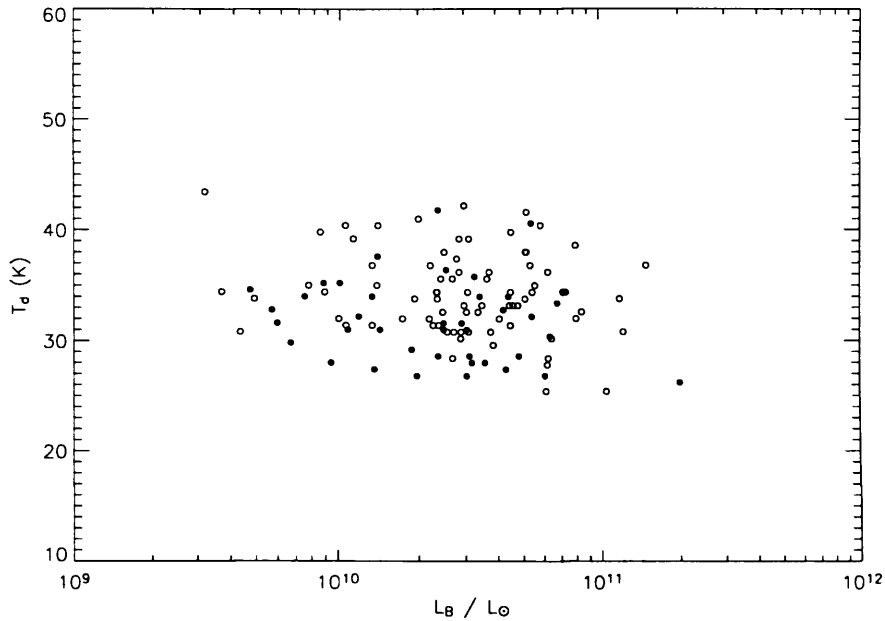
Figure 4.8: Dust temperature (from isothermal SED fitting) versus optical blue luminosity for the OS and IRS SLUGS samples (filled and open circles respectively).

that no objects are seen here, especially for the OS sample, suggests that earlier types must contain similar amounts of dust to later types (also see Sections 4.3 and 4.4). In fact, all the elliptical and other early types in the OS sample have dust masses which place them squarely on the same relationship as the later types — the most optically luminous object on the OS relation in Figure 4.4 is the elliptical NGC 6166; the other ellipticals and early types in the OS sample which were only detected at 850 μm (and not in either *IRAS* band) are indicated by filled triangles and star symbols respectively. However, it should be noted that the 850 μm fluxes for some of these are potentially contaminated by radio synchrotron emission, as discussed in Chapter 3. I will return to the investigation of submillimetre properties along the Hubble sequence in Section 4.3.

Dust temperature

For the IRS sample D00/LD00 found a correlation between $60\,\mu$m luminosity and dust temperature, with T_d increasing with increasing L_{60}, potentially suggesting that more luminous systems are hotter. However, finding no correlation between T_d and dust mass, and an inverse correlation between T_d and blue luminosity (both of which are used as a measure of the galaxy mass), D00 explain this L_{60}-T_d correlation as being simply due to the sensitivity of the 60μm flux to the dust temperature.

For the OS sample I also find a similar correlation between L_{60} and T_d (Figure 4.7) and no correlation between T_d and dust mass ($r_s = -0.19$, probability $= 0.25$), but I also find no correlation between T_d and blue luminosity (Figure 4.8; $r_s = -0.22$, probability $= 0.16$). However, the anti-correlation found by D00 was relatively weak, so it can be concluded from the addition of the OS sample that there is in fact no anti-correlation between T_d and blue luminosity. These results strengthen the conclusion of D00 that there is no trend for big galaxies to be hotter and that the L_{60}-T_d correlation is due to the sensitivity of the 60μm flux to dust temperature, and hence imply that the chance of a merger-driven starburst is independent of galaxy mass.

4.2.2 Colour-colour analysis

Colour-colour diagrams can be a useful way of seeing how the SEDs of galaxies differ, and potentially (for example as shown by Spinoglio, Andreani & Malkan 2002) can separate out different classes of galaxy. Figures 4.9 to 4.11 show the OS and IRS galaxies plotted on various two-colour diagrams (filled and open symbols respectively). For each of the colour-colour diagrams the IRS and OS galaxies clearly have different distributions, and in particular there are OS galaxies in parts of the diagram where there are no IRS galaxies. For example, in Figure 4.9 $\sim 50\%$ of the OS galaxies are in a region of the colour-colour diagram completely unoccupied by IRS galaxies. This shows there are galaxies 'missing'
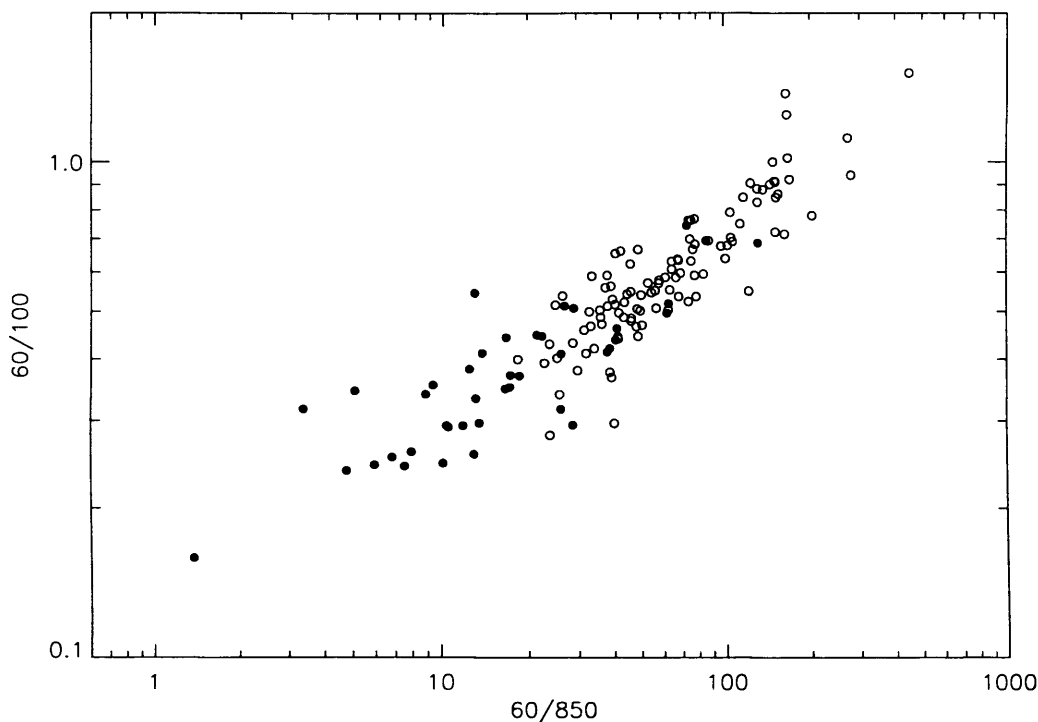
Figure 4.9: Colour-colour plot: S_{60}/S_{100} versus S_{60}/S_{850} colours for the optically-selected (this work) and *IRAS*-selected (D00) SLUGS (filled and open points respectively).

from IR samples, with important implications for the submillimetre LF (see Chapter 5).

There is a strong correlation between the S_{60}/S_{100} and S_{60}/S_{850} colours (Figure 4.9). The S_{100}/S_{850} colour is also tightly correlated with S_{60}/S_{850} colour (Figure 4.10(a)) while it is much less tightly correlated with S_{60}/S_{100} colour. This reflects the differences in the shape of the galaxies' SEDs, which have been shown (for those galaxies with flux measurements at both $850\,\mu$m and 450 micron) in Chapter 3 Figure 3.20. For example, there is not a tight correlation between the S_{60}/S_{100} and S_{100}/S_{850} colours since neither of these parameters describes the full 'cold' component of the SED (the S_{60}/S_{850} colour would be required), and so from these colours one cannot gain any information about the size of the cold component and hence the relative amounts of dust in the cold and warm com-
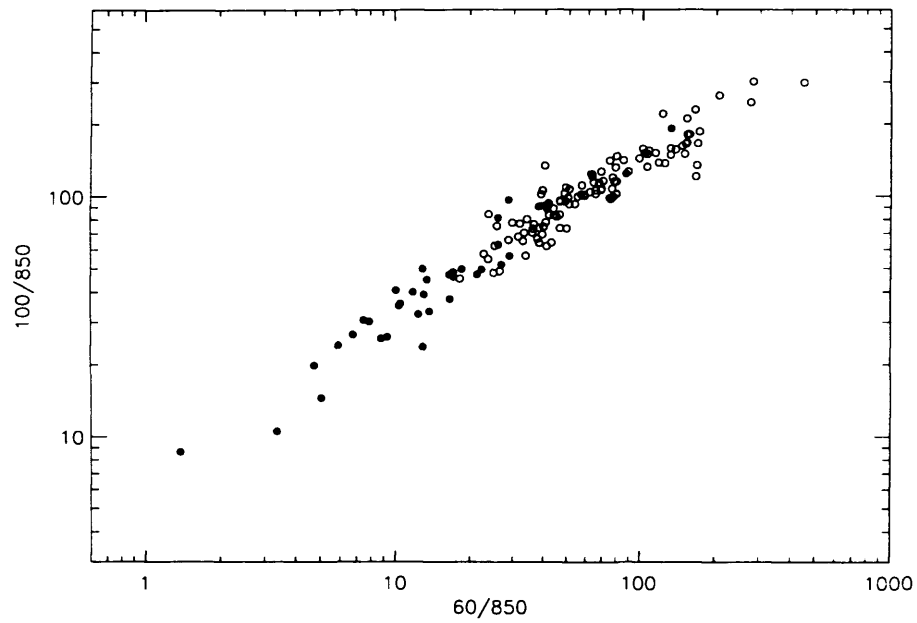
(a)
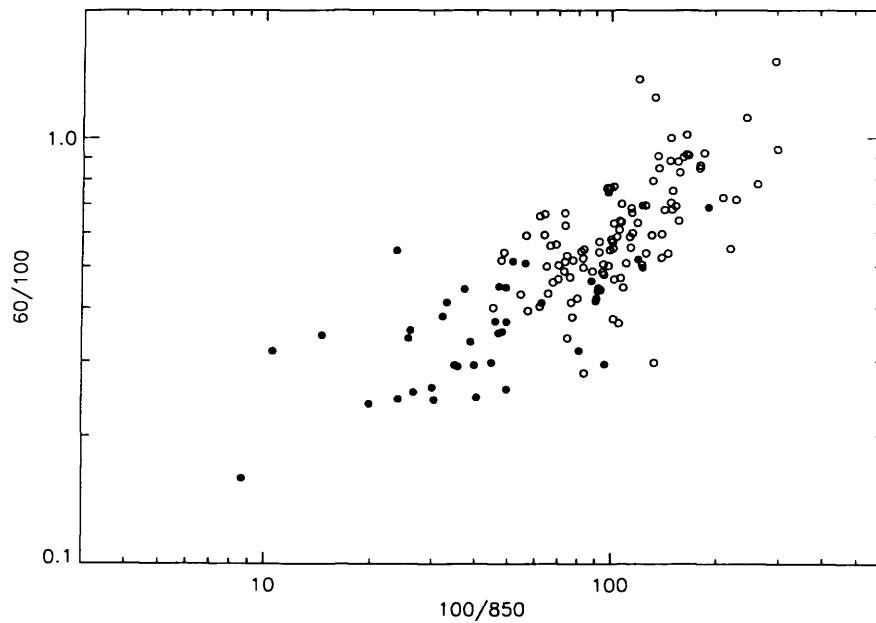
(b)

Figure 4.10:   Other colour-colour plots for the optically-selected (this work) and *IRAS*-selected (D00) SLUGS (filled and open points respectively): (a) S_{100}/S_{850} vs S_{60}/S_{850} colours and (b) S_{60}/S_{100} vs S_{100}/S_{850} colours.
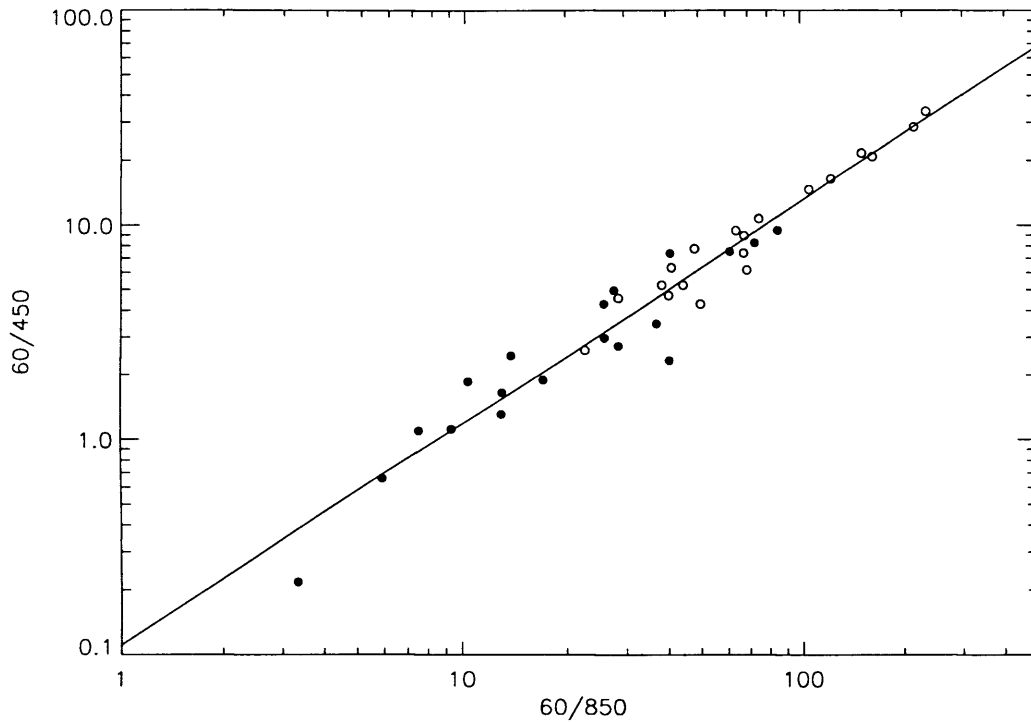
Figure 4.11: Colour-colour plot: S_{60}/S_{450} versus S_{60}/S_{850} colours for the optically-selected (this work) and *IRAS*-selected (D00) SLUGS (filled and open points respectively).

ponents. Figure 4.10(a) on the other hand provides a tight correlation irrespective of the prominence of the cold component, for which (as can be seen in Figure 3.20 in Chapter 3) the ratio S_{60}/S_{100} can vary significantly. I will return to the discussion of colour-colour plots, and in particular the fitting of a linear colour-colour relation, in Chapter 5, where I will use the S_{60}/S_{100} versus S_{60}/S_{850} two-colour relation (Figure 4.9) to produce the submillimetre luminosity function.

Figure 4.11 shows the S_{60}/S_{450} versus S_{60}/S_{850} colour-colour plot for the OS sample objects and IRS sample objects which have 450 μm fluxes. We confirm the very tight correlation found by DE01 (here the correlation coefficient $r_s = 0.96$, significance $= 9.20$e-21), and the scatter for the OS sample may be completely explained by the uncertainties in the

fluxes. Importantly, this relationship holds for all the objects in the OS sample for which we have $450\,\mu$m fluxes, which include a wide range of galaxy types (t-type=0 to 10) and with L_{fir} ranging over 2 orders of magnitude. The (least-squares) best-fitting line to the *combined* OS + IRS samples shown in Figure 4.11 is given by

$$\log(S_{60}/S_{450}) = (1.03 \pm 0.05)\log(S_{60}/S_{850}) - (0.955 \pm 0.070) \qquad (4.1)$$

(or re-written $S_{60}/S_{450} = 0.119\,(S_{60}/S_{850})^{1.03}$) and is very similar to that found by DE01, confirming the finding for the IRS sample that, within the uncertainties, the ratio S_{450}/S_{850} is constant. DE01 conclude, from the results of simulations of the $450/850\,\mu$m flux ratio and from the fitted β values for those galaxies whose SEDs require a cold component, that $\beta \sim 2$ for all galaxies, and that therefore the cold dust component in all galaxies has a similar temperature ($T_c \sim 20$–21 K). The fact that we also find the S_{450}/S_{850} ratio constant for the OS sample suggests that these conclusions are true for all Hubble types (only t-types<0 are unrepresented in the OS sub-sample with $450\,\mu$m data).

4.2.3 Spectral fit analysis

The positions of the OS galaxies in the colour diagrams suggest there is more cold dust in the OS galaxies than in the IRS galaxies. This can be investigated further with the results of the spectral fits. Figure 4.12(a) shows the comparison between the distribution of β values (found from the isothermal fits) for the OS and IRS samples. There are OS sample galaxies with β values lower than any found in the IRS sample. The two-sided Kolmogorov–Smirnov (K-S) test shows that the distributions of the two samples are significantly different (the probability that the two samples come from the same distribution function is only 1.8e-5). Though this clearly demonstrates that the properties of the dust in the OS and IRS samples are different, rather than interpreting this as a physical difference in the emissivity behaviour of the grains (β) it seems likely that it is instead a difference in the two samples' ratios of cold/warm dust.
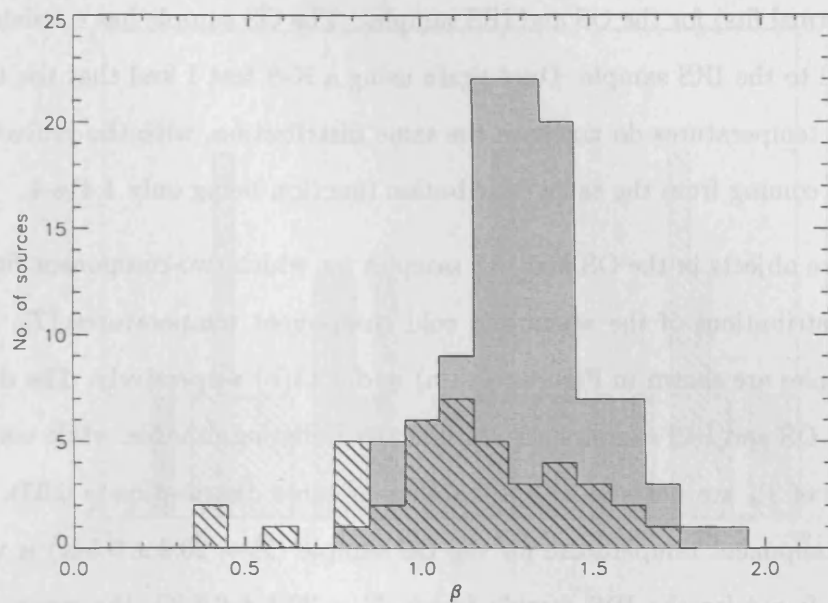
(a)
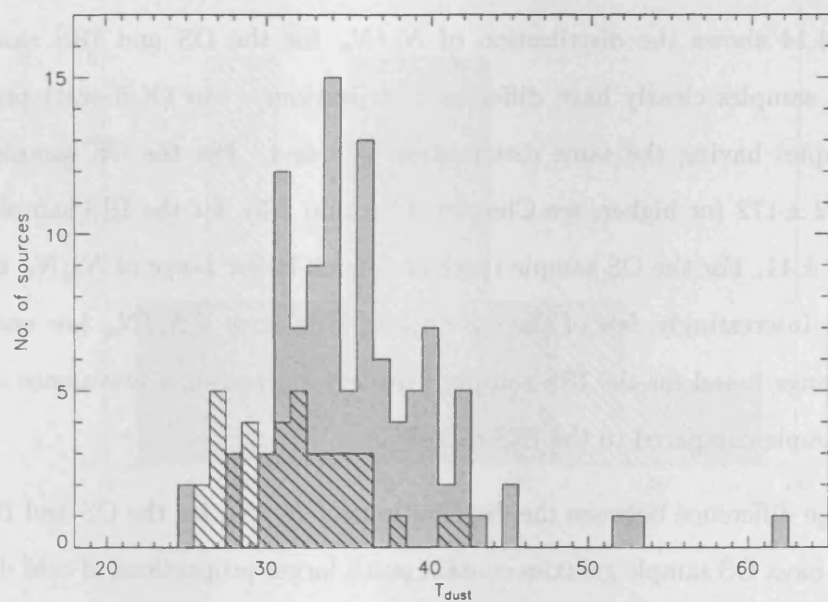
(b)

Figure 4.12: Distributions of (a) β values and (b) T_d values for the optically- and *IRAS*-selected SLUGS (line-filled and shaded histograms respectively).

Figure 4.12(b) shows the comparison between the distribution of dust temperatures (from isothermal fits) for the OS and IRS samples. The OS sample has consistently colder T_d compared to the IRS sample. Once again using a K-S test I find that the OS and IRS sample dust temperatures do not have the same distribution, with the probability of the two samples coming from the same distribution function being only 1.41e-4.

For those objects in the OS and IRS samples for which two-component fits were possible, the distributions of the warm and cold component temperatures (T_w and T_c) for the two samples are shown in Figures 4.13(a) and 4.13(b) respectively. The distributions of T_c for the OS and IRS samples are statistically indistinguishable, while conversely the distributions of T_w are not similar (probability of same distribution is 0.03). While the mean cold component temperature for the OS sample ($\bar{T}_c = 20.2 \pm 0.5$ K) is very similar to the value found for the IRS sample (mean $\bar{T}_c = 20.1 \pm 0.4$ K), the mean warm component temperature is rather higher ($\bar{T}_w = 47.4 \pm 2.4$ K for the OS sample as opposed to $\bar{T}_w = 39.3 \pm 1.4$ K for the IRS sample).

Figure 4.14 shows the distribution of N_c/N_w for the OS and IRS samples. The OS and IRS samples clearly have different distributions – the (K-S test) probability of the two samples having the same distribution is 8.4e-4. For the OS sample the mean $N_c/N_w = 532 \pm 172$ (or higher, see Chapter 3 Section 3.5), for the IRS sample the mean $N_c/N_w = 38 \pm 11$. For the OS sample there is a much larger range of N_c/N_w than for the IRS sample. Interestingly, few of the OS objects even have a N_c/N_w low enough to fall within the range found for the IRS sample, strongly suggesting a prevalence of cold dust in the OS sample compared to the IRS sample.

The large difference between the distributions of N_c/N_w for the OS and IRS galaxies implies that most OS sample galaxies contain much larger proportions of cold dust relative to warm dust than found for the IRS galaxies, additional evidence that *IRAS* missed a population of cold-dust-dominated objects. The similarity of the temperature of the cold
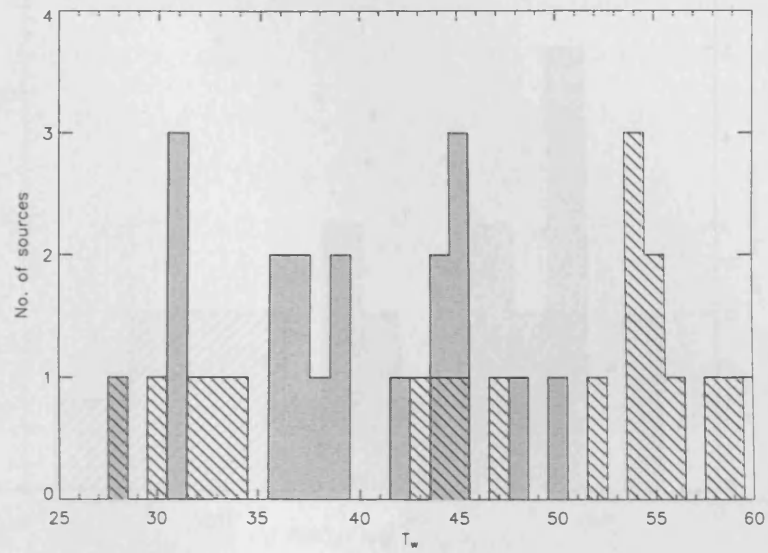
(a)
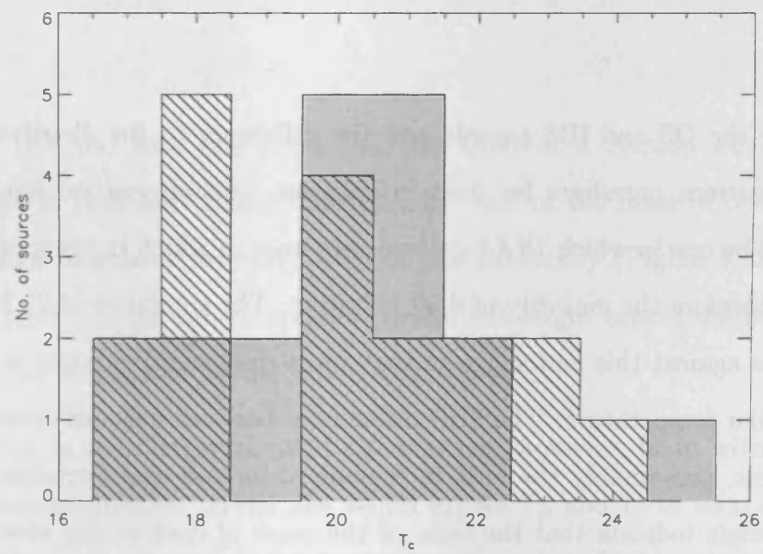
(b)

Figure 4.13:   Distributions of warm component (a) and cold component (b) temperatures for the OS and IRS samples (line-filled and shaded histograms respectively).
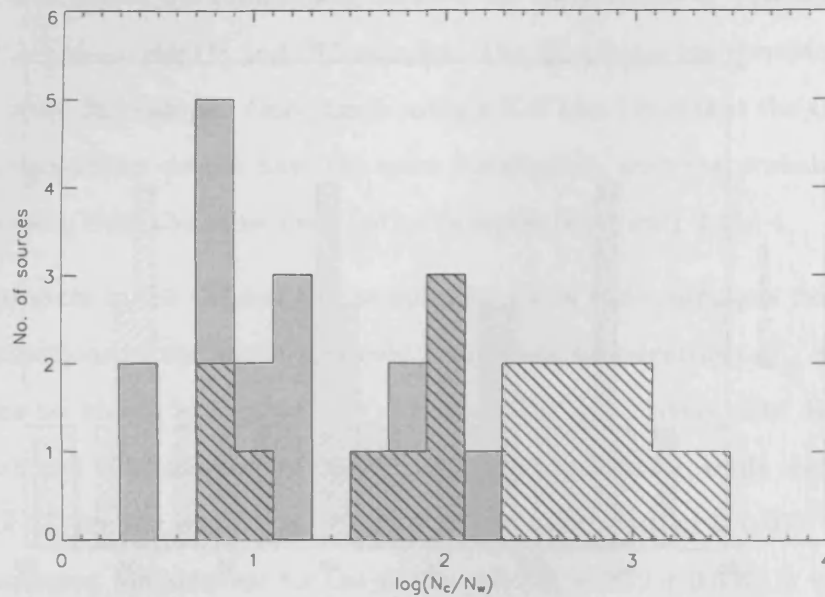
Figure 4.14:   Distribution of $\log(N_c/N_w)$ for the OS and IRS samples (line-filled and shaded histograms respectively).

component for the OS and IRS sample and the difference in the distribution of N_c/N_w supports the current paradigm for dust in galaxies. An alternative model for dust in galaxies would be one in which *IRAS* galaxies are ones in which the general ISRF is more intense, and therefore the majority of dust is hotter. The similarity of T_c for the different samples argues against this and suggests that most dust in all galaxies is relatively cold and has a similar temperature. The SED differences between galaxies arise from a second dust component, presumably the dust in regions of intense star formation. The results for the OS sample indicate that the ratio of the mass of dust in this second component to the mass of dust in the first component can vary by roughly a factor of 1000. There are two other pieces of evidence in favour of the two-component model. First, the ISO $170\,\mu$m flux densities that exist for 3 of the two-component-fitted galaxies (Stickel et al. 2004; Chapter 3 Section 3.5) agree very well with the model SEDs (I did not use these
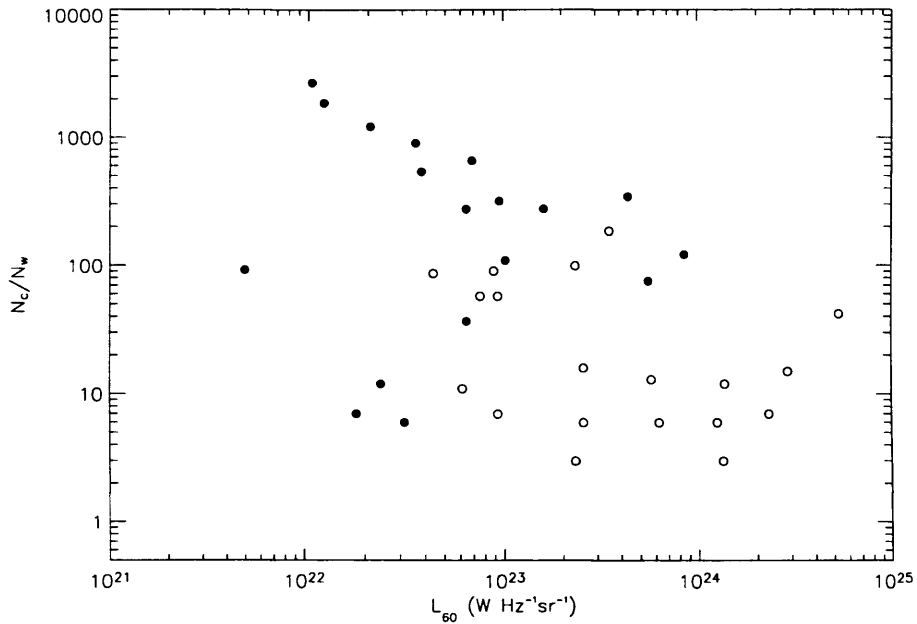
Figure 4.15: N_c/N_w versus 60 μm luminosity for the OS and IRS samples (filled and open points respectively).

data in making the fits, with one exception; see Chapter 3 Section 3.5), as was also found by Serjeant & Harrison (2005). Second, the ratio of the mass of cold dust to the mass of warm dust correlates inversely with 60 μm luminosity (Figure 4.15; $r_s = -0.41$, significance $= 1.24$e-2); in the two-component model one might expect the most luminous *IRAS* sources to be dominated by the warm component.

The difference in the distributions of T_w does not, however, fit in with this general picture. In the two-component model one would expect T_w and T_c to be constants, with the only thing changing between galaxies being the proportion of cold and warm dust. The difference in the distributions of T_w may indicate that this model is too simplistic. Two things may be relevant here. Firstly, as can be seen in Chapter 3 Figure 3.20 it is those OS galaxies with very prominent cold components which typically account for the high-

est warm component temperatures (for example PGC 35952 or NGC 6090). Secondly, the model SEDs with high values of T_w also generally provide a good fit to the 25 μm flux density, whereas the model values with low values of T_w tend to underestimate the 25 μm flux density. This last point suggests that to fully understand dust in galaxies one cannot ignore the measurements at wavelengths $< 60\,\mu$m; however, if these measurements were included then more than two dust components would definitely be needed. This is clearly demonstrated by Sievers et al. (1994) who, for NGC 3627, fit a three-component model. A two-component model is nonetheless adequate for the purposes of this present work, since I am interested in the cold component rather than a third hot component.

4.3 Submillimetre Properties along the Hubble Sequence

In this section I investigate the submillimetre properties of galaxies as a function of Hubble type (t).

Figures 4.16(a) to 4.16(c) show the distributions of various global properties (listed in Table 3.4 in Chapter 3) with different Hubble types indicated by different shaded regions (E-S0 (t=-5 to 0), Early-type spirals (t=1 to 4), S? (t=5) and Late-type spirals (t=6 to 10)). Each of the Hubble types seems fairly evenly distributed across the 850 μm luminosity range (Figure 4.16(a)), with no obvious tendency for different Hubble types to favour either lower or higher 850 μm luminosities. Likewise, the distribution of the ratio of 850 μm–optical luminosity (Figure 4.16(b)) and the distribution of dust masses (Figure 4.16(c)) suggest there is no obvious tendency for the ratio of submillimetre to optical blue luminosity to vary with Hubble type, nor for the dust mass to vary with Hubble type.

However, this result is not what would be expected theoretically based on the assumption that the dust and gas in a given galaxy are associated with the disk and not the bulge. As I showed in Chapter 1, using a simple analysis one can show that as the

(a)

(b)

(c)
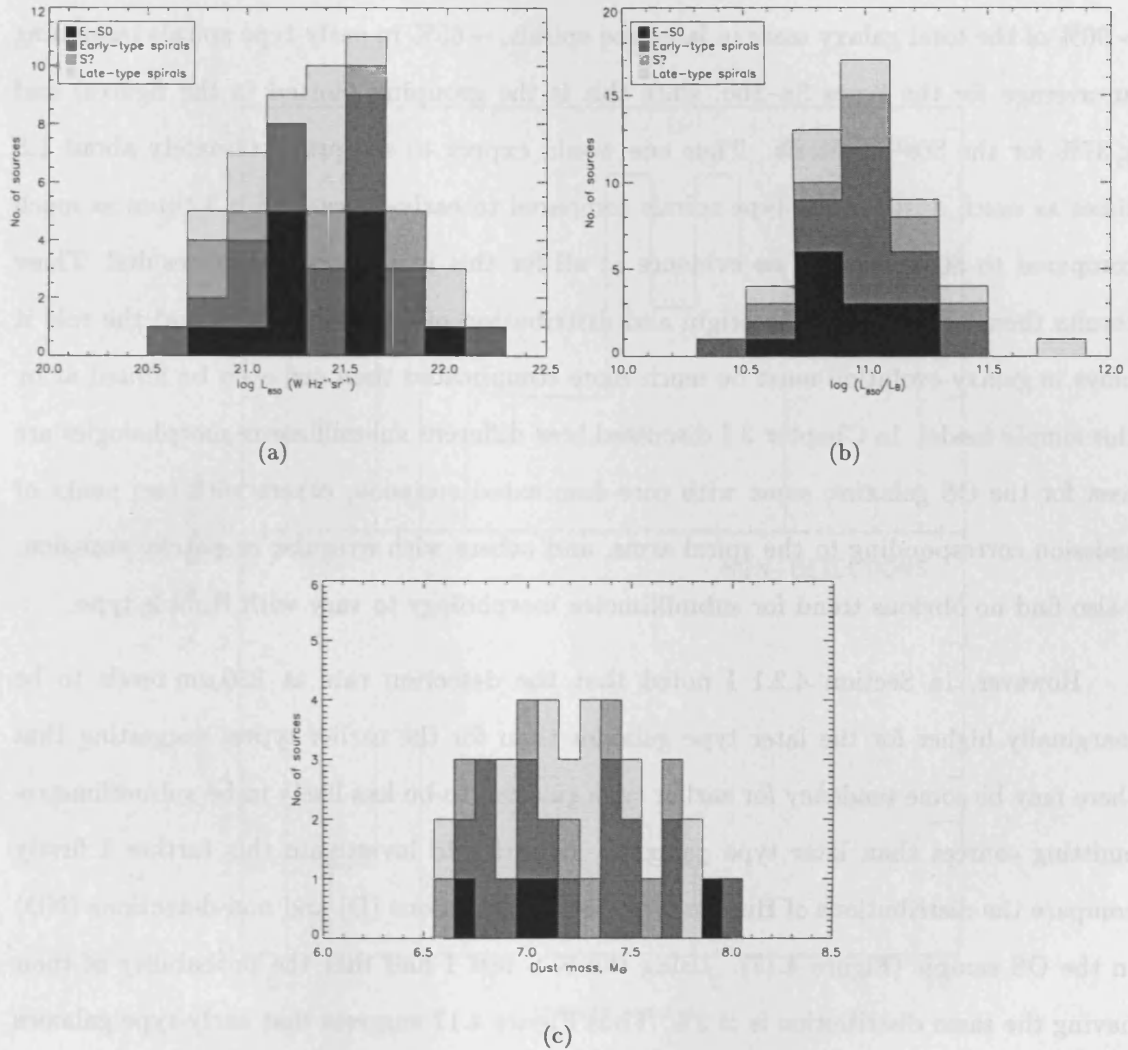
Figure 4.16: Distribution of (a) 850 μm luminosity, (b) 850 μm luminosity / optical blue luminosity, and (c) dust masses, for the Optically-Selected SLUGS (as listed in Chapter 3 Table 3.4, with different Hubble types (as given in the LEDA database according to the RC2 code, and listed in Chapter 3 Table 3.1) indicated by different shaded regions: E-S0(t=-5 to 0), Early-type spirals(t=1 to 4), S?(t=5), Late-type spirals(t=6 to 10).

bulge-to-disk ratio decreases towards later Hubble types the fraction of dust should in-
crease towards later Hubble types. This is not at all what is observed for the OS sample!
Using the dust fractions listed in Chapter 1 we would expect dust to be proportional to
$\sim 90\%$ of the total galaxy mass in late-type spirals, $\sim 65\%$ in early-type spirals (assuming
an average for the types Sa–Sbc, since this is the grouping plotted in the figures) and
$\lesssim 37\%$ for the S0s–ellipticals. Thus one would expect to see proportionately about 1.5
times as much dust for late-type spirals compared to early-types, and $\gtrsim 3$ times as much
compared to S0s. There is no evidence at all for this in the OS sample results! These
results then indicate that the origin and distribution of dust in galaxies and the role it
plays in galaxy evolution must be much more complicated than can even be hinted at by
this simple model. in Chapter 3 I discussed how different submillimetre morphologies are
seen for the OS galaxies, some with core-dominated emission, others with two peaks of
emission corresponding to the spiral arms, and others with irregular or patchy emission.
I also find no obvious trend for submillimetre morphology to vary with Hubble type.

However, in Section 4.2.1 I noted that the detection rate at $850\,\mu$m tends to be
marginally higher for the later type galaxies than for the earlier types, suggesting that
there may be some tendency for earlier type galaxies to be less likely to be submillimetre-
emitting sources than later type galaxies. In order to investigate this further I firstly
compare the distributions of Hubble type for the detections (D) and non-detections (ND)
in the OS sample (Figure 4.17). Using the K-S test I find that the probability of their
having the same distribution is $\simeq 2\%$. Thus Figure 4.17 suggests that early-type galaxies
are less likely to be submillimetre sources than later types. In fact, all the objects *not*
detected at $850\,\mu$m but which have IRAS fluxes (11 in total) are early-types, with the
exception of one multiple system (i.e. 1 E/S0, 8 early-type spirals, and 1 interacting sys-
tem). But, early types *are* detected at $850\,\mu$m— 6 E-S0s were detected (although some
of these $850\,\mu$m fluxes may possibly be contaminated by radio synchrotron emission, see
Chapter 3) and 19 early-type spirals.
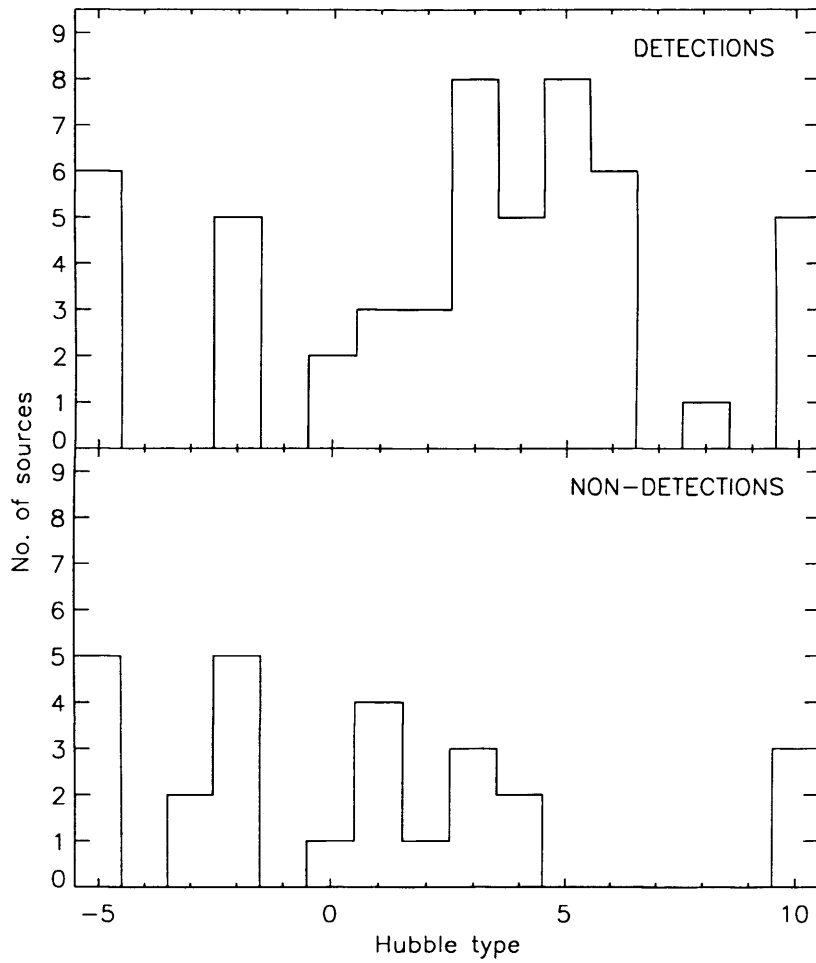
Figure 4.17: Distribution of Hubble types for the OS sample 850 μm detections (upper panel) and non-detections (lower panel).
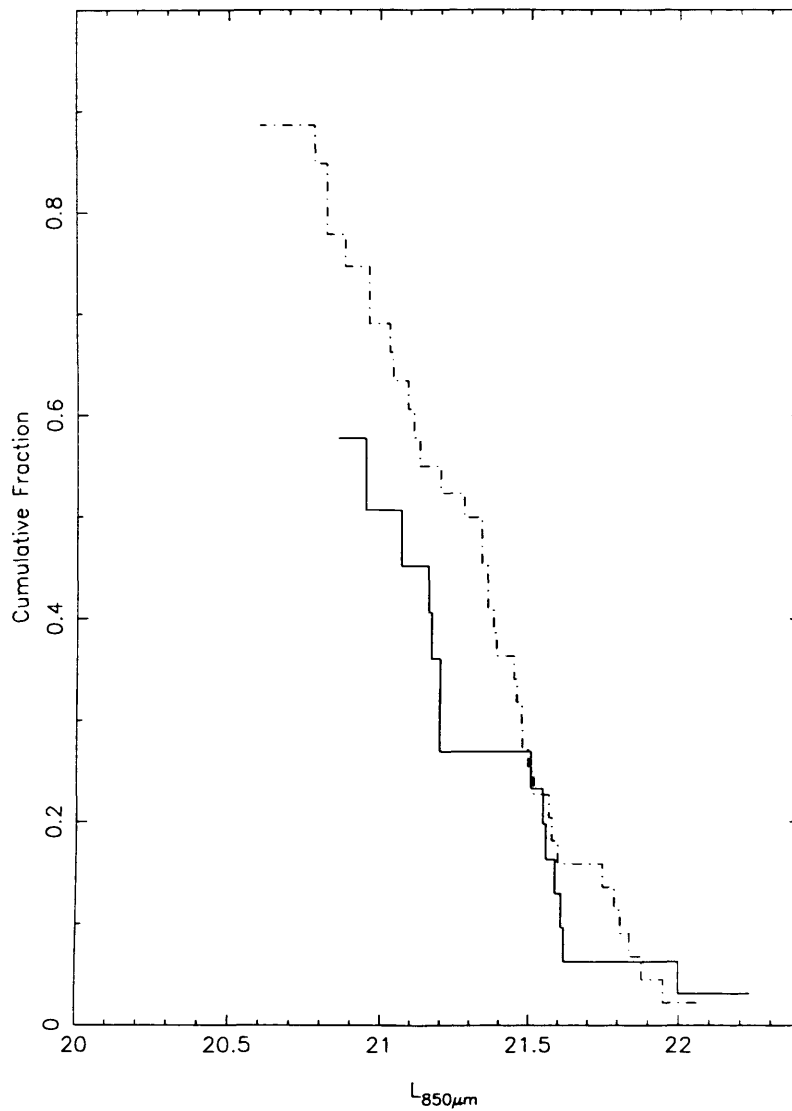
Figure 4.18:   Cumulative luminosity distributions for early-type galaxies (solid line) and late-type galaxies (dot-dashed). The maximum values for both samples are less than one because of the upper limits that fall below the lowest actual measurement.
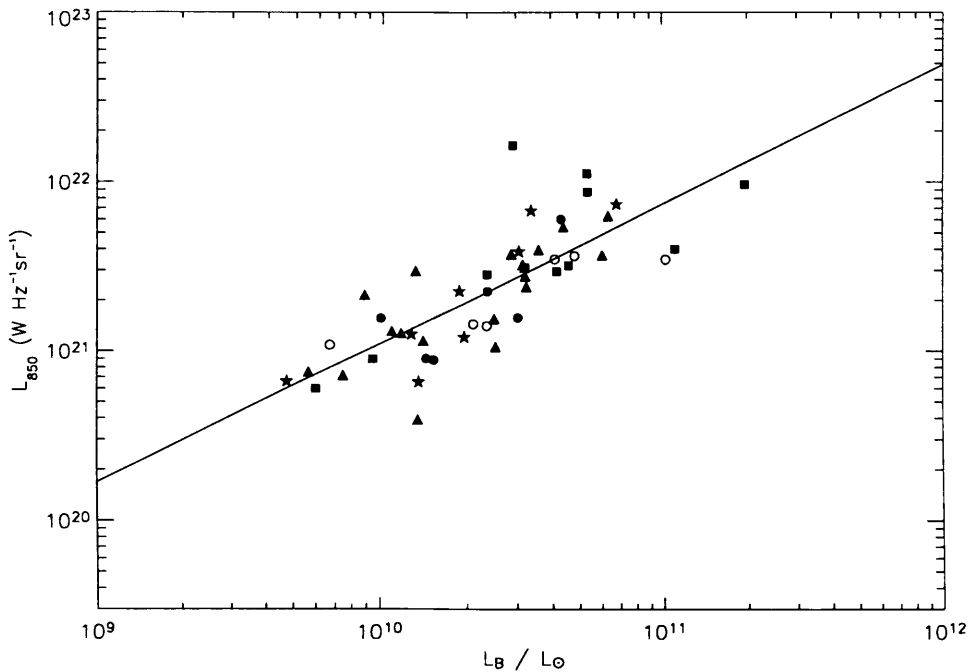
Figure 4.19: 850 μm luminosity versus optical luminosity L_B for the OS sample, with different Hubble types (as given in the LEDA database) indicated by different symbols: E-S0(t=-5 to 0), Early-type spirals(t=1 to 4), S?(t=5), Late-type spirals(t=6 to 10): circles, triangles, stars, and squares respectively. The 6 detected ellipticals are highlighted as open circles.

To investigate this apparent morphological difference further we estimated the submillimetre luminosity distributions of early- and late-type galaxies. A major complication is the large number of upper limits. The Kaplan-Meier estimator (Wall & Jenkins 2003) was used to incorporate information from both the upper limits and the measurements. Early-type galaxies were defined as all those with $t \leq 1$ and late-type galaxies as those with $t > 1$. This division was used because the greatest difference between the cumulative distributions of Hubble type for detected and non-detected galaxies (Figure 4.17) was found at t=1. Figure 4.18 shows the cumulative luminosity distributions estimated in this way for the early-type and late-type galaxies. There appears to be a tendency for

the late-type galaxies to be more luminous submillimetre sources. However, the tendency is not very strong. Also the ASURV statistical package for censored data (Feigelson & Nelson 1985) was used to compare the results for the two samples, using the Gehan test and the log-rank test (see Wall & Jenkins 2003). A marginally significant (10%) difference was found using the log-rank test but no significant difference was found using the Gehan test. Figure 4.19 shows a plot of 850 μm luminosity versus optical luminosity. For clarity I simply divide the sample into 4 broad groups based on the galaxies' t-type parameter given in LEDA (which uses the standard numerical codes for the de Vaucoulers morphological type, as defined in RC2): E-S0 (t=-5 to 0), Early-type spirals (t=1 to 4), S? (t=5) and Late-type spirals (t=6 to 10). The different Hubble types show similar relationships. On further inspection of the data, the more marked dependence on Hubble type visible in Figure 4.17 appears to be at least partly caused by the early-type galaxies being observed in worse conditions. In summary, there appears to be some difference in submillimetre properties as one moves along the Hubble sequence, but it is not very strong.

Another way to investigate whether there are any trends with Hubble type is using the results of the SED fits. As above, I simply divided the sample into 4 broad groups based on the galaxies' t-type. Figures 4.20(a) and 4.20(b) show the distributions of β and T_d (derived from the single-component fits) for the OS sample. The objects of each type appear fairly evenly distributed across the bins from $\beta = 0$ to 2 (Figure 4.20(a)), and in order to test this statistically I divide the sample into two broad groups: early types ($-5 \leq$ t-type ≤ 4) and late types (5 $\leq$ t-type $\leq$ 10), and perform a K-S test on the two groups. I find that the distributions of the early and late type groups are not significantly different. The distribution of isothermal dust temperatures appears similar for all Hubble types (Figure 4.20(b)); I find no significant differences between the early and late types. I also investigated the distributions of the warm and cold component temperatures found from the two-component fits to look for any differences between early and late types; for example Popescu et al. (2002) find a tendency for the temperatures of the cold dust component to
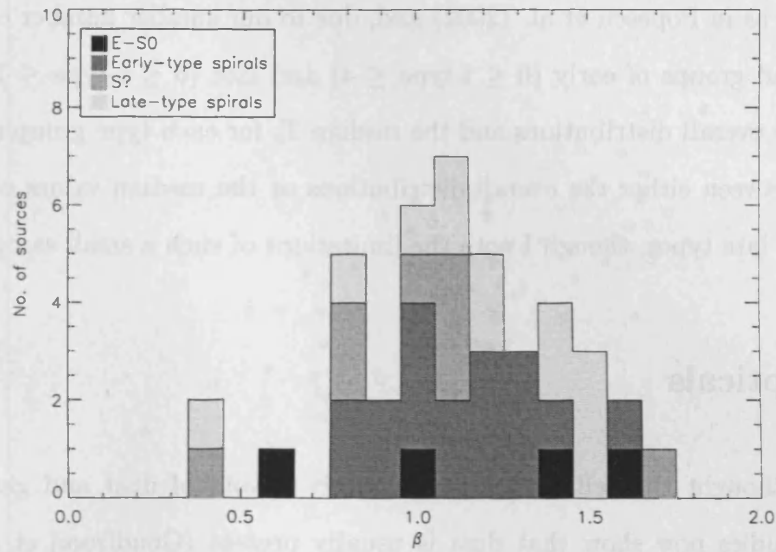
(a)
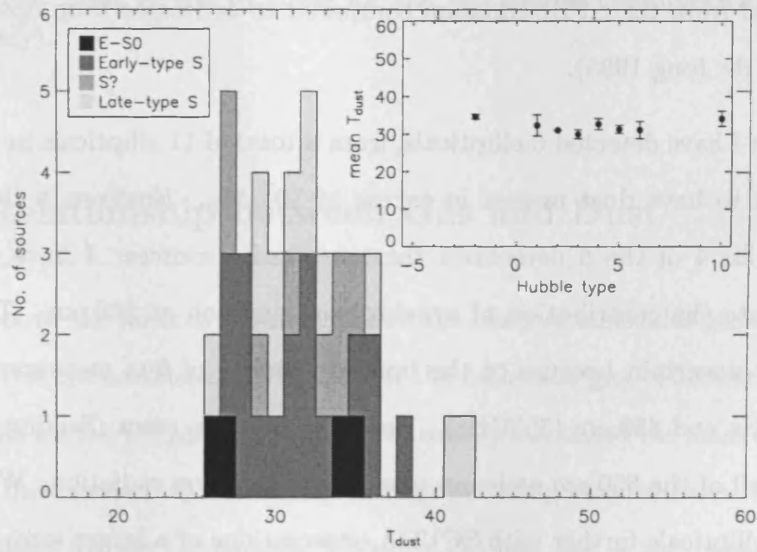
(b)

Figure 4.20: Distribution of (a) β values and (b) T_d values for the OS SLUGS, with different Hubble types (as given in the LEDA database) indicated by different shaded regions: E-S0 (t=-5 to 0), Early-type spirals (t=1 to 4), S? (t=5), Late-type spirals (t=6 to 10). ((b): Inserted panel: mean T_d for the OS SLUGS for different Hubble types, with error bars of error on the mean (bins with only 1 source are not plotted)).

become colder for later types. I divided the 18 two-component fitted temperatures into Hubble types as in Popescu et al. (2002) and, due to our smaller number of sources, also into two broad groups of early ($0 \leq$ t-type ≤ 4) and late ($6 \leq$ t-type ≤ 10) types, and compared the overall distributions and the median T_c for each type grouping. I found no differences between either the overall distributions or the median values of T_c or T_w for the early and late types, though I note the limitations of such a small sample.

4.4 Ellipticals

It was once thought that ellipticals were entirely devoid of dust and gas, but optical absorption studies now show that dust is usually present (Goudfrooij et al. 1994; van Dokkum & Franx 1995). Furthermore, dust masses for the $\sim 15\%$ of ellipticals detected by *IRAS* (Bregman et al. 1998) have been found to be as much as a factor of 10–100 higher when estimated from their FIR emission compared to estimates from optical absorption (Goudfrooij & de Jong 1995).

At 850 μm I have detected 6 ellipticals, from a total of 11 ellipticals in the OS sample, and find them to have dust masses in excess of 10^7 $M_\odot$. However, a literature search revealed that for 4 of the 6 detections there are radio sources. I have used the radio data to estimate the contribution of synchrotron emission at 850 μm. These estimates are often very uncertain because of the limited number of flux measurements available between 1.4GHz and 850 μm (353GHz). However, in some cases (Section 3.3) it is clear that some or all of the 850 μm emission may be synchrotron radiation. We are currently investigating ellipticals further with SCUBA observations of a larger sample.
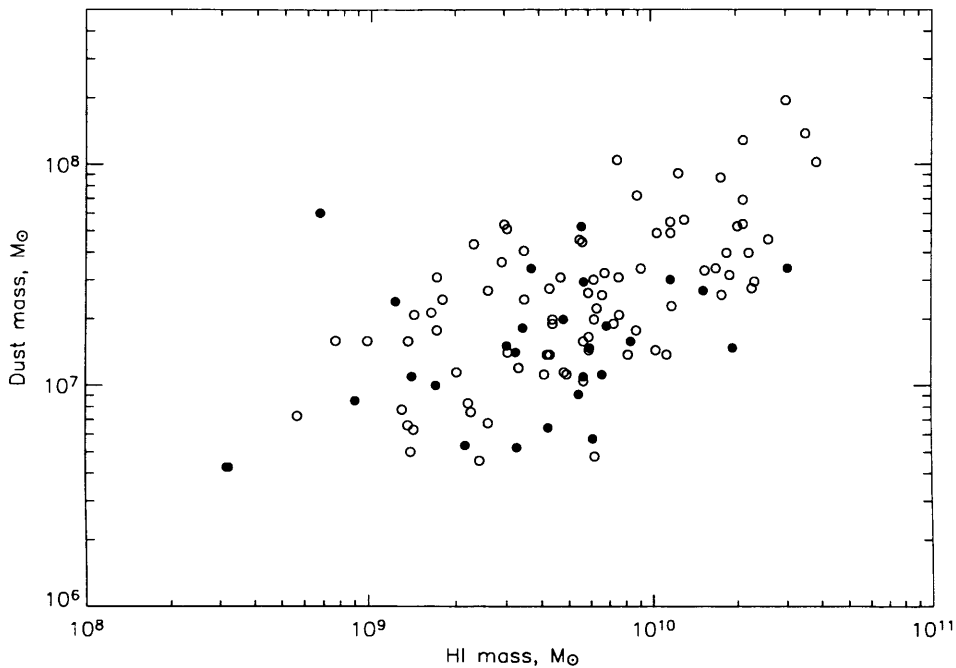
Figure 4.21: Dust mass versus HI mass for the OS and IRS samples (filled and open circles respectively).

4.5 The Relationship between Gas and Dust

D00 found that both the mass of atomic gas and the mass of molecular gas are correlated with dust mass, but the correlation is tighter for the molecular gas. There are virtually no CO measurements for the OS sample, so here I have only estimated the mass of atomic gas. I compared the dust mass (M_d, calculated using dust temperatures from the isothermal fits) to the HI mass for the OS sample (Figure 4.21) and find a very weak correlation. Though the correlation for the OS sample alone is very weak it is nonetheless consistent with the correlation found by D00 for the IRS sample; most of the OS points lie within the region covered by the IRS points, but though they cover the same range of HI masses I note that we do not have any HI masses for the OS sample objects with the higher dust
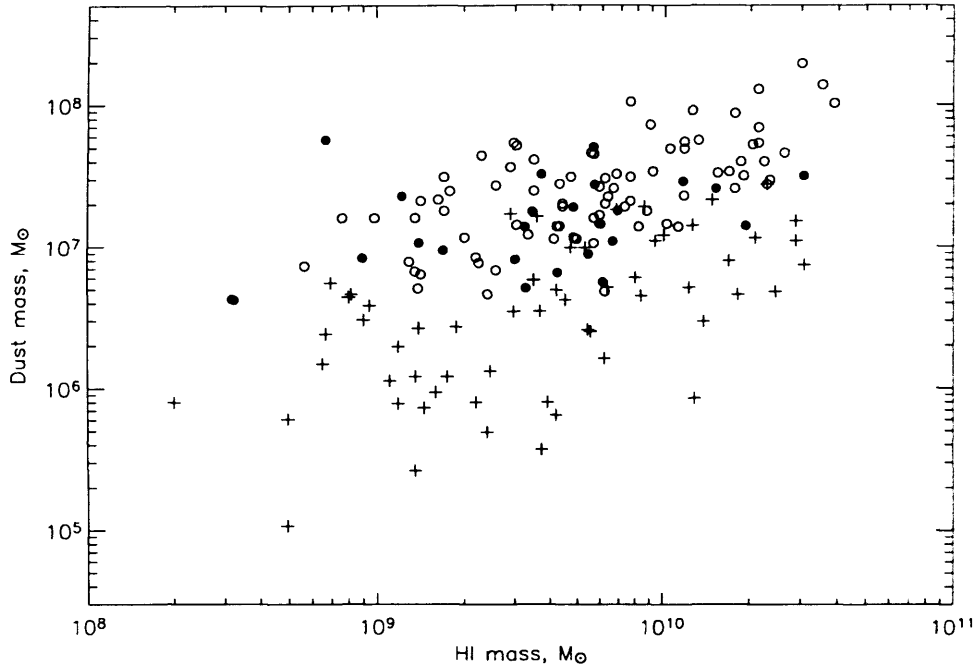
Figure 4.22:   Dust mass versus HI mass for the OS and IRS samples (filled and open circles respectively), with the Devereux & Young sample of spirals shown as crosses.

masses. The weakness of the correlation for the OS sample is therefore likely due simply to the small number of OS sample $850\,\mu m$ detections for which there is also HI data (28 objects).

The mean neutral gas-to-dust ratio for the OS sample is $M_{HI}/M_d=395\pm71$, where the error given is the error on the mean. The (neutral + molecular) gas-to-dust ratios for the IRS SLUGS sample and the Devereux & Young (1990; herein DY90) sample of spiral galaxies are respectively $M_{H_2+HI}/M_d=581\pm43$ and $M_{H_2+HI}/M_d=1080\pm70$ (DY90 calculate this value for the inner disk), but since for the OS sample there are no CO measurements and therefore no measure of the mass of molecular hydrogen I can at this stage only compare the neutral gas-to-dust ratio for the OS sample. I therefore compare the OS value to mean neutral gas-to-dust ratios which I calculate, for the IRS sample and

the DY90 sample respectively, to be M_{HI}/M_d=305±24 and M_{HI}/M_d=2089±341. There is a large difference between the values for both SLUGS samples and the value determined by DY90. This can be seen clearly in Figure 4.22 by plotting the DY90 objects on the SLUGS plot of dust mass versus HI mass described above — the DY90 galaxies occupy an almost entirely separate region of the plot compared to the SLUGS galaxies, with obviously much lower dust masses. This is almost certainly due to the fact that DY90's dust masses were estimated from *IRAS* fluxes and therefore, for the reasons noted in Section 1, will have 'missed' the cold dust.

There is also a difference between the SLUGS values and the Galactic value of 160 for the (neutral + molecular) gas-to-dust ratio (the value derived from Sodroski et al. (2004) by D00). The neutral gas-to-dust ratios for both the SLUGS samples are at least a factor of 2 larger than this Galactic value, and as shown by D00 when the molecular gas is included the value of the gas-to-dust ratio for the IRS sample is more than 3 times larger than the Galactic value. D00 attribute this discrepancy to a missed 'cold dust' component ($T_d \leq 20\,\mathrm{K}$) in the IRS sample. I have already noted in this thesis that the single-temperature fits lead to dust masses approximately a factor of 2 lower than the more realistic two-component fits (see Chapter 3 Section 3.6). Using the dust masses calculated using the two-component fits (M_{d2}; see Chapter 3 Table 3.3), for the 13 galaxies for which there are HI masses I find the mean neutral gas-to-dust ratio for the OS sample is then M_{HI}/M_{d2}=192±44. This is in good agreement with the Galactic value, although if there is a significant amount of molecular gas this value would obviously be higher.

4.6 Summary

In this Chapter I have presented an analysis of the OS sample results, compared to the previous results for the IRS sample, and have discussed what this tells us about the properties of 'normal' galaxies, drawn from right along the Hubble sequence, compared to

IRAS-bright galaxies in the local Universe.

I have found differences in the relations between FIR luminosity and optical blue luminosity, between the ratio of 850 μm-to-optical luminosity and FIR luminosity, and between dust mass and optical luminosity for the OS and IRS galaxies, and conclude that a likely explanation would be the presence of significant extinction at optical wavelengths in the *IRAS*-selected galaxies.

There are strong correlations of both the S_{60}/S_{100} and S_{100}/S_{850} colours with S_{60}/S_{850} colour for both the OS and IRS samples. This relationship is important as it will allow the production of the submillimetre luminosity function using a large sample of galaxies from the PSCz survey (Saunders et al. 2000) which have 60 μm and 100 μm (but not 850 μm) fluxes, as I will describe in the following Chapter.

I find that the ratio of the mass of cold dust to the mass of warm dust is much higher for the optically-selected galaxies than for the previous work on *IRAS*-selected galaxies (DE01/LD00), and can reach values of $\sim$1000. By comparing the results for the *IRAS*- and optically-selected samples I have shown that there is a population of galaxies containing a large proportion of cold dust that is unrepresented in the *IRAS* sample.

I find a mean neutral gas-to-dust ratio $\bar{M}_{HI}/M_{d2}$=192$\pm$44 for the OS galaxies with two-component fits which, in the absence of significant amount of molecular gas, is in good agreement with the Galactic value.

There appears to be little change in the properties of dust in galaxies along the Hubble sequence, except a marginally significant trend for early-type galaxies to be less luminous submillimetre sources than late-types. This is not what one might expect, a priori, if a galaxy's dust and gas are associated with its disk; a simple analysis of typical bulge-to-disk ratios showed that we should expect to find at least 3 times as much dust in late-types as in early types such as S0s; in fact in the OS sample the distribution of dust masses is relatively similar across all Hubble types.

Chapter 5

Luminosity and Dust Mass Functions

5.1 Overview

The 'accessible volume' method (Avni & Bahcall 1980) will, in principle, produce unbiased estimates of the submillimetre luminosity function (LF) and dust mass function (DMF) provided that no population of galaxies is unrepresented by the sample used to derive the LF and DMF. D00/LD00 produced a first estimate of the LF and DMF from the IRS sample. However, since the new observations of the OS sample have shown the existence of a population of 'cold-dust-dominated' galaxies with low values of the S_{60}/S_{100} and S_{60}/S_{850} flux ratios (see discussion and Figure 4.9 in Section 3.5) *of which there is not a single representative in the IRS sample*, D00/LD00's earlier estimates of the LF and DMF are likely to be biased.

In this Chapter I use the new (OS sample) results to produce new estimates of the local submillimetre LF and DMF. I will produce the LF and DMF by two different methods: 1) directly from the OS SLUGS sample, and 2) by extrapolating the spectral energy

distributions of the galaxies in the *IRAS* PSCz catalogue (Saunders et al. 2000) out to

850 μm. This second method will probe a wider range of luminosities than probed directly

by the OS and IRS SLUGS samples. I will then compare the results for the two SLUGS

samples in order to investigate whether the IRS sample luminosity function and dust mass

function are likely to have been biased, and compare the both SLUGS sample results to

the results using the PSCz galaxies.

5.2   Method

I derive the local submillimetre LF and DMF by two different methods: 1) directly from

the OS SLUGS sample, and 2) by extrapolating the spectral energy distributions of the

galaxies in the *IRAS* PSCz catalogue out to 850 μm. The PSCz catalogue (Saunders et al.

2000) is a complete redshift survey of $\sim$15000 *IRAS* galaxies in the *IRAS* Point Source

Catalogue. Serjeant & Harrison (2005; herein SH05) used the PSCz galaxies and the IRS

SLUGS submm:far-IR two-colour relation to extrapolate the SEDs of the PSCz galaxies

out to 850 μm and produce an 850 μm LF. Importantly, this method allows us to probe a

wider range of luminosities than probed directly by the SLUGS samples.

The LF for both methods is estimated using

$$\Phi(L)\Delta L = \sum_i \frac{1}{V_i}$$ (5.1)

(Avni & Bahcall 1980). Here $\Phi(L)\Delta L$ is the number density of objects (Mpc^{-3}) in the

luminosity range L to $L + \Delta L$, the summation is over all the objects in the sample lying

within this luminosity range, and V_i is the accessible volume of the ith object in the

sample. Throughout we use an H_0 of 75 km s^{-1}Mpc^{-1} and a 'concordance' universe with

Ω_M=0.3 and Ω_Λ=0.7. I estimate the dust mass function (the space density of galaxies as a

function of dust mass) in the same way as the LF, substituting dust mass for luminosity in

Table 5.1: Directly measured OS SLUGS luminosity and dust mass functions.

850 μm luminosity function		
$logL_{850}$ (W Hz^{-1}sr^{-1})	ϕ(L) (Mpc^{-3}dex^{-1})	σ_ϕ (Mpc^{-3}dex^{-1})
20.75	9.17e-3	3.47e-3
21.01	3.83e-3	1.15e-3
21.27	2.10e-3	6.32e-4
21.52	1.20e-3	3.10e-4
21.78	6.03e-4	2.46e-4
22.04	9.14e-5	5.28e-5

α	L_* (W Hz^{-1}sr^{-1})	ϕ_* (Mpc^{-3}dex^{-1})	χ_ν^2
$-1.71^{+0.60}_{-0.57}$	$4.96^{+6.1}_{-2.5} \times 10^{21}$	$1.67^{+5.21}_{-1.18} \times 10^{-3}$	0.31

850 μm dust mass function		
$logM_d$ ($M_\odot$)	ϕ(M) (Mpc^{-3}dex^{-1})	σ_ϕ (Mpc^{-3}dex^{-1})
6.75	9.08e-3	3.03e-3
6.99	3.99e-3	1.33e-3
7.23	3.09e-3	8.57e-4
7.48	9.25e-4	3.08e-4
7.72	8.14e-4	2.45e-4
7.96	5.69e-5	4.02e-5

α	M_* ($M_\odot$)	ϕ_* (Mpc^{-3}dex^{-1})	χ_ν^2
$-1.67^{+0.24}_{-0.25}$	$3.09^{+1.09}_{-0.64} \times 10^7$	$3.01^{+1.62}_{-1.38} \times 10^{-3}$	1.17

Equation 5.1. The details of these two methods, hereafter referred to as 'directly measured' and 'PSCz-extrapolated', are discussed in Sections 5.2.1 and 5.2.2 respectively.

5.2.1 Directly measured 850 μm Luminosity Function and Dust Mass Function

I calculated the directly measured LF and DMF from the 52 objects in the OS sample which were detected at 850 μm. For the DMF I use the dust masses listed in Table 3.4, which were calculated using the isothermal SED-fitted temperatures or, where no fit was made (11 objects), using an assumed dust temperature of 20K (assumed since 20 K is the mean temperature of the cold dust component, and thus the largest proportion of dust, found for the OS galaxies with two-component fits; see Chapter 3 Section 3.5). For the OS sample the accessible volume is the maximum volume in which the object would still be detected at 850 μm and also still be below the magnitude limit of the CfA sample. Since objects with $cz < 1900 \, \text{km s}^{-1}$ were excluded from the OS sample this volume is not included in the calculation of V_i. When calculating the maximum redshift at which an object would still be detected at 850 μm I used the noise appropriate for the observation of that object. I corrected the LF by the factor 97/81 to account for the CfA galaxies not observed at all at 850 μm (Section 2.2).

The corrected directly measured 850 μm LF and DMF are shown as star symbols in Figures 5.3 and 5.4 respectively, and are given in tabular form in Table 5.1. The errors on the directly measured LF and DMF are standard Poisson errors. One effect that may lead to the estimates of the LF and DMF being slight underestimates is that I noticed that the OS galaxies not detected at 850 μm were generally observed under worse weather conditions than the sources that were detected. About half of all the non-detections were observed in grade 3 or worse weather conditions ($\tau_{225GHz} > 0.08$) compared to only a quarter of the detections. This implies that approximately a quarter of all the galaxies not

detected (i.e. ~ 7) would probably have been detected had they been observed in better weather, and thus this would lead to an additional correction factor of about 13%.

5.2.2 *IRAS* PSCz-extrapolated 850 μm Luminosity Function and Dust Mass Function

In order to better constrain the LF at the lower luminosity end more data points are needed, probing a wider range of luminosities than probed directly by the SLUGS samples. This is achieved using a method described by SH05, whereby the 850 μm LF is determined by extrapolating the spectral energy distributions of the ~ 15000 *IRAS* PSCz survey galaxies (Saunders et al. 2000) out to 850 μm. Since, as described in Chapter 4 Section 4.2.2, for the two SLUGS samples there is a strong correlation between the S_{60}/S_{100} and S_{60}/S_{850} colours (Figure 4.9) a linear fit to this colour-colour relation can be used to make the extrapolation from 60 μm to 850 μm flux density. This method will be valid as long as the galaxies in the PSCz sample have similar 100/60 colours to the SLUGS galaxies (see discussion in the following sections).

Fitting the SLUGS colour-colour relation

There are some slight differences between the way SH05 used the two-colour relation and the way I have adapted the method in this work. Firstly, SH05 plotted the S_{850}/S_{60} versus S_{100}/S_{60} colours but rather than making a direct linear fit to the data they used a predicted linear relation based on a grey-body with $\beta = 1.3$. This was sufficient for their purposes, since they simply wanted a phenomenonological model which they could use to predict the fluxes at 850 μm by interpolating the predicted SEDs, such that they predict the fluxes to within a factor of 2. For the purposes of the present work, however, the best possible estimate of the 850 μm fluxes is desirable, and since there is a strong correlation between the submm:far-IR colours (see Chapter 4 Section 4.2.2 and Figure 5.1
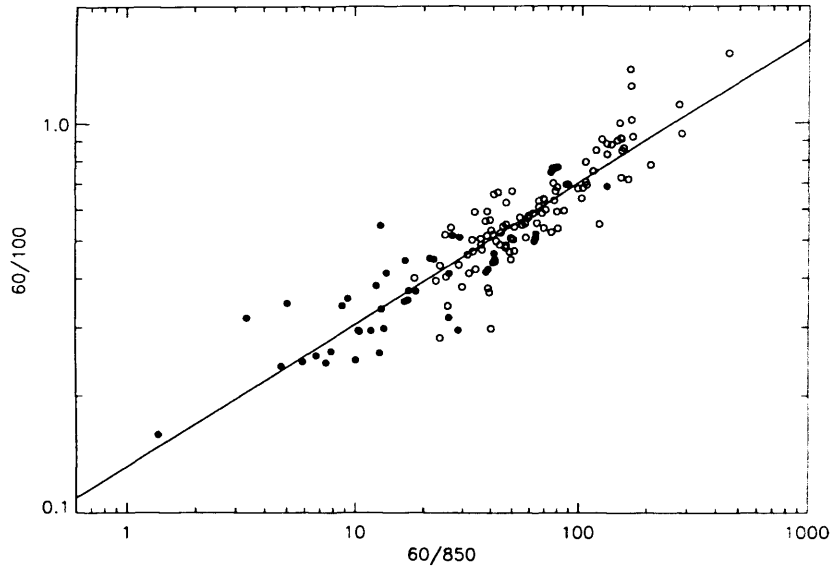
(a)
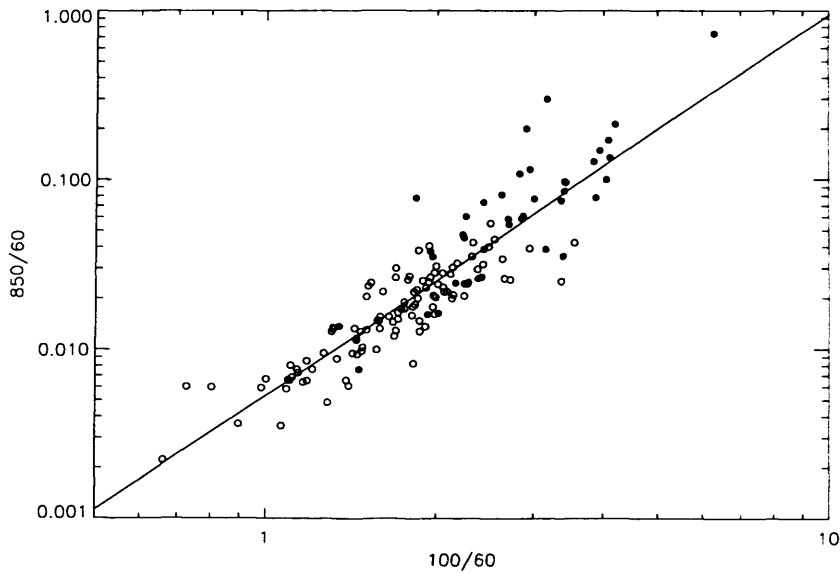
(b)

Figure 5.1: Colour-colour plots for the OS (this work) and IRS (D00) SLUGS (filled and open points respectively), with linear (least-squares) fit to the *combined* OS+IRS data: (a) S_{60}/S_{100} versus S_{60}/S_{850} colours, and (b) S_{850}/S_{60} versus S_{100}/S_{60} colours (as used by Serjeant & Harrison 2005).
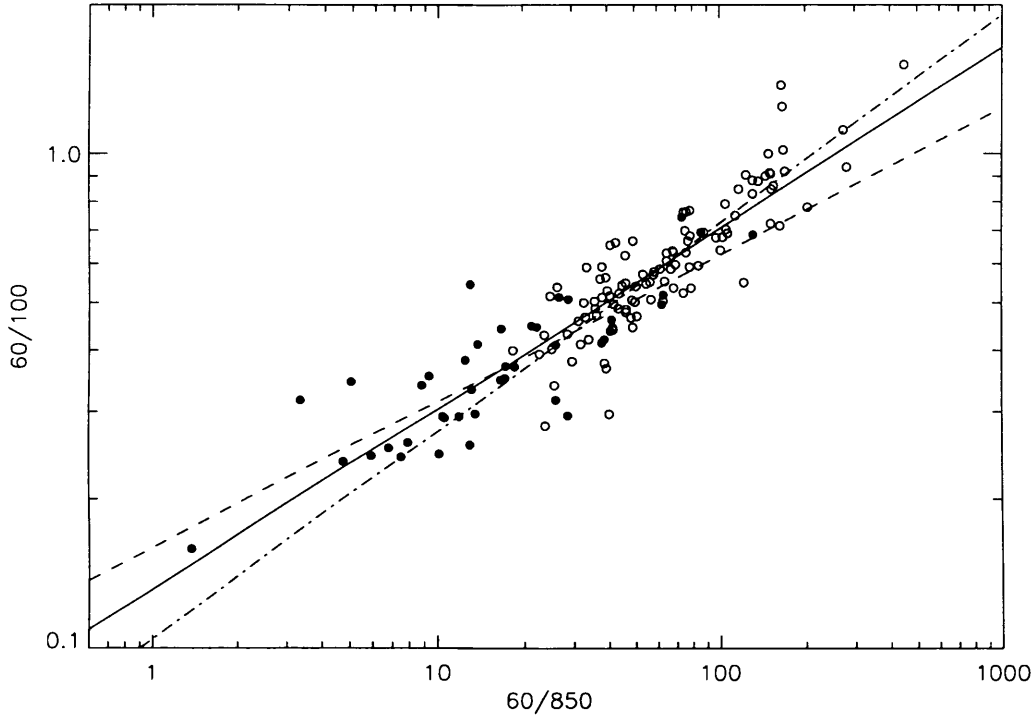
Figure 5.2: Colour-colour plot: S_{60}/S_{100} versus S_{60}/S_{850} colours for the OS (this work) and IRS (D00) SLUGS (filled and open points respectively) with (least squares) fitted linear relations, as listed in Table 5.2. The solid line is the fit to the *combined* OS + IRS sample, the dashed line the fit to the OS data alone, and the dot-dash line the fit to the IRS data alone.

in the current Chapter) the obvious way to proceed is to simply make a direct linear fit to the two-colour relation. Secondly, SH05 derived the submm:far-IR two-colour relationship from the IRS SLUGS sample alone. However, I have shown in this thesis that the OS and IRS samples have quite different properties. In order to determine the sensitivity of the LF/DMF to the colour relationship I have therefore derived colour relationships for the combined OS + IRS sample, the OS sample alone, and the IRS sample alone (Table 5.2).

Thirdly, while SH05 used the S_{850}/S_{60} versus S_{100}/S_{60} colours I have instead fitted the S_{60}/S_{100} versus S_{60}/S_{850} colours. Both of these plots are shown in Figure 5.1, where

Table 5.2:   Linear fit parameters for the SLUGS colour-colour plot $(\log(S_{60}/S_{100})$ vs $\log(S_{60}/S_{850}))$ shown in Figure 5.2.

SLUGS data fitted	linear fit (y=mx+c)	
	m	c
OPT+*IRAS*	0.365 ± 0.014	-0.881 ± 0.024
OPT	0.296 ± 0.031	-0.797 ± 0.039
IRAS	0.421 ± 0.023	-0.981 ± 0.042

the solid line shows the direct linear (least-squares) fit I have made for each of the plots. There are some subtle, but important, differences between these two relations. Although in theory either of these two relations could be used to predict the 850 μm flux from the 60-100 μm colour, from Figure 5.1 it is clear that in practice the fit to the S_{850}/S_{60} versus S_{100}/S_{60} colours does not fit the OS data well (the filled points in Figure 5.1). For most of the OS galaxies this linear relation underestimates the 850 μm flux, while the relation does adequately fit the IRS data. I have already stressed the importance of using *both* the IRS *and* the OS samples, as the two samples clearly have quite different properties, and in order to try to ensure that this method will successfully predict the 850 μm fluxes of all populations of galaxy in the PSCz sample, and not be biased towards warmer objects, it is vital that the two-colour fit well-describes both the OS and IRS galaxies and the warmer and colder 60-100 μm colours. In order to achieve this I instead fit the S_{60}/S_{100} versus S_{60}/S_{850} colour plane, which as can be seen clearly in Figure 5.1(a), does indeed provide a much better fit to both the SLUGS samples and a good fit at both warmer and colder 60-100 μm colours.

Thus the 850 μm fluxes of the PSCz galaxies are predicted using the following relationship

$$\log S_{850} = \frac{S_{60} + (\log(\frac{100}{60}) - 0.881)}{0.365} \qquad (5.2)$$

Table 5.3: PSCz-extrapolated luminosity function.

$\log L_{850}$ ($\mathrm{W\,Hz^{-1}sr^{-1}}$)	$\phi(\mathrm{L})$ ($\mathrm{Mpc^{-3}dex^{-1}}$)	σ_ϕ^{down} ($\mathrm{Mpc^{-3}dex^{-1}}$)	σ_ϕ^{up}
18.52	3.42e-02	2.42e-02	2.74e-02
18.75	6.30e-02	2.38e-02	2.83e-02
18.99	3.90e-02	1.62e-02	9.45e-03
19.23	3.20e-02	1.06e-02	6.17e-03
19.47	2.35e-02	3.50e-03	7.86e-03
19.70	3.08e-02	8.14e-03	3.42e-03
19.94	1.85e-02	2.81e-03	5.72e-03
20.18	1.26e-02	1.98e-03	1.34e-03
20.42	1.16e-02	1.14e-03	6.74e-04
20.65	1.02e-02	1.70e-03	4.41e-04
20.89	6.67e-03	1.12e-03	8.25e-04
21.13	4.30e-03	6.77e-04	3.01e-04
21.36	2.73e-03	7.59e-04	1.63e-04
21.60	1.34e-03	4.61e-04	1.00e-04
21.84	4.43e-04	1.75e-04	1.36e-04
22.08	1.17e-04	6.67e-05	2.36e-05
22.31	1.85e-05	7.86e-06	1.45e-05
22.55	4.27e-06	2.64e-06	3.81e-07
22.79	2.91e-07	1.28e-07	9.39e-07
23.03	9.86e-08	5.62e-08	3.49e-08

α	L_* ($\mathrm{W\,Hz^{-1}sr^{-1}}$)	ϕ_* ($\mathrm{Mpc^{-3}dex^{-1}}$)	χ^2_ν
$-1.38^{+0.02}_{-0.03}$	$3.73^{+0.29}_{-0.32} \times 10^{21}$	$4.17^{+0.41}_{-0.45} \times 10^{-3}$	1.0

Table 5.4: PSCz-extrapolated single-temperature dustmass function.

$\log M_d$ ($M_\odot$)	$\phi(\mathrm{M})$ (Mpc^{-3}dex^{-1})	σ_ϕ^{down} (Mpc^{-3}dex^{-1})	σ_ϕ^{up}
4.30	3.26e-02	2.30e-02	2.30e-02
4.55	1.62e-02	7.26e-03	4.37e-02
4.80	6.78e-02	4.22e-02	1.70e-02
5.05	3.11e-02	8.74e-03	9.10e-03
5.30	2.58e-02	6.36e-03	3.77e-03
5.54	2.36e-02	5.72e-03	8.87e-03
5.79	2.68e-02	8.69e-03	2.48e-03
6.04	1.46e-02	1.62e-03	3.60e-03
6.29	1.19e-02	2.41e-03	6.62e-04
6.54	9.29e-03	3.93e-04	8.97e-04
6.79	7.68e-03	1.68e-03	2.53e-04
7.04	4.67e-03	8.33e-04	3.80e-04
7.29	2.80e-03	7.87e-04	1.03e-04
7.54	1.38e-03	4.83e-04	1.94e-04
7.79	4.51e-04	2.12e-04	1.87e-04
8.04	1.06e-04	6.10e-05	3.12e-05
8.29	1.44e-05	7.21e-06	1.48e-05
8.54	3.10e-06	2.22e-06	1.18e-06
8.79	4.82e-07	4.21e-07	5.94e-07
9.04	5.24e-08	5.64e-08	5.24e-08

α	M_* ($M_\odot$)	ϕ_* (Mpc^{-3}dex^{-1})	χ_ν^2
$-1.34^{+0.13}_{-0.08}$	$2.74^{+1.23}_{-1.13} \times 10^7$	$5.16^{+3.90}_{-1.74} \times 10^{-3}$	0.65

Table 5.5: PSCz-extrapolated 20K 'cold' dustmass function.

log M_d	ϕ(M)	σ_ϕ^{down}	σ_ϕ^{up}
4.65	3.41e-02	2.41e-02	2.76e-02
4.88	6.28e-02	2.37e-02	2.82e-02
5.12	3.88e-02	1.61e-02	9.42e-03
5.36	3.20e-02	1.06e-02	6.16e-03
5.60	2.59e-02	4.59e-03	6.08e-03
5.84	2.86e-02	4.67e-03	3.24e-03
6.07	1.85e-02	2.60e-03	4.39e-03
6.31	1.29e-02	1.82e-03	1.13e-03
6.55	1.17e-02	1.11e-03	6.77e-04
6.79	1.02e-02	1.58e-03	4.37e-04
7.03	6.75e-03	1.21e-03	5.96e-04
7.26	4.29e-03	6.15e-04	4.09e-04
7.50	2.79e-03	7.83e-04	1.07e-04
7.74	1.35e-03	4.65e-04	1.07e-04
7.98	4.54e-04	1.81e-04	1.37e-04
8.22	1.19e-04	6.64e-05	2.08e-05
8.45	1.91e-05	7.57e-06	1.47e-05
8.69	4.56e-06	3.07e-06	3.27e-07
8.93	2.87e-07	9.82e-08	9.94e-07
9.17	1.03e-07	5.48e-08	3.26e-08

α	M_* ($M_\odot$)	ϕ_* (Mpc^{-3}dex^{-1})	χ_ν^2
$-1.39^{+0.03}_{-0.02}$	$5.28^{+0.45}_{-0.55} \times 10^7$	$4.04^{+0.74}_{-0.50} \times 10^{-3}$	1.28

where S_{850} is the predicted $850\,\mu$m flux, S_{60} is the IRAS $60\,\mu$m flux and $100/60$ is the S_{100}/S_{60} colour.

Producing the sample of PSCz galaxies

In order to produce unbiased estimates of the LF and DMF I have excluded some PSCz galaxies. Firstly I exclude all those objects that do not have redshifts, those that have velocities $< 300\,\mathrm{km\,s^{-1}}$ (to ensure that peculiar velocities are unimportant), and those that have redshifts > 0.2 (thus excluding any ultra-luminous, high-redshift objects). I then exclude all objects with upper limits at $100\,\mu$m, since for these objects the SH05 method cannot be applied; this procedure is valid provided that the excluded objects are randomly distributed in redshift, which indeed they are found to be. Finally, I use the *IRAS* Point Source Catalogue flags, as listed in the PSCz catalogue, to exclude sources which are likely to be either solely or strongly contaminated by Galactic cirrus. It is important to exclude these sources because they are very cold sources and so potentially can have a large effect on the $850\,\mu$m LF. If two or more of the flags indicate Galactic cirrus (using flag value limits indicated in the *IRAS* Explanatory Supplement) I exclude that object. As a check on the validity of this method I inspected by eye (using the IRSA ISSA Image Server) a sample of $\sim$40 objects randomly chosen from those excluded as Galactic cirrus, and a further sample of $\sim$40 objects randomly chosen from those that made it into the final sample. I found that 98% of the sources with cirrus flags and 7% of the sources without cirrus flags showed signs of significant cirrus, although for two thirds of the sources with cirrus flags there still appeared to be a genuine source present. In total, from the $\sim$14500 galaxies with redshifts in the *IRAS* PSCz catalogue I exclude $\sim$4300 objects because of either $100\,\mu$m upper limits or Galactic cirrus. This leaves 10252 galaxies in the PSCz-selected sample.
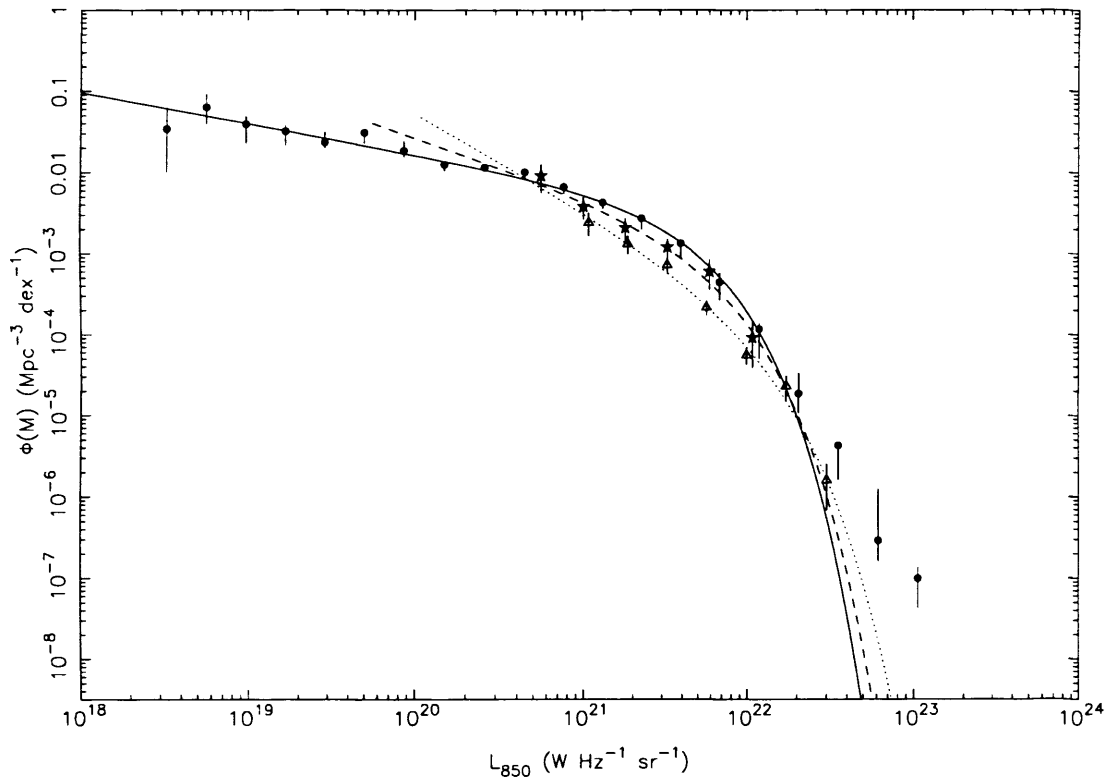
Figure 5.3: PSCz-extrapolated 850 μm Luminosity Function (filled circles) with best-fitting Schechter function (solid line). The parameters for the Schechter function are $\alpha = -1.38$, $L_* = 3.7 \times 10^{21}$ W Hz^{-1}sr^{-1}. Also shown are the directly measured 850 μm Luminosity Function for the OS SLUGS sample (filled stars) with best-fitting Schechter function (dashed line) and the results for the IRS SLUGS sample from Dunne et al. (2000)(open triangles and dotted line).
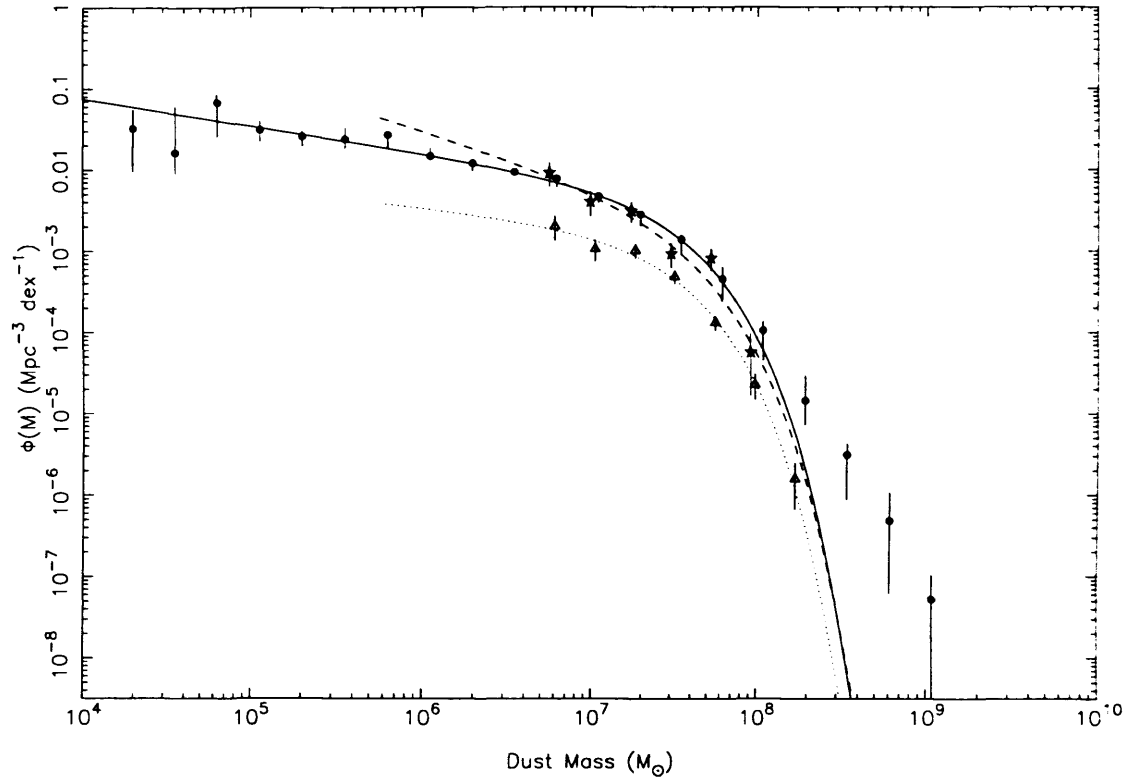
Figure 5.4:   PSCz-extrapolated Dust Mass Function (filled circles) with best-fitting Schechter function (solid line) — the dust masses were calculated using T_d derived from the *IRAS* 100/60 colour and $\beta=2$. The parameters for the Schechter function are $\alpha = -1.34$, $M_* = 2.7 \times 10^7 M_\odot$. Filled stars indicate the directly measured Dust Mass Function for the OS SLUGS sample with best-fitting Schechter function shown as a dashed line — the dust masses were calculated using T_d from isothermal SED fitting. Also shown are the results for the IRS SLUGS sample from Dunne et al. (2000) (open triangles; dotted line: best-fitting Schechter function).
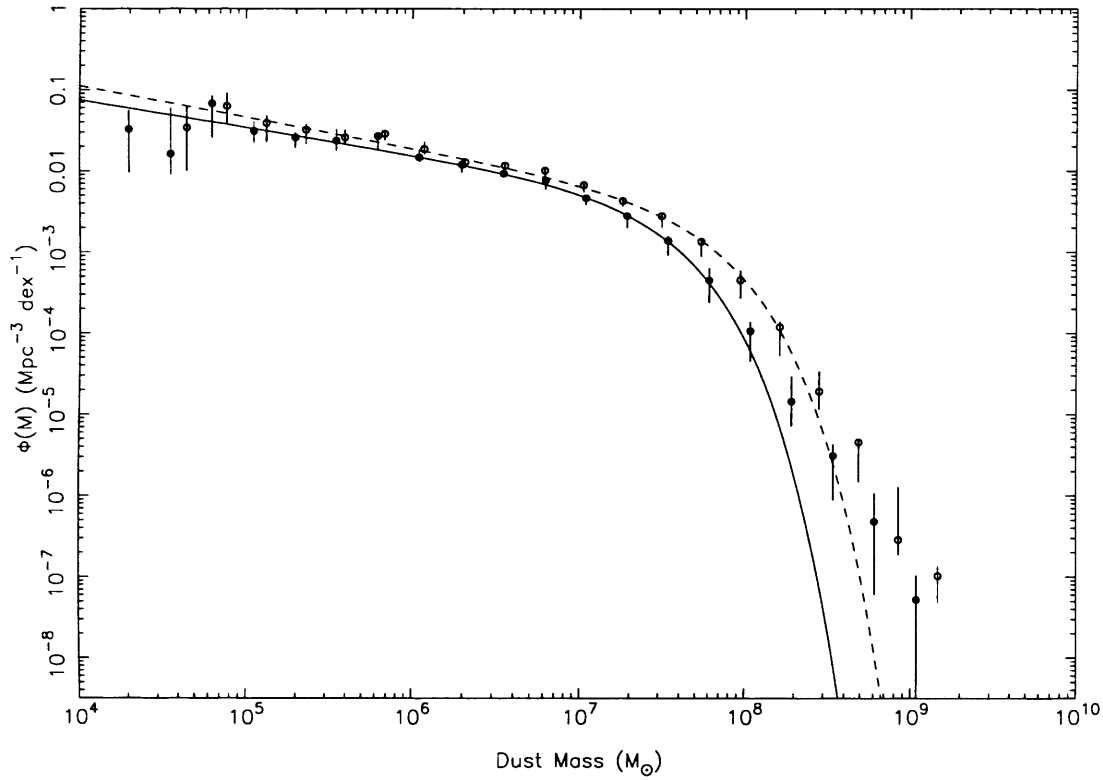
Figure 5.5: PSCz-extrapolated 'cold' Dustmass Function (open circles), in which dust masses are calculated using $T_d = 20$ K and $\beta = 2$. The dashed line shows the best-fitting Schechter function, parameters are $\alpha = -1.39$, $M_* = 5.1 \times 10^7 M_\odot$. For comparison the PSCz-extrapolated DMF shown in Figure 5.4 is also shown (filled points and solid line).
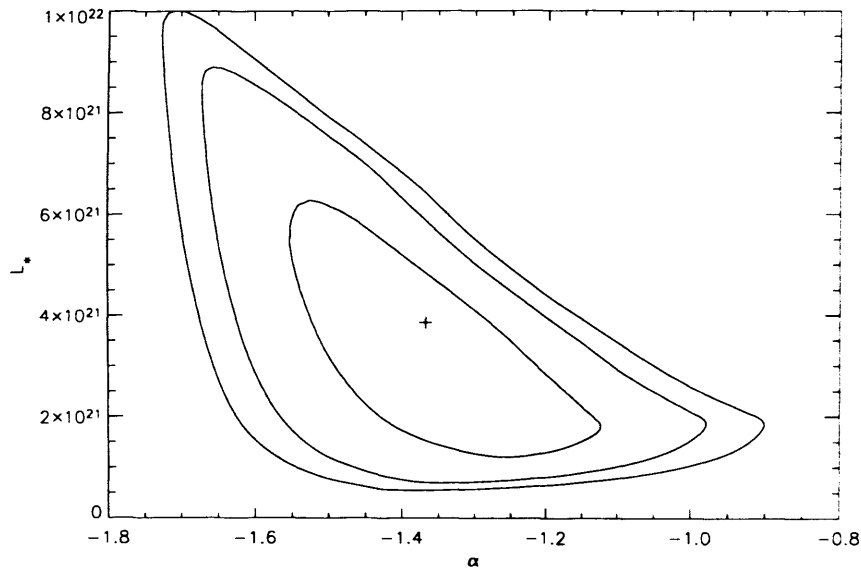
(a)
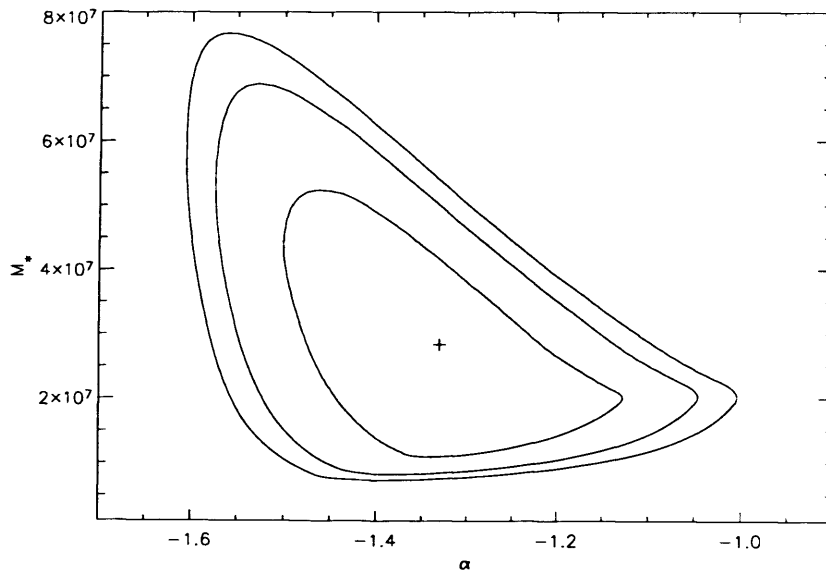
(b)

Figure 5.6:   Joint confidence χ^2 contours for (a) the 850 μm (PSCz-extrapolated) Luminosity Function parameters α and L_*, (b) the 850μm (PSCz-extrapolated) Dustmass Function parameters α and M_*. Contours shown at the 68, 90 and 95% (1.5, 2 and 2.5σ) confidence levels.

Is the PSCz sample representative of the SLUGS galaxies?

The SH05 method of deriving 850 μm luminosities for the PSCz galaxies will be valid as long as the galaxies in the PSCz sample have similar 100/60 colours to the SLUGS galaxies. Figure 5.7 shows the comparison between the distributions of 100/60 colour for the OS and IRS SLUGS samples and the distribution of 100/60 colour for the PSCz sample. It is quite clearly seen that, although the two SLUGS samples themselves have very different 100/60 properties (as discussed in detail in Chapter 4), the PSCz sample has a very similar distribution of 100/60 colours to the *combined* SLUGS sample. Importantly, this confirms that the SH05 method is a valid way of deriving 850 μm fluxes for the PSCz galaxies.

Another potential factor is the fact that $\sim 20\%$ of the OS sample were not detected in both *IRAS* (60 μm and 100 μm) bands though they were detected at 850 μm, suggesting the possibility of a population of strong submillimetre-emitting galaxies which would not be represented in an *IRAS*-selected sample such as the PSCz. However, I have shown in Chapter 3 that a significant amount of the 850 μm flux for some of these objects (specifically the ellipticals) may be due to contamination by radio synchrotron emission from a radio source associated with the galaxy.

The PSCz-extrapolated LF and DMF

For the PSCz-extrapolated sample the accessible volume is the maximum volume in which the object could still be seen and still be included in the *IRAS* PSCz catalogue. Since objects with $cz < 300\,\mathrm{km\,s^{-1}}$ were excluded from the sample this volume is not included in our calculation of V_i. For the PSCz-extrapolated DMF the dust masses were calculated using T_d derived from the *IRAS* 100/60 colour and $\beta=2$.

For completeness, the effect of excluding real 60 μm sources must be taken into account by applying a correction factor to the LF and DMF. This correction factor will be uncertain, since some excluded sources will be real and some not. Therefore I correct using
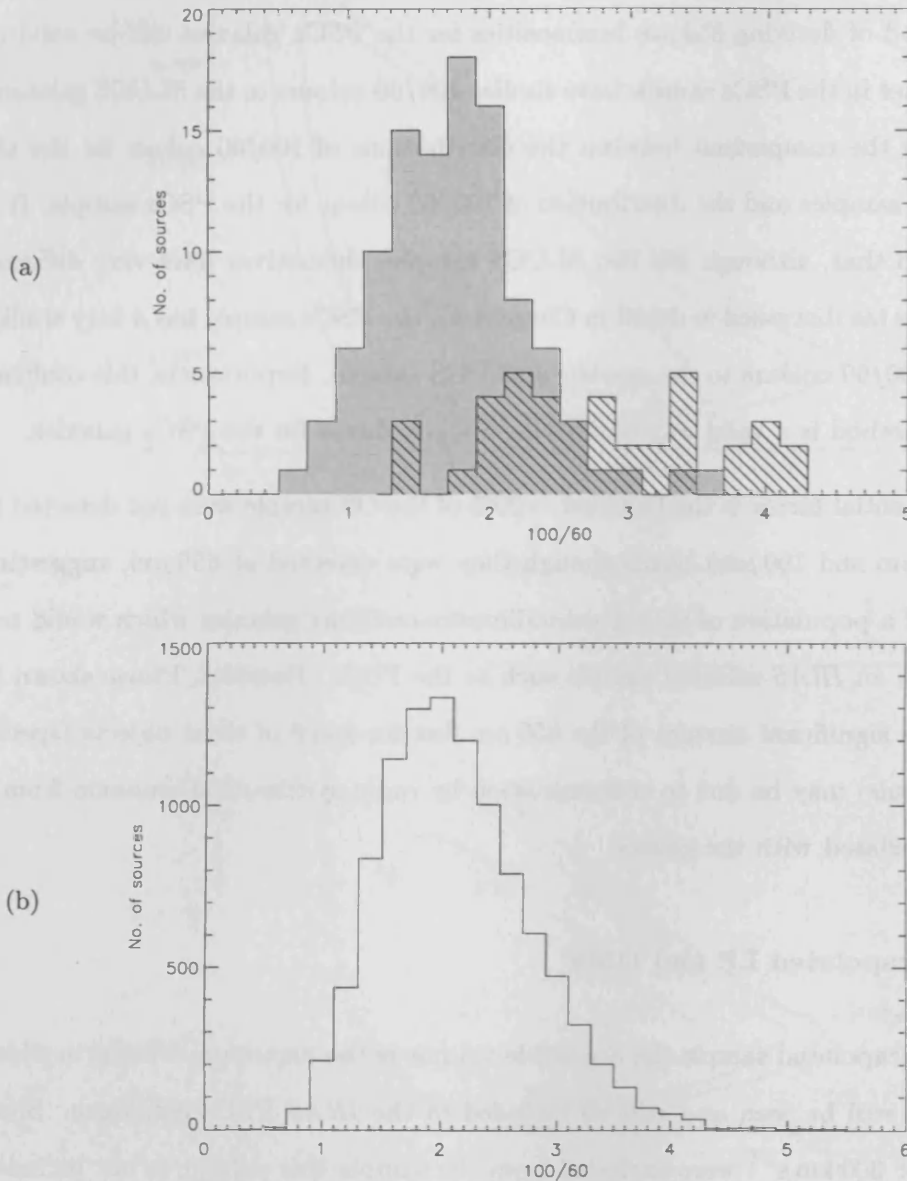
Figure 5.7: Distributions of 100/60 colour for (a) the OS and IRS SLUGS samples and (b) the PSCz sample. Although the two SLUGS samples themselves have very different distributions, importantly the PSCz sample has a very similar distribution of 100/60 colours to the *combined* SLUGS sample.

our best estimate of real sources as follows. I corrected for two thirds of the sources I excluded as being contaminated by cirrus. The correct correction factor for the sources that were excluded because they have 100 μm upper limits is even more uncertain. These are probably all genuine sources, but they will generally have warmer colours than the sources that were not excluded. I arbitrarily corrected for 50% of these. Including the correction for ~100 sources without redshifts, the final correction factor for excluded sources is 1.27. This is obviously very uncertain, however at the most it could be 1.43 and at the least it could be 1.00. This produces maximum errors of +13% and −21% on the LF and DMF in addition to the errors described below.

I also made a correction for evolution out to z=0.2 using a density evolution $\propto (1+z)^7$ (Saunders et al. 1990). I confirmed that the strength assumed for the evolution made negligible difference to the results, by producing the LF using various different assumed strengths for the evolution term (see Figure 5.8).

The PSCz-extrapolated 850 μm LF and DMF are shown as filled circles in Figure 5.3 and Figures 5.5 and 5.4 respectively, and are given in tabular form in Tables 5.3 and 5.4. For comparison I have also produced a 'cold' PSCz-extrapolated DMF, produced as above but with dust masses calculated using T_d=20K and β=2; this is shown as open circles in Figure 5.5 and listed in Table 5.4.

While the errors on the directly measured LF and DMF are standard Poisson errors, the errors on the PSCz-extrapolated LF and DMF are derived from a combination of Poisson errors and the errors resulting from the fact that the 850 μm luminosities have been derived using the best-fitting linear relation to our SLUGS colour-colour plot (Figure 5.2). In order to take into account how the 'choice' of linear fit affects the LF produced, I additionally generate two 'extremes' of the PSCz-extrapolated LF and DMF using two alternative fits to the SLUGS colour-colour plot: 1) a fit to the OS data only, and 2) a fit to the IRS data only (linear fit parameters listed in Table 5.2). I then use the maximum
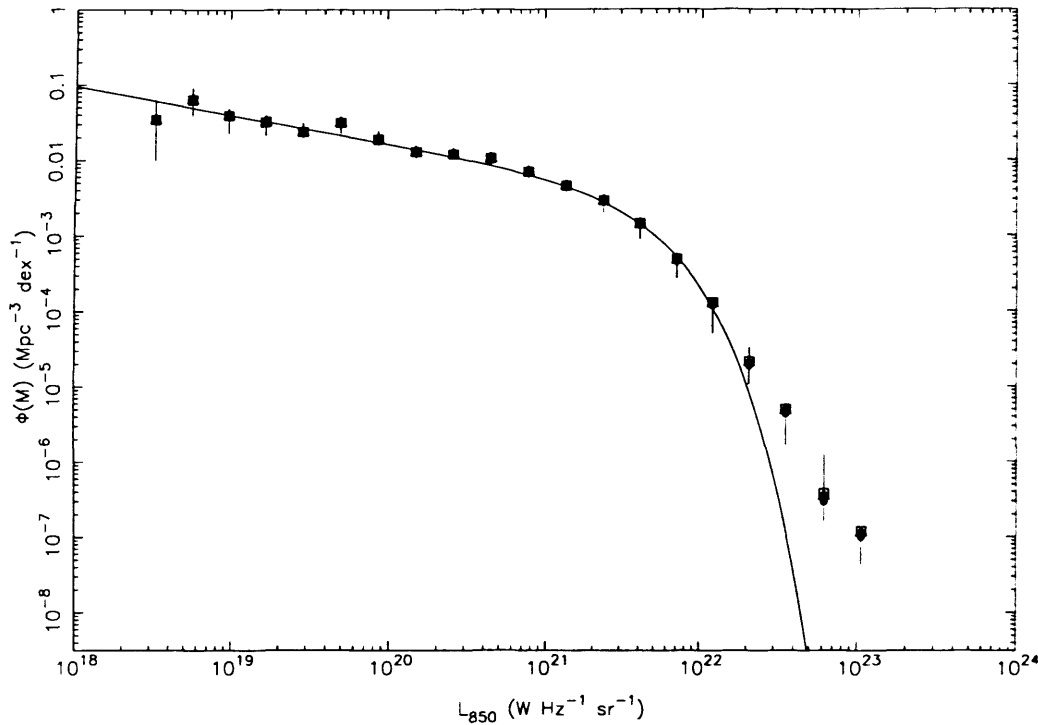
Figure 5.8: PSCz-extrapolated 850 μm Luminosity Function for different strengths of the $(1+z)^{\alpha}$ density evolution: $\alpha = 7, 6, 5, 4$ shown as filled circles, open circles, open triangles and open squares respectively. The assumed α makes virtually no difference to the results of the LF, and in fact only the evolution $\propto (1 + z)^4$ even begins to be distinguishable (at the high luminosity end) from the other values of α.

difference between these 'extreme' LF values and our actual PSCz-extrapolated LF data points as the errors on our LF due to the 'choice' of colour-colour linear relation. I then also take into account the number statistics, and thus add in quadrature the standard Poisson errors and the 'choice of colour-colour fit' errors to obtain our total errors listed in Tables 5.3 and 5.4. Thus, the variation in the size of error bars from bin to bin is simply dependent on whether in a particular bin, and in a particular direction, there is only a Poisson error or also a colour-colour fit error. This is shown graphically in Figure 5.9, where in addition to the PSCz-extrapolated LF and error bars as listed in Table 5.3 I have also plotted the two 'extreme' LFs (open squares and filled diamonds represent the IRS
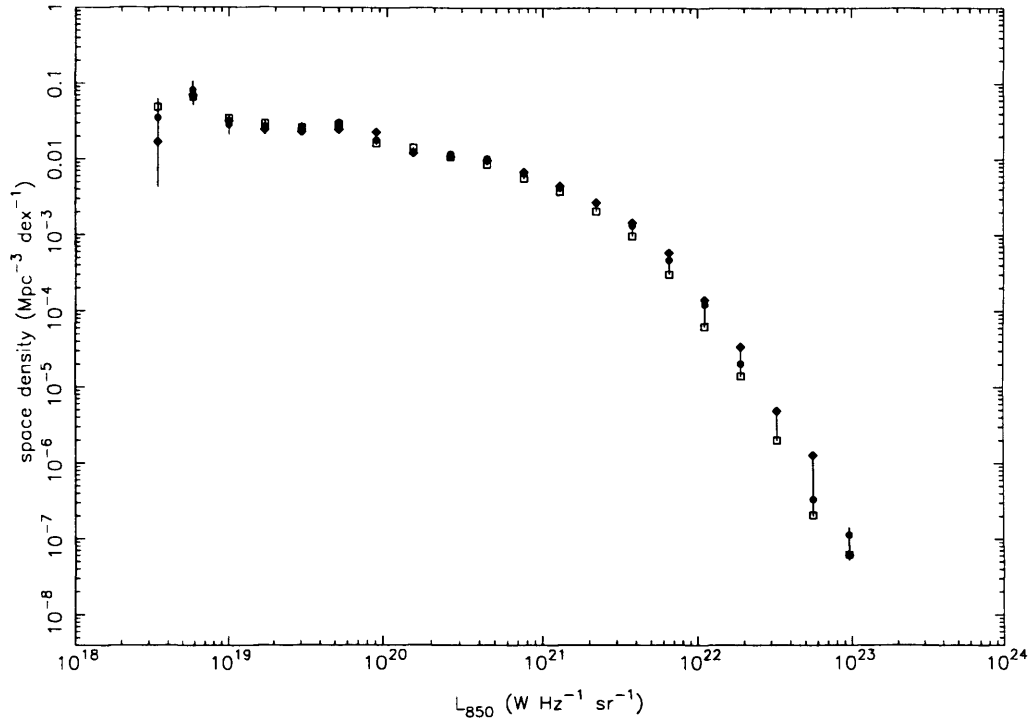
Figure 5.9: PSCz-extrapolated 850 μm Luminosity Function produced using the *combined* OS+IRS SLUGS two-colour relation (filled circles), the IRS relation (open squares) and the OS relation (filled diamonds).

and OS relations respectively). As discussed above, in addition to these errors there are, at most, upper and lower errors of +13% and −21% from the choice of correction factors.

5.3 Results and discussion

The directly measured OS LF and PSCz-extrapolated LF agree remarkably well over the range of luminosities covered by the SLUGS samples, yet I find that in comparison the IRS sample of D00 (plotted as triangles in Figures 5.3 and 5.4) consistently underestimates the submillimetre LF by a factor of 2 and the DMF by a factor of 4. The fact that this underestimate is seen compared to the OS sample, which by definition should be free from

any dust temperature selection effects, is strong evidence that a population of 'cold' dusty galaxies was indeed 'missed' by *IRAS* and that therefore the IRS sample was missing ~half the galaxies. The bigger difference between the DMFs is probably due to the fact that, unlike the IRS sample, for the OS sample I do not have fitted isothermal SEDs for all galaxies and therefore have calculated dust masses using an assumed T_d=20K for ~20% of the sample (Section 5.2.1). (While 20K is likely to be a good estimate of the temperature of the majority of dust in a two-component model (Section 3.5) it is also colder than we typically found from our isothermal fits, so results in larger 'isothermal' dust masses).

I fit both the directly measured and PSCz-extrapolated 850 μm LFs and DMFs with Schechter functions of the form

$$\Phi(L)dL = \phi(L) \left(\frac{L}{L_*}\right)^{\alpha} e^{-(L/L_*)} dL/L_*$$
(5.3)

(Press & Schechter 1974; Schechter 1975). The best-fitting parameters for the PSCz-extrapolated 850 μm LF and DMF are listed in Tables 5.3 and 5.4 respectively, along with the reduced chi-squared values (χ_ν^2) for the fits (Figure 5.6 shows the joint confidence χ^2 contours for α and L_* for the PSCz-extrapolated functions); likewise best-fitting parameters for the directly measured 850 μm LF and DMF are shown in Table 5.1.

I find that both the directly measured and PSCz-extrapolated LFs and DMFs are well-fitted by Schechter functions. For the PSCz-extrapolated LF and DMF the best-fitting Schechter function ($\alpha = -1.38$) fits the data points extremely well across most of the luminosity range – however, the PSCz-extrapolated functions are much less well fitted at the high luminosity end. Investigation of the 3 or 4 high end luminosity bins has found several anomalies for the objects in these bins, the most striking of which is the fact that in each bin there are typically a few objects (~5% of the total number in each bin) with accessible volumes 2 or 3 orders of magnitude lower than the rest of the objects in that bin, and thus it is these few objects in each of these bins which are the main contributors
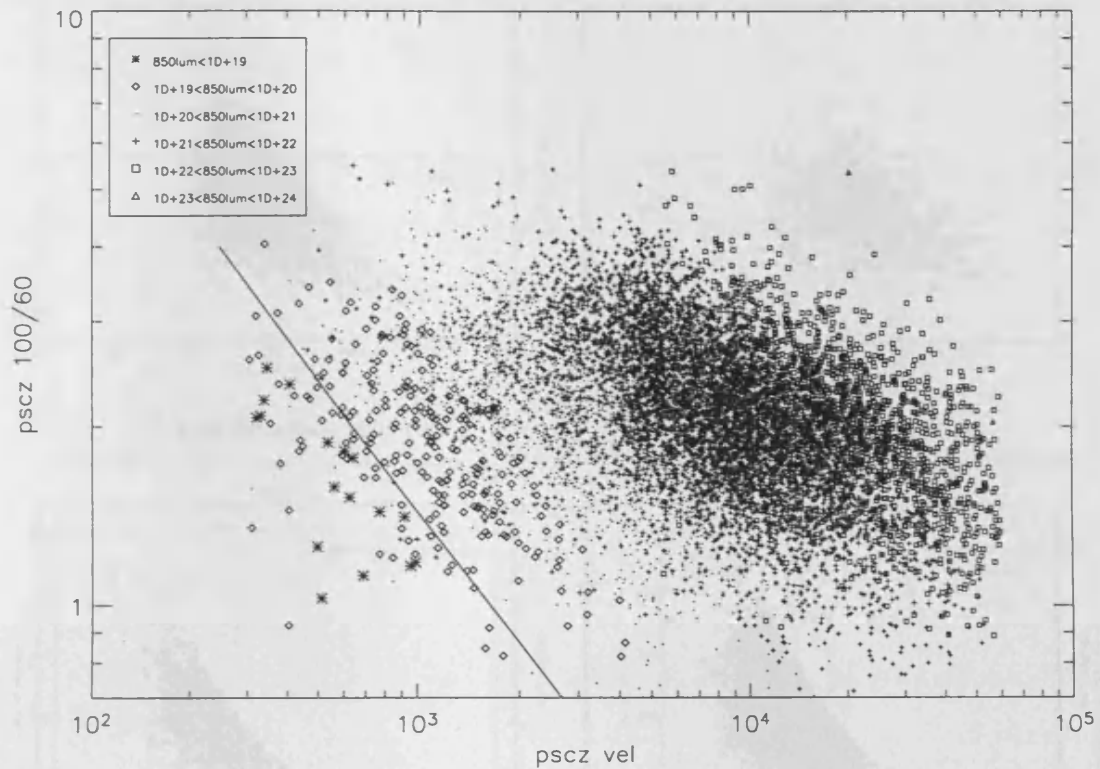
Figure 5.10:   PSCz sample: 100–60 μm colour versus velocity (km s^{-1}), with different 850 μm luminosity ranges indicated by different symbols. The plotted line indicates the upper limit to the range of 100/60 colours and velocities for $L_{850} = 1 \times 10^{19}$.

to the high space density. These objects all have cold 100/60 colours, but have a range of 60 μm fluxes and velocities (ranging from ~ 0.6–7.5 Jy and ~ 5000–20000 km s^{-1}).

There are many possible explanations for the excess at the high luminosity end. One possible explanation could be that the objects in these bins are multiple systems. At larger distances *IRAS* galaxies are mostly very luminous starbursts and are frequently in interacting pairs. The density of galaxy pairs at these distances might by substantially higher than the local galaxy density which may produce an excess in the LF at high luminosities. Several authors find this excess at high luminosities or high masses. For

(a) $300 < \mathrm{vel} < 1900\,\mathrm{km\,s^{-1}}$

(b) $1900 \leq \mathrm{vel} < 500\,\mathrm{km\,s^{-1}}$

(c) $5000 \leq \mathrm{vel} < 10000\,\mathrm{km\,s^{-1}}$

(d) $10000 \leq \mathrm{vel} < 20000\,\mathrm{km\,s^{-1}}$

(e) $20000 \leq \mathrm{vel} < 40000\,\mathrm{km\,s^{-1}}$

(f) $40000 \leq \mathrm{vel} < 60000\,\mathrm{km\,s^{-1}}$

Figure 5.11:   PSCz sample: 100–60 μm colour versus extrapolated 850 μm luminosity for the PSCz sample selected in this work, plotted for different velocity ranges.
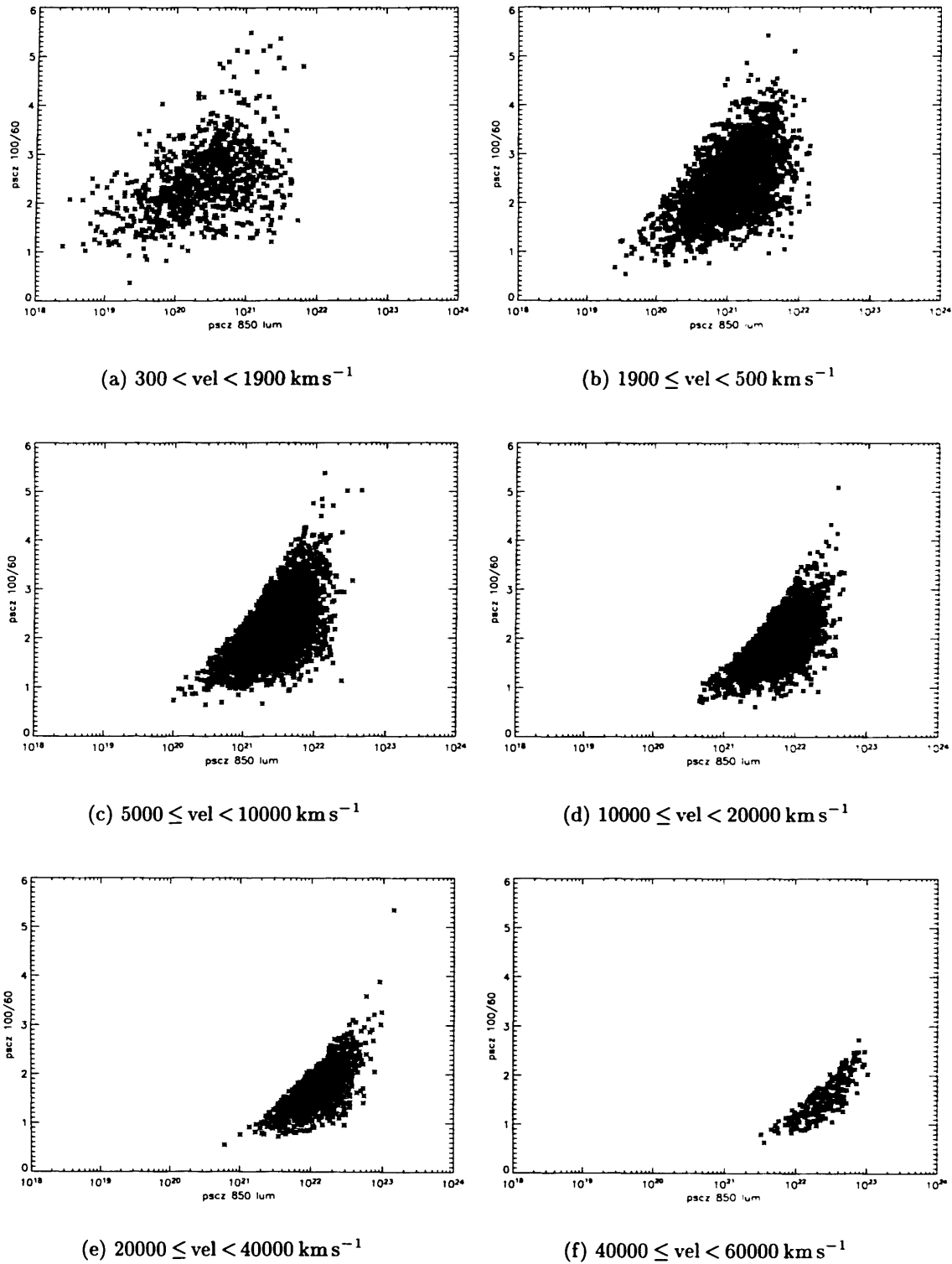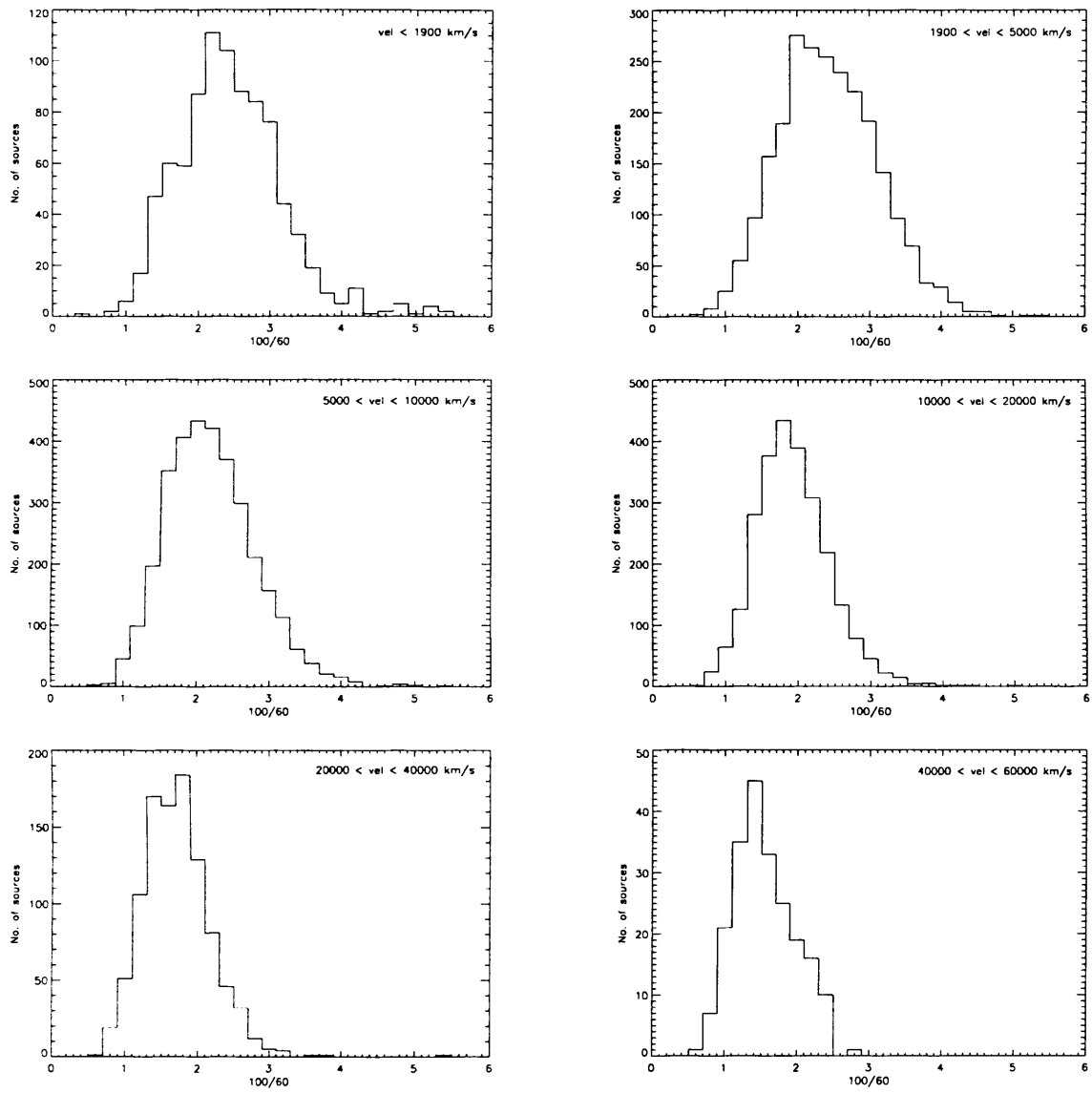
Figure 5.12: Distribution of 100–60 μm colour for the PSCz sample selected in this work, for different velocity ranges.

example Lawrence et al. (1999) find a similar excess in their 60 μm LF, as do Garcia-Appadoo, Disney & West (in preparation; priv. comm.) for their Equatorial Strip Sample HI Mass Function (their sample is a blind HI survey of gas-rich galaxies selected from the HI Parkes All Sky Survey), who find that the higher HI masses are typically multiple systems. Galactic cirrus could be another consideration. In producing a PSCz-selected sample from which to derive this LF I have excluded galaxies from the PSCz sample if two or more of the *IRAS* flags indicated cirrus. However, if a more stringent approach is taken and galaxies are excluded if just one of the *IRAS* flags indicates cirrus then approximately twice as many galaxies would be excluded, including *all* the objects in the high luminosity end bins — the Schechter function of course then fits well over the whole remaining luminosity range. One can also think of ways our use of a global colour-colour relation might have produced a spurious excess if, for example, the galaxies at the highest luminosities have systematically different colours. This would not, however, explain the excess seen in the 60 μm LF.

It is to a degree true that, because of selection effects, at the highest luminosities in the PSCz sample we will see progressively colder colours. Due to the imposed velocity cutoff at 60 000 km s^{-1}, together with the direct dependence of the derived 850 μm luminosity on the 100/60 colour, galaxies with 100/60 colours warmer than ~ 2 will simply fall out of our selection criteria at an 850 μm luminosity $\sim 10^{23}$ W Hz^{-1}sr^{-1}. This is best viewed graphically, as shown in Figure 5.10 — here the 100/60 colour is plotted against velocity for the PSCz sample selected according to the selection criteria described in Section 5.2.2, with different ranges of 850 μm luminosity indicated by different symbols. From the SLUGS Far-IR:submm colour-colour relation (see Section 5.2.2) the 100/60 colour is related to the 850 μm luminosity such that a given range of 850 μm luminosity will have an upper limit defined by the linear relation between 100/60 colour and velocity. The plotted line in Figure 5.10 indicates the upper limit to the range of colours and velocities for each luminosity range (due to the linear relation used to derive the 850 μm luminosity). In order

to investigate the effect of this on the LF in Figure 5.11 I plot the 100–60 μm colour versus the extrapolated 850 μm luminosity, plotted for different velocity ranges. The distributions of 100/60 colour for these velocity ranges are shown in Figure 5.12. At the lowest velocities the PSCz selection limit at 0.6 Jy combined with our lower velocity limit of 300 km s^{-1} can clearly be seen — towards the lower luminosities only the warm 100/60 colours do not fall below the selection criteria. At the highest velocities, where we can see the highest luminosities (the two lower panels in Figure 5.11), although there is a tendency towards colder colours towards the highest luminosities this effect is only slight, and in fact only really affects the highest luminosity bin in the LF. Overall (as shown in Figure 5.10), other than relatively slight selection effects, over the range of 850 μm luminosities in the sample there does not appear to be any tendency for galaxies at the highest luminosities have systematically different colours.

Finally, D00/LD00 found the 850 μm LF derived from the IRS sample to have a slope steeper than -2 at the low luminosity end, suggesting that the submillimetre sky should be infinitely bright (a submillimetre 'Olbers' Paradox'). Using the OS sample I find the slope of the PSCz-extrapolated 850 μm LF is -1.38, showing that the LF does flatten out at luminosities lower than those probed by the IRS sample, thus, as also found by SH05,solving the submillimetre 'Olbers' Paradox'.

5.4 Summary

In this Chapter I have used the OS sample results to produce new estimates of the local submillimetre luminosity and dust mass functions.

I have derived local submillimetre luminosity and dust mass functions, both directly from the optically-selected SLUGS sample and by extrapolation from the *IRAS* PSCz survey, and find excellent agreement between the two. By extrapolating the spectral energy distributions of the *IRAS* PSCz survey galaxies out to 850 μm we probe a wider

range of luminosities than probed directly by the SLUGS samples.

The LFs are well-fitted by Schechter functions except at the highest luminosities. Whereas the slope of the IRS sample LF (D00/LD00) at low luminosities was steeper than -2 (a submillimetre 'Olbers' Paradox'), I have shown that the PSCz-extrapolated LF, as expected, flattens out at the low luminosity end and has a slope of -1.38.

I have shown that as a consequence of the omission of a population of 'cold' dusty galaxies from the IRS sample the LF presented by D00/LD00 is too low by a factor of 2, and the DMF by a factor of 4.

Chapter 6

The Radio-Submillimetre Properties of Galaxies

6.1 Overview

In this Chapter I will investigate the relationships between the FIR–submillimetre and radio properties of the OS and IRS SLUGS samples, specifically the FIR–radio and submillimetre–radio luminosity correlations, and whether there are any differences in the relationships for the two samples. In particular I will investigate the implications of this for the radio–submillimetre redshift indicator technique of Carilli & Yun (1999, 2000a).

6.2 Background

6.2.1 The problem of determining redshifts for deep SCUBA sources

Significant numbers of faint sources have been found in the many deep SCUBA surveys that have been carried out (e.g. Smail, Ivison & Blain 1997; Hughes et al. 1998; Barger
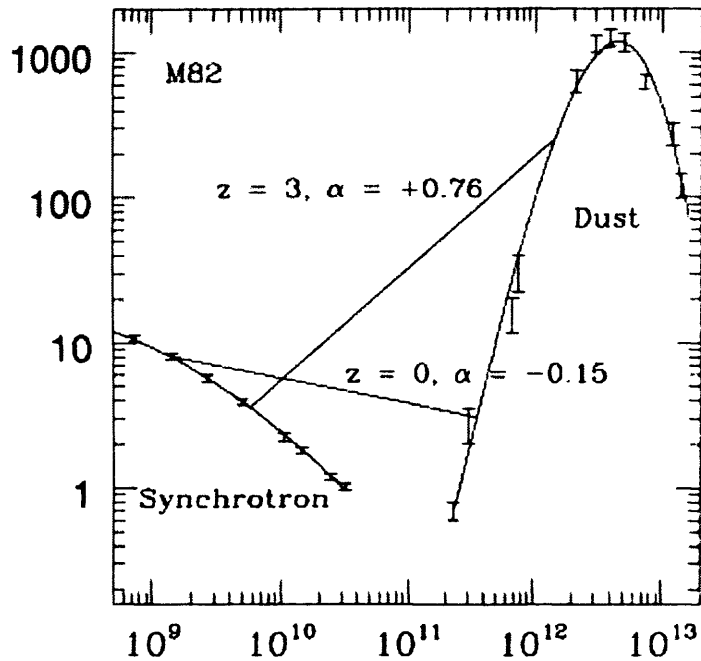
Figure 6.1:   The radio-IR spectral energy distribution of M82, part of a figure taken from Carilli & Yun (2000a). The curves show polynomial fits to the data points. The submillimetre part of the SED has a steep spectral slope, and a break occurs at around 3 mm where the thermal dust emission takes over from the declining synchrotron tail, effectively creating a redshift-sensitive ratio by placing the submillimetre on one side of the spectral break and the radio on the other. The two straight lines show the 1.4GHz-to-850 μm spectral index derived for z=0 and z=3, demonstrating how the ratio of submillimetre-to-radio flux (i.e. spectral index) increases with redshift.

et al. 1998, 1999; Blain et al. 1999a; Eales et al. 1999; Lilly et al. 1999; Mortier et al. 2005). This is important because since the discovery of ultraluminous infrared galaxies (ULIRGs) (Joseph & Wright 1985; Sanders et al. 1988), objects which can emit as much as 99% of their bolometric luminosity at far-IR wavelengths, and the discovery of the cosmic IR background (Puget et. al 1996; Fixsen et al. 1998; Hauser et al. 1998), it has been suggested that our optical view of the high-redshift universe might be obscured by large amounts of dust — deep submillimetre surveys were required to uncover these distant dusty sources.

However, in order to trace the star-formation history of the Universe these faint sources detected in the submillimetre then need to be identified and their redshifts determined. This is problematic, however, due to the large beamsize of SCUBA (~ 15 arcsec at 850 μm) and hence the positional uncertainty in SCUBA maps (Ivison et al. 1998, 2000; Downes et al. 1999; Barger, Cowie & Richards 2000; Eales et al. 2000). Even though the majority of deep submillimetre sources seem to have radio counterparts (Barger et al. 2000), and radio observations of the deep surveys can provide more accurate positions, determining their redshifts is still problematic since many are still too faint for spectroscopy or have no detectable optical/IR counterpart at all.

6.2.2 The radio–submillimetre redshift indicator

In the local Universe there is a known tight linear correlation between FIR luminosity and radio synchrotron (1.4 GHz) luminosity (Helou, Soifer & Rowan-Robinson 1985; Condon 1992; Helou & Bicay 1993) for star-forming galaxies. This relationship is believed to arise due to young high-mass stars both acting as a heating source for the dust, resulting in the FIR flux, and being responsible for the radio-synchrotron emission (by providing relativistic electrons when at the end of their life cycle they explode as supernovae). Also, the submillimetre part of the SED has a steep spectral slope, and at around 3 mm the thermal dust emission takes over from the declining radio synchrotron emission (see Figure 6.1, reproduced from CY00), causing a break in the spectral slope — this effectively creates a redshift-sensitive ratio by placing the submillimetre on one side of the spectral break and the radio on the other. This radio-submillimetre flux density ratio is related to the radio-submillimetre spectral index between 1.4 GHz and 850 μm, $\alpha_{1.4}^{850}$, by the equation

$$\alpha_{1.4}^{850} = 0.42 \times \log\left(\frac{S_{850}}{S_{1.4}}\right) \tag{6.1}$$

where S_{850} and $S_{1.4}$ are the fluxes at 850 μm and 1.4 GHz respectively (as defined in Carilli

& Yun (1999)). I note here that since $\alpha_{1.4}^{850}$ and the logarithm of the flux ratio $S_{850}/S_{1.4}$ are simply related by a scale factor either parameter can be used to investigate the redshift indicator, and while some authors refer to $\alpha_{1.4}^{850}$ (e.g. CY00) others (e.g Blain 1999) adopt the ratio $\log(S_{850}/S_{1.4})$.

Carilli & Yun (1999) suggested the redshift-sensitive nature of this ratio means it could potentially be used to address the problem of measuring the redshifts of faint submillimetre sources found in the deep surveys, and hence proposed a method of using $\alpha_{1.4}^{850}$ as a redshift estimator. However, this is based on the assumption that the FIR-radio luminosity relation is the same at low and high redshifts, i.e. that more distant galaxies have similar properties (e.g. magnetic field strength or dust grain properties) to those observed in the local universe. Other factors potentially affecting the reliability of this method include the slope assumed for the radio synchrotron emission (which typically has values of -0.7 to -0.8 for star-forming galaxies (Condon 1992)), and any dependence on galaxy properties such as dust temperature; Blain (1999) showed that the presence of cold dust ($T < 30$ K) can break down this predicted relationship between $\alpha_{1.4}^{850}$ and redshift. This is in addition to the presence of any AGN, which (due to any excess radio emission associated with the AGN) will also not follow the expected relationship.

In the standard explanation of the tight FIR–radio luminosity relation the 60 μm and radio luminosities are both related to star-forming regions, but there is in fact no real observational evidence for this scenario rather than some other underlying process — alternative explanations have been proposed. For example, Bettens et al. (1993) propose a 'chemical evolution' explanation. In their model the cosmic ray flux which, as in the standard explanation, produces the non-thermal radio emission, drives the chemical evolution of molecular clouds and determines the degree of ionisation as a function of time within the clouds; clouds with stronger cosmic ray fluxes undergo more ionisation, last longer before collapse and thus accrete more mass, ultimately producing larger fractions of OB stars and hence more FIR emission from dust; clouds which undergo less ionisation
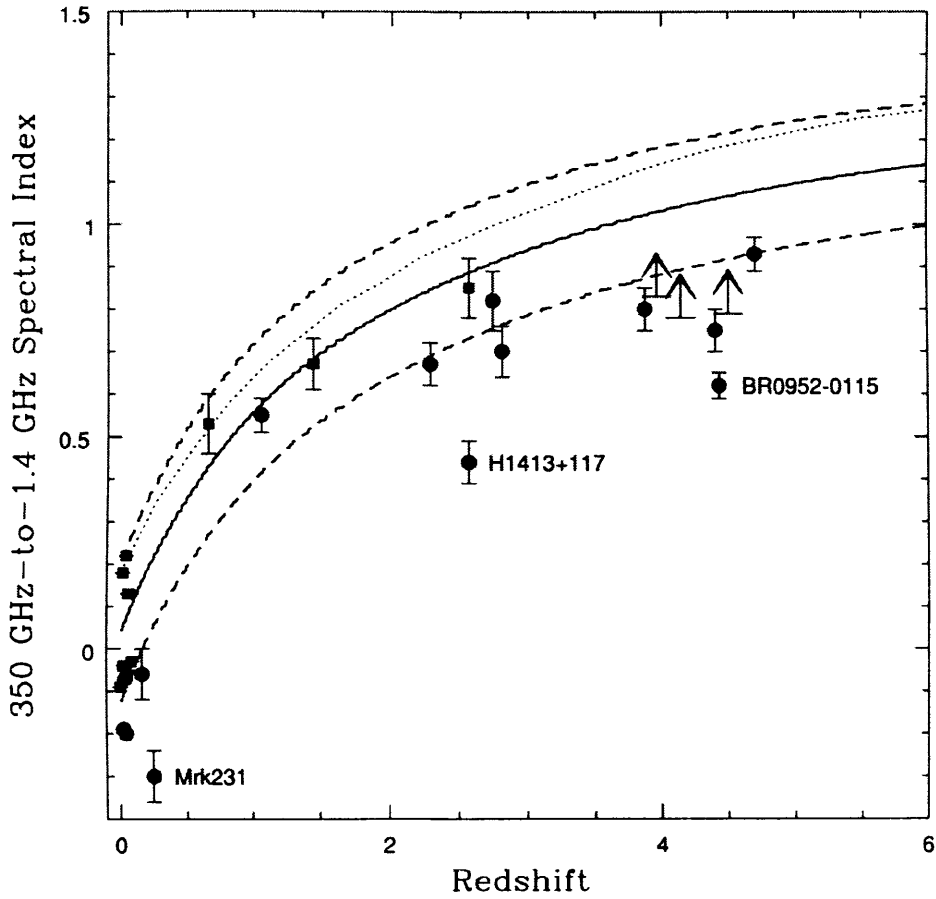
Figure 6.2: The relationship between the radio–submillimetre spectral index and redshift derived by Carilli & Yun (2000a), figure from Carilli & Yun (2000b; Erratum to 2000a). The solid line shows their mean relation and the dashed lines represent the $\pm 1\sigma$ curves. The filled circles represent sources with AGN-type spectra, while the filled squares are sources without AGN. The dotted line indicates the relationship found by Dunne, Clements & Eales (2000) for the IRS SLUGS galaxies.
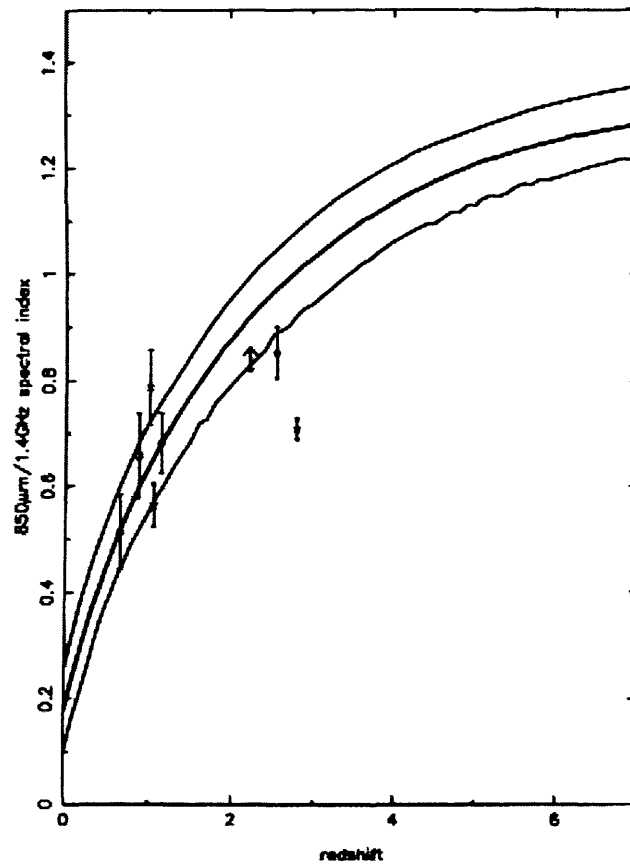
Figure 6.3:   The derived relationship between the radio–submillimetre spectral index and redshift for the IRS SLUGS galaxies, figure from Dunne, Clements & Eales (2000). The thick line shows the median estimator (this is also shown in the estimator plot from Carilli & Yun (2000b) shown in Figure 6.2) and the thin lines show the $\pm 1\sigma$ curves. The plotted points are sources from various deep surveys (Eales et al. 1999, 2000; Lilly et al. 1999; Ivison et al. 1998, 2000; Smail et al. 2000; Barger et al. 2000). The point lying below the curves is believed to be an AGN (Ivison et al. 1998).

are more likely to produce cooler, less massive, stars.

However, if the standard explanation is true then for galaxies contaning large proportions of cold dust we should expect to see a much weaker correlation of the radio with 850 μm luminosity than with 60 μm luminosity because of the additional contribution to the 850 μm luminosity from the cold dust components. Previous investigations of the submillimetre–radio relation, i.e. DCE00/LD00 for the IRS SLUGS sample, have been based on samples of mainly warm-dust-dominated galaxies and thus, since it is the same warm dust component which is responsible for the emission at 60- and 850-μm, the submillimetre-radio relation cannot provide any more information than found from the 60 μm–radio relation. The OS SLUGS sample, on the other hand, which, as has been shown in the previous chapters, contains large fractions of cold dust (up to three orders of magnitude more cold dust than warm dust), will therefore provide the first direct evidence of whether the standard explanation is correct.

Previous investigations of the redshift indicator using bright *IRAS* galaxies

CY00 predicted the evolution of $\alpha_{1.4}^{850}$ with redshift for 17 low-redshift star-forming galaxies by making polynomial fits to the observed FIR-radio SEDs of these galaxies. These results are shown in Figure 6.2 (figure from Carilli & Yun (2000b)); here the solid line shows their mean relation and the dashed lines represent the $\pm 1\sigma$ curves. There are two interesting points to note about the results from CY00. Firstly, the filled circles in Figure 6.2 represent sources with AGN-type optical spectra, while the filled squares are sources without AGN, suggesting that the position of a source on the plot (if its redshift is known) could potentially be used to distinguish sources with radio-loud AGN (as was suggested by Condon et al. 1992). Secondly, as discussed by Blain (1999), if dust temperature has a significant effect on the relationship between $\alpha_{1.4}^{850}$ and redshift it will have an important effect on the scatter of the relationship, such that there may be a degeneracy between hot

dusty high-redshift sources and cold dusty low-redshift sources. CY00 showed that when they took into account the dust temperature in their plot (Figure 6.2) they *did* indeed find a decreased scatter, indicating that the dust temperature of galaxies used to derive the redshift indicator may be an important factor to take into account.

Dunne, Clements & Eales (2000; hereafter DCE00; also LD00) used the IRS SLUGS sample galaxies to investigate whether there is any correlation of $\alpha_{1.4}^{850}$ with dust temperature or $850\,\mu m$ luminosity. If this were the case the CY00 results would be biased towards higher redshift estimates. DCE00 concluded that there are no significant correlations. They also derived a redshift indicator using the observed SEDs of the IRS SLUGS galaxies, and this plot from DCE00 is shown in Figure 6.3 (CY00 also plot this IRS SLUGS relationship in their figure (the dotted line in Figure 6.2)). However, DCE00 find that the IRS sample predicts systematically higher values of S_{850}/S_{radio} at a given redshift, implying that redshifts estimated using the CY00 results might be overestimates.

The need for a sample of 'cold' dusty galaxies

As described above, D00/LD00 used the IRS SLUGS sample to investigate this potential bias in the results presented by CY00. However, the IRS sample is, by definition, biased towards warm dust, and as discussed in the previous chapters the results from the OS sample have shown that the IRS sample missed a population of galaxies which contain large proportions of cold dust. The CY00 galaxies are also *IRAS*-selected, but perhaps more importantly the CY00 sample was small and selected ad-hoc, and was also found to be based on underestimated submillimetre measurements (DCE00). Thus the new results from the OS sample may represent an important population of 'cold' dusty galaxies previously unrepresented in the radio–submillimetre redshift estimator models. This is important because deep SCUBA surveys will be biased towards bright $850\,\mu m$ sources and are sensitive to the mass of dust rather than dust temperature; at high redshifts there

may be some bias towards warmer dust, but at intermediate redshifts ($z \lesssim 2$) it is possible there are SCUBA sources containing significant fractions of cold dust. Thus the results of the OS sample, which does represent a population of cold dusty galaxies seen in the local universe, allows comparison of the differences between FIR–submillimetre and radio properties in 'warm' bright *IRAS* galaxies and those in 'cold' local galaxies, and as such provides a new, less biased, basis for assessing the reliability of the Carilli & Yun (1999, 2000a) radio–submillimetre redshift estimator.

6.3 The far-IR and submillimetre versus radio properties of 'normal' galaxies

The radio parameters for the OS sample are given in Table 6.1. Radio (1.4 GHz) fluxes were taken from the literature, mostly from the NRAO/VLA Sky Survey (NVSS; Condon et al. 1998) or from the VLA FIRST (Faint Images of the Radio Sky at Twenty Centimeters) survey (Becker, White & Helfand 1995). For objects without literature radio fluxes the NVSS radio images were used to either measure the flux of a faint source or, where no source was seen, to measure an upper limit. The 1.4 GHz luminosities were calculated using the standard equation. Measured radio spectral indices were used where available and otherwise a value of -0.7 was assumed (Condon 1992). Parameters for the correlations between radio and FIR–submillimetre properties investigated in the following sections are given in Tables 6.2 and 6.3.

6.3.1 The FIR–radio and submm–radio luminosity correlations

The relationship between 1.4 GHz luminosity and 60 μm or FIR luminosity is shown in Figure 6.4. The filled points indicate OS objects detected at 850 μm while for comparison the open points represent the OS non-detections at 850 μm. Also for comparison the IRS

Table 6.1: Literature 1.4 GHz Radio fluxes.

(1) Name	(2) $S_{1.4}$ (mJy)	(3) $\log L_{1.4}$ $(\mathrm{W\,Hz^{-1}sr^{-1}})$	(4) $\alpha_{1.4}^{850}$
UGC 148	17.8	20.71	0.21
NGC 99	8.2	20.58	0.37
PGC 3563	4.1	20.31	0.34
NGC 786	6.1	20.31	0.43
NGC 803	<1.5	<19.02	>0.75
UGC 5129	1.8	19.68	<0.54
NGC 2954	<0.84	<19.30	...
UGC 5342	3.8	20.11	0.39
PGC 29536	1.0	20.15	<0.68
NGC 3209	1.11	19.84	<0.54
NGC 3270	6.2	20.60	0.41
NGC 3323	13.4	20.76	0.30
NGC 3689	27.1	20.52	0.24
UGC 6496	1.5	19.98	0.47
PGC 35952	3.8	19.99	0.47
NGC 3799/3800	49.3	20.94	0.18
NGC 3812	1.96	19.62	<0.54
NGC 3815	3.2	19.85	0.47
NGC 3920	7.6	20.21	0.27
NGC 3987	56.3	21.27	0.22
NGC 3997	5.2	20.28	<0.27
NGC 4005	2.4	19.89	<0.33
NGC 4015	<1.5	<19.66	...
UGC 7115	87.3	21.82	−0.10
UGC 7157	<1.4	<19.92	...
IC 797	11.5	19.91	0.36
IC 800	1.4	19.09	0.73
NGC 4712	<1.2	<19.57	>0.81
PGC 47122	<1.8	<20.17	...
MRK 1365	23.0	21.06	0.06
UGC 8872	<1.1	<19.74	...
UGC 8883	3.0	20.18	<0.47
UGC 8902	12.4	21.08	0.31
IC 979	<1.5	<20.17	>0.66
UGC 9110	7.3	20.41	<0.34
NGC 5522	17.6	20.78	0.26

Continued on Next Page...

Table 6.1: – *continued*

(1) Name	(2) $S_{1.4}$ (mJy)	(3) $\log L_{1.4}$ (W Hz^{-1}sr^{-1})	(4) $\alpha_{1.4}^{850}$
NGC 5953/4	91.4	20.76	0.20
NGC 5980	25.3	20.84	0.42
IC 1174	<1.5	<19.73	>0.51
UGC 10200	11.2	19.85	<0.11
UGC 10205	2.9	20.31	0.55
NGC 6090	48.0	21.79	0.12
NGC 6103	5.9	20.94	0.40
NGC 6104	6.4	20.87	<0.30
IC 1211	<1.3	<19.83	>0.56
UGC 10325	11.2	20.77	0.24
NGC 6127	<1.2	<19.66	>0.78
NGC 6120	33.7	21.67	0.12
NGC 6126	<1.5	<20.37	>0.50
NGC 6131	6.5	20.44	0.39
NGC 6137	438.7	22.80	−0.50
NGC 6146	162.7	22.32	−0.32
NGC 6154	1.2	19.85	<0.64
NGC 6155	13.9	20.12	0.08
UGC 10407	18.4	21.33	0.06
NGC 6166	3713.0	23.70	−0.72
NGC 6173	6.9	20.94	<0.23
NGC 6189	7.9	20.61	0.40
NGC 6190	4.8	19.94	0.55
NGC 6185	62.1	22.04	< −0.13
UGC 10486	<1.5	<19.96	...
NGC 6196	1.0	20.17	<0.57
UGC 10500	<1.4	<19.79	...
IC 5090	32.6	21.67	0.23
IC 1368	23.7	20.80	0.12
NGC 7047	3.9	20.31	0.48
NGC 7081	18.2	20.50	0.16
NGC 7280	<1.2	<18.82	...
NGC 7442	7.8	20.83	0.32
NGC 7448	81.5	20.80	0.16
NGC 7461	<1.4	<19.62	...
NGC 7463	16.3	20.16	

Continued on Next Page...

Table 6.1: – *continued*

(1)	(2)	(3)	(4)
Name	$S_{1.4}$ (mJy)	$\log L_{1.4}$ (W Hz^{-1}sr^{-1})	$\alpha^{850}_{1.4}$
III ZW 093	5.3	21.30	<0.29
III ZW 095	1.5	20.14	<0.46
UGC 12519	4.6	20.16	0.51
NGC 7653	92.2	21.43	0.04
NGC 7691	4.5	20.08	<0.31
NGC 7711	<1.2	<19.51	...
NGC 7722	4.7	20.09	0.47

(1) Galaxy name; (2) 1.4 GHz radio flux taken from the literature; NVSS (most) or FIRST; (3) 1.4 GHz luminosity; (4) radio-submm spectral index, calculated using Equation 6.1. Upper limits on $\alpha^{850}_{1.4}$ correspond to upper limits at 850 μm.

galaxies are plotted as cross symbols. For the OS sample there is a very tight correlation between 1.4 GHz luminosity and 60 μm and FIR luminosity ($r_s = 0.97$, probability=9.13e-24, for L_{60}; see Table 6.2). Fitted linear (least-squares) relations for each of the OS and IRS samples are shown in Table 6.2. Interestingly, there are 7 extreme outliers in the upper part of the plot, which are galaxies which have excess 1.4 GHz emission relative to this correlation. These are mainly elliptical galaxies (they are NGC 6166, NGC 6137, NGC 6146, UGC 7115 and NGC 6173), although there are also two early-type spirals (NGC 6185 and NGC 7653). As discussed in Section 6.2.2, the 'excess' 1.4 GHz emission may indicate the presence of an AGN in these galaxies. There are also two objects in the OS sample (NGC 803 and NGC 4712) and one in the IRS sample (NGC 4418) which appear to be underluminous in the radio. There is no obvious explanation for these objects, which are all early-type spirals. However, as I showed in Chapter 3 NGC 803 has a large proportion of cold dust, and for NGC 4418 (which is also in the sample of Lisenfeld, Isaak & Hills

(2000) used by Carilli & Yun for their redshift indicator) Lisenfeld et al. conclude that this galaxy's anomalous spectrum is most likely due to the presence of multi-temperature dust components and/or high dust opacity. Though one could argue many possibilities, one possible explanation would be the presence of very small grains stochastically heated by single photons to very high temperatures (Li 2004a; Li 2004b) and thus contributing strongly to wavelengths $\lesssim 60\,\mu$m. The OS galaxies appear to follow an even tighter 60 μm–radio relation than the IRS galaxies. The reason for this is not clear, but it could be related to the fact that the bright *IRAS* galaxies tend to be mergers or more active systems, which would also explain why the scatter in the IRS sample appears to be less at the lower luminosities. Other possible explanations range from free-free emission at radio wavelengths to dust opacity at FIR–submillimetre wavelengths; I will mention some of the outliers individually later in this section.

The relationship between 1.4 GHz luminosity and 850 μm luminosity is shown in Figure 6.5. For the OS sample there is a correlation ($r_s = 0.73$, probability=3.41e-8), but there is clearly a much tighter correlation between radio and 60 μm luminosity than between radio and 850 μm luminosity (the rms scatter is 0.13 for 60 μm–radio and 0.40 for 850 μm–radio). In the standard explanation of the tight 60μm–radio luminosity relation the 60 μm and radio luminosities are both related to star-forming regions, but there is in fact no real observational evidence for this scenario rather than some other underlying process — alternative explanations have been proposed (e.g. Bettens et al. 1993). However, if the standard explanation is true then for the OS sample we should expect to see a much weaker correlation of the radio with 850 μm luminosity because of the additional contribution to the 850 μm luminosity from the cold dust components; as has been shown in the previous chapters the OS galaxies contain large proportions of cold dust, with up to three orders of magnitude more cold dust than warm dust. The fact that a much larger scatter at 850 μm is precisely what we see in Figure 6.5 thus provides evidence that the standard explanation for the FIR–radio luminosity correlation is correct and that it is the
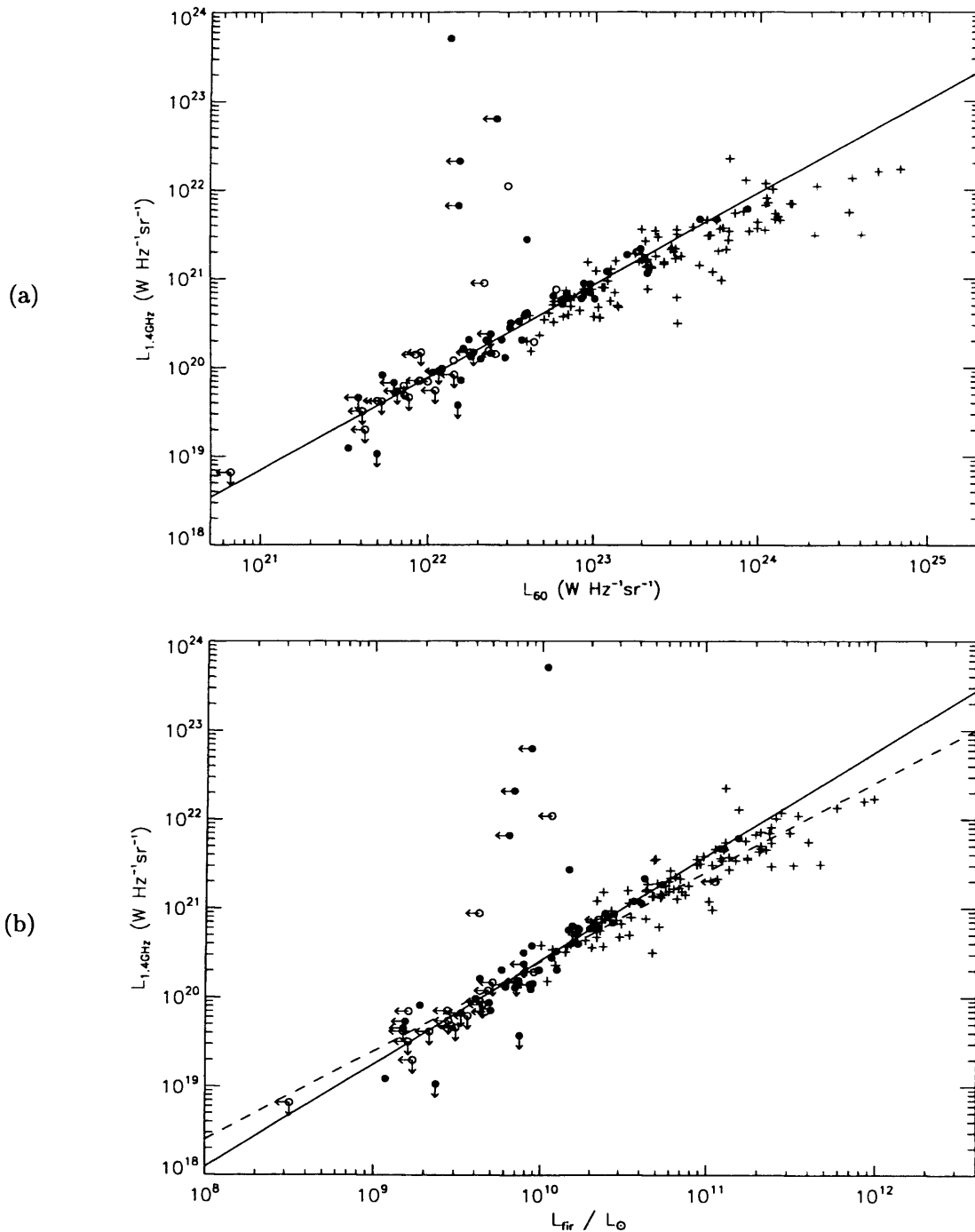
Figure 6.4:   1.4 GHz luminosity versus (a) $60\,\mu$m luminosity and (b) FIR luminosity for the OS and IRS samples (circles and crosses respectively; for the OS galaxies filled circles indicate those detected at $850\,\mu$m while open circles indicate the non-detections at $850\,\mu$m). The solid lines show the linear fits to the OS data. In (a) the slope is unity and in (b) it is slightly greater than unity; the dashed line indicates a slope of unity for comparison. The 7 OS outliers which have excess 1.4 GHz emission relative to this correlation are mainly ellipticals (NGC6166, NGC6137, NGC6146, UGC7115 and NGC6173; the other two outliers are NGC6185 and NGC7653).
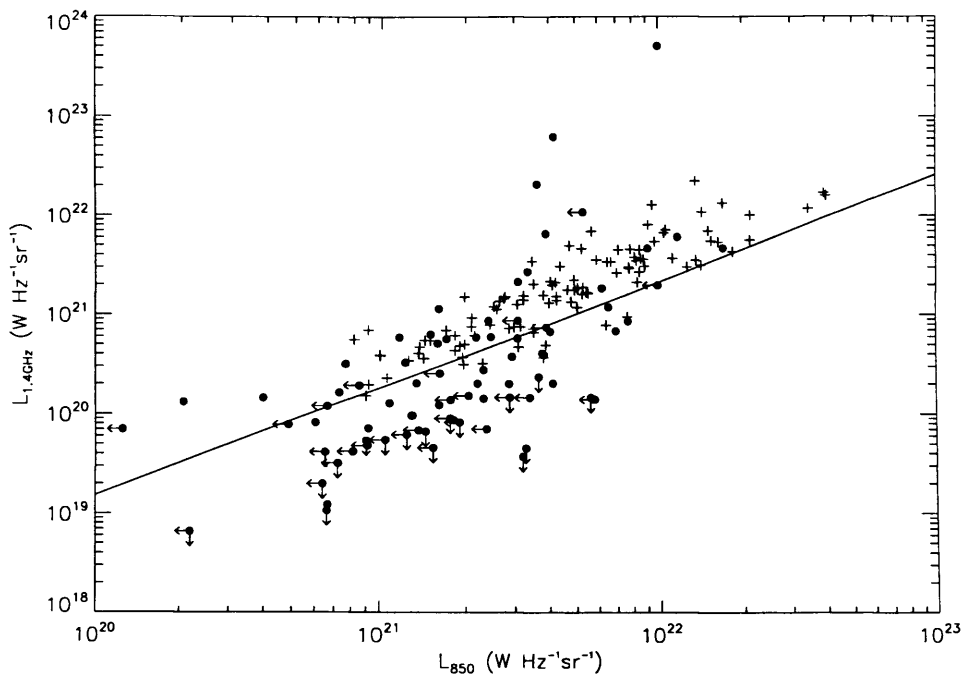
Figure 6.5: 1.4 GHz luminosity versus 850 μm luminosity for the OS and IRS samples (filled circles and crosses respectively).The solid line shows the linear fit to the OS data, which has slope unity (slope=1.08±0.16). There is a correlation between radio and 850 μm luminosity for the OS sample ($r_s = 0.71$, probability $= 3.89$e-13) but there is much more scatter than for the relation with 60 μm luminosity. This difference suggests that, while the 60 μm and radio luminosities are both related to star-forming regions, a significant amount of the 850 μm emission is due to colder (20 K) dust heated by the general interstellar radiation field.

population of young (OB) stars which both heats the dust and provides the source of radio emission. Comparing the OS sample to the IRS sample there are a number of interesting points to note. i) Both the OS and IRS samples follow a slope of about unity (slope $= 1.08$ for the OS sample, shown as a solid line in Figure 6.5). ii) For the OS sample the scatter is very much greater than seen for the 60μm–radio relation, but for the IRS sample there is a similar amount of scatter for both 60 μm and 850 μm luminosity with the radio (~ 0.2). iii) There is a much larger scatter for the OS sample than the IRS sample (0.22 for the

Table 6.2:   Correlation parameters for the radio versus FIR and submillimetre luminosity for the OS and IRS samples.

y	x	r_s	significance	linear fit (y=mx+c)	
				m	c
			OS sample		
$L_{1.4}$	L_{60}	0.97	9.13e-24	1.04±0.04	−3.04±0.96
$L_{1.4}$	L_{fir}	0.96	2.13e-21	1.16±0.05	8.79±0.52
$L_{1.4}$	L_{850}	0.73	3.41e-8	1.08±0.16	−2.34±3.47
			IRS sample		
$L_{1.4}$	L_{60}	0.88	4.99e-35	0.81±0.04	2.36±1.05
$L_{1.4}$	L_{fir}	0.91	3.03e-41	0.94±0.04	11.11±0.47
$L_{1.4}$	L_{850}	0.90	3.88e-38	1.12±0.06	−2.97±1.26

Column 3: r_s is the Spearman rank correlation coefficient; Column 4: probability that x and y are unrelated; Columns 5 and 6: linear (least-squares) fit parameters. Note:- the outlying objects which, due to their extreme radio luminosities, are likely to be AGN-type objects are not included in these correlations.

IRS sample and 0.40 for the OS sample). However, this increased scatter is confined to the left half of the diagram, at radio luminosities lower than found for the IRS relation. The scatter is due to about a dozen objects, in addition to the upper limits, and the remainder of the OS sample agree well with the IRS sample. iv) At $L_{850} \gtrsim 6 \times 10^{21}$ W Hz^{-1}sr^{-1} there are no longer any OS galaxies with radio luminosities lower than expected from the IRS relationship.

I will now attempt to address some of these issues. The fact that there is a similar

amount of scatter in the relationships of both the 60 μm and submillimetre with the radio for *IRAS*-selected galaxies while for optically-selected galaxies the radio is much more tightly correlated with 60 μm is further evidence that the standard explanation for the 60 μm–radio correlation is correct. There is already considerable evidence, shown in the previous chapters, that the OS sample contains much larger proportions of cold (20 K) dust than the mainly warm-dust-dominated IRS sample. It then follows that if the source of the FIR–radio relation is the OB stars responsible for heating the warm dust, then the warm dust (and hence the IRS sample) should follow the correlation while any cold dust components, heated by the general interstellar radiation field (ISRF), will not. This has important implications for the reliability of $\alpha_{1.4}^{850}$ as a redshift indicator, which I will investigate in Section 6.4. In fact the 'warm' OS galaxies do follow the same 850 μm–radio relationship as the IRS galaxies, and with a similar amount of scatter. It is not unexpected that the two samples should contain at least some objects which have similar dust properties. However, the most likely explanation for the OS objects which lie below the IRS relationship is simply the presence of dust at more than one temperature. If the warm dust in the OS galaxies which have large cold components correlates as expected with the radio, then the much larger contribution from the cold dust (remembering that the ratio of cold-to-warm dust was found in Chapter 3 to be as much as ~ 1000) would push the 850 μm luminosity to significantly higher values and hence away from the relation (Devereux & Eales 1989). This would explain the agreement of the OS and IRS samples at the higher luminosities, the absence of any OS galaxies at the low luminosity end of the relation, and the clustering of the radio and 850 μm upper limits at the bottom of the diagram.

Although the increased scatter in the 850 μm–radio relationship is in good qualitative agreement with the standard explanation of the FIR–radio correlation, quantitatively it is not in good agreement. In order for the warm dust in the 'cold' OS galaxies to follow the submm–radio relation indicated by the IRS galaxies the contribution to the

850 μm luminosity from the warm dust is estimated, from Figure 6.5, to be typically ∼ one third of that from the cold dust (and at least ∼ one tenth). This is interesting because we know from the results in Chapter 3 that the ratio of the mass of cold-to-warm dust is at least two orders of magnitude larger than this (on average ∼ 500 and with values ranging up to ∼ 1000), and since in the submillimetre mass only goes as T^{-1} this difference must be due to the physical properties of the dust grains in those components. Possible explanations could include differences in the composition, emissivity or magnetic field strength for the two components (particularly if the warm and cold dust components are not spatially co-extensive in the galaxy), and hence also differences in the value of the dust mass opacity coefficient (the value of which must be assumed in order to calculate the dust mass (see Chapter 3)); of course there are also many other possibilities, and in reality it is likely that it is a combination of many factors which makes up the differences we observe between the cold and warm dust components.

While the above explanations of the observed data are plausible I have also noticed additional factors which seem likely to complicate the explanation further. On close inspection of the OS objects in Figure 6.5 I have found that the 'outlying' low-radio-luminosity 'cold' objects are either the objects that have very large ratios of cold-to-warm dust from the two-component fits or objects whose isothermal fits yielded extremely low values of β emissivity index (< 1) and hence indicating they likely also have a large cold component. While this would provide a nice explanation for the deviation from the IRS submm–radio relation the true explanation cannot be that straightforward — there are objects (e.g. NGC 3987 and IC 5090) which have large ratios of cold-to-warm dust (∼ 300) but agree well with the IRS objects even though they are at different ends of the range of 850 μm luminosity. There are also objects, with apparently similar cold dust properties (UGC 12519 and NGC 6155) in that both the two fitted dust components are relatively cold, and yet while the former lies well below the IRS relation the latter agrees well. Thus, the position of an OS galaxy in Figure 6.5 does not appear to have any *straightforward*
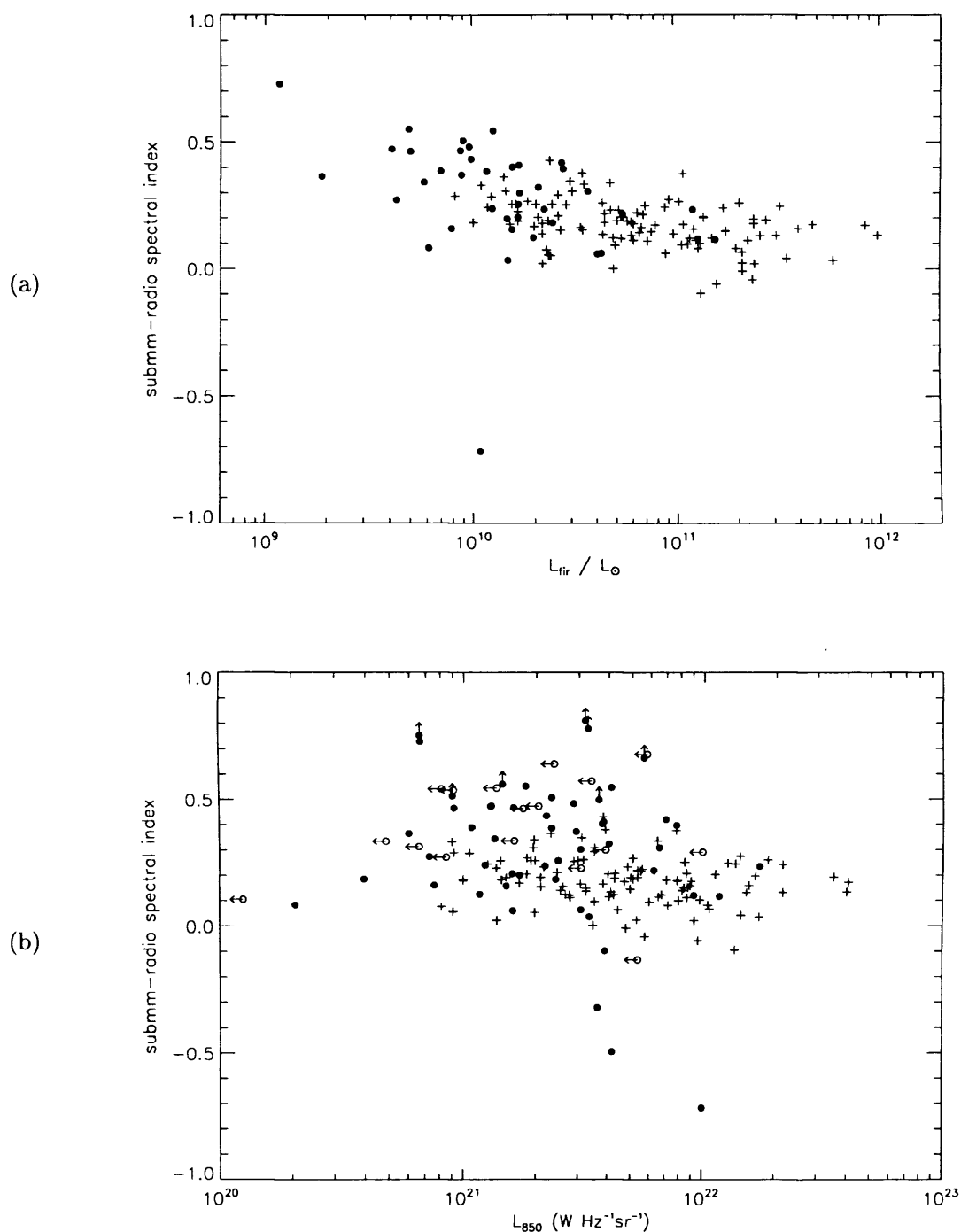
Figure 6.6: $\alpha_{1.4}^{850}$ versus (a) FIR luminosity and (b) 850 μm luminosity, for the OS and IRS samples. Filled points indicated objects detected at 850 μm while open points represent the non-detections at 850 μm. The IRS galaxies are plotted as cross symbols.
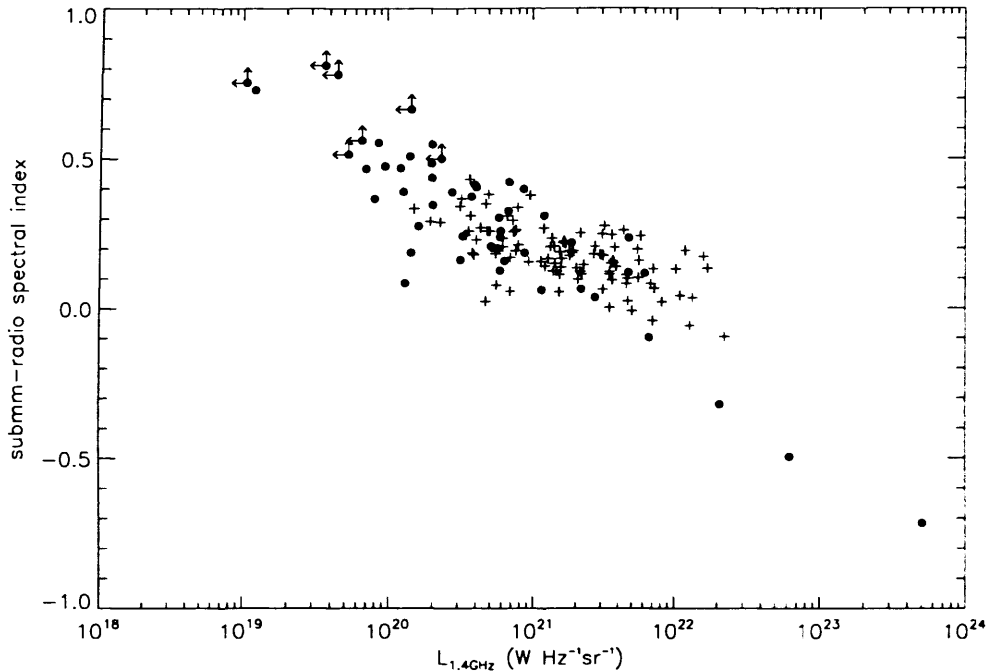
Figure 6.7: $\alpha_{1.4}^{850}$ versus 1.4GHz luminosity for the OS and IRS samples (filled circles and crosses respectively).

dependence on the relative amount of cold dust, nor on Hubble type.

6.3.2   Correlations with radio-submillimetre spectral index

In order to investigate the reliability of $\alpha_{1.4}^{850}$ as a redshift estimator in this section I investigate the possible variation of $\alpha_{1.4}^{850}$ (i.e. the ratio $S_{850}/S_{1.4}$) with FIR, 1.4 GHz and 850 μm luminosity, as well as dust temperature, comparing the results for the OS and IRS galaxies. These plots are shown in Figures 6.6 and 6.7.

There is a correlation of $\alpha_{1.4}^{850}$ with L_{fir} for the OS sample (Figure 6.6(a)), and although for the OS it is not as strong a correlation as found for the IRS sample (Figure 6.6(b)) this likely due to the smaller number statistics and the outlier NGC6166 (with

very low $\alpha_{1.4}^{850}$) which is likely harbours an AGN (as discussed in Chapter 3 this elliptical/3C object is well-documented in the literature to have both associated dust arms and a radio source with a parsec-scale two-sided jet). There is no dependence of $\alpha_{1.4}^{850}$ on L_{850} for either sample (Figures 6.6(b) and 6.6(b)), but there is a strong correlation of $\alpha_{1.4}^{850}$ with $L_{1.4}$ (Figure 6.7).

As discussed by DCE00 for the IRS sample, the fact that we see correlations between $\alpha_{1.4}^{850}$ and both L_{fir} and $L_{1.4}$ but not L_{850} most likely indicates that, while L_{fir} and $L_{1.4}$ are both related to star-forming regions, significant proportions of the 850 μm emission must be due to colder dust heated by the ISRF. Importantly, the fact that there is no correlation between $\alpha_{1.4}^{850}$ and L_{850} for either the OS or IRS sample, together with the fact that as shown in Chapter 4 there is no significant difference between the 850 μm luminosities in the two samples (despite any other differences in properties), is evidence that $\alpha_{1.4}^{850}$ may be a reliable redshift estimator and that the Carilli-Yun technique calibrated using the SLUGS galaxies would not lead to biased redshift estimates.

Is there a relationship between $\alpha_{1.4}^{850}$ and dust temperature?

Another possible cause for bias in using $\alpha_{1.4}^{850}$ as a redshift estimator is if $\alpha_{1.4}^{850}$ varies with dust temperature, as has been suggested by Blain (1999). Furthermore, unlike the 850 μm luminosity which has a similar distribution for both the OS and IRS samples there are marked differences between the fitted dust temperatures for the two samples (see Chapter 4), suggesting that any relationship between $\alpha_{1.4}^{850}$ and dust temperature may be different for the two samples.

The possible dependence of $\alpha_{1.4}^{850}$ on fitted (isothermal; see Chapter 3) dust temperature is investigated in Figure 6.8. For the OS alone there is no correlation found, although there is a very weak correlation found for the IRS sample. However, for the two SLUGS samples together there *does* seem to be some correlation between $\alpha_{1.4}^{850}$ and

Table 6.3: Correlation parameters for $\alpha_{1.4}^{850}$.

y	x	r_s	significance	notes
			OS sample	
$\alpha_{1.4}^{850}$	L_{fir}	-0.49	1.50e-3	
$\alpha_{1.4}^{850}$	$L_{1.4}$	-0.74	6.71e-9	
$\alpha_{1.4}^{850}$	L_{850}	-0.18	0.232	
$\alpha_{1.4}^{850}$	T_d	-0.28	0.071	not including NGC6166
			IRS sample	
$\alpha_{1.4}^{850}$	T_d	-0.23	0.020	
			OS+IRS sample *combined*	
$\alpha_{1.4}^{850}$	T_d	-0.34	2.86e-5	not including NGC6166

Column 3: r_s is the Spearman rank correlation coefficient; Column 4: probability that x and y are unrelated. Note:- the outlying objects which, due to their extreme radio luminosities, are likely to be AGN-type objects are not included in these correlations.
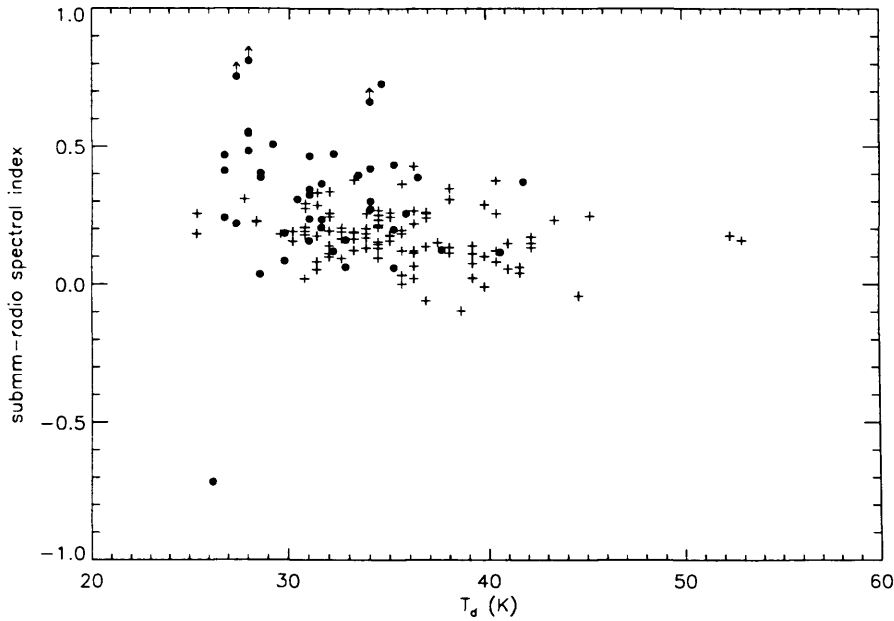
Figure 6.8: $\alpha_{1.4}^{850}$ versus isothermal fitted dust temperature for the OS and IRS samples (filled circles and crosses respectively).

fitted dust temperature ($r_s = -0.29$, probability $= 4.26e-4$), with $\alpha_{1.4}^{850}$ tending to increase with decreasing dust temperature. The correlation parameters found for the OS, IRS and combined OS+IRS samples are listed in Table 6.3. This trend seen for the combined OS+IRS SLUGS sample is once again indicative of the presence of large proportions of cold dust in the OS galaxies — although the range of $\alpha_{1.4}^{850}$ occupied by both the OS and IRS galaxies is similar at the higher dust temperatures, at the lower dust temperatures the OS galaxies tend to have higher $\alpha_{1.4}^{850}$. Importantly, the scatter in the combined SLUGS sample is roughly the same at the lower and higher temperatures. This result must be considered with some caution, since these isothermal dust temperatures are not the actual temperatures of the dust — as described in Chapter 3 we have found the SLUGS galaxies to be well-described by a two-component dust model, with the OS galaxies having large proportions of dust in their cold (~ 20 K) component. However, such isothermal tempera-

tures are nonetheless good indicators of both the differences between the two samples and (since the OS sample also tend to have a much flatter emissivity index (β) than the IRS galaxies, see Chapter 3) of the temperature of the largest proportion of dust.

6.4   The radio-submillimetre redshift indicator for 'normal' galaxies

I have described in the sections above how previous work on constraining the radio-submillimetre redshift indicator using observed galaxy spectral energy distributions (SEDs) (e.g. CY00 and DCE00) has used samples of galaxies which contain only *IRAS*-bright objects with relatively high FIR luminosities. In this current work we have found the OS SLUGS sample to contain a population of cold dusty galaxies (dust temperature ~ 20 K) which is missed by *IRAS* (see Chapters 4 and 5), and thus these 'cold' galaxies have so far been unrepresented in any analysis of the effectiveness of this method as a redshift indicator. As discussed in the previous sections, since SCUBA surveys will be biased towards high $850\,\mu$m luminosities and are sensitive to the mass as opposed to the temperature of the dust, any deep SCUBA sources at intermediate redshifts ($z \lesssim 2$) could potentially contain significant proportions of cold dust.

In this section we use the OS SLUGS galaxies to make a new analysis of the $\alpha_{1.4}^{850}$–redshift relation, in a similar way to that carried out by DCE00 for the IRS sample. We use the fitted SEDs for the 17 OS galaxies detected at both $850\,\mu$m and $450\,\mu$m (fitted using a two-component model to the $60\,\mu$m, $100\,\mu$m, $450\,\mu$m and $850\,\mu$m data points as described in Chapter 3; fitted parameters listed in Table 3.3 in Chapter 3). The 1.4 GHz fluxes used are listed in Table 6.1.

In Figure 6.9 the change in $\alpha_{1.4}^{850}$ with redshift is plotted for each of the OS galaxy SEDs, shown as the dashed lines. The thick solid line shows the median estimators pre-
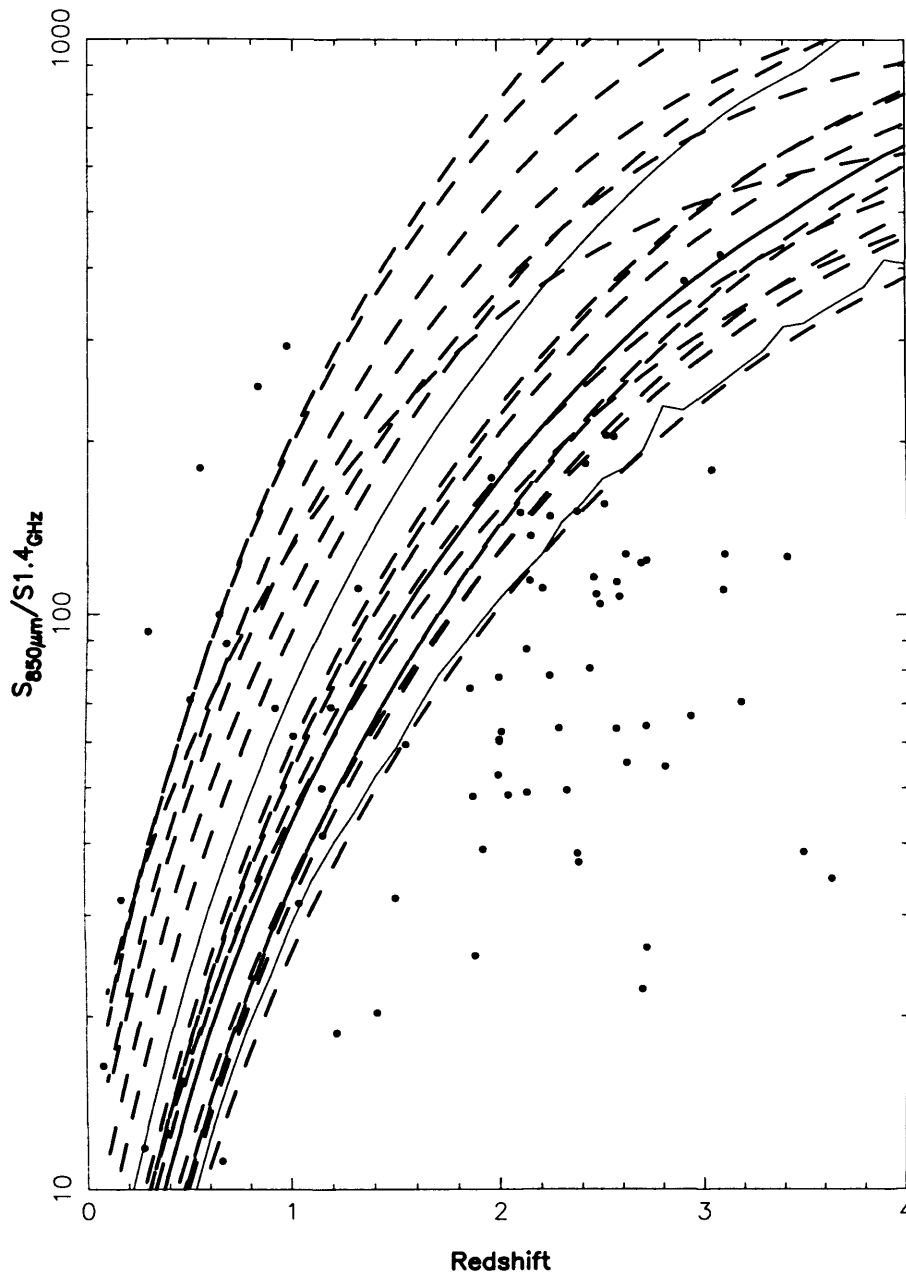
Figure 6.9: The $\alpha^{850}_{1.4}$-z relationship for the 17 OS SLUGS galaxies detected at both 850- and 450-μm, shown as the dashed lines. The thick solid line shows the median estimators predicted for the IRS sample from DCE00, with the thin solid lines showing their $\pm 1\sigma$ predictions. The plotted points in the diagram show all the deep SCUBA sources with both spectroscopic redshifts and radio measurements from Chapman et al. (2005). The fact that the OS galaxies tend to have higher values of $\alpha^{850}_{1.4}$ than the IRS galaxies can clearly be seen, with almost half the OS curves having higher $\alpha^{850}_{1.4}$ at a given redshift than the 1σ uncertainty of the median IRS sample estimator.

dicted for the IRS sample from DCE00, with the thin solid lines showing their $\pm 1\sigma$ predictions. The plotted points in the diagram show all the deep SCUBA sources with both spectroscopic redshifts and radio measurements from Chapman et al. (2005).

It is immediately evident that many of the OS galaxies follow a very different $\alpha_{1.4}^{850}$–redshift relationship to the IRS galaxies, with almost half of the OS galaxies lying outside the 1σ uncertainties of the median IRS sample estimator and having higher $\alpha_{1.4}^{850}$ at a given redshift. This result seems to agree well with the finding in the previous section that the OS sample galaxies can have values of $\alpha_{1.4}^{850}$ higher than any in the IRS sample though they cover a similar range of lower $\alpha_{1.4}^{850}$. The three uppermost curves in Figure 6.9 correspond to the objects UGC12519, PGC35952 and NGC7722, the former as discussed previously has two 'cold' components and the latter two have ratios of cold-to-warm dust in excess of 1000. A particular galaxy that should be mentioned is NGC6190 which can be seen quite clearly to follow a much flatter curve in the $\alpha_{1.4}^{850}$–redshift diagram. This object has the highest ratio of cold-to-warm dust (~ 3000) and consequently the spectrum peaks at $\sim 200\,\mu$m. This is significant because it means that after $z \approx 3$ the $\alpha_{1.4}^{850}$–z relation for this object will not be valid as the SED will turn over.

As DCE00 found for the IRS sample compared to the CY00 sample, we find for the OS sample the shape of the estimator curves are different to either of those samples because of the different shapes of the SEDs in the OS sample — many of these galaxies have extremely prominent cold dust components, where the ratio of cold-to-warm dust can be as much as ~ 1000. It is interesting to note, however, that although there is a much larger scatter in the $\alpha_{1.4}^{850}$–redshift relationship for the OS sample virtually none of the OS galaxies falls below the -1σ IRS sample estimator. This probably reflects the fact that some of the OS galaxies have similar properties to those in the IRS sample, with relatively small cold dust components in their SED, while others have very much larger proportions of cold dust and consequently occupy a different region of the $\alpha_{1.4}^{850}$–z diagram. Ultimately this has the effect that, in the absence of an independent measurement of redshift, a given

source could be either IRS-like and at higher redshift or OS-like and at lower redshift.

In other words, the uncertainty in this redshift estimator method at a given redshift, which can be estimated from the spread in the 17 curves, is also much higher for the OS sample — ultimately this has the effect that, in the absence of an alternative measure of redshift, a given source could be either at higher-redshift and *IRAS*-like or at lower-redshift and OS-like — indicating that it is probably much more difficult to obtain reliable estimates of redshift using this method than previously thought. In fact, it seems that the temperature of the dust does affect the position of a galaxy on the $\alpha_{1.4}^{850}$–z diagram, and that as a consequence of the differing proportions of warm and cold dust in local galaxies, which has quite clearly been shown for the two SLUGS samples, the CY00 radio-submillimetre redshift indicator is unlikely to be reliable as a redshift estimator for deep submillimetre sources without first making assumptions about the temperature of the dust in those objects.

6.4.1 Comparison of the SLUGS redshift indicators with deep SCUBA observations

It is also immediately evident that the Chapman et al. (2005) sources mostly do not agree at all with the redshift indicators found for either the OS or IRS SLUGS, the majority of them lying at much lower $\alpha_{1.4}^{850}$ at a given redshift. Lewis, Chapman & Helou (2005) find a similar result comparing their model predictions to measurements of deep submillimetre sources. From the FIR–radio relationship we see at low redshifts we would expect the Chapman et al. sources to follow a tight relationship between $\alpha_{1.4}^{850}$ and redshift, but they quite clearly do not.

There are many possible explanations. One potential explanation could be that the Chapman et al. sources have significant AGN-type activity contributing to their 1.4 GHz emission (an extreme example in the local universe would be NGC6166 and the other six

or so outliers in the OS sample FIR-radio correlation plot shown in Figure 6.4) — if dust is heated to higher temperatures in stronger radiation fields, e.g. near to AGN, we could expect to see both higher 1.4 GHz emission and higher dust temperature — however, based on observations at low redshift the amount of contamination at high redshift by FRI radio sources has been estimated to be less than 30% (e.g. Yun et al. 1999), unless the contribution from radio-loud AGN changes with redshift (Gruppioni et al. 1999). Another possibile explanation could be that dust properties are different at high-redshift, for example if there are different metallicities, magnetic field strengths or dust opacities. This leads to yet another possibility, which is that the tight FIR–radio correlation we see in the local universe in fact changes with redshift; potentially this could occur if the dust mass opacity coefficient is different at higher redshifts, for example if the dust composition or size differs due to lower metallicities. This would not explain the scatter, however, since if this were the case then there should still be some kind of trend with redshift.

Chapman et al. suggest that the large scatter seen for these deep submillimetre sources could also possibly be explained by variations in the dust temperature. The marked differences seen between the OS and IRS galaxies may provide some evidence for this, although it is noted that the increased scatter in the $\alpha_{1.4}^{850}$-z relation for the OS sample arises because of increased cold dust components while for warmer objects the two samples are very similar. A handful of the Chapman et al. sources do agree with the predictions for the IRS galaxies, and because of the much wider scatter for the OS sample about twice as many agree with the OS sample galaxies, thus if temperature variations are to explain the scatter for the Chapman et al. points then at least half of those objects must be very much hotter than any seen in the SLUGS samples. Although the results of the OS SLUGS FIR–radio and submillimetre–radio luminosity correlations (Section 6.3) are evidence that, in the local universe at least, the tight FIR–radio relation is due to massive star-formation, the Bettens et al. (1999) chemical evolution explanation for the FIR–radio relation would provide for both higher radio emission and hotter temperature

and so could potentially explain some of the scatter for the high-redshift sources. That model would also imply that those high-redshift sources would have much higher star-formation rates than we see at lower redshifts. One might also argue that the difference between the SLUGS curves and the deep SCUBA sources arises because the latter are more luminous objects, but the fact that we see no correlation in our plot of $\alpha_{1.4}^{850}$ versus 850 μm luminosity (Figure 6.6(b)) argues strongly against that.

Although the meaning of these results is still unclear, the inherent scatter seen for the deep sources compared to the $\alpha_{1.4}^{850}$–z relation for the SLUGS samples suggests it is unlikely there is any single factor which will explain the variation of $\alpha_{1.4}^{850}$ at higher redshifts. It does seem evident, though, that in the large majority of cases the high-redshift SCUBA sources would have to be quite different to the objects we are seeing in the local universe, whether in terms of dust temperature, opacity or other properties (luminosity, AGN-contribution etc.). If only a small proportion of high-redshift submillimetre sources, if any, are similar to those we see in the local universe then it would also mean that the radio-submillimetre redshift indicator is unlikely to provide reliable estimates of the redshifts of majority of deep submillimetre sources.

6.5 Summary

Using the results of the OS SLUGS sample I have investigated the relationships between far-IR–submillimetre and radio properties for 'normal' local galaxies, compared to the bright *IRAS* galaxies in the IRS SLUGS sample (D00/LD00). The results for the OS galaxies have then been used to assess the reliability of the Carilli & Yun (1999, 2000a) radio–submillimetre redshift estimator technique, for the first time using a sample containing significant fractions of cold dust.

There is a very tight correlation between 1.4 GHz luminosity and 60 μm and FIR luminosity for the OS sample gaalaxies. There is much more scatter in the correlation between

radio and 850 μm luminosity, suggesting that, while the 60 μm and radio luminosities are both related to star-forming regions, a significant amount of the 850 μm emission from 'normal' galaxies must be due to colder (20 K) dust heated by the general interstellar radiation field (ISRF). The scatter in the 850 μm–radio relation is also much larger than found for the previous sample of IRS galaxies (D00/LD00), indicating that optically-selected galaxies must contain larger proportions of cold dust.

There is a correlation between $\alpha_{1.4}^{850}$ and both FIR and radio luminosity, but there is no correlation of $\alpha_{1.4}^{850}$ with 850 μm luminosity. These results most likely indicate that the radio and FIR emission are both related to star-forming regions while significant proportions of the 850 μm emission must be related to colder dust heated by the ISRF. From this we conclude that 850 μm luminosity is unlikely to be a source of bias for the Carilli & Yun redshift estimator technique.

Using the SEDs of the 17 OS galaxies detected at both 850- and 450- μm we have shown that for a sample of 'normal' galaxies there is much more scatter in the $\alpha_{1.4}^{850}$-redshift relation than seen for the bright *IRAS* galaxies of the IRS SLUGS sample or the CY00 sample, most likely due to the inclusion of objects containing large fractions of cold dust. From this we conclude that in order for the CY00 radio-submillimetre redshift indicator to be reliable as a redshift estimator for deep submillimetre sources one would first be required to make assumptions about the temperature of the dust in those objects.

We have compared our OS $\alpha_{1.4}^{850}$-redshift relations to the deep submillimetre observations of Chapman et al. (2005) and demonstrate that the large majority of these deep SCUBA sources must have very different properties to our sample of 'normal' low-redshift galaxies; if this is indicative of the submillimetre population as a whole then the Carilli & Yun method is unlikely to provide reliable estimates of the redshifts of majority of deep submillimetre sources.

Chapter 7

Conclusions

This thesis has presented new results from the SCUBA Local Universe Galaxy Survey (SLUGS) — the first systematic submillimetre survey of the local Universe free from dust temperature selection effects. I have presented a sample of 81 optically-selected galaxies – the OS sample – observed with the SCUBA camera on the James Clerk Maxwell Telescope at 850 μm and 450 micron. Since SCUBA is sensitive to the 90% of dust too cold to radiate significantly in the *IRAS* bands this new optically-selected sample represents the first unbiased survey of dust in galaxies along the whole length of the Hubble sequence. An unbiased survey of the dust in galaxies is also important because of the need to interpret the results from surveys of the distant Universe. The previous SLUGS sample consisted of 104 *IRAS*-selected galaxies (D00/LD00), and though it provided the first direct local measurement of the submillimetre luminosity function (LF), because of its selection at 60 μm the sample was by definition biased towards warmer dust. The optically-selected sample presented in this thesis should by definition be free from dust temperature selection effects, and as such a main aim of this work was to produce a fully representative sample and address the possibility that the previous *IRAS* sample 'missed' a population of cold-dust-dominated galaxies.

7.1   The submillimetre properties of 'normal' galaxies in the local universe

Chapter 3 presented the results of the OS SLUGS sample, including 850 μm and 450 μm fluxes and fitted dust spectral energy distributions. The results can be summarised as follows.

- Out of 81 galaxies in the OS sample 52 were detected at 850 μm and 19 were detected at 450 μm. Many of these galaxies have 850 μm emission which appears extended with respect to the DSS optical emission, and which appears to correspond to very faint optical features.

- I have produced 850 μm S/N maps of the OS galaxies and by comparing them to optical DSS images I have found that there is a variety of submillimetre morphologies in the sample. Some galaxies exhibit core-dominated emission, similar to that found for the previous IRS SLUGS sample of bright *IRAS* galaxies, while others exhibit two distinct peaks of emission associated with the spiral arm structure. These results are consistent with numerous other mm/submm studies of nearby galaxies in the literature. Others still exhibit a combination of these features and some have apparently asymmetric or offset submillimetre emission compared to the optical.

- I have fitted two-component dust spectral energy distributions to the 60, 100, 450 and 850 μm flux densities for 18 of the galaxies which were detected at 850 μm *and* at 450 μm. I have shown that the *IRAS* and submillimetre fluxes are well-fitted by a two-component dust model with dust emissivity index β=2. The tight and fairly constant ratio of S_{450}/S_{850} for both the OS galaxies and the IRS galaxies is evidence that $\beta \approx 2$. The temperatures of the warm component range from 28 to 59 K; the cold component temperatures range from 17 to 24 K.

- I have found the ratio of the mass of cold dust to the mass of warm dust is much

higher for our optically-selected galaxies than for the previous SLUGS sample of *IRAS*-selected galaxies (DE01), and can reach values of $\sim$1000. By comparing the results for the *IRAS*- and optically-selected samples I have shown that there is a population of galaxies containing a large proportion of cold dust that is unrepresented in the *IRAS* sample.

- I also fitted single-temperature dust spectral energy distributions (to the 60, 100 and 850 μm flux densities) for the 41 galaxies in the OS sample with detections in all 3 wavebands. The mean best-fitting temperature for the sample is $\bar{T}_d = 31.6 \pm 0.6$K and the mean dust emissivity index is $\bar{\beta} = 1.12 \pm 0.05$. These values are significantly lower than for the IRS sample. The very low value of β is additional evidence that galaxies, across all Hubble types, contain a significant amount of cold dust.

- I find a mean dust mass $\bar{M}_d = (2.34 \pm 0.36) \times 10^7$ $M_\odot$ using the isothermal fits. However, using the two-component fits I find a mean dust mass a factor of two higher.

- I find a mean neutral gas-to-dust ratio $\bar{M}_{HI}/M_{d2}$=192$\pm$44 for the OS galaxies with two-component fits which, in the absence of significant amount of molecular gas, is in good agreement with the Galactic value.

- Out of 11 elliptical galaxies in the sample 6 were detected, and found to have dust masses in excess of 10^7 $M_\odot$. It is possible, however, that for some of these galaxies the submillimetre emission may be synchrotron emission rather than dust emission.

In **Chapter 4** I have presented an analysis of the OS sample results, compared to the previous results for the IRS sample, and have discussed what this tells us about the properties of 'normal' galaxies in the local Universe, along the whole length of the Hubble sequence, compared to bright *IRAS* galaxies.

- There are strong correlations of both the S_{60}/S_{100} and S_{100}/S_{850} colours with S_{60}/S_{850}

colour for both the OS and IRS samples. This relationship is important as it will allow the production of the submillimetre luminosity function using a large sample of galaxies from the PSCz survey (Saunders et al. 2000) which have 60 μm and 100 μm (but not 850 μm) fluxes, as I will describe in the following Chapter.

- I find that the ratio of the mass of cold dust to the mass of warm dust is much higher for the optically-selected galaxies than for the previous work on *IRAS*-selected galaxies (DE01/LD00), and can reach values of ~1000. By comparing the results for the *IRAS*- and optically-selected samples I have shown that there is a population of galaxies containing a large proportion of cold dust that is unrepresented in the *IRAS* sample.

- The OS galaxies also have very much lower FIR luminosities, with the mean FIR luminosity being an order of magnitude lower.

- I have found differences in the relations between FIR luminosity and optical blue luminosity, between the ratio of 850 μm-to-optical luminosity and FIR luminosity, and between dust mass and optical luminosity for the OS and IRS galaxies, and conclude that a likely explanation would be the presence of significant extinction at optical wavelengths in the *IRAS*-selected galaxies.

- There appears to be little change in the properties of dust in galaxies along the Hubble sequence, except a marginally significant trend for early-type galaxies to be less luminous submillimetre sources than late-types. This is not what one might expect, a priori, if a galaxy's dust and gas are associated with its disk; a simple analysis of typical bulge-to-disk ratios showed that we should expect to find at least three times as much dust in late-types as in early types such as S0s; in fact in the OS sample the distribution of dust masses is relatively similar across all Hubble types.

In **Chapter 5** I used the new OS sample results to produce new estimates of the local submillimetre luminosity and dust mass functions.

- I have derived local submillimetre luminosity and dust mass functions, both directly from the optically-selected SLUGS sample and by extrapolation from the *IRAS* PSCz survey, and find excellent agreement between the two. By extrapolating the spectral energy distributions of the *IRAS* PSCz survey galaxies out to 850 μm we have probed a wider range of luminosities than probed directly by the SLUGS samples.

- The LFs are well-fitted by Schechter functions except at the highest luminosities. Whereas the slope of the IRS sample LF (D00/LD00) at low luminosities was steeper than −2 (a submillimetre 'Olbers' Paradox'), I have shown that the PSCz-extrapolated LF, as expected, flattens out at the low luminosity end and has a slope of −1.38.

- I have shown that as a consequence of the omission of a population of 'cold' dusty galaxies from the IRS sample the LF presented by D00/LD00 is too low by a factor of two, and the DMF by a factor of four.

7.2 Applications of the OS SLUGS results to the high-redshift universe

Chapter 6. Using the results of the OS SLUGS sample I have investigated the relationships between far-IR–submillimetre and radio properties for 'normal' local galaxies, compared to the bright *IRAS* galaxies in the IRS SLUGS sample (D00/LD00). The results for the OS galaxies have then been used to assess the reliability of the Carilli & Yun (1999, 2000a) radio–submillimetre redshift estimator technique, for the first time using a sample containing significant fractions of cold dust.

- There is a very tight correlation between 1.4 GHz luminosity and 60 μm and FIR luminosity for the OS sample gaalaxies. There is much more scatter in the corre-

lation between radio and $850\,\mu$m luminosity, suggesting that, while the $60\,\mu$m and radio luminosities are both related to star-forming regions, a significant amount of the $850\,\mu$m emission from 'normal' galaxies must be due to colder (20 K) dust heated by the general interstellar radiation field (ISRF). The scatter in the $850\,\mu$m–radio relation is also much larger than found for the previous sample of IRS galaxies (D00/LD00), indicating that optically-selected galaxies must contain larger proportions of cold dust.

- There is a correlation between $\alpha_{1.4}^{850}$ and both FIR and radio luminosity, but there is no correlation of $\alpha_{1.4}^{850}$ with $850\,\mu$m luminosity. These results most likely indicate that the radio and FIR emission are both related to star-forming regions while significant proportions of the $850\,\mu$m emission must be related to colder dust heated by the ISRF. From this we conclude that $850\,\mu$m luminosity is unlikely to be a source of bias for the Carilli & Yun redshift estimator technique.

- Using the SEDs of the 17 OS galaxies detected at both 850- and 450-μm we have shown that for a sample of 'normal' galaxies there is much more scatter in the $\alpha_{1.4}^{850}$-redshift relation than seen for the bright *IRAS* galaxies of the IRS SLUGS sample or the CY00 sample, most likely due to the inclusion of objects containing large fractions of cold dust. From this we conclude that in order for the CY00 radio-submillimetre redshift indicator to be reliable as a redshift estimator for deep submillimetre sources one would first be required to make assumptions about the temperature of the dust in those objects.

- We have compared our OS $\alpha_{1.4}^{850}$-redshift relations to the deep submillimetre observations of Chapman et al. (2005) and demonstrate that the large majority of these deep SCUBA sources must have very different properties to our sample of 'normal' low-redshift galaxies; if this is indicative of the submillimetre population as a whole then the Carilli & Yun method is unlikely to provide reliable estimates of the

redshifts of majority of deep submillimetre sources.

7.3 Future Work

Further observations from which the OS SLUGS sample would benefit are as follows.

- Due to the increased sensitivity to weather conditions at 450 μm, sources emitting at 450 μm will only be detected if they are relatively bright at 850 μm. This, together with the wide range of observing conditions for this sample, meant that useful 450 μm data was found for only 19 objects. For these objects, however, I have fitted two-component dust models and found this subsample to have very large cold dust components (ratio of cold-to-warm dust ∼ 1000). From many of the results listed above I have shown the presence of large proportions of cold dust, but in order to quantify this for the whole OS sample further shorter wavelength submillimetre observations are needed.

- Additional submillimetre observations (both the long and short wavelengths) of some objects whose existing SCUBA observations were taken in very bad weather would provide confirmation of those results (many of which in this current sample did not meet the 3σ detection criterion).

- It would also be very useful to obtain additional HI measurements (as currently we only have HI data for ∼ half the sample) in order to increase the statistical significance of the gas and dust comparisons, and also CO measurements (as currently we have no CO data for the sample) in order to determine the total (molecular + neutral) gas-to-dust ratio.

- In order to further investigate the properties of dust in galaxies follow-up optical imaging (to obtain deeper images than available from the DSS) for the whole OS

sample detected at 850 μm is needed, in order to make a full comparison of the optical versus submillimetre emission. This is important since for many of the OS sample galaxies the 850 μm emission appears extended with respect to the DSS optical emission. Work on obtaining this data is in progress.

- Work on the existing optical follow-up data is in progress.

- Also of importance would be to investigate the dust content of a larger sample of early-type galaxies.

Appendix A

Isothermal Spectral Energy Distributions

This appendix contains the isothermal spectral energy distributions (SEDs) for all the OS SLUGS sample objects with fluxes at $850\,\mu$m (SCUBA), $100\,\mu$m and $60\,\mu$m (*IRAS*) (41 objects). The SEDs are fitted to these 3 data points as described in Chapter 3 Section 3.5.2.

NGC 6189
T = 28.6 K
β = 1.1

NGC 6190
T = 28.0 K
β = 1.0

IC 5090
T = 31.6 K
β = 1.2

IC 1368
T = 37.6 K
β = 1.3

NGC 7047
T = 28.0 K
β = 1.1

NGC 7081
T = 32.8 K
β = 1.3
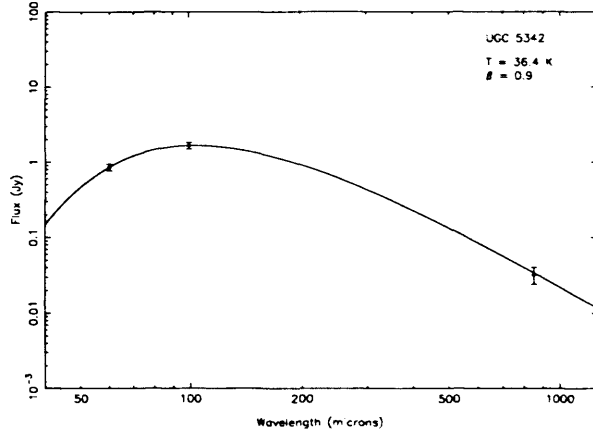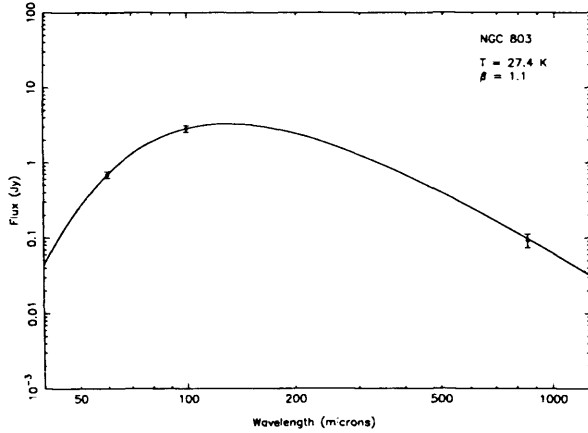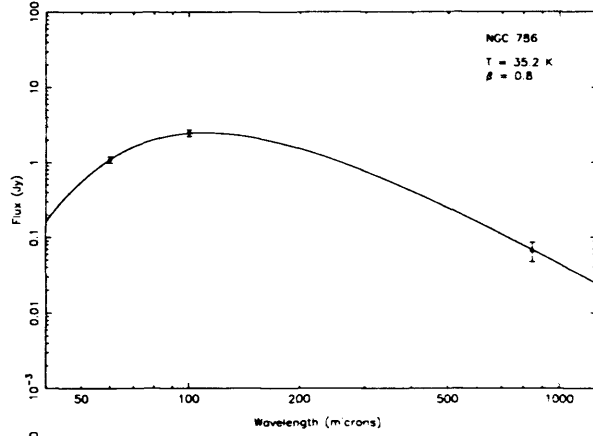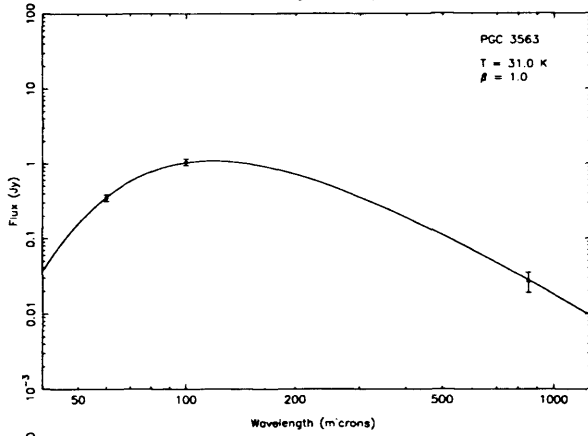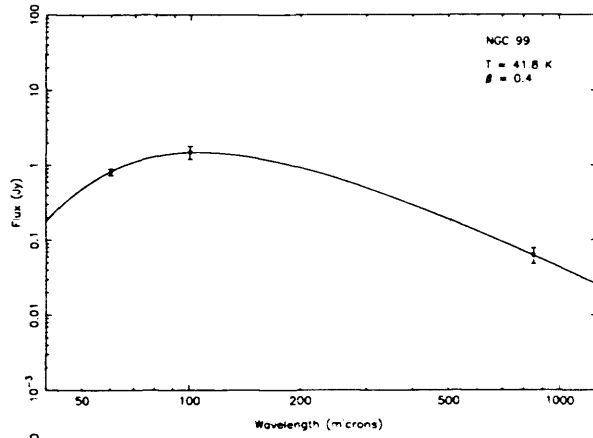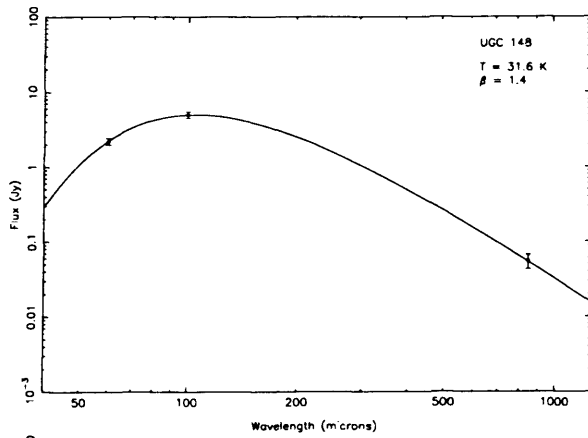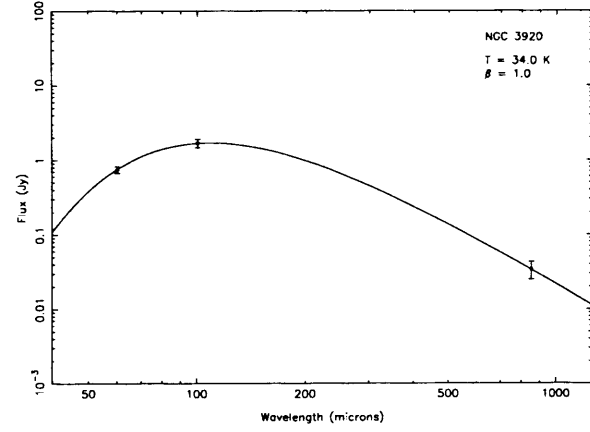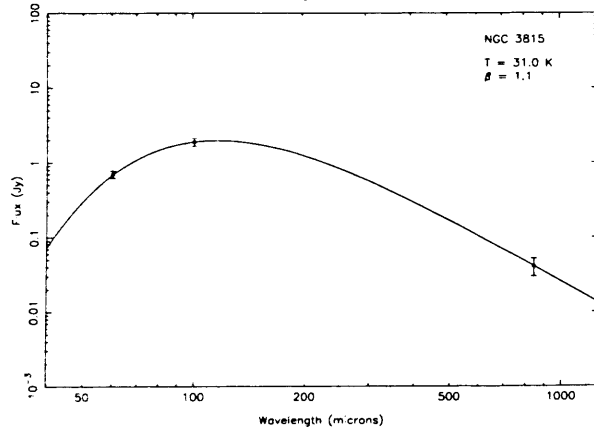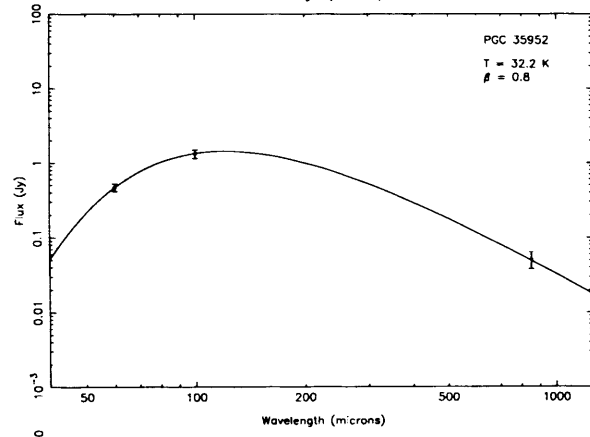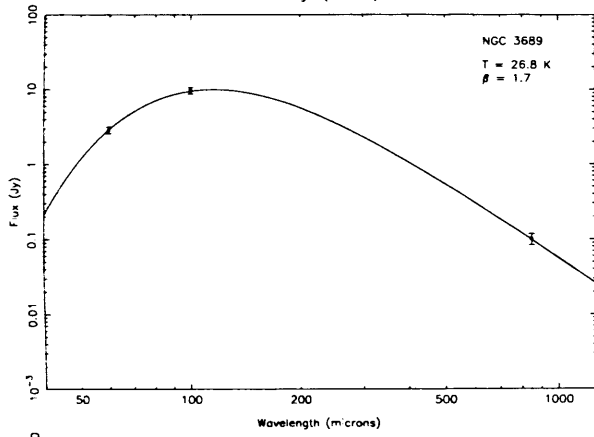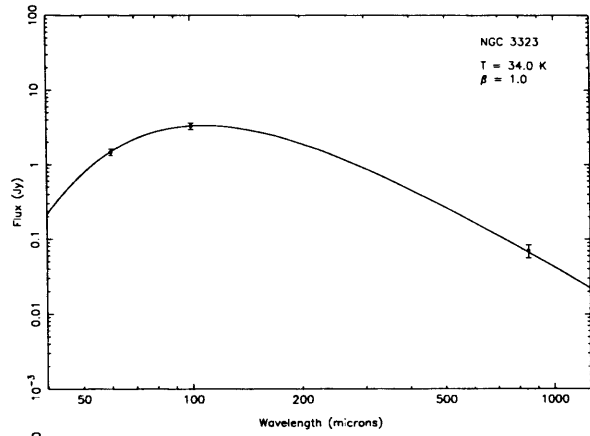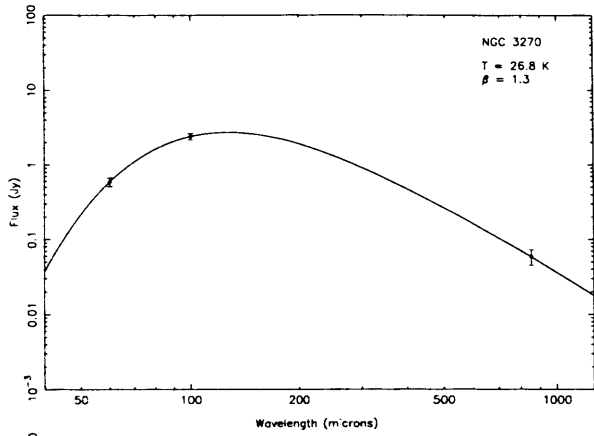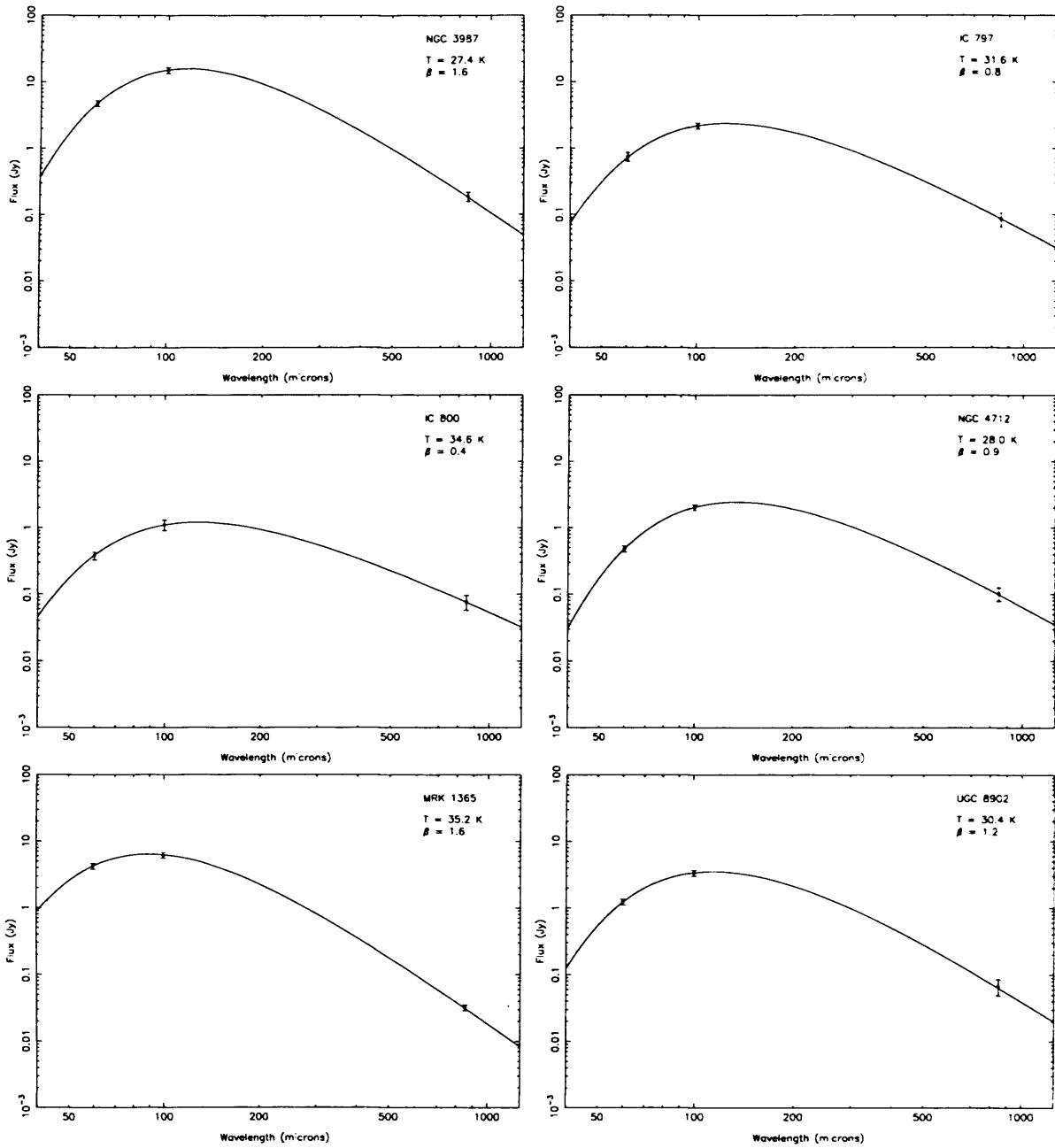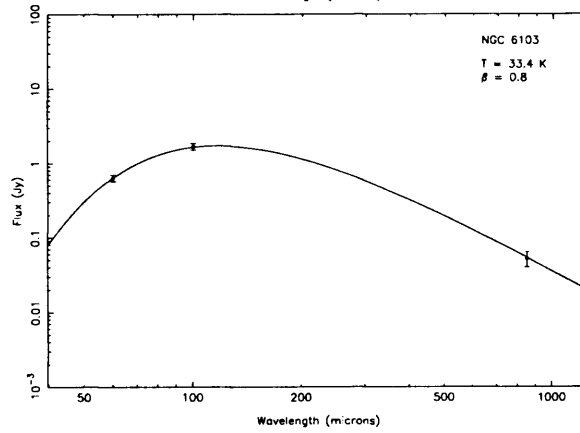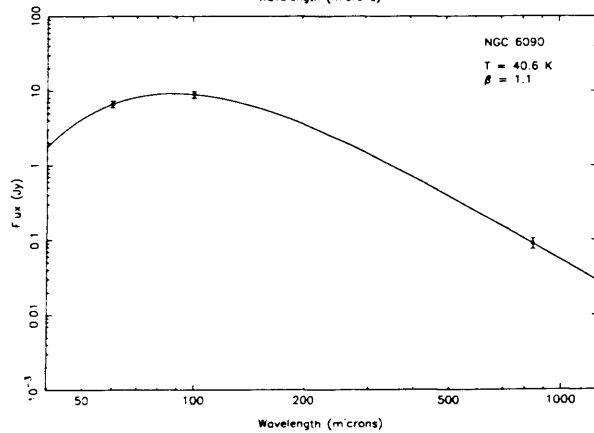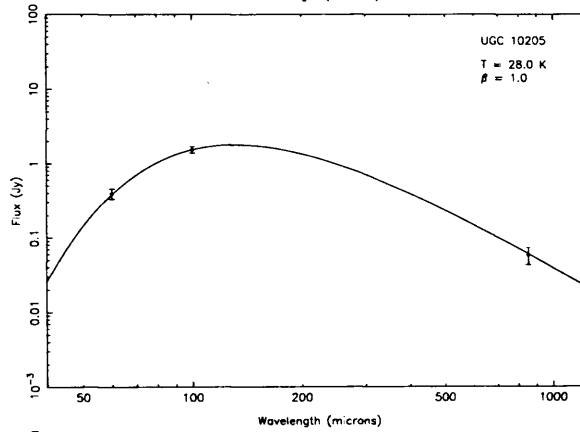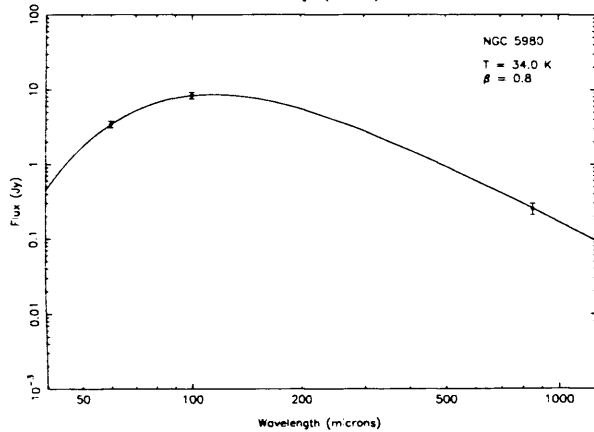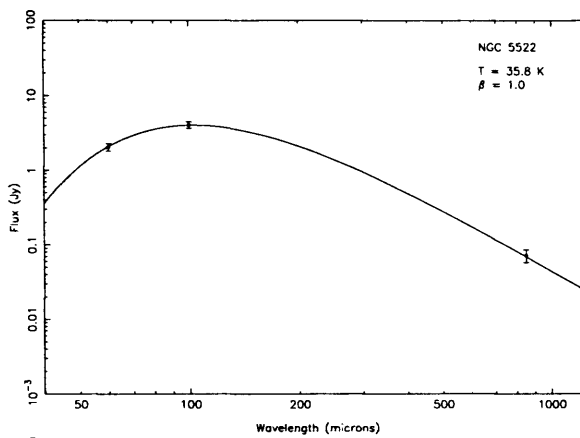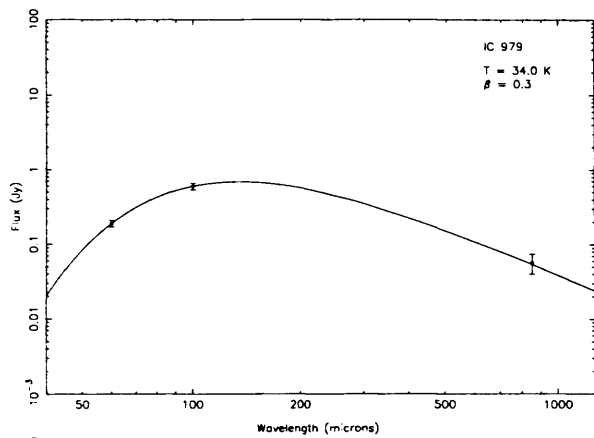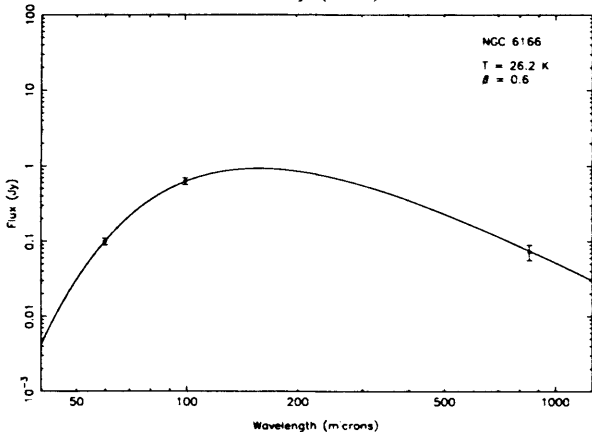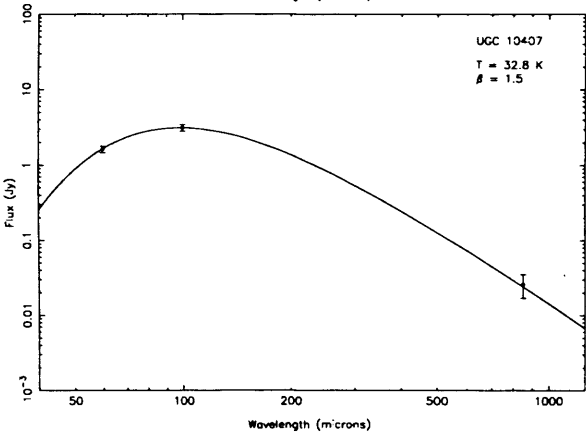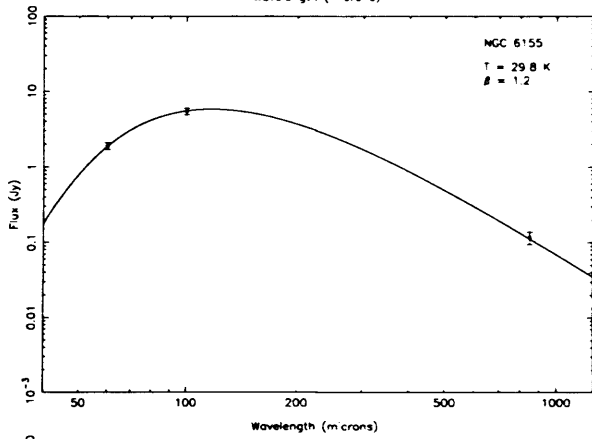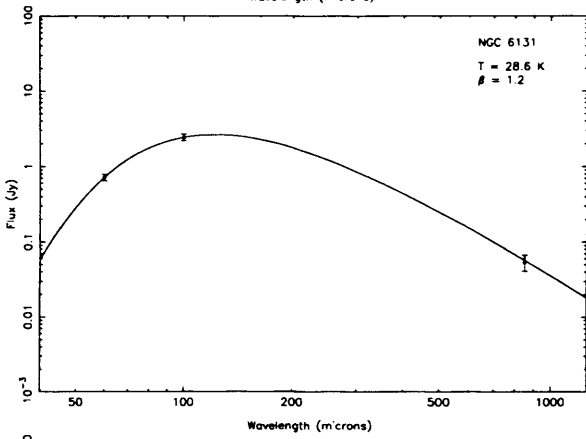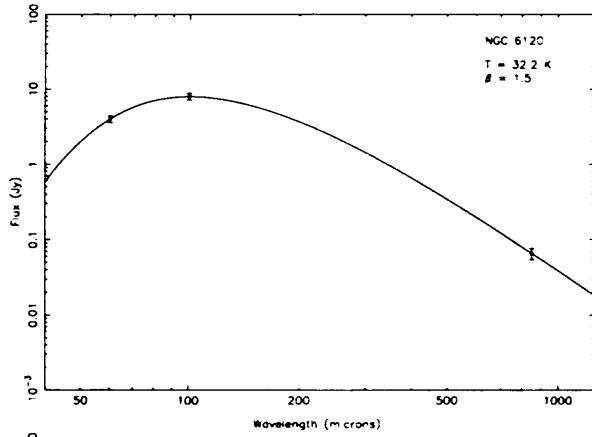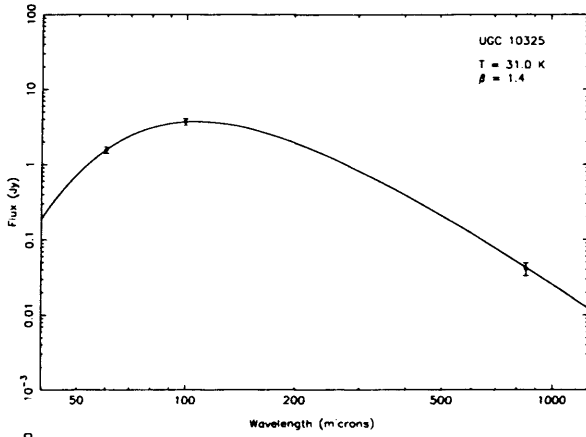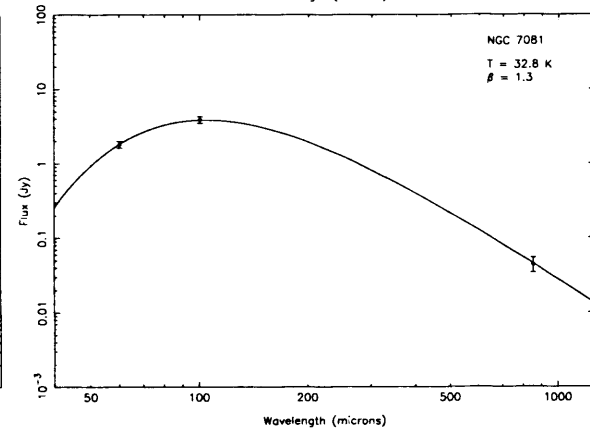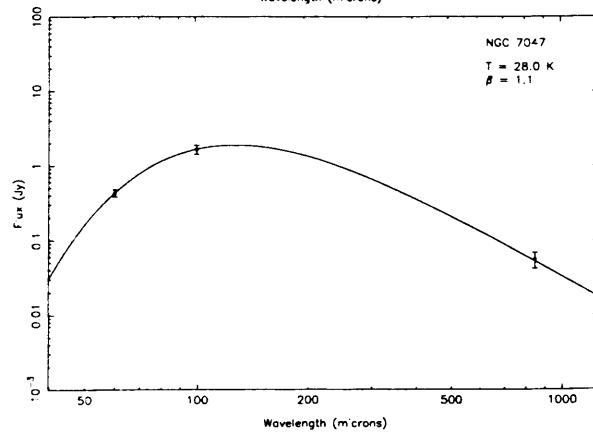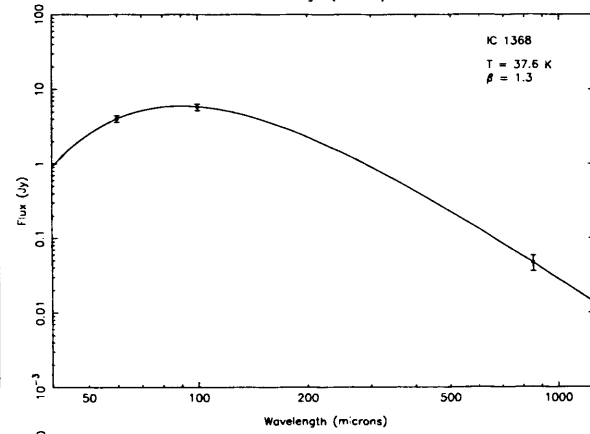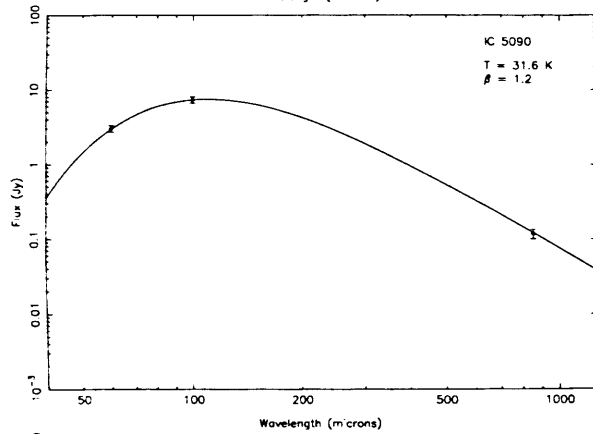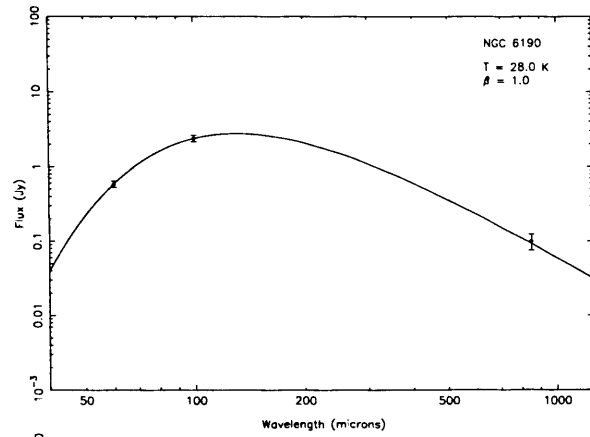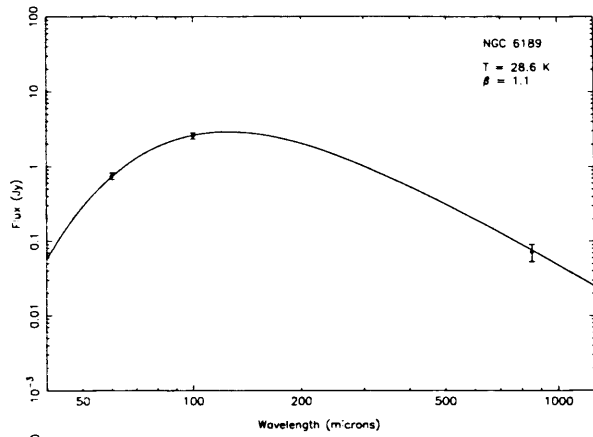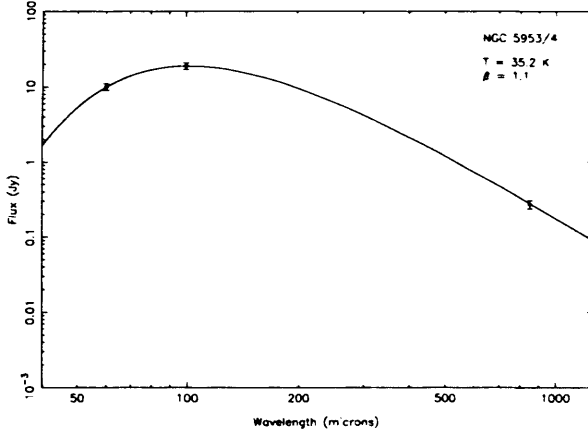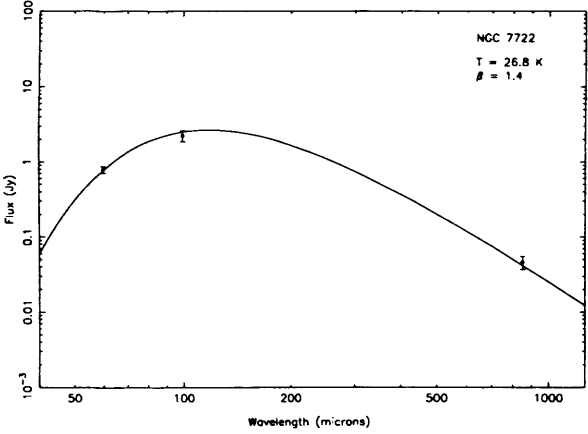
Bibliography

[1] Abazajian K. et al. 2005, AJ, 129, 1755

[2] Alton P.B. et al., 1998a, A&A, 335, 807

[3] Alton P.B., Bianchi S., Rand R.J., Xilouris E., Davies J.I., Trewhella M., 1998b, ApJ, 507, L125

[4] Alton P.B., Lequeux J., Bianchi S., Churches D., Davies J., Combes F., 2001, A&A, 366, 451
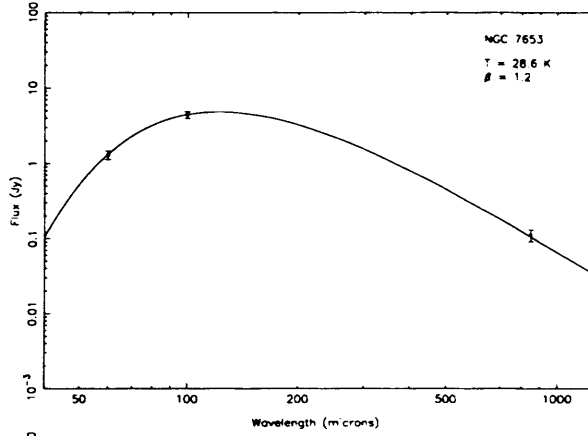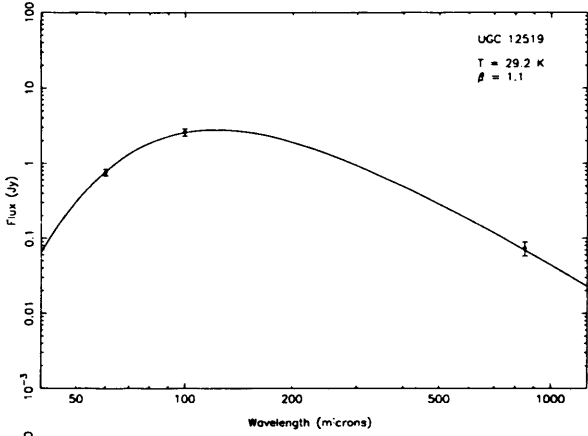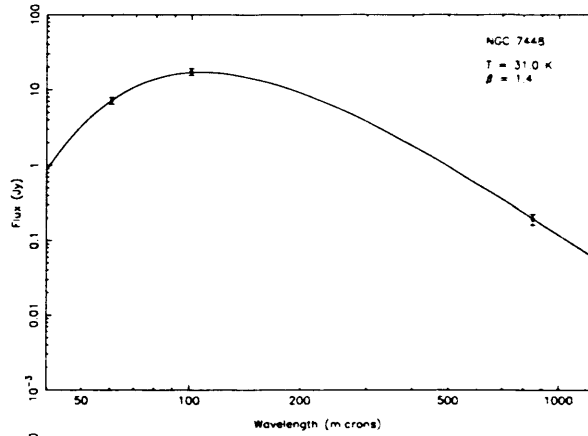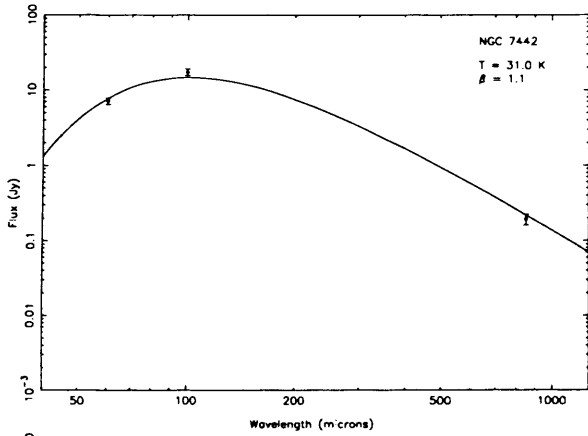
[5] Archibald E.N. et al., 2002, MNRAS, 336, 1

[6] Aumann H.H., Fowler J.W., Melnyk M., 1990, ApJ, 99, 1674

[7] Avni Y., Bahcall J.N., 1980, ApJ, 235, 694

[8] Barger A.J., Cowie L.L., Sanders D.B., Fulton E., Taniguchi Y., Sato Y., Kawara K., Okuda H., 1998, Nat, 394, 248

[9] Barger A.J., Cowie L.L., Sanders D.B., 1999, ApJ, 518, L5

[10] Barger A.J., Cowie L.L., Richards E.A., 2000, AJ, 119, 2092

[11] Becker R.H., While R.L., Helfand D.J., 1995, ApJ, 450, 559

[12] Bettens R.P.A., Brown R.D., Cragg D.M., Dickinson C.J., Godfrey P.D., 1993, MN-RAS, 263, 93

[13] Bianchi S., Alton P.B., Davies J.I., Trewhella M., 1988, MNRAS, 298, L49

[14] Bianchi S., Davies J.I., Alton P.B., Gerin M., Casoli F., 2000, A&A, 353, L13

[15] Blain A.W., 1999, MNRAS, 309, 955

[16] Blain A.W., Kneib J.-P., Ivison R.J., Smail I., 1999a, ApJ, 512, L87

[17] Blain A.W., Smail I., Ivison R.J., Kneib J.-P., 1999b, MNRAS, 302, 632

[18] Bothun G.D., Lonsdale C.J., Rice W., 1989, ApJ, 341, 129

[19] Braine J., Guélin M., Dumke M., Brouillet N., Herpin F., Wielebinski R., 1997, A&A, 326, 963

[20] Bregman J.N., Snider B.A., Grega L., Cox C.V., 1998, ApJ, 499, 670

[21] Calzetti, D., 2001, PASP, 113, 1449

[22] Carilli C.L., Yun M.S., 1999, MNRAS, 513, L13

[23] Carilli C.L., Yun M.S., 2000, AJ, 530, 618

[24] Catalogued Galaxies and Quasars Observed in the *IRAS* Survey, 1989, Version 2. Prepared by Fullmer L., Lonsdale C.J., JPL, Pasadena

[25] Chamaraux P., Balkowski C., Fontanelli P., 1987, A&AS, 69, 263

[26] Chapman S.C., Blain A.W., Smail I., Ivison R.J., 2005, AJ, 622, 772

[27] Chini R., Krügel E., Kreysa E., Gemuend H.-P., 1989, A&A, 216, L5

[28] Chini R. & Krügel E., 1993, A&A, 279, 385

[29] Clements D.L., Andreani P., Chase S.T., 1993, MNRAS, 261, 299

[30] Clerke A.M., 1903, Problems in Astrophysics, Black, London, p.567

[31] Condon J.J., 1992, ARA&A, 30, 575

[32] Condon J.J., Broderick J.J., 1988, AJ, 96, 30

[33] Condon J.J., Yin Q.F., 1990, ApJ, 357, 97

[34] Condon J.J., Frayer D.T., Broderick J.J., 1991, AJ, 101, 362

[35] Condon J.J., Huang Z.-P., Yin Q.F., Thuan T.X., 1991, ApJ, 378, 65

[36] Condon J.J., Greisen E.W., Yin Q.F., Perley R.A., Taylor G.B., Broderick J.J., 1998, AJ, 115, 1693

[37] Condon J.J., Cotton W.D., Broderick J.J., 2002, AJ, 124, 675

[38] Contursi A., Boselli A., Gavazzi G., Bertagna E., Tuffs R., Lequeux J., 2001, A&A, 365, 11

[39] Cox C.V., Bregman J.N., Schombert J.M., 1995, ApJS, 99, 405

[40] Cox P., Krügel E., Mezger P.G., 1986, A&A, 155, 380

[41] Davies J.I., Alton P., Trewhella M., Evans R., Bianchi S., 1999, MNRAS, 304, 495

[42] Devereux N.A., Eales S.A., 1989, AJ, 340, 708

[43] Devereux N.A., Young J.S., 1990, ApJ, 359, 42

[44] Downes D. et al., 1999, A&A, 347, 809

[45] Draine B.T., Lee H.M., 1984, AJ, 285, 89

[46] Dumke M., Braine J., Krause M., Zylka R., Wielebinski R., Guélin M., 1997, A&A, 325 124

[47] Dunne L., 2000, PhD thesis, University of Wales

[48] Dunne L., Clements D.L., Eales S.A., 2000, MNRAS, 319, 813

[49] Dunne L., Eales S., Edmunds M., Ivison R., Alexander P., Clements D.L., 2000, MNRAS, 315, 115

[50] Dunne L., Eales S.A., 2001, MNRAS, 327, 697

[51] Dunne L., Eales S., Ivison R., Morgan H., Edmunds M., 2003, Nat, 424, 285

[52] DuPrie K., Schneider S.E., 1996, AJ, 112 937

[53] Eales S.A., Wynn-Williams C.G., Duncan W.D., 1989, ApJ, 339, 859

[54] Eales S.A., Lilly S.J., Gear W.K., Dunne L., Bond R.J., Hammer F., Le Fèvre O., Crampton D., 1999, ApJ, 515, 518

[55] Eales S.A., Lilly S.J., Webb T., Dunne L., Gear W.K., Clements D.L., Yun M.S., 2000, AJ, 120, 2244

[56] Economou F., Jenness T., Currie M., Adamson A., Allan A., Cavanagh B., 2004, Starlink User Note 230, Starlink Project, CLRC

[57] Feigelson, E.D., Nelson, P.I., 1985, ApJ, 293, 192

[58] Fixsen D.J., Dwek E., Mather J.C., Bennett C.L., Shafer R.A., 1998, ApJ, 508, 123

[59] Frayer D.T., Ivison R.J., Smail I., Yun M.S., Armus L., 1999, AJ, 118, 139

[60] Freudling W., 1995, A&AS, 112, 429

[61] Genzel R. et al., 1998, ApJ, 498, 579

[62] Giovanelli R., Haynes M.P., 1993, AJ, 105, 1271

[63] Gordon, M.A., 1995, A&A, 301, 853

[64] Goudfrooij P., Hansen L., Jørgensen H.E., Nørgaard-Nielsen H.U., 1994, A&AS, 105, 341

[65] Goudfrooij P., de Jong T., 1995, A&A, 298, 784

[66] Guélin M., Zylka R., Mezger P.G., Haslam C.G.T., Kreysa E., Lemke R., Sievers A.W., 1993, A&A, 279, L37

[67] Guélin M., Zylka R., Mezger P.G., Haslam C.G.T., Kreysa E., 1995, A&A, 298 L29

[68] Haas M., Lemke D., Stickel M., Hippelein H., Kunkel M., Herbstmeier U., Mattila K., 1988, A&A, 338, L33

[69] Haas M., Klaas U., Coulson I., Thommes E., Xu C., 2000, A&A, 356, L83

[70] Hambly N.C. et al., 2001, MNRAS, 326, 1279

[71] Haynes M.P., Giovanelli R., 1988, AJ, 95, 607

[72] Haynes M.P., Giovanelli R., 1991, ApJS, 77, 331

[73] Haynes M.P., Giovanelli R., Chamaraux P., da Costa L.N., Freudling W., Salzer J.J., Wegner G., 1999, AJ, 117, 2039

[74] Hauser M.G. et al., 1998, ApJ, 508, 25

[75] Helou G., Soifer B.T., Rowan-Robinson M., 1985, ApJ, 298, L7

[76] Helou G., Khan I.R., Malek L., Boehmer L., 1988, ApJS, 68, 151

[77] Helou G., Bicay M.D., 1993, ApJ, 415, 93

[78] Herschel W., 1785, Philosophical Transactions of the Royal Society of London, vol.75, p.213

[79] Hildebrand R.H., 1983, QJRAS, 24, 267

[80] Hippelein H., Haas M., Tuffs R.J., Lemke D., Stickel M., Klaas U., Völk H.J., 2003, A&A, 407, 137

[81] Holland W.S. et al., 1999, MNRAS, 303, 659

[82] Huchra J., Davis M., Latham D., Tonry J., 1983, ApJS, 52, 89

[83] Huchtmeier W.K., 1997, A&A, 319, 401

[84] Huchtmeier W.K., Richter O.-G., 1989, A General Catalog of HI Observations of Galaxies: The Reference Catalog, XIX. Springer-Verlag, Berlin, Heidelberg, New York

[85] Hughes D.H. et al., 1998, Nat, 394, 241

[86] *IRAS* Explanatory Supplement, 1988, Beichman C.A., Neugebauer G., Habing H.J., Clegg P.E., Chester T.J., eds, Jet Propulsion Laboratory, Pasadena

[87] Ivison R.J., Smail I., Le Borgne J.-F., Blain A.W., Kneib J.-P., Bezecourt J., Kerr T.H., Davies J.K., 1998, MNRAS, 298,583

[88] Ivison R.J., Smail I., Barger A.J., Kneib J.-P., Blain A.W., Owen F., Kerr T.H., Cowie L., 2000, MNRAS, 315, 209

[89] James A., Dunne L., Eales S., Edmunds M.G., 2002, MNRAS, 335, 753

[90] Jenness T., Lightfoot J.F., 1998, in Albrecht R., Hook R.N., Bushouse H.A., eds, ASP Conf. Ser. Vol. 145, Astronomical Data Analysis Software & Systems VII. Astron. Soc. Pac., San Francisco, p. 216

[91] Jenness T., Lightfoot J.F., 2000, SURF – SCUBA User Reduction Facility. Starlink User Note 216, Starlink Project, CLRC

[92] Jenness T., Stevens J.A., Archibald E.N., Economou F., Jessop N.E., Robson E.I., 2002, MNRAS, 336, 14

[93] Joseph R.D., Wright G.S., 1985, MNRAS, 214, 87

[94] Kennicutt, R.C., 1983, A&A, 120, 219

[95] Kent S.M., 1985, ApJS, 59, 115

[96] Knapp G.R., Guhathakurta P., Kim D.-W., Jura M., 1989, ApJS, 70, 329

[97] Lawrence A. et al., 1999, MNRAS, 308, 897

[98] Lewis G.F., Chapman S.C., Helou G., 2005, AJ, 621, 32

[99] Li A., 2004a, Penetrating Bars Through Masks of Cosmin Dust, Block D.L., Freeman K., eds., Kluwer Academic Press

[100] Li A., 2004b, Astrophysics of Dust, Mitt A.N., Clayton G.C., Draine B.T., eds., ASP Conference Series, Vol. 309

[101] Li A., Draine B.T., 2001, AJ, 554, 778

[102] Lilly S.J., Eales S.A., Gear W.K., Hammer F., Le Fèvre O., Crampton D., Bond R.J., Dunne L., 1999, ApJ, 518, 641

[103] Lisenfeld U., Isaak K.G., Hills R., 2000, MNRAS, 312, 433

[104] Lu N.Y., Hoffman G.L., Groff T., Roos T., Lamphier C., 1993, ApJS, 88, 383

[105] Lonsdale Persson C.J., Helou G., 1987, 314, 513

[106] Márquez I. et al., 1999, A&AS, 140,1

[107] Masi S. et al., 1995, ApJ, 452, 253

[108] Mathis J.S., Mezger P.G., Panagia N., 1983, A&A, 128, 212

[109] Meijerink R., Tilanus R.P.J., Dullemond C.P., Israel F.P., van der Werf P.P., 2005, A&A, 430, 427

[110] Mortier A.M.J. et al., 2005, accepted to MNRAS

[111] Moshir M. et al., 1990, Infrared Astronomical Satellite Catalogs, The Faint Source Catalog, version 2.0

[112] Neininger N., Guélin M., García-Burillo S., Zylka R., Wielebinski R., 1996, A&A, 310, 725

[113] Papadopoulos P.P., Seaquist E.R., 1999, ApJ, 514, L95

[114] Paturel G., Fouque P., Bottinelli L., Gouguenheim L., 1989, A&AS, 80, 299

[115] Paturel G., Petit C., Prugniel Ph., Theureau G., Rousseau J., Brouty M., Dubois P., Cambrésy L., A&A, 412 45

[116] Popescu C.C., Tuffs R.J., Völk H.J., Pierini D., Madore B.F., 2002, ApJ, 567, 221

[117] Press W.H., Schechter P., 1974, ApJ, 187, 425

[118] Puget J.-L., Abergel A., Bernard J.-P., Boulanger F., Burton W.B., Desert F.-X., Hartmann D., 1996, A&A, 308, L5

[119] Purcell E.M., 1976, ApJ, 206, 685

[120] Reach W.T. et al., 1995, ApJ, 451, 188

[121] Roche P.F., Aitken D.K., Smith C.H., James S.D., 1986, MNRAS, 218, 19R

[122] Rowan-Robinson M., Crawford J., 1989, MNRAS, 238, 523

[123] Sanders D.B., Soifer B.T., Elias J.H., Madore B.F., Matthews K., Neugebauer G., Scoville N.Z., 1988, ApJ, 325, 74

[124] Saunders W., Rowan-Robinson M., Lawrence A., Efstathiou G., Kaiser N., Ellis R.S., Frenk C.S., 1990, MNRAS, 242, 318

[125] Saunders W. et al., 2000, MNRAS, 317, 55

[126] Schechter P., 1975, PhD thesis, California Institute of Technology

[127] Seaquist E., Yao L., Dunne L., Cameron H., 2004, MNRAS, 349, 1428

[128] Serjeant S., Harrison D., 2005, MNRAS, 356, 192

[129] Sievers A.W., Reuter H.-P., Haslam C.G.T., Kreysa E., Lemke R., 1994, A&A, 281, 681

[130] Smail I., Ivison R.J., Blain A.W., 1997, ApJ, 490, L5

[131] Sodroski T.J., et al., 1994, ApJ, 428, 638

[132] Sodroski T.J, Odegard N., Arendt R.G., Dwek E., Weiland J.L., Hauser M.G., Kelsall T., 1997, ApJ, 480, 173

[133] Soifer B.T., Neugebauer G., 1991, AJ, 101, 354

[134] Soifer B.T., Boehmer L., Neugebauer G., Sanders D.B., 1989, AJ, 98, 766

[135] Spinoglio L., Andreani P., Malkan M.A., 2002, ApJ, 572, 105

[136] Spinoglio L., Malkan M.A., Rush B., Carrasco L., Recillas-Cruz E., 1995, ApJ, 453, 616

[137] Stark A.A., Davidson J.A., Platt S., Harper D.A., Pernic R., Loewenstein R., Engargiola G., Casey S., 1989, ApJ, 337, 347

[138] Stevens J.A., Amure M., Gear W.K., 2005, MNRAS, 357, 361

[139] Stickel M., et al., 2000, A&A, 359, 865

[140] Stickel M., Lemke D., Klaas U., Krause O., Egner S., 2004, A&A, 422, 39

[141] Theureau G., Bottinelli L., Coudreau-Durand N., Gouguenheim L., Hallet N., Loulergue M., Paturel G., Teerikorpi P., 1998, A&AS, 130, 333

[142] Thomas H.C., Dunne L., Clemens M.S., Alexander P., Eales S., Green D.A., James A, 2002, MNRAS, 331 853

[143] Thomas H.C., Dunne L., Green D.A., Clemens M.S., Alexander P., Eales S., 2004, MNRAS, 348, 1197

[144] Trumpler, R.J., 1930, PASP, 42, 214

[145] van Dokkum P.G., Franx M., 1995, AJ, 110, 2027

[146] Wall , Jenkins, 2003, Practical Statistics for Astronomers, CUP

[147] Xilouris E.M., Byun Y.I., Kylafis N.D., Paleologou E.V., Papamastorakis J., 1999, A&A, 344, 868

[148] Yun M.S., Hibbard J.E., Condon J.J., Reddy N., Ap&SS, 266, 29